INFLEXION INSTABILITY

AND

THE INSTABILITY OF TIME-DEPENDENT FLOW

Thesis submitted by

MOHAMMED HASSAN A. SINADA

For the degree of

DOCTOR OF PHILOSOPHY

The Fluid Dynamics Unit

Department Of Physics

UNIVERSITY OF EDINBURGH

May 1984

IN THE NAME OF GOD, MOST GRACIOUS, MOST MERCIFUL

TO MY SON

AUSAMA

ACKNOWLEDGEMENTS

The author gratefully acknowledges the helpful and friendly advice of his supervisor **Dr. C. A. Greated**. He would also like to thank **the Physics Department** and the **Edinburgh Regional Computing Centre** for providing an excellent environment.

Special thanks are due to **Mr. D. Molyneux** for his help during the experimental work, and to **Dr. Q. I. Daudpota** and **Dr. M.A.S. Ross** for their help in the early stages of the numerical work.

His thanks also to countless friends who made it easier for him here. The author gratefully appreciates the financial support of **the Sudan Government**.

Finally, the author would like to thank **his family** for their understanding and encouragement.

ABSTRACT

1) The linear instability of a large number of profiles with inflexion points was studied numerically. In **chapter 4**, it is shown that the instability wavelength is given by the relation $\lambda = K L$ at the critical Re and at both the temporally and spatially most amplified wavenumbers, where the proportionality factor K, has three corresponding values. L is the characteristic width of the flow. Any number of profiles sharing the same values of K, constitute a group. It is shown that both the temporal and the spatial growth rates scale with the corresponding factor K which was found to be proportional to the momentum thickness. The implications of having the above relation are discussed. It is also shown that the relation is satisfied at the upper branch of the neutral stability curve. A comprehensive set of stability data for several time-dependent flow profiles, wake profiles and flows with sinusoidal velocity gradients is given.

2) In **chapter 5**, the stability of time-dependent flow is investigated experimentally for the frequency parameter $3.6 \leqslant \beta \leqslant 8$. The transition Reynolds numbers for both low and high frequency instabilities are determined.

3) In **chapter 6**, the results of the theoretical investigation of the instability of time-dependent flow agree well with the available experimental data for $\beta \geqslant 6$. The critical Reynolds number asymptotically approaches the value $R\delta = 563$. The low frequency instability was also investigated.

4) An extensive comparative study of the energy balance in inflexion instability for both the fundamental and the subharmonic disturbances has been made in **chapter 7**. General rules governing the energy balance distribution in symmetrical profiles are drawn.

LIST OF SYMBOLS

The following symbols are used to describe the quantities indicated in the list, unless otherwise stated in the text.

a- The higher harmonics or the subharmonics order.

b- the half width of the wake

$b_{1/2}$- the half width at half depth

$c=c_r+c_i$- the complex phase velocity

Cd- the drag coefficient

d- the diameter of the pipe, or

the diameter of the cylinder producing the wake

$F(y)=-U''/(U-c)$

F,G,H- matrices (chapter 3)

h- interval size in the finite difference scheme (chapter 3)

or, the width of the channel (chapters 4 and 6)

K- the proportionality factor in $\lambda=KL$,

[For subscripts see the end of this list]

L- the characteristic width of the flow, usually the distance between the points with $U'=0$

N- the expansion order in Galerkin's method, and the number of the intervals in the finite difference scheme

p- the mean flow + the disturbance pressure

P- the mean flow pressure

p- the fundamental disturbance pressure

p- the subharmonic's pressure

q- the velocity ratio in the mixing layer

r- the fundamental disturbance vorticity

r- the subharmonic's vorticity

Re- the Reynolds number

Rδ- the Stokes length Reynolds number

S- the Strouhal number

[For subscripts see the end of this list]

t- time

T- transpose of the matrix

u- the x-component of the mean + the disturbance velocity

u- the x-component of the fundamental disturbance velocity

u- the x-component of the subharmonic's velocity

U- the x-component of the mean flow velocity

Ui- the velocity at the inflexion point

U_o- the mean velocity

U'- the mean flow vorticity

Ui'-the mean flow vorticity at the inflexion point

v- the y-component of the disturbance velocity

v- the y-component of the fundamental disturbance velocity

v- the y-component of the subharmonic's velocity

W- the complex amplitude of the time-dependent flow

also, the distortion (chapter 7)

W_o- the mean of the amplitude of the time-dependent flow

[For subscripts see the end of this list]

x- axis parallel to the main flow direction

positive down stream

x1= x Cd d - a distance parameter for the wake

y- the transverse direction of the flow

yi- the transverse position of the inflexion point

α- the wavenumber [For subscripts see the end of this list]

$\beta=0.5(\omega_o/\nu)^{1/2}$- the dimensionless frequency parameter of the time-dependent flow

$\gamma=0.5(i\omega_o/\nu)^{1/2}$- the complex dimensionless frequency parameter

δ- the Stokes length

ε- the perturbation amplitude

$\eta=1.67789\ y/b_{1/2}$ - the independent variable of the wake

θ- the momentum thickness

θ_o- the phase lag behind the pressure gradient

θ_i- the phase lag of the time-dependent flow unstable profile behind the pressure gradient

λ- the wavelength of the disturbance

μ- the coefficient of viscosity

ν- the kinematic viscosity

$\varphi=\varphi_r+\varphi_i$- the complex amplitude of the stream function of the disturbance (the eigenfunction)

φ_1- the fundamental disturbance eigenfunction

φ_2- the subharmonic eigenfunction

ψ- the stream function of the disturbance

ψ_1- the fundamental disturbance stream function

ψ_2- the subharmonic's stream function

ω- the fundamental disturbance frequency [For subscripts see the end of this list]

$\omega_o t$- the phase angle of the time-dependent flow in degrees

$\partial\omega/\partial\alpha$- the complex group velocity

SUBSCRIPTS

c- at the critical Reynolds number

m- maximum amplification

mt- maximum temporal amplification

ms- maximum spatial amplification

t- temporal

s- spatial

i- imaginary part

r- real part

SUPERSCRIPTS

j- the iteration order

CONTENTS

CHAPTER FOUR
INFLEXION INSTABILITY

****
****
***
*

CHAPTER ONE

INTRODUCTION

The main objective for this thesis was to study the stability of time-dependent flows, both experimentally and theoretically. For the theoretical side the plane time-dependent flow (i.e. in a duct) was considered since it is easier to tackle than the counterpart in a circular pipe. Because such a flow contains an infinite number of inflexion points, part of the research was devoted to studying the inflexion instability in general. The inviscid form of this instability ($Re \to \infty$), has been studied by various authors for various flows. Therefore, this was considered a good opportunity to extend such studies in the viscous case (finite Re). In order to generalize the results, comparison between the stability characteristics of different profiles was considered the best. Such comparative studies have not been reported. Alongside these studies the transition of the (real) time-dependent flow will be examined in detail both experimentally and theoretically.

The importance of inflexion instability arises from the fact that all flows in nature, if they are not of this type, pass through it in their life time through secondary

instabilities. The majority of flows of practical importance possess inflexion points. Examples are jets, wakes, time-dependent flows, boundary layers at separation and the mixing layers of all flows. The direct product of these inflexion points are large vortex systems, to which was given the name large scale coherent structure or just large scale structure.

The existence of large scale structures has been known for several decades. For a long time they were known to control turbulence in free shear layers. More of their influence became apparent when recent research implicated them in several important phenomena. First, was their relation to noise generation (for a recent review see Gatski 1978). Next came the observation of these structures in turbulent boundary layers (Kim, Kline and Reynolds 1971). Later, Winant and Brownd (1974) implicated the structure in the phenomenon of pairing, while at the same time Brown and Roshko (1974) implicated it in the entrainment process. These structures were observed by several investigators (section 7.4) to keep their two-dimensionality for long distances downstream of the origin. Since the vortex stretching, which reduces any instability structure to fine scale turbulence is a three-dimensional process, the persistence of such structures is a manifestation of their two-dimensionality. Therefore two-dimensional stability analysis is appropriate for investigating the characteristics of the large scale coherent structures as was done in this

thesis. Equally, three-dimensional stability analysis is the one appropriate for studying their breakdown. The latter has not been attempted in this thesis. The calculations of Michalke (1969) showed that the three-dimensional disturbances are less unstable than the two-dimensional disturbances.

The time-dependent flows, which contain an infinite number of profiles the majority of which contain inflexion points are the centre of this general study of inflexion instability. The main body of this study is given in chapter 4 and chapter 7. In **chapter 4** the general quantitative characteristics of the instability are given, while **chapter 7** contains a qualitative study of the disturbance distribution and its energy balance for several profiles selected in such a way as to gain an overall view of these distributions.

Two chapters of the thesis are devoted to the main tool: the numerical procedures. **Chapter 2** is a survey of the main numerical procedures used in hydrodynamic stability in general, while **chapter 3** explains two procedures used during the investigations.

The stability of the (real) time-dependent flow is investigated in chapter 5 and chapter 6. **Chapter 5** describes the experimental investigation of the stability of the flow in a circular pipe. Determination of the critical Reynolds numbers at low frequency of the flow

oscillation is the main topic. This range of oscillations has not been investigated in a detailed study previously, although the transition at high frequencies has been studied by various authors. **Chapter 6** tackles the problem from the theoretical side. However this theoretical study concentrates on the whole flow oscillation range of frequencies. It will be clear in this chapter that the study was successful except in the lower end of the range.

From this short review, it is clear that each chapter has its own identity due to the different nature of the problem. Therefore each has its own introduction and its own literature review. Despite that it was considered better to leave the conclusions to the end of the thesis in order to be combined with the suggestions for future work in one part. This way, what has been done and what further can be done will be clearer.

C H A P T E R T W O

GENERAL SURVEY OF
NUMERICAL SOLUTIONS OF THE ORR-SOMMERFELD EQUATION

2.1: Introduction

The stream function of a two-dimensional disturbance superimposed on a two-dimensional laminar flow is given by

$$\psi(x,y,t) = \varphi(y)\, e^{i\alpha(x-ct)} \qquad (2.1)$$

where x is the distance downstream, y is the perpendicular direction and t is the time. $\varphi(y)$ is the complex amplitude, α is the wavenumber and c is the phase velocity of the disturbance.

From the continuity equation

$$\partial u(x,y,t)/\partial x + \partial v(x,y,t)/\partial y = 0 \qquad (2.2),$$

it follows that the disturbance velocities u and v in the x and the y directions respectively are given by

$$u = \partial\psi(x,y,t)/\partial y; \quad \text{and} \quad v = -\partial\psi(x,y,t)/\partial x \qquad (2.3)$$

Substituting (2.3) in the two-dimensional Navier-Stokes equation and after linearisation we have the Orr-Sommerfeld equation

$$(U(y)-c)[\varphi''(y)-\alpha^2\varphi(y)]-U''(y)\varphi(y)+$$
$$(i/\alpha Re)[\varphi''''(y)-2\alpha^2\varphi''(y)+\alpha^4\varphi(y)]=0 \qquad (2.4)$$

where the primes denote differentiation with respect to y, U(y) is the mean flow velocity and Re is the mean flow Reynolds number. All quantities have been made dimensionless with respect to the mean velocity of the flow U_o and the width of the flow h=y2-y1, where y1 and y2 are the flow boundaries. The Reynolds number in (2.4) is defined as Re=Uoh/v, where v is the kinematic viscosity of the fluid concerned. For boundary layer flows whose second boundary y2 ->∞, h is replaced by δ the boundary layer thickness or sometimes by δ^* the displacement thickness.

Equation (2.4) is accompanied by the boundary conditions

$$\varphi(y1)=\varphi'(y1)=\varphi(y2)=\varphi'(y2)=0 \qquad (2.5a)$$

for channel flows, and

$$\lim_{y2\to\infty}\varphi(y2)=\varphi'(y2)=0 \qquad (2.5b)$$

for free stream conditions in boundary layer flows. Condition (2.5a) follows from the fact that u and v should satisfy the no-slip conditions at the walls, whilst in the boundary layers free stream conditions, the disturbances are required to vanish (2.5b). This last condition however, should be reviewed when the eigenvalues of (2.4)

are a part of a continuous spectrum where the requirement is that $\varphi(y2)$ is bounded at infinity [Grosch and Salwen (1978)].

Besides being fourth order and complex, equation (2.4) represents an eigenvalue problem; facts which make its solution difficult. $\varphi(y)$, α and c can all be unknown and all are complex. However, for monochromatic disturbances either α or c can be assigned a real value, in which case the other becomes the eigenvalue of the equation and $\varphi(y)$ is the eigenfunction in either case. For wavepackets however both α and c are necessarily complex and the solution in this case is more complicated.

Since its derivation by Orr (1907) and Sommerfeld (1908) the analytical solution of equation (2.4) has been the centre of much of the work in hydrodynamic stability. These analytical solutions have been advanced considerably by the works of Heisenberg(1924), Tollmein(1929), Schlichting(1932) and Lin (1945,1955). However, these contributions in addition to those of some other authors have not resolved the controversies about the stability of some flows. For this purpose numerical work was required and because of the laborious task for the flows in question, this was only possible after the appearance of electronic computers. The task was carried out for the first time by Von Neuman, Pekeris and Lin for plane Poiseuille flow (see Thomas1953), but the results were not published as they did not settle the controversies. However, their work has been subsequently expanded by

Thomas(1953) who has proved beyond doubt the instability of channel Poiseuille flow. These numerical methods are now routine in the solution of stability problems. As an example about 300 hours were required for Thomas to finish his published results, while the same results obtained by the present author starting with his initial values required only about 30 seconds (CPU time) on the ICL2972 computer, and an overall time of 5 minutes.

2.2: Numerical Methods

The numerical methods used for solving the Orr-Sommerfeld equation are one of two types:

i-Conversion of the problem into an initial value problem which is solved using numerical integration (The shooting method).

ii-Representation of the equation by a matrix, which is subsequently solved by any method many of which are well established (Matrix Methods).

2.2.1: The shooting method

One of the advantages of the linearity of the Orr-Sommerfeld equation is that it allows for its conversion from a boundary value problem to an initial value problem. Considering equation (2.4) for Blasius flow at the free stream ($y2 \to \infty$), where $U(y2)=1$ and $U''(y2)=0$, it is easy to verify that the equation is satisfied by the following two linear independent solutions

$$\varphi_1 = e^{-\alpha y} \quad , \quad \varphi_2 = e^{-\gamma y} \qquad (2.6)$$

where α is the wavenumber and $\gamma = \{\alpha^2 + iRe(\alpha - \omega)\}^{1/2}$. The general solution is a linear combination of these two solutions.

The integration method depends first on converting equation (2.4) into a first order equation. Starting from one of the boundaries, the known initial conditions there are used to find the value of $\varphi(y_j)$ at the subsequent points j, looking for the other boundary conditions to be satisfied at the other end. This task is accomplished usually using either Runge-Kutta or Adam-Bashforth methods (Froberg 1969). For boundary layer flows, as initial solutions the following two solution vectors which follow directly from (2.6) are used

$$(1, -\alpha, \alpha^2, -\alpha^3)e^{-\alpha y}$$

$$(1, -\gamma, \gamma^2, -\gamma^3)e^{-\gamma y}$$

For channel flows any two linear independent constants satisfying (2.4) will be suitable as initial values, e.g.

$(0,0,1,1)$, or

$(0,0,1,i)$

In this case, the centre is usually considered as a boundary with boundary conditions

$$\varphi'(0) = \varphi'''(0) = 0$$

If the other boundary condition is not satisfied, a

corrected estimate of the eigenvalue is given and the process is repeated (new iteration) starting every time from the same end. The number of iterations required to find the eigenvalue, which satisfies both boundary conditions, depends naturally on the initial guess of the eigenvalue, and for the closest estimate about three iterations are required. If the solution is found using a large number of points the method usually is extremely accurate. However, the procedure has long been recognised not to be straightforward. Due to the limited accuracy of the computer φ_1 at some stage of the the integration will have small (parasitic) errors proportional to φ_2 , thus making both solutions dependent. Therefore, at different stages during integration it is necessary to remove this error so that the solutions remain independent.

Several procedures have been suggested to overcome this difficulty, the most famous of which are

a) Kaplan(1964): Filtering Process.

b) Wazan et al (1967): Gram-Schmidt Orthogonalisation

c) Davey (1977): The Transfer Matrices Process (Riccati Matrices).

d) Monkewitz (1978): Pseudoorthogonalisation Method

e) Ng & Reid (1979): Compound Matrices Method.

f)Vanstijn & Van De Vooren (1980): The Method of Order Reduction

Claims supporting the success of each method were provided by their authors, but due to the relatively long

computer time required by the shooting method as a whole, our judgement will be based on the length of the time required by one iteration for each method. Gupta and Garg (1981) made a comparison between a) and b) and concluded that the Gram-Schmidt orthogonalisation process is the best of the two. The time required by the computer Central Processing Unit (CPU), using this procedure is about 3 seconds per iteration for a step size $\Delta y=0.01$. Davey (1977) claimed that his method c) is faster by about a factor of 2. Method e) is expected to require an equal time, whilst there is no available information about both d) and f). Even if we consider that these last two methods require an amount of time about the same as that of Davey's method, it can be concluded that generally the shooting method requires a large amount of time compared to finite difference methods. The calculations made by the author using the latter (chapter 3) have shown that only 0.13 seconds were required by one iteration for $\Delta y=0.01$, and generally not more than 4 seconds were necessary to find an eigenvalue with the worst initial guess. There is a further limitation in the use of the shooting method, namely that not all processes in a)-f) are suitable at high αRe. For more about this the reader is referred to the articles mentioned here. Details about the Gram-Schmidt orthogonalisation can be found in Wazan et al (1967).

2.2.2: Matrix methods

The Orr-Sommerfeld Equation is transformed into a matrix using any suitable procedure which ensures that the solution obtained will be close to the actual solution, and if possible, without the matrix being too large. There are basically two different methods to perform such a conversion:

a) Orthonormal functions. (sections 2.3 and 2.4 and Chapter 3, section 3.2).

b) Finite difference Methods (Chapter 3,section 3.3)

Both methods have been used during this investigation for a variety of purposes. They do not suffer from breakdown as does the shooting method at reasonably high αRe, due to the instability of the methods used in the removal of the (parasitic) error. As long as the number of terms in a) or the number of mesh points in b) are increased, both methods can safely be used for high αRe.

Method b) has several advantages over method a)

1) It can easily be adapted to any flow domain.

2) It can be used to find a single eigenvalue in a relatively shorter time than a), while a) is the best when the whole spectrum of the eigenvalues of the matrix is required.

3) The matrix can be arranged in the appropriate way so that minimal storage and computational time are achieved. This can be done thanks to the pentadiagonal nature of the matrix in b)(at least for the method used during this investigation). In fact, as a result of this the

computation time is made directly proportional to N, in contrast to method a) where it remains proportional to N^3 .

2.3: The Orthonormal Expansions

This approach is the most widely used when the temporal higher eigenvalues of the Orr-Sommerfeld equation are required alongside the most stable eigenvalue. The method has been used for the first time in hydrodynamic stability studies by Taylor (1923) for the case of Couette flow [see also Lin (1955)]. The first computational study, using this approach, was due to Dolph and Lewis (1958) for the case of plane Poiseuille flow. Subsequently, the method has been used successfully for studying the stability of a variety of flows, including the time-dependent flow, as was done by Grosch and Salwen(1968), Hino and Sawamoto (1976), von Kerczek and Davis (1974) and von Kerczek (1982). The only difference in the application of the method between different authors is the choice of the orthonormal functions used. The choice needs careful consideration due to the difference in convergence of different orthonormal functions.

The Orr-Sommerfeld equation (2.4) is written in the form

$$\mathcal{L}\varphi(y)=L\varphi(y) - c\, M\, \varphi(y)=0 \qquad (2.7)$$

where,

$$L=\{U(y)[(d^2/dy^2)-\alpha^2]-U''(y)+ i[(d^4/dy^4)-2\,\alpha^2(d^2/dy^2)+\alpha^4]/\alpha Re\} \qquad (2.8a)$$

and

$$M=[(d^2/dy^2)-\alpha^2] \qquad (2.8b)$$

The Orr-Sommerfeld operator $\int\varphi(y)$ is accompanied by the boundary conditions (2.5).

It is assumed the $\varphi(y)$ in equation (2.7) is expandable in the infinite series

$$\varphi(y)=\sum_{n} a_n\varphi_n(y) \qquad \text{for } n\leqslant N \qquad (2.9)$$

where $\{\varphi_n(y)\}$ is a complete set of orthogonal functions which satisfy the orthogonality conditions:

$$[2/(y2-y1)]\int_{y1}^{y2} w(y)\,\varphi_m(y)\,\varphi_n(y)dy=\delta_{mn} \qquad (2.10)$$

for $n,m \leqslant N$

where $w(y)$ is a weight function, the value of which depends on the choice of the orthonormal function used. $\{\varphi_n(y)\}$ is assumed to be four times differentiable, since the Orr-Sommerfeld equation is a fourth order equation.

The completeness of the set $\{\varphi_n(y)\}$ requires that the limit of the mean square error vanishes [Courant and Hilbert (1953)]. Thus,

$$\delta=\lim_{N\to\infty}\,[2/(y2-y1)]\int_{y1}^{y2} w(y)[\varphi(y)-\sum_{n=0}^{N} a_n\varphi_n(y)]^2\,dy=0 \qquad (2.11)$$

For a series truncated at a finite N, condition (2.11) will not be satisfied. Therefore instead, the least square criterion (Fox and Parker, 1968) which requires that

$$\delta = [2/(y2-y1)] \int_{y1}^{y2} w(y)[\varphi(y) - \sum_{n=0}^{N} a_n \varphi_n(y)]^2 \, dy = \text{minimum} \qquad (2.12)$$

is used. For (2.12) to be satisfied, a necessary condition is that

$$(d\delta/da_n) = 0 \quad \text{for } n = 0, \ldots\ldots, N$$

or

$$-[4/(y2-y1)] \int_{y1}^{y2} w(y)\varphi_n(y)[\varphi(y) - \sum_{n=0}^{N} a_n \varphi_n(y)]dy = 0$$

from which we have

$$a_n = \frac{\int_{y1}^{y2} w(y)\varphi_n(y)\varphi(y)dy}{\int_{y1}^{y2} w(y)\varphi^2{}_n(y)dy} \qquad (2.13)$$

For $w(y)=1$, equation (2.13) reduces to the well known Fourier cosine coefficients formula, since the denominator reduces to 1 for $n \geq 0$. For the Orr-Sommerfeld problem, equation (2.13) will not be used for the determination of the coefficients a_n, since $\varphi(y)$ is unknown. Instead (2.13) is useful in the examination of the convergence of the set $\{ \varphi_n(y)\}$, whose weight function is $w(y)$.

2.4: The Galerkin Method

Despite the possibility of using other transformations, the Galerkin method is the most widely used for transforming equation (2.7), in which $\varphi(y)$ is given by (2.9), into a matrix. It was first used by Chandrasekhar (1954) for the solution of the narrow-gap Couette flow (Taylor problem). Simplicity is the basic characteristic of the method, but its success depends entirely on the

rate of convergence of the orthonormal polynomial used. The general convergence of the Galerkin method as applied to the Orr-Sommerfeld problem has been proved by Diprima and Sani (1965) for all orthonormal trial functions in (2.9), though its application continued for some time before that.

Considering only a finite number of terms N in (2.9), and after substitution in equation (2.7),the resulting error is

$$e(y)= \mathcal{L}\left(\sum_{n=0}^{N} a_n \varphi_n(y)\right)-\mathcal{L}(\varphi(y)) \qquad (2.14)$$

The Galerkin approach requires that this error is to be orthogonal to the orthonormal function $\varphi_m(y)$,in which case

$$\int_{y1}^{y2} e(y)w(y)\varphi_m(y)dy=\int_{y1}^{y2} w(y)\varphi_m(y)\left\{\mathcal{L}\left(\sum_{n=0}^{N} a_n \varphi_n(y)\right)-\mathcal{L}(\varphi(y))\right\}dy=0$$

$$\text{for } n,m=0,1,.....,N \qquad (2.15)$$

Equation (2.15) replaces equation (2.7) by an N x N matrix which is also accompanied by the boundary conditions (2.5).

Using (2.10), equation (2.7) can be written as

$$(D - c E) =0 \qquad (2.16)$$

where,

$$D=(2./(y2-y1))\int_{y1}^{y2} w(y)\varphi_m(y)\ L\ \left(\sum_{n=0}^{N} a_n \varphi_n(y)\right)dy$$

$$E=(2./(y2-y1))\int_{y1}^{y2} w(y)\varphi_m(y)\ M\ \left(\sum_{n=0}^{N} a_n \varphi_n(y)\right)dy$$

for $n,m \leq N$

Both D and E are matrices of order N x N. Alternatively, in the standard eigenvalue problem notation

$$(A - c I) = 0 \qquad (2.17)$$

where $A = D E^{-1}$ and I is a unit matrix. E^{-1} is the inverse of the matrix E (which is equivalent to finding the NxN eigenvectors of E). c_n is an eigenvalue of matrix A if and only if $(A-c_n I)$ is singular since $a_n \neq 0$. The eigenvalues of A are the values of c_n which satisfy the equation

$$f(c_n)=\det(A - c_n I)=0 \qquad (2.18)$$

By the cofactor expansion of det(A-cI), it can be shown that f(c) is an N th degree polynomial and due to the fundamental theorem of Algebra any polynomial of degree N should have N zeros. Therefore, there are exactly N eigenvalues. Due to the fact that for some flows (e.g. boundary layer flows), the Orr-Sommerfeld equation does not possess a complete set of eigenfunctions, it is obvious that some of the eigenvalues produced should be interpreted with caution. It should be noticed that the matrix A representing the Orr-Sommerfeld problem is a complex matrix but not Hermitian, since equation (2.7) is not self adjoint. However, the adjoint problem has the same eigenvalues as the original problem, a fact which is usefully employed as a check for correctness of the methods as well as the programing, as was done during this

study.

There are several numerical procedures which can be used for finding individual eigenvalues c_n . These will be discussed in chapter 3. For the calculations of the whole spectrum, there are two numerical procedures which are well known and well established, namely the LR and the QR algorithms. The first has been developed by Rechishauser (1958). It gives a reduction of the general matrix A to triangular form by means of non-unitary transformations as A=LR, where L and R are the lower and the upper triangles respectively. The QR algorithm which has been developed by Francis (1961,1962) is closely related to the LR algorithm, but it is based on the use of unitary transformations. It has been described as being the most effective of the known methods for the solution of the general algebraic eigenvalue problem (Wilkinson 1965).

The LR and the QR algorithms are now available on almost all computers as subroutines based mostly on the the works of Wilkinson (1965) and co-workers. On the Edinburgh Regional Computer Centre ICL 2972 and ICL 2988 machines, these routines are available in the Numerical Algorithm Group (NAG) library. For our problem (2.17), these are of the LR type. Details about the implementation of the QR algorithm specifically to the Orr-Sommerfeld problem, can be found in the paper by Gary and Helgason (1970).

2.5: The Convergence of Orthonormal Functions

In his application of the Galerkin method to the narrow-gap Couette flow (Taylor problem), Chandrasekhar (1961, 71,b and c) used for (2.9) the expansion

$$\varphi(y) = \sum_{n=0}^{N} a_n \sin(n\pi y) \qquad (2.19)$$

He obtained accurate results using only a few terms (up to 6) for $-3 \leqslant \mu \leqslant 0$, where μ is the ratio of the angular velocities of the outer cylinder to the inner cylinder. For values of $\mu \geqslant -1$, only 3 terms were required for obtaining the critical Taylor number to within 1% accuracy. This fast convergence behaviour is not general for all hydrodynamic stability problems. Using the most convergent orthogonal polynomial -the Chebychev polynomial- Orszag (1971) found that more than 25 terms were necessary for reasonably accurate eigenvalues for plane Poiseuille flow. The reason behind this behaviour is the rapid variation of the derivatives of $\varphi(y)$ near the critical point (where $U(y)=c$) as well as near the wall. In flows with inflexion points these variations are smaller than those in flows without inflexion points.

For faster convergence Dolph and Lewis (1958) and some subsequent authors decided to choose trial functions $\varphi_n(y)$ which were closely related to the Orr-Sommerfeld equation. These trial functions are the solution of

$$\varphi_n'''' - 2\alpha^2\varphi_n'' + \alpha^4\varphi_n + c(\varphi_n''-\alpha^4\varphi_n)=0 \qquad (2.20)$$

with the boundary conditions being (2.5). Orszag (1971) has shown that the error after N terms of the expansion in $\varphi_n(y)$ satisfying (2.20) is generally of order N^{-4} as $N\to\infty$, and he pointed out that this behaviour is due to the nonuniform convergence of the four times differentiable series near the end points.

Grosch and Salwen (1968) in their famous study of the stability of plane Poiseuille and time-dependent flows, chose trial functions which again are thought to be closely related to the Orr-Sommerfeld equation since they satisfy the equation

$$\varphi_n'''' - 2\alpha^2\varphi_n'' + \alpha^4\varphi_n = c^4\varphi_n \qquad (2.21)$$

These functions reduce to Chandrasekhar-Reid functions when $\alpha=0$ (Chandrasekhar 1961, Appendix V). The solution of (2.21) is

$$\varphi_n(y)=\left\{ \frac{\cosh(\beta_n y)}{\cosh(0.5\,\beta_n)} - \frac{\cos(\gamma_n y)}{\cos(0.5\,\gamma_n)} \right\} \qquad (2.22)$$

where $\beta_n=(c_n^2+\alpha^2)^{1/2}$, $\gamma_n=(c_n^2-\alpha^2)^{1/2}$

and $c_n = (2n-0.5)\,\pi$ for $|y|\leq 0.5$

Using (2.21) in equation (2.13) and after integration by parts, it can be shown (chapter 3, section 3.2) that the coefficients a_n after N terms, are proportional to N^{-4} as $N\to\infty$. It can also be shown that the residue $[\sum_{n=N+1}^{\infty} a_n \varphi_n(y)]$ is

of order of magnitude N^{-4} as $N \to \infty$. This result will be discussed in the next chapter in connection with the trigonometric functions.

In contrast to these trial functions which are closely related to the Orr-Sommerfeld equation, the Chebychev polynomials have been shown to have faster convergence to the same equation (Fox and Parker 1968). The nth degree Chebychev polynomial is defined by

$$T_n(y) = \cos(n\theta) \tag{2.23}$$

for $|y| \leq 1$. The Chebychev polynomials (2.23) are orthogonal, but only with respect to the weight function

$$w_1(y) = (1-y^2)^{-1/2} \tag{2.24}$$

which arises on account of the transformation of the Fourier series from the angle variable θ to the variable

$$y = \cos(\theta), \tag{2.25}$$

i.e.

$$\int_{-1}^{+1} T_m(y) T_n(y) w_1(y) dy = (2/\pi) \int_{-1}^{+1} \cos(m\theta) \cos(n\theta) d\theta = 0,$$

for $m \neq n$

In terms of these polynomials, the expansion (2.9) is given by

$$\varphi(y) = \sum_{n=0}^{N} a_n T_n(y) , \quad \text{for large } N \qquad (2.26)$$

Where the coefficients a_n in (2.26) are determined using equation (2.13) with the weight function (2.24), i.e.

$$a_n = (2/\pi) \int_{-1}^{+1} w_1(y) \varphi(y) T_n(y) dy \qquad (2.27)$$

It has been shown that (Fox and Parker 1968) these coefficients have an order of magnitude

$$1/\ 2^{n-1} n! \qquad (2.28)$$

for large n, which is considerably smaller than the coefficients of the best of the trial functions discussed above. As Lanczos (1966) pointed out, this fast convergence is due to the uniform convergence of this polynomial near the end points.

Another candidate as a trial function for the solution of the Orr-Sommerfeld equation is the Legendre polynomial Pn(y), since it shares with the Chebychev polynomial the transformation (2.25), although its weight function is equal to 1. The oscillations of this polynomial happen with unequal amplitude with the largest occurring at y=± 1 and the maxima and minima gradually decrease as we move from the end points to the centre of the channel. Therefore, the Legendre polynomial has a tendency to give large errors around the end points, while the Chebychev polynomial keeps the magnitude of the error constant

through out the range. Accordingly, it is expected to obtain a less convergent solution if this polynomial is used e.g. for plane Poiseuille flow instead of the expansion (2.26). However its overall behaviour is certainly better than that of the trial functions given by the solution of (2.20) or by (2.22).

Other orthogonal functions which satisfy the boundary conditions, e.g. Bessel functions, have also been used as trial functions, e.g. by Salwen and Grosch(1972) in their study of Poiseuille flow in a pipe.

C H A P T E R T H R E E

NUMERICAL SOLUTIONS OF THE ORR-SOMMERFELD EQUATION FOR CHANNEL AND BOUNDARY LAYER FLOWS

3.1: Introduction

During this study, three different numerical methods have been investigated, though the original intention was to use only one method. After the implementation of the first method (section 3.2), it was felt that a check was necessary since there were no available results to compare with directly in the case of time-dependent flow. The generalised Chebychev expansion method based on the paper of Orszag (1971) was thought to be the best due to the expected high accuracy and flexibility. However, large discrepancies appeared soon between the results from the two methods. The LR algorithm was used with a finite difference matrix for checking the Galerkin solution and a complete agreement was found.

Since then, the Galerkin solution has been improved and higher accuracy achieved (subsection 3.2.3). At a later stage in this study, the finite difference solution has been developed into a major program based on a single eigenvalue iterative procedure in order

a) to investigate the spatial stability

b) to calculate to a higher accuracy the eigenvalues obtained using the first method

c) to calculate accurately the eigenfunctions and the energy balance of the fundamental and the subharmonic disturbances

d) to investigate the development of wavepackets in different flows.

3.2: Solution of the Orr-Sommerfeld Equation Using the Galerkin Method

3.2.1: Trigonometric functions

The discussions in the previous chapter lead to the conclusion that orthogonal functions with reasonable convergence are suitable for the solution of the Orr-Sommerfeld equation. This fact also follows from the proof given by Diprima and Sani (1965) which confirms the convergence of the Galerkin method with all orthogonal functions.

Trigonometric functions are relatively rarely used in the study of the stability of channel flows. Among the users were Hino and Sawamoto (1975) in their study of time-dependent flow stability. They used trial functions given by

$$\varphi_n(y)=\sin^2(n\pi y)\cos((n-1)\pi y)=$$

$$0.5(\cos((n-1)\pi y)-0.25((\cos(n+1)\pi y)-\cos((n-3)\pi y))$$

$$\text{for } 0\leqslant y\leqslant 1 \qquad (3.2.1)$$

In the study presented here, it was decided to use a simpler form, namely

$$\varphi_n(y) = \cos(n\pi y) \quad \text{and} \quad \varphi(y) = \sum_{n=0}^{N} a_n \varphi_n(y) \qquad (3.2.2)$$

for $0 \leqslant y \leqslant 1$.

These functions are symmetric for even n and antisymmetric for odd n. From (2.13) with the weight function $w(y)=1$, we have

$$a_n = \int_0^1 \varphi(y)\cos(n\pi y)\,dy \qquad (3.2.3)$$

The convergence of the expansion (3.2.2) requires that $a_n \to 0$ as $n \to \infty$, and under normal situations a_n at least should be very small at reasonably large n.

Integrating (3.2.3) by parts, we have

$$a_n = (n\pi)^{-1}[\varphi(y)\sin(n\pi y)]_0^1 + (n\pi)^{-2}[\varphi'(y)\cos(n\pi y)]_0^1 -$$

$$(n\pi)^{-3}[\varphi''(y)\sin(n\pi y)]_0^1 - (n\pi)^{-4}[\varphi'''(y)\cos(n\pi)]_0^1 +$$

$$(n\pi)^{-4}\int_0^1 \varphi''''(y)\cos(n\pi y)\,dy$$

Only the fourth and the fifth terms survive, since the first and the third terms vanish automatically, while the second term vanishes due to the boundary conditions. For the fourth term to vanish it is required that

$\varphi'''(1) = \varphi'''(0)$ for symmetric stream functions and

$\varphi'''(1) = -\varphi'''(0)$ for antisymmetric stream functions.

These conditions are easily found to be satisfied in the range required. Therefore,

$$a_n = [1/(n\pi)]^4 \int_0^1 \varphi'''(y)\cos(n\pi y)dy \qquad (3.2.4)$$

Similar results are found in the range $|y| \leq 1$ ($\cos(0.5n\pi y)$). It is clear that expressions (3.2.1),(2.22) and (3.2.2) have the same order of convergence. Therefore, it is pointless to use complicated expressions like (3.2.1) or (2.22), since these will complicate the integration required by the Galerkin method (2.15) and consequently complicate the programs without improving the convergence. It should be pointed out that expansions in the sine function do not have this rate of convergence. Simple investigations as that already used to derive (3.2.4), show that expansion in $\sin(n\pi y)$ is only $(N\pi)^{-3}$ order of convergence for both symmetric and antisymmetric stream functions. Nevertheless, these are considered high rates of convergence due to the special boundary conditions which the Orr-Sommerfeld equation has. Usually expansions in trigonometric functions are less convergent for other equations with simpler or no boundary conditions.

For boundary layer flows $y2=Z \rightarrow \infty$, and the trial function is $\cos(n\pi y/Z)$. The Nth coefficient a_N is of order of magnitude $Z^4/(N\pi)^4$ resulting in a poor convergence for large values of Z.

3.2.2: The Galerkin method for time-dependent and plane Poiseuille flows

The Galerkin Method using expansion (3.2.2) has been investigated for both plane and time-dependent Poiseuille flows. The laminar plane Poiseuille flow between two parallel planes of distance 1 apart is given by

$$U(y)=4y(1-y) \quad \text{for } 0 \leqslant y \leqslant 1 \qquad (3.2.5)$$

While the velocity distribution of the two-dimensional oscillatory laminar flow between two parallel planes which is driven by sinusoidally changing pressure gradient of frequency ω_o is given by

$$U(y)=0.5[W(y)e^{i\omega_o t}+W^{*}(y)e^{-i\omega_o t}] \qquad (3.2.6)$$

where the astrisk denote the complex conjugate and

$$W(y)=\frac{\dfrac{[e^{2\gamma(1-y)}-e^{-2\gamma(1-y)}+e^{2\gamma y}-e^{-2\gamma y}]}{(e^{2\gamma}-e^{-2\gamma})}-1}{(2/\gamma)\dfrac{(e^{2\gamma}-e^{-2\gamma}-2)}{(e^{2\gamma}-e^{-2\gamma})}-1} \qquad (3.2.7)$$

where $\gamma=(i\omega_o/\nu)^{1/2}$ and ν is the kinematic viscosity of the fluid which is considered to be water throughout this investigation ($\nu=0.01$). The frequency ω_o is related to the non-dimensional frequency parameter β by

$$\beta = 0.5(\omega_0/\nu)^{1/2} \qquad (3.2.8)$$

The velocity distribution in (3.2.5) is normalised by the maximum velocity at the centre of the channel, while in (3.2.6) the normalisation is made by the average velocity in the channel.

Substituting (3.2.2) and the velocity either from (3.2.5) or (3.2.6) into the Orr-Sommerfeld equation and applying the Galerkin method (2.15), we have

$$\sum_{n=0}^{N+1} a_n \, (F_{mn} + iG_{mn}) = c \sum_{n=0}^{N+1} a_n \, H_{mn} \qquad (3.2.9)$$

where,

$$F_{mn} = \int_0^1 [U(y)(\varphi_n'' - \alpha^2 \varphi_n(y)) - U''(y)\varphi_n(y)]\varphi_m(y)dy$$

$$G_{mn} = (1/\alpha Re) \int_0^1 [\varphi_n'''' (y) - 2\alpha^2 \varphi_n''(y) + \alpha^4 \varphi_n(y)]\varphi_m(y)dy$$

$$H_{mn} = \int_0^1 [\varphi_n''(y) - \alpha^2 \varphi_n(y)]\varphi_m(y)dy$$

$$\text{For } n,m = 0, 1, \ldots\ldots, N+1 \qquad (3.2.10)$$

where as before the primes denote differentiation with respect to y, and c is the phase velocity.

In matrix notation

$$F + i\,G = c\,H \qquad (3.2.11)$$

where F,G and H are matrices of order N+1 x N+1. From (3.2.10) it can be verified that the matrix F is a full

matrix while G and H contain only diagonal elements. The matrix resulting from these three matrices is of the type now known as the Dolph and Lewis matrix (Dolph and Lewis 1958), which originated from their solution of the Orr-Sommerfeld equation using trial functions satisfying (2.20). The elements of this type of matrix are real except for the diagonal elements which are complex.

The boundary conditions (2.5) after substitution of (3.2.2) reduce to

$$\sum_{n=0}^{N+1} a_n = 0$$

$$\text{or,} \quad \sum_{n=0}^{N} a_n = - a_{N+1} \qquad (3.2.12)$$

Using (3.2.12), equation (3.2.9) is transformed into

$$\sum_{n=0}^{N} a_n \, [F_{mn} - F_{mN+1}] + i \sum_{n=0}^{N} a_n \, [G_{mn} - G_{N+1N+1}] = c \sum_{n=0}^{N} a_n \, [H_{mn} - H_{N+1N+1}]$$

$$\text{For } n,m = 0,1,\ldots\ldots\ldots,N \qquad (3.2.13)$$

It should be noted that the boundary condition (3.2.12) is applied correctly on the matrices G and H if the diagonal elements only are considered involved, since these are the only nonzero elements resulting from the original equation. The matrix arising from (3.2.13) is no longer Dolph and Lewis type.

For actual computation (3.2.11) is written as

$$A = H^{-1} (F + i\, G) = cI \qquad (3.2.14)$$

where I is the identity matrix.

The eigenvalues of (3.2.14) have been found using the LR algorithm as implemented in the NAG (Numerical Algorithm Group) library. For this purpose, the inversion and the multiplication of the matrices were performed prior to the call of the LR algorithm. The LR algorithm constitutes a part of the NAG routine F02BDF.

The time required to calculate the three matrices in (3.2.14) (see also 3.2.10), is only about 1/6 of the total computation time. It should be noticed that each routine requires an amount of time proportional to the cube of the first dimension of the matrix (N^3). The inversion requires about 1/3 of the time required by the routine F02BDF, while the multiplication requires about one third of the inversion time. For a matrix of order 30, the overall time is about 7 seconds on the ICL 2972 and 2988 machines, while it took only 3.5 seconds when the 2980 machines were in use (almost all the calculations were made on this particular machine).

The convergence of the method has been examined for plane Poiseuille flow. For Re=20000 and α=2 the least stable eigenvalue is

c=0.237601 i0.0036718

when using 50 terms in the expansion (3.2.2). Grosch and Salwen (1968) using 50 terms in an expansion in the trial functions (2.22) found

c=0.237413 i0.003681

The two results confirm that our simple expansion (3.2.2) leads to the same convergence as the more complicated trial function (2.22). It should be noticed that the Reynolds numbers and the wavenumbers in the range adopted ($0 \leqslant y \leqslant 1$) are twice those in the range $-1 \leqslant y \leqslant 1$. This is due to the normalisation by the half width of the channel.

3.2.3: Acceleration of the convergence of the Galerkin Method

The integral on the left hand side of equation (2.15) approaches zero only when $N \to \infty$. This fact also follows from the behaviour of a_n as given by (3.2.4). Although the error in (2.15) is not exactly known, it is possible to introduce an estimate to it on the right hand side, so that a more accurate solution is obtained. This approach is similar to the perturbation scheme devised by Lanczos (1957) and known as the τ method. Here the τ method will not be used explicitly, since it is more appropriate to the cases of Chebychev polynomials and power series, because the perturbation term usually introduced is related directly to both of them.

Let (2.15) be written in the form

$$\sum_{n=0}^{N-1} a_n \int_0^1 \varphi_m \mathcal{L}(\varphi_n)\,dy = a_{N+1} \int_0^1 \varphi_m \mathcal{L}(\varphi_{N+1})\,dy - a_N \int_0^1 \varphi_m \mathcal{L}(\varphi_N)\,dy \qquad (3.2.15)$$

In (3.2.15) the series is truncated at the (N-1)th term. However, in the right hand side, an error equal to the difference between the two next higher terms was introduced. As can be seen, this error vanishes as $N \to \infty$. It should be noticed that a_{N+1} should be known in order to solve the system (3.2.15). Assigning a numerical value to a_{N+1} can be avoided by relating it to a_N through the relation $|a_{N+1}| = s|a_N|$, where s is a constant. From the D'Alembert theorem of convergence of a series, $s \leqslant 1$. Noting the boundary conditions (3.2.12), equation (3.2.13) is then written in the following form:

$$\sum_{n=0}^{N-1} a_n \{F_{mn} - (F_{mN} - sF_{mN+1})\} + i\sum_{n=0}^{N-1} a_n \{G_{mn} - (G_{NN} - sG_{N+1N+1})\}$$

$$= c \sum_{n=0}^{N-1} a_n \{H_{mn} - (H_{NN} - sH_{N+1N+1})\}$$

for $0 \leqslant m \leqslant N-1$ (3.2.16)

where,

$$G_{mn} = H_{mn} = 0, \text{ for } m \neq n.$$

Equation (3.2.16) reduces to (3.2.13) when **s=0**. This allows the same program written previously for (3.2.13) to be used for (3.2.16). The value **s=1** has been chosen, although other (less) values could be chosen. This has not been done here.

Table 3.1 (page 37) shows the behaviour of the least stable eigenvalues of the plane Poiseuille flow for $\alpha=2$ and Re=20000 for symmetric stream functions. These results

should be compared with the more accurate values listed at the bottom of the table and which have been obtained using the Chebychev polynomial solution.

Although the accuracy of the Chebychev polynomial has not been achieved, it is clearly seen that in comparison with the results of the previous section, equation (3.2.16) gives a better approximation using expansions of lower order. For the first higher eigenvalue, results accurate to 9 decimal places have been obtained with an expansion of 23 terms only. The next eigenvalue is accurate to 8 decimal places using the same matrix. It is well known that the accuracy of the higher eigenvalues decreases as the absolute value of the imaginary part increases. However, close comparison has shown that the error in the higher eigenvalues obtained using the present method is less by one order of magnitude than that of the same eigenvalues calculated using the Chebychev polynomial solution. This may place the method at the top of those used for studying the temporal spectrum of the eigenvalues of the Orr-Sommerfeld equation.

The convergence of the method has also been been examined for the time-dependent flow (3.2.6) at the frequency parameter $\beta=5$. The dependence of the accuracy of the eigenvalues on the number of terms N is demonstrated by providing the eigenvalues calculated for two profiles, namely $\omega_0 t=90^\circ$ and $\omega_0 t=0^\circ$ both at Re=5000 and $\alpha=5$. The three least stable eigenvalues are presented in table 3.2 (page

38) for both profiles. For $\omega_0 t=90°$, the convergence of the least stable eigenvalue is very fast as N increases. The eigenvalue is accurate to 7 significant figures at N=19 and to 8 significant figures at N=25. The first stable eigenvalue is accurate to 9 significant figures at N=23. However, for the least stable eigenvalue of $\omega_0 t=0°$, the convergence is slow indeed, and the eigenvalue is accurate only to 5 decimal places when N=28.

These results demonstrate the strong dependence of the convergence of the method on the value of the phase velocity. For small values of the phase velocity the convergence is slow, while the opposite is true for large values. This behaviour is common for both time-dependent and plane Poiseuille flows. Comparison with the results obtained using other orthonormal expansions described in chapter two confirm the general nature of this behaviour for all numerical methods including the finite difference method. However, the Chebychev polynomial solution does remove this dependence at a relatively low N, due to its uniform convergence in the whole range.

From various results obtained using the method described (this can be checked from tables 1 and 2), it can be deduced that for any two different phase velocities c1 and c2 to have the same accuracy, the following relation holds

$$c1/c2 = N2/N1 \qquad (3.2.17)$$

where c1 is the small phase velocity and c2 is the larger. N1 and N2 are the orders of the two expansions used, where N2<N1. Since high accuracy is achieved for N between 20 and 25 when the phase velocity is large, (3.2.17) can give an estimate to the order of the matrix required to achieve the same accuracy when the small phase velocities are calculated. This will be very easy for the critical and the most amplified phase velocities of any time-dependent flow profile, since these are very close to the velocity at the inflexion point which is known. Two or three trials are required when the phase velocity is unknown.

It should be remembered that despite these disappointing results for the small phase velocities, the use of the modification (3.2.16) has improved the convergence considerably. This is demonstrated in figures 3.1 and 3.2 where the behaviour of the eigenvalues is shown for both cases, s=0 and s=1. The accelerated method used for $\beta=6$ and $\omega_0 t=30^\circ$ shows a reduction in the matrix order by 1.5 (from 50 when s=0 to 32 when s=1 in figure 3.1 and from 50 when s=0 to 36 when s=1 in figure 3.2). This corresponds to about threefold reduction in computation time and twofold reduction in the storage.

TABLE 3.1

The least stable eigenvalues of the plane Poiseuille flow using the accelerated Galerkin method

Matrix Order	The least Stable Eigenvalues	
15	0.24496277	-i 0.00153400
	0.96463018	-i 0.03518347
	0.93718937	-i 0.06523803
20	0.23820930	+i 0.00462490
	0.96464248	-i 0.03518660
	0.93635090	-i 0.06325123
23	0.23761857	+i 0.00388651
	0.96464248	-i 0.03518658
	0.93635176	-i 0.06325154
25	0.23760512	+i 0.00375116
	0.96464248	-i 0.03518658
	0.93635175	-i 0.06325157
27	0.23759505	+i 0.00371564
	0.96464248	-i 0.03518658
	0.93635175	-i 0.06325157
32	0.23756475	+i 0.00370270
	0.96464248	-i 0.03518658
	0.93635175	-i 0.06325157
40	0.23754254	+i 0.00371239
	0.96464248	-i 0.03518658
	0.93635175	-i 0.06325157

The Chebychev Polynomial Solution (Matrix order=32):

0.23752649 +i 0.0037396

0.96464251 -i 0.0351866

0.93635178 -i 0.0632516

TABLE 3.2

The least stable eigenvalues of the time-dependent flow (β=6) using the accelerated the Galerkin method

MATRIX Order	β=6 Re=5000 ωot=90°	α=5.0 ωot=0°
14	1.17512112 +i0.00349107	-0.08523387 +i0.05116135
	1.15534885 -i0.03091800	0.15984197 -i0.02050189
	0.52466730 -i0.03732281	0.13978149 -i0.04905914
17	1.17512185 +i0.00349800	-0.08537795 +i0.05027805
	1.15533801 -i0.03090355	0.15984333 -i0.02050127
	0.49279862 -i0.03548849	0.13981470 -i0.04910389
21	1.17512113 +i0.00349744	-0.08546004 +i0.04991676
	1.15533772 -i0.03090589	0.15984335 -i0.20501382
	0.49255293 -i0.04500012	0.13981263 -i0.04910469
23	1.17512120 +i0.00349745	-0.08548386 +i0.04984539
	1.15533784 -i0.03090574	0.15984336 -i0.02050140
	0.49297186 -i0.04594778	0.13981268 -i0.04910476
25	1.17512121 +i0.00349746	-0.08549670 +i0.04980300
	1.15533781 -i0.03090570	0.15984336 -i0.02050140
	0.49291743 -i0.04622600	0.13981270 -i0.04910483
28	1.17512121 +i0.00349746	-0.08550520 +i0.04976650
	1.15533780 -0.030905703	0.15984336 -i0.02050141
	0.49269234 -i0.04651582	0.13981273 -i0.04910489
32	1.17512121 +i0.00349747	-0.08550809 +i0.04974160
	1.15533780 -i0.03090570	0.15984336 -i0.02050142
	0.49253638 -i0.04671864	0.13981274 -i0.04910493
36	1.17512121 +i0.00349747	-0.08550789 +i0.04972879
	1.15533780 -i0.03090570	0.15984336 -i0.02050142
	0.49245420 -i0.04678800	0.13981274 -i0.04910495
40	1.17512122 +i0.00349747	-0.08550694 +i0.04972162
	1.15533780 -i0.03090570	0.15984336 -i0.02050142
	0.49240316 -i0.04681002	0.13981274 -i0.04910496

3.3: THE FINITE DIFFERENCE SOLUTION

3.3.1. Introduction

Generally, there are two approaches for solving the Orr-Sommerfeld equation using the finite difference approximation:

a) The first approach is relatively new. The method starts by reducing the equation to a first order system (which is the usual shooting method approach). Then the boundary conditions are written in the new variables. The method will reduce the problem to a matrix having 4 x 4 blocks which is then solved using the box method developed by Cebeci and Keller (1977).

b) The second approach was first applied to the Orr-Sommerfeld equation by Thomas (1953). This method does not alter the order of the equation. The derivatives are replaced by difference equations which will lead finally to a matrix (normally pentadiagonal) and this is then solved using any suitable iterative procedure. This type of solution will be described in this section.

There is another version of this method due to Gary and Helgason (1971). In this method, by stretching the original coordinate y, it is possible to obtain a convergent matrix at a lower N in order to use the QR algorithm (which is very uneconomical for large matrices and cannot differentiate between sparse and nonsparse matrices).

3.3.2: The finite difference scheme

The flow domain Z is divided into N-1 equal intervals of length h, so that the eigenfunction $\varphi(y)$ becomes a vector whose components φ_n are the values of $\varphi(y)$ at the points $y=nh$ for $0 \leqslant y \leqslant Z$ and $n \leqslant N$. The flow domain Z is usually taken equal to 1 for channel flows and equal to 6 for Blasius flow.

The central difference expressions are adopted for representing the derivatives of φ in the Orr-Sommerfeld equation. For the fourth derivative this takes the form:

$$h^4 \varphi_n'''' = (\delta^4 - (1/6)\delta^6 + (7/240)\delta^8 - \ldots.)\varphi_n \qquad (3.3.1)$$

where δ is the difference operator, so that

$$\delta\varphi_n = \varphi_{n+1/2} - \varphi_{n-1/2} \qquad (a)$$

$$\delta^2\varphi_n = \varphi_{n+1} - 2\varphi_n + \varphi_{n-1} \qquad (b)$$

$$\delta^3\varphi_n = \varphi_{n+2} - 2\varphi_{n+1} + 2\varphi_{n-1} - \varphi_n \qquad (c) \qquad (3.3.2)$$

$$\delta^4\varphi_n = \varphi_{n+2} - 4(\varphi_{n+1} + \varphi_{n-1}) + 6\varphi_n + \varphi_{n+2} \qquad (d)$$

For the odd derivatives δ is used with the mean difference operator μ, so that

$$\mu\delta\varphi_n = 0.5(\varphi_{n+1} - \varphi_{n-1})$$

It is a common practice (which is a mere simplification) to equate the order of the differential

equation to the order of the difference equation. Looking back to equation (3.3.1), this means that the right hand side is to be terminated after the first term, but as a result a truncation error $O(h^2)$ is automatically introduced into the expressions for the derivatives. This truncation error is too high to be acceptable in view of the fact that a large number of points will be required for computation. Thomas (1953) encountering such problems, showed that it is possible to reduce the truncation error to $O(h^4)$ by making a suitable change in the dependant variable using a Gauss-Jackson-Numerov type of discretisation (also known shortly as Numerov). Jordinson (1968) used a variation of this technique to reduce the truncation error to $O(h^6)$ by changing the dependent variable from φ_n to V_n, where

$$\varphi_n = (1 + k_1\delta^2 + k_2\delta^4)V_n \qquad (3.3.3)$$

To find k_1 and k_2, the highest order in the central difference operator on the right hand side of (3.3.1) is required to be equal to the order of the Orr-Sommerfeld equation.

Substitution of (3.3.3) into (3.3.1) yields

$$h^4\varphi''''_n = \delta^4 V_n + [k_1 - (1/6)]\delta^6 V_n + [k_2 - (k_1/6) + (7/240)]\delta^8 V_n + O(h^{10}) \qquad (3.3.4)$$

Equating the second and the third terms to zero (so that δ^4 is the highest operator retained), we have

$k_1 = 1/6 \qquad k_2 = -1/720$

Therefore,

$$\varphi_n = [1 + (1/6))\delta^2 - (1/720)\delta^4]V_n \qquad (3.3.5)$$

The central difference for the other higher derivatives is

$$h^3\varphi_n''' = \mu[\delta^3 - 0.25\delta^5 + (7/120)\delta^7 - \ldots]\varphi_n$$

$$h^2\varphi_n'' = [\delta^2 - (1/12)\delta^4 + (1/90)\delta^6 - \ldots]\varphi_n$$

$$h\varphi_n' = \mu[\delta - (1/6)\delta^3 + (1/30)\delta^5 - \ldots]\varphi_n$$

Using these expressions together with (3.3.5) we have

$$h^4\varphi_n'''' = [\delta^4]V_n + O(h^{10}) \qquad (a)$$

$$h^3\varphi_n''' = \mu[\delta^3]V_n + O(h^5) \qquad (b)$$

$$h^2\varphi_n'' = [\delta^2 + (1/12)\delta^4]V_n + O(h^6) \qquad (c) \qquad (3.3.6)$$

$$h\varphi_n' = \mu[\delta]V_n + O(h^5) \qquad (d)$$

3.3.3: The matrix and the boundary conditions

Substituting equations (3.3.5) and (3.3.6 a and c) into the Orr-Sommerfeld equation; a pentadiagonal matrix is obtained, in each of its rows, the coefficients of $V_{n-2}, V_{n-1}, V_n, V_{n+1}$ and V_{n+2} are the only nonzero elements of the matrix. The matrix represents N equations with N+4 unknowns. These extra 4 unknowns come as a result of the central difference representation (3.3.2) for n=0 and n=N. Therefore, there are an extra 2 columns at the left hand

side in addition to another 2 at the right hand side of the matrix. Due to the fact that the matrix is pentadiagonal, only the top element of the first column and the two top elements of the second column are nonzeros. The last two columns are an inverted mirror image of the first two.

In order to keep the number of unknowns and the number of equations equal, these extra columns should be eliminated. This is done with the help of the boundary conditions (2.5). For the left boundary these are

$$\varphi(y1)=\varphi'(y1)=0 \qquad (3.3.7)$$

From (3.3.5) and (3.3.6) it follows that

$$(1+(1/6)\delta^2-(1/720)\delta^4)V_o=0 \qquad (3.3.8a)$$

$$\mu\delta V_o=0 \qquad (3.3.8b)$$

Equation (3.3.8b) implies that $V_{-1}=V_1$. Substituting this into equation (3.3.8a) gives

$$V_{-2}=474V_o+248V_1-V_2 \qquad (3.3.9)$$

Thus adding the coefficients of V_{-1} to the coefficients of V_1 in the first and the second rows, where these are nonzeros, will eliminate the second column of the matrix. Whilst adding the coefficients of V_{-2} according to (3.3.9) to V_o, V_1 and V_2 in the first row will eliminate the first

column of the matrix. These boundary conditions are equally applicable in the case of unbounded jets and shear layers.

In contrast to the left boundary conditions, the right hand side boundary conditions are classified according to the flow in question. For Poiseuille flow, since the profile is symmetrical, the right boundary conditions are applied at the centre of the channel (y=0). The choice of this point increases the accuracy since it reduces the size of h. The boundary conditions at the centre are

$$\varphi'(0)=\varphi'''(0)=0 \qquad (3.3.10)$$

for both symmetrical stream functions (u is antisymmetric and v is symmetric) and antisymmetric stream functions (u and v are given by (2.2)). Since these two types of disturbance are uncoupled in the case of symmetrical flows, the boundary conditions for each type should be applied separately. Using (3.3.2 a and c) equation (3.3.10) reduces to

$$V_{N+1}=V_{N-1} \qquad V_{N+2}=V_{N-2} \qquad (3.3.11)$$

for symmetrical stream functions, and

$$V_{N+1}=-V_{N-1} \qquad V_{N+1}=-V_{N-1} \qquad (3.3.12)$$

for antisymmetrical stream functions.

Adding the coefficients in similar manner as was done with the left boundary conditions, the last two columns of the matrix will be eliminated.

In the case of boundary layer flows, there are two possibilities for the application of the right boundary conditions. The first is to apply (3.3.8) directly (equation (2.5b)). The second possibility will be slightly simpler. It is assumed that V_{N-1}, V_N, V_{N+1} and V_{N+2} satisfy the equation

$$V_{N+k} = Ae^{-k\alpha h} + Be^{-k\gamma h} \qquad ,k=-1,0,1,2 \qquad (3.3.13)$$

where $\gamma^2 = \alpha^2 + iRe(\alpha - \omega)$. Eliminating A and B we have

$$V_{N+1} = (e^{-h\alpha} + e^{-h\gamma})V_N - e^{-h(\alpha+\gamma)}V_{N-1} \qquad (3.3.14a)$$

$$V_{N+2} = (e^{-2h\alpha} + e^{-h(\alpha+\gamma)} + e^{-2h\gamma})V_N - e^{-h(\alpha+\gamma)}(e^{-h\alpha} + e^{-h\gamma})V_{N-1} \qquad (3.3.14b)$$

Following the approach of Jordinson (1971), this equation can be greatly simplified if $\gamma_r >> \alpha_r$ since the γ term dies out rapidly with y. Equation (3.3.14) then reduces to

$$V_{N+k} = V_N e^{-k\alpha h} \qquad k=1,2 \qquad (3.3.15)$$

Because γ is a double valued function, the solution with

$\gamma_r > 0$ is the only relevant solution (bounded solution for φ). Houston (1976), in order to consider half of the Reiman surface in which $\gamma_r \geq 0$, defined the line $\gamma_r = 0$ to be the branch line. Accordingly, for the spacial problem, the branch line $\gamma_r = 0$ is that portion of the hyperbola

$$\alpha_r [1 + (2\alpha_i / Re)] = \omega \qquad (a)$$

which lies above

$$\alpha_1 = \omega + (i\omega^2 / Re) + O(Re^{-2}) \qquad (b) \qquad (3.3.16)$$

and below

$$\alpha_2 = -\omega - i[Re + (\omega^2 / Re)] + O(Re^{-2}) \qquad (c)$$

where α_1 and α_2 are the location of the branch points.

For the temporal problem, the branch line $\gamma_r = 0$ is that portion of the line $c_r = 1$ which lies below the branch point

$$c = 1 - (i\alpha / Re) \qquad (3.3.17)$$

3.3.4: The solution of the eigenvalue problem

Before discussing the numerical procedures it should be noticed that the problem in hand is a twofold eigenvalue problem because either the phase velocity c or the wavenumber α can be the eigenvalue. In the first case where c is the eigenvalue, we have the classical eigenvalue problem

$$A - c\,I = 0 \qquad (3.3.18)$$

whose solutions are discussed in any good book in numerical analysis (e.g. Froberg 1969). The apex of these solutions are the LR, the QR and the QZ (Moler and Stewart 1973) algorithms which produce all the eigenvalues c of the problem, as was demonstrated when the LR was used in the last sections with the spectral expansion solutions. Although that was possible with the spectral expansion representation of the Orr-Sommerfeld equation, these algorithms are expensive in terms of both time and storage for finite difference matrices due to their lower order of convergence. Therefore, unless it is necessary as in the case of the temporal spectrum, or for finding rough estimates for the eigenvalues, the single route algorithms are the appropriate choice and these can be very fast as will be shown later.

The second case is a rare type of eigenvalue problems. In this case the wavenumber α is the eigenvalue, and because it enters nonlinearly in the Orr-Sommerfeld equation, the final solution cannot be represented by (3.3.18). Therefore, there is no alternative but a successful single route routine, in which case it will be equally successful in the temporal case.

Here, three methods will be discussed. The first because it is used successfully by Edinburgh University investigators and for the sake of comparison with the

other two which have been used by the author with equal success.

The solution of the discretised Orr-Sommerfeld equation can be written in the algebraic form

$$B(c)V=0 \qquad (3.3.19)$$

where B(c) is a matrix with complex coefficients and V is the eigenvector. Note that A in(3.3.18) is different from B(c).

For the sake of generality we will describe the three methods for the temporal eigenvalue c only with the understanding that it is valid also for the eigenvalue α.

3.3.4.1: Method1: The Osborne iterative procedure

This procedure was originally due to Osborne and Michaelson (1964) and subsequently developed by Osborne (1967). According to this method equation (3.3.19) is written in the form

$$B(c)V=f(c)X \qquad (a)$$

$$S^{T}V=1 \qquad (b) \qquad (3.3.20)$$

where S^{T} is a transposed vector with its mth entry, which corresponds to the entry of V with maximum modulus, set to unity. As c varies so does f(c) and when c passes through

an eigenvalue of B(c), f(c) vanishes. Therefore, the eigenvalue of B(c) can be calculated using Newton's method which requires that

$$0 = f(c) + (df(c)/dc)\delta c \qquad (3.3.21)$$

In order to find the derivative in equation (3.3.21), equation (3.3.20) is differentiated with respect to c. This gives

$$(dB/dc)V + B(dV/dc) = (df/dc)X \qquad (a)$$
$$S^T(dV/dc) = 0 \qquad (b) \qquad (3.3.22)$$

Premultiplying (3.3.22 a) by (B^{-1}), estimating (dV/dc) using (3.3.22b), using (3.3.20) to estimate X and using (3.3.21), we have

$$-\delta c = (S^T V)/[S^T(B^{-1}dB/dc)V]$$

According to Osborne, this iteration takes in practice the form:

$$B(c^j)V^{j+1} = (dB(c^j)/dc)Q^j/Q^j{}_m \qquad (a)$$
$$B(c^j)Q^{j+1} = (dB(c^j)/dc)V^{j+1} \qquad (b) \qquad (3.3.23)$$

hence,

$$c^{j+1} = c^j - (V^{j+1})_m/(Q^{j+1})_m$$

where j stands for the stage of the iteration and m for the component with the maximum modulus.

In equation (3.3.23), $dB(c^j)/dc$ is a discretised matrix

and the inverse $B^{-1}(c)$ is obtained using the Gaussian elimination. These calculations are supposed to take minimal time since the pentadiagonality of the matrix can be utilized to reduce the amount of computation as will be demonstrated below. Starting values of the eigenvalue to within 0.02 of their final value have been proved successful. Six or seven iterations are required in order to reduce the difference between two successive values of c^j to $O(10^{-10})$.

3.3.4.2: Method 2:The zero of the determinant method

It was mentioned in chapter 2 that finding the eigenvalues of a matrix is equivalent, (by the cofactor expansion), to finding the N zeros of the determinant B(c), or

$$|B(c)|=0 \qquad (3.3.24)$$

Using any trianglisation method like Gaussian elimination or Crout's factorisation, the determinant can be found readily as the product of the diagonal elements. It turns out that equation (3.3.24) can be satisfied with rather less computation by utilising one of the theorems of the determinants, which states that: "If every element of a row (column) of a square matrix B(c) is zero then $|B(c)|=0$"(Ayres (1962)). This fact has been utilised by (Wilkinson 1965) for accelerating the convergence of the eigenvalues in the LR algorithm.

After subjecting the matrix B(c) to the Gaussian elimination, the elements of the last row are all zeros, except the last right hand side element which, by the appropriate change in the eigenvalue c, is reduced to zero, then the determinant is zero according to the theorem above and the eigenvalue is found. Thomas (1953) who first used the method for solving this problem for the channel Poiseuille flow, realised that the Gaussian elimination would lead to a convergent solution only if it was observed from the wall to the centre of the channel, since the elimination in the opposite direction will lead to an element very sensitive to the change in the eigenvalue c due to the imposition of the boundary condition $\varphi=0$. Bearing this situation in mind, the finite difference solution given in subsection 3.3.2 was arranged in the same direction as the one which the Gaussian elimination would follow in order to obtain a convergent solution, i.e from the wall in the top left of the matrix to the centre of the flow or to the free stream of the boundary layer flow in the bottom right.

To sum up, the Gaussian elimination is carried out towards the second boundary condition and the resulting last element L(c) is used for finding the next estimate of the eigenvalue, say through the Newton-Raphson method

$$c^{j+1}=c^{j}-[L(c)/(dL(c)/dc)] \qquad (3.3.25)$$

In comparison with the Osborne method this scheme is extremely simple and straightforward. Besides reducing the storage and simplifying the programming, it cuts the time required to find an eigenvalue by a factor of 3. The time taken by one iteration using this method on the ICL 2972 and 2988 is about 0.13 seconds for a step size h=0.01. This should be compared with the 3 seconds reported by Gupta and Garg (1981) for the same step size, using the shooting method with a Gram-Schmidt orthogonalisation procedure on an IBM7044 machine. For channel flows the method is successful even with a starting value as far from the eigenvalue as 0.05. For the Blasius boundary layer however, a close starting value is required, which is generally to within 0.02 of the eigenvalue. The Blasius flow requires close estimates with all methods as is apparent from the discussions of Jordinson (1968), who used the Osborne method and of Mack(1976) who used the shooting method.

For Stokes Layer flow, the starting value should be very close, some times to within 0.003, otherwise the solution will converge to one of the closely situated damped eigenvalues, which is an unexpected result, since these eigenvalues are the most difficult to find in the channel flows. The obvious solution is to use in the start the false position method before using the iterative procedure.

3.3.4.3: Method 3:The boundary condition method

This method is also simple and the first one which comes to mind when encountering the problem, although surprisingly enough, it is seldom used. The method is similar to that used for finding the eigenvalues in the shooting method, where the correct eigenvalue is found only if at the end of the integration procedure the second boundary condition was found to be satisfied. Since in the shooting method there are two independent solutions [see (2.4)], a secular determinant is formed from the four components φ and φ', then this determinant is required to reduce to zero. [These conditions are the wall conditions (3.3.7) given as an example, but the other side boundary conditions can equally be used since in the shooting method the direction of integration does not pose any problem (Gupta and Garg 1981)].

To be consistent with the direction which we adopted in the derivation of the finite difference system we will leave the left hand side boundary condition imposed using (3.3.8) and will require the right hand side boundary condition to be satisfied when the correct eigenvalue is found. These conditions in the case of channel Poiseuille flow are

$$\varphi'(0)=\varphi'''(0)=0 \qquad (3.3.10)$$

Equation (3.3.10) requires the determination of the eigenvectors V which makes this method, similar to the previous one, dependent on Gaussian elimination. From (3.3.2) and (3.3.5)

$$\varphi'''(0)=V_{N+2}-2V_{N+1}+2V_{N-1}-V_{N-2}=0 \qquad (3.3.26)$$

which shows that only the last 4 eigenvectors are required, in which case the increase in computational time over the previous method will be minimal. If (3.3.26) is satisfied, then $\varphi'(0)=0$ automatically. The problem however is not that straightforward. In the shooting method the final result is not independent of the initial conditions on the first boundary (initial value problem) and a convergent solution can be obtained. In the case in hand the situation is the same (boundary value problem) and the solution will not converge to (3.3.26) unless some other boundary condition is imposed on the right hand side boundary so that the solution will sense the position where (3.3.26) will be satisfied. This will be referred to as the replacement condition. For channel flows this replacement condition, due to the fact that the flow is symmetrical, can be written

$$V_{N+3}=\pm V_{N-3} \qquad (3.3.27)$$

where (±) signs correspond to the similar situations given by (3.3.11) and (3.3.12). After applying (3.3.27) some manipulations are required in order to retain the pentadiagonality of the matrix.

In the boundary layer cases, we will require that the condition $\varphi'=\varphi=0$ is satisfied when the correct eigenvalue is found, in which case the replacement condition is (see 3.3.15)

$$V_{N+3}=V_N e^{-3h\alpha} \qquad (3.3.28)$$

According to (3.3.27) and (3.3.28), the velocity distribution should be obtained at only N-1 points in order to accommodate the replacement boundary conditions. It should be noted that in the final result, the determinant is not necessarily zero.

In comparison with the zero of the determinant method, this method is slightly complicated. However, it does converge:

1) to the same eigenvalues

2) in the same number of iterations

3) to the same degree of accuracy

4) in almost the same amount of computational time.

The method has also two advantages over the zero of the determinant method

a) It can be used in either direction, the advantage which it shares with the shooting method.

b) It does show the position of the eigenvalues in a clearer way when the contours of the two solutions are drawn for locating the difficult routes, as will be demonstrated later.

3.3.5: The iterative procedures

The aim of the three methods described in the last subsections is to find a good estimate to δc so that

$$c^{j+1} = c^{j} + \delta c \qquad (3.3.29)$$

will converge to c after a certain number of iterations when $\delta c \leqslant \varepsilon$, where ε is a preset parameter say $\varepsilon = 10^{-10}$.

In the Osborne method (subsection 3.3.4.1), finding δc is a part of the method itself, and hence, there is no way to choose the iterative procedure since the method has been derived through Newton's method. However, for the other two methods, the iterative procedure can be chosen since we know exactly the function and its final required value. Using the the appropriate method, the function L(c) or the boundary condition will be reduced to zero. The Newton-Raphson method is the most popular method for this purpose, but it suffers from one disadvantage, namely all the calculations should be repeated twice for each iteration in order to obtain an accurate derivative. This process will lead to a considerable amount of computation, for example, in the case of a constant amplification curve or wavepacket calculations. (Note that Osborne´s method does not suffer from this disadvantage since the derivative of the matrix is obtained through discretisation of the derivative).

The problem of convergence speed is the most important after the conditions for convergence have been satisfied. The speed is measured using the so called order of convergence p, which is defined by

$$\lim_{j \to \infty} (c^{j+1} - c) / |c^{j} - c|^{p} = C \qquad (3.3.30)$$

if there exists a constant C>0 (called the asymptotic

error constant). If p=1, then C<1 and the convergence is called linear, while it is called quadratic if p=2 (Froberg 1969).

The effectiveness of the iterative method is defined as $E=p^{1/s}$, where s (called horner) is the number of new evaluations of the function and its derivatives required per iteration j. The best iterative methods are those with large E. It turns out that the methods which do not require the evaluation of the derivatives like Regula falsi (some times this is called variable secant), and Muller(1956) methods are those with large E. The value of E for Regula falsi and Muller methods is 1.62 and 1.84 respectively, while for Newton-Raphson method, E=1.41 (Froberg 1969)

By the Regula falsi method

$$c^{j+1}=c^{j}-[f(c^{j})(c^{j}-c^{j-1})]/[f(c^{j})-f(c^{j-1})] \qquad (3.3.31)$$

in which case, the first two estimates c^{j-1} and c^{j} are supplied.

The Muller iteration gives

$$c^{j+1}=c^{j}+k^{j+1} \qquad (3.3.32)$$

where,

$$k^{j+1}=2f^{j}\delta^{j}/ g^{j}\pm\{(g^{j})^{2}-4f^{j}\delta^{j}k^{j}[f^{j-2}k^{j}-f^{j-1}\delta^{j}+f^{j}]\}^{1/2} \qquad (a)$$

(3.3.33)

where,

$$\delta^{j}=1+k^{j} \qquad (b)$$

$$k^j = (c^j - c^{j-1}) / (c^{j-1} - c^{j-2}) \qquad (c)$$

$$g^j = f^{j-2}(k^j)^2 - f^{j-1}(\delta^j)^2 + f^j(k^j + \delta^j) \qquad (d)$$

For the full derivation of the method the reader is refered to Muller (1956). It is obvious that the first three estimates of the eigenvalue c and the corresponding values of the function f should be supplied and the procedure will start working in the fourth iteration. Normally the first value of c is supplied by the user of the program, while the second is obtained from the first by adding a fixed increment to it, and the third is obtained using the Newton-Raphson method once.

The method takes 3 or 4 iterations to converge when $|c^{j+1} - c^j| < 10^{-10}$. This number of iterations does not include the three starting values. It should be noted that the shooting method converges in the same number of iterations. The Regula falsi method takes fewer iterations for close estimates, but takes more than the Muller method when the estimate is poor. The number of Muller iterations changes very slowly as the estimate gets poorer.

In this study, the Muller method with the Newton-Raphson method as the starter is used throughout for calculating the eigenvalues, while the Regula falsi method is used for other calculations like the maximum amplification and constant amplification curves.

3.3.6: Numerical examples

In order to make the calculations efficient the final matrix B(c) which is pentadiagonal has been arranged in five single dimensional arrays. Array calculations are linear, consequently the speed and the storage increases are linear. The number of arithmetic operations required by the Gaussian elimination after these arrangements are only 16N compared to $N^3/3$ required by the full matrix, while the storage is only 7N compared with N^2 for the full matrix. The arithmetic operations required to find the eigenvectors V are only 8N compared to $N^2/2$ required by the full matrix. (Note that these are complex arithmetic operations). The overall storage required for finding the eigenvalue is only 60N,i.e. 6 Kbyte for a matrix of N=100 in comparison with a code of 16 Kbyte.

TABLE 3.3

The unstable mode of the plane Poiseuille flow

Re=10000.0 and α=1.0

Starter X=0.25, 7 iterations.

N	c	CPU sec.	Error x 10^{-8}
050	0.23752273 i0.00362990	0.504	379 i10976
100	0.23752558 i0.00373286	0.954	094 i00680
150	0.23752630 i0.00373833	1.404	022 i00133
200	0.23752644 i0.00373925	1.854	008 i00041
250	0.23752649 i0.00373940	2.304	002 i00026
300	0.23752652 i0.00373962	2.754	000 i00004
500	0.23752652 i0.00373966	4.554	000 i00000

It is clear from the above table that:

a) The accuracy of the Chebychev solution with 26 terms is achieved only at N higher than 250, but in less than half of the computational time.

b) The actual time required by one iteration for N=100 is only 0.13 second. The same amount of time is required for an increase of N by 100.

c) The error in the imaginary part is larger than the error in the real part.

These results were obtained using the zero of the determinant method. The method will collapse due to the increase in the roundoff error at N greater than 500, although a 64 bit mantissa (double precision) was used throughout the calculations. This collapse happens during the Gaussian elimination. With single precision arithmetic, the collapse happens at approximately N=55 which demonstrates the importance of the double precision calculations for this purpose. It should be mentioned that these results apply when no pivoting is used. Exactly the same can be said about the boundary condition method.

For the time-dependent flow eigenvalues, the convergence is faster than in the case of plane Poiseuille flow and an accuracy of eight significant figures can be obtained with N=150. As in the case of other methods, the error is larger for the same value of N if the quantity αRe is large, and a corresponding increase in N is required for any large increase in αRe.

Another check on the accuracy is made by comparing the

eigenvalues from the Orr-Sommerfeld equation with the eigenvalues from the adjoint equation

$$(U-c)(\varphi''-\alpha^2\varphi)+2U'\varphi'+(i/\alpha Re)(\varphi''''-2\alpha^2\varphi''+\alpha^4\varphi)=0 \qquad (3.3.34)$$

For N=200,

$c_{adjoint}$=0.23752689 i0.00373922

There is an agreement to 6 decimal places between the above value and table 3.3 for the same N. However, comparison with other solutions and extrapolated eigenvalues indicate that the error in the adjoint solution is more than $O(h^6)$, which is due to the the fact that equation (3.3.34) contains the first derivative of φ. An extensive check on the the accuracy of the eigenvalues for different flows was also made by comparing them with those reported by Corner et al (1976), Mack (1976) and Nayfeh and Padhye (1979) for both the temporal and the spatial cases. The comparison also showed that the results in the last reference are of low accuracy.

3.3.7: Contour methods

The disadvantage of the single route methods appear as soon as an attempt is made to find an eigenvalue, a close estimate of which is unknown. In such cases, the iterative procedure either will not converge to any eigenvalue, or will converge to one dominant eigenvalue time after time. This behaviour is mostly noticeable

with the eigenvalues of boundary layer flows. In the temporal problem, close estimates to the eigenvalues can always be found using the LR algorithm with a small matrix say 30 x 30 . Another method which was found to be convenient is the use of the deflation procedures (Johnson and Reiss 1977). In the spatial case however, both these procedures are irrelevant due to the fact that the eigenvalue α enters in the equation nonlinearly. Again for obvious reasons, both procedures are not relevant in the case of the shooting method. The transformation from the temporal to the spatial case due to Nayfeh and Padhye (1979) can be of help, but it is not conclusive in many cases as was discovered by the author. The contour methods are the most appealing and can be used in the spatial as well as the temporal cases. In fact, there are two types of contour methods. Since there are no distinct names known for these methods, they will be given names in order to to distinguish between them.

a) The number of zeros contour method

The number of zeros N and the number of poles P of a function f(z) included within a contour C are given by (Arfken 1970)

$$(1/2\pi i)\oint_C [f'(z)/f(z)]dz=N-P \qquad (3.3.35)$$

If the function f(z) is completely analytic, then it

has no poles P. The function under consideration here is the determinant |B(c)| which can be shown to be completely analytic except possibly near any branch point γ. If instead of the boundary conditions (3.3.15), the left hand side boundary conditions were repeated on the right hand side boundary then |B(c)| is completely analytic (Houston 1976). Accordingly

$$N=(1/2\pi i)\oint_C [B'(c)/B(c)]dc \qquad (3.3.36)$$

Another form of this equation can be obtained using the polar form:

$$B|(c)|= re^{i\theta}$$

from which

$$Ln|B(c)|=Ln\ r+i\theta$$

Hence,

$$B'(c)/B(c)=d[Ln(B(c)]/dc$$

Finally (Arfken 1970), we have

$$N=(1/2\pi)\oint_C d[argB(c)] \qquad (3.3.37)$$

Equation (3.3.37) is used for calculations where the contour C can be either rectangular or circular. The rectangular form is the suitable form, since the search area can be divided conveniently into several rectangles. The integral is evaluated at a sufficiently large number of points; therefore, a long computation time is required. After finding the number of the eigenvalues within a contour, the search area is reduced

and the search for the eigenvalue continues until its approximate value is found. The task is cumbersome, therefore, the next method is more suitable for determining the locations of individual eigenvalues.

b) The zero of the determinant contour method

This method follows from the simple fact that the eigenvalue is found if both the real and the imaginary parts of the determinant (or the second boundary conditions) are zero. A small rectangle with c_r in the x axis and the c_i in the y axis is considered. The zeros of the real and the imaginary parts of the function in question are found and the corresponding values of c_r and c_i are noted. The resulting curves are plotted. The crossing points of the real and the imaginary curves give a very close estimate to the value of the eigenvalue $c=c_r+ic_i$, which is then used as a starter in the main program to find the accurate value.

Figures 3.3 and 3.4 show the application of such a method to find the first family of the eigenvalues of the plane Poiseuille flow at Re=10000 and $\alpha=1$. In figure 3.3 the contours of the zeros of the function L(h) are shown, while in figure 3.4 the contours of the zeros of the boundary condition $\varphi'''(0)=0$ are shown. Both figures cover the same area. The positions of the eigenvalues are marked with o in both figures. In figure 3.3, the two contours come very close to crossing at some points

other than the well documented eigenvalues. Examining very small rectangles containing these controversial positions will reveal that there are no crossings. It is obvious that using the number of zeros contour method is valuable in these areas, since it can determine whether there are any eigenvalues there. In figure 3.4, a clearer picture appears because the crossing points are more distinct, an advantage of the boundary condition contour method.

Table 3.4 demonstrates the reliability of the estimates from the two versions of the second contour method. There is no way to obtain such close values using the number of zeros contour method. The accurate values of the eigenvalues are listed in first column.

TABLE 3.4

The first family of the plane Poiseuille flow eigenvalues from the contour methods. Re=10000, α=1.

Accurate Eigenvalues	Zeros of the Determinant Meth.	Zeros of the Boundary Condit.
0.19001 -i0.18283	0.1900 -i0.1820	0.1870 -i0.1825
0.23753 i0.00374	0.2375 i0.0040	0.2375 i0.0040
0.34910 -i0.12450	0.3500 -i0.1245	0.3500 -i0.1255
0.36850 -i0.23883	0.3680 -i0.2375	0.3650 -i0.2370
0.47490 -i0.20873	0.4760 -i0.2075	0.4750 -i0.2080

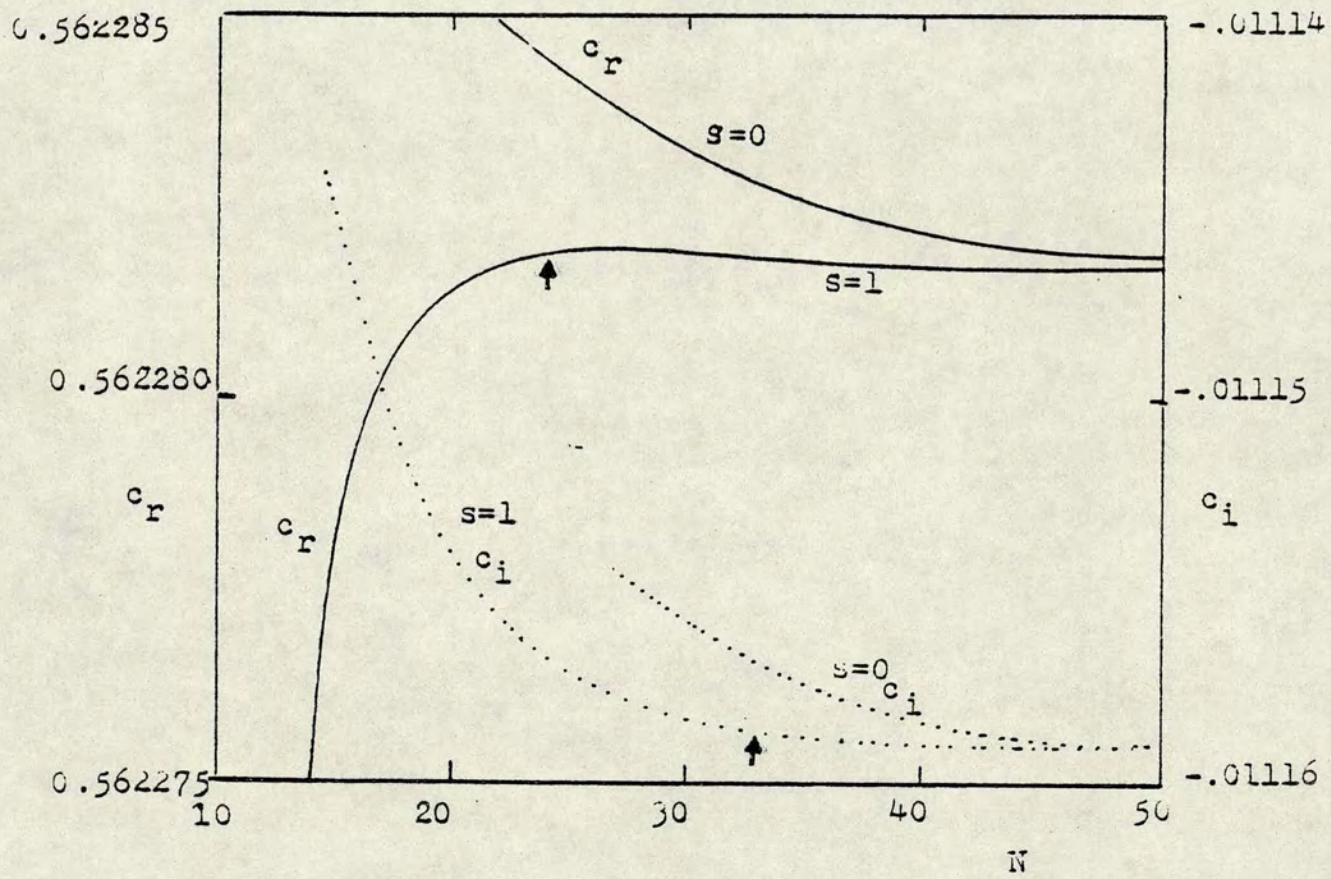

↑ Accurate to 6 decimal places

Figure 3.1: c_r and c_i vs the first dimension of the matrix N, for both unimproved (s=0) and improved (s=1) Garlerkin's methods. Time-dependent flow. β =6, $\omega_0 t$ =30°, Re=500, α =4.0

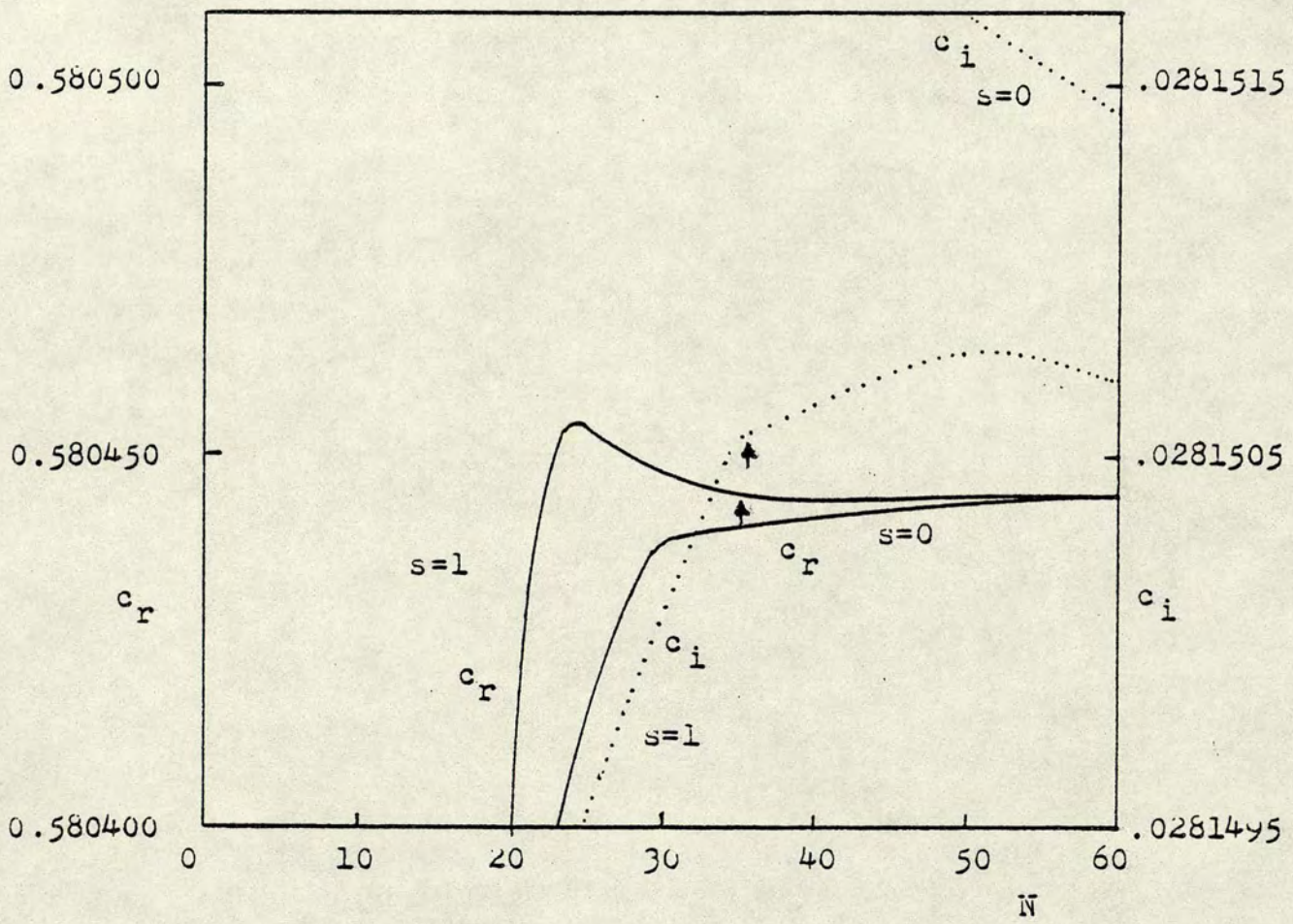

↑ Accurate to 6 decimal places

Figure 3.2: c_r and c_i vs the first dimension of the matrix N, for both the unimproved (s=0) and the improved (s=1) Garlerkin's methods. Time-dependent flow. β =6, ωt =30°, Re=10000, α =4.0

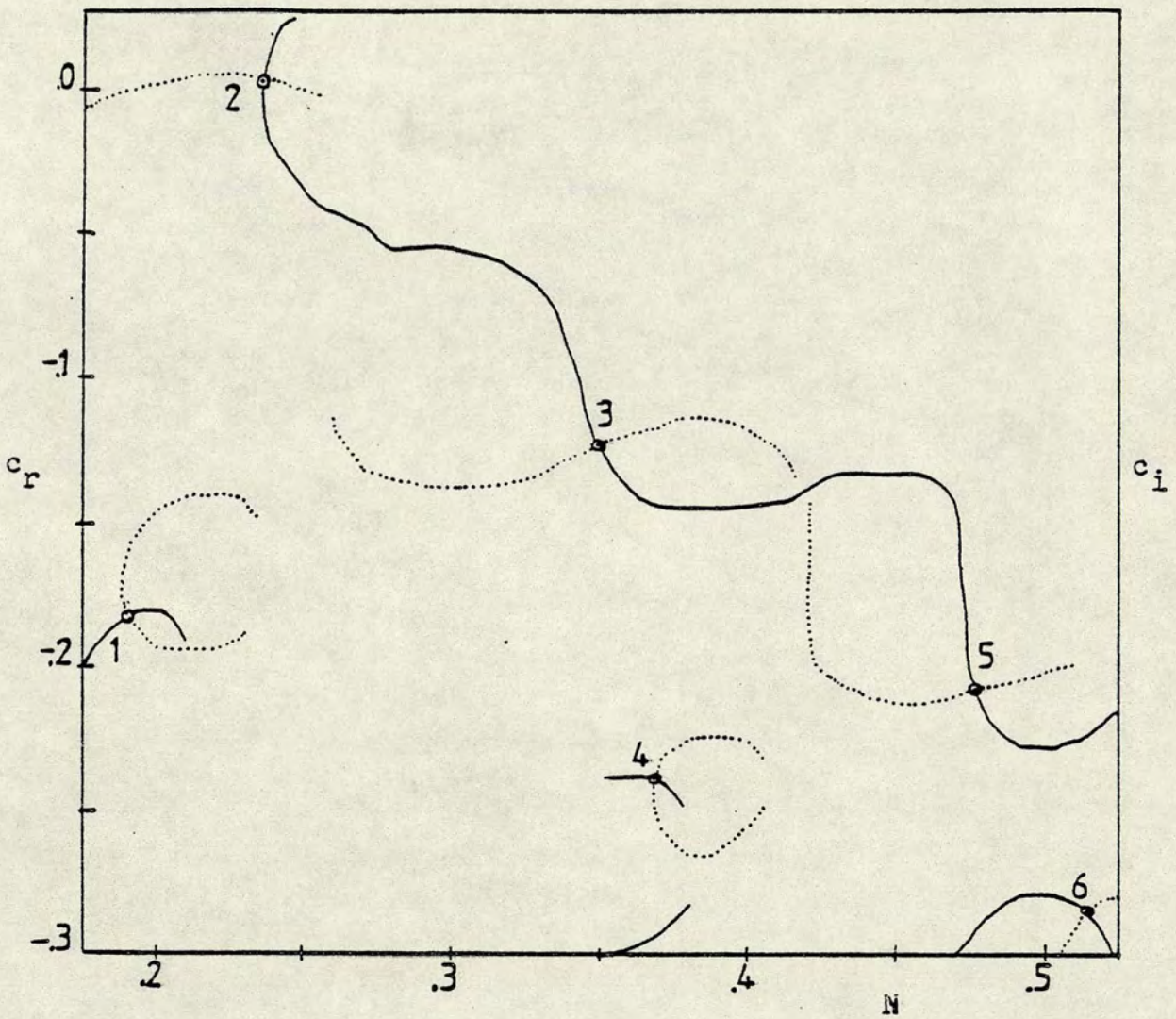

——— The real part

..... The imaginary part

o The eigenvalue

Figure 3.3: Contours of the zeros of the determinant of the Orr-Sommerfeld equation for the first family of the eigenvalues of the plane Poiseuille flow. Re=10000 and α =1.0

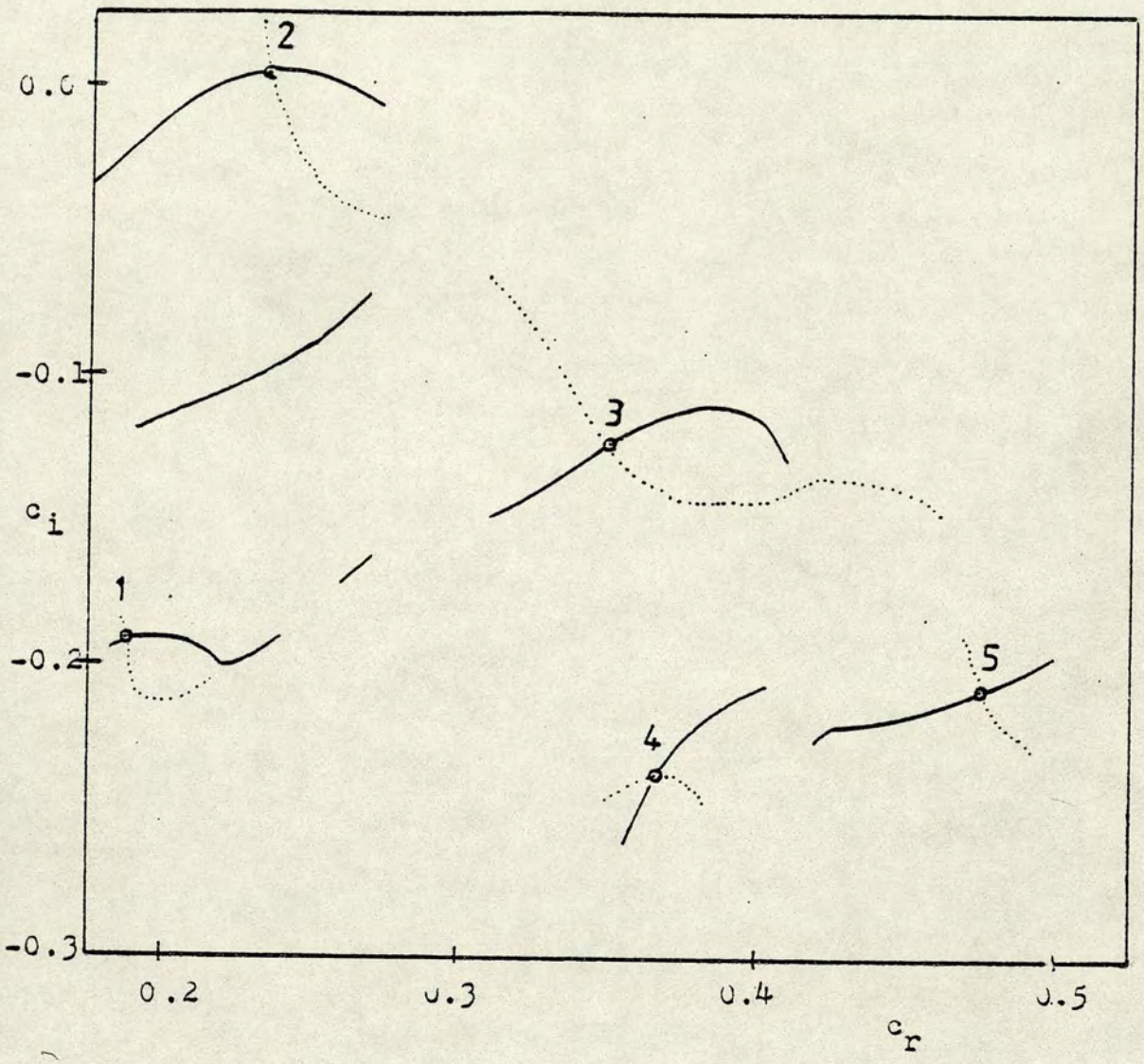

——— The real part

..... The imaginary part

o The eigenvalue

Figure 3.4: Contours of the zeros of the boundary conditions ($\varphi'''=0$), of the Orr-Sommerfeld equation for the first family of the eigenvalues of the plane Poiseuille flow. Re=10000, α =1.0

CHAPTER FOUR

INFLEXION INSTABILITY

4.1: INTRODUCTION

The Orr-Sommerfeld equation is given by

$$[U-c](\varphi''-\alpha^2\varphi)-U''\varphi=-[i/\alpha Re](\varphi''''-2\alpha^2\varphi''+\alpha^4\varphi) \qquad (4.1)$$

Ignoring the right hand side of this equation, the left hand side is the "Rayleigh equation" or the inviscid equation. It is equivalent to having zero viscosity (i.e $Re\to\infty$). In the Rayleigh equation

$$[U - c](\varphi''-\alpha^2\varphi)-U''\varphi=0 \qquad (4.2)$$

where $U=U(y)$ is the velocity of the mean flow, c is the phase velocity and α is the wavenumber of the disturbance. Either c or α can be the eigenvalue of the equation, while the eigenfunction $\varphi(y)$ is the amplitude of the stream function

$$\psi(x,y,t)=\varphi(y)e^{i\alpha(x-ct)} \qquad (4.3)$$

The boundary condition is

$$\alpha\varphi(y)=0 \qquad (4.4)$$

at y1 and y2, the two boundaries of the flow.

Despite the fact that the Rayleigh equation is simpler than the Orr-Sommerfeld equation, only in a small number of cases have analytical solutions been found. Some of these solutions are given by Drazin and Howard (1966) and Drazin and Reid (1981). For the majority, the solution has to be obtained numerically. Drazin and Reid also give an account of another class of approximate solutions which is originally due to Rayleigh(1880). In order to simplify the problem, the velocity profile is broken into several straight line segments. The solutions of the Rayleigh equation for the different segments are then matched in order to obtain the overall solution.

The Rayleigh equation has several important properties:

1) The boundary condition is unchanged when α is replaced by $-\alpha$. From (4.3), for $\alpha<0$ the flow is unstable if $c_i<0$. Therefore, without loss of generality, α is taken to be greater than zero and the condition for instability in the temporal case is $c_i>0$, while in the spatial case, where α is complex, $\alpha_i<0$ for instability.

2) The complex conjugates φ^* and c^* are also solution of (4.2) for the same α. In other words for each unstable wave there is a damped stable wave and vice-versa. Since the Orr-Sommerfeld equation, unlike the Rayleigh equation (4.2), is not invariant under a

complex conjugate transformation, and since from 1) the disturbances grow only if $c_i>0$, then the only meaningful unstable solution in the inviscid case is that with $c_i>0$ and the conjugate is ignored.

3) Lin (1955) has shown than the solution of the Rayleigh equation when $c_i>0$ is a limit of some solution of the Orr-Sommerfeld equation. He also stated that when the Orr-Sommerfeld equation gives instability for some viscous basic flow, the Rayleigh equation may give a stable basic flow. Plane Poiseuille and Blasius flows are examples where this occurs. This follows from the Rayleigh inflexion point theorem given in the next section.

4) In contrast to the Orr-Sommerfeld equation the singularity of the Rayleigh equation, where $U(y)=c$, leads to a continuous spectrum whose eigenvalues are real. This is basically different from the continuous spectrum of the Orr-Sommerfeld equation (see Grosch and Salwen 1978)

4.2: The Inviscid Criteria of Instability

The Rayleigh equation

$$\varphi''-\alpha^2\varphi-[U''/(U-c)]\varphi=0. \qquad (4.5)$$

is singular if c is real. Therefore only $c_i>0$ is considered. Multiplying (4.5) by the complex conjugate φ^*, integrating by parts and after imposing the boundary

condition (4.4), we have

$$\int_{y1}^{y2}(|D\varphi|^2+\alpha^2|\varphi|^2)dy+\int_{y1}^{y2}[U''/(U-c)]|\varphi|^2dy=0 \qquad (4.6)$$

Since $c_i>0$, the imaginary part of this equation is equal to zero only if

$$c_i\int_{y1}^{y2}[U''/(U-c)^2]|\varphi|^2dy=0 \qquad (4.7)$$

This is true only if U'' changes sign once in the interval y1, y2. This is the proof given by Lord Rayleigh (1880) for the inflexion point theorem which states that: " **A necessary condition for instability is that U" changes sign at some point in the flow**". In other words, the basic flow velocity profile should have an inflexion point.

It has already been mentioned that according to this theorem, flows without inflexion points like plane Poiseuille flow are stable. Since this flow is known to be unstable, it has been suggested that the viscosity is a destabilising factor in such flows. Accordingly, the general belief is that there are two mechanisms of instability: viscous and inviscid. Further discussions about the mechanism of inflexion instability will be presented in chapter 7.

However, the condition that U'' should change sign in order that the flow be unstable was shown by Tollmein (1935) to be insufficient. He demonstrated this by studying the instability of U(y)=sin(y) for $-n\pi\leqslant y\leqslant n\pi$, which has an inflexion point at y=0. The phase velocity

$c_r=0$ since the inflexion point velocity Ui=0. Then, the Rayleigh equation is

$$\sin(y)[\varphi''+(1-\alpha^2)\varphi]=0$$

with the boundary conditions $\varphi(y1)=\varphi(y2)=0$. The neutral solution is then

$$\varphi_s=\sin\{[n\pi(y-y1)/(y2-y1)]\} \qquad (4.8)$$

and the wavenumber of the neutral solution

$$\alpha_s=\{1-[n^2\pi^2/(y2-y1)^2]\}^{-1/2} \qquad (4.9)$$

Equation (4.9) shows that α is real only if $n<(y2-y1)/\pi$. Therefore, for n=1, the flow is stable despite the existence of the inflexion point if $(y2-y1)<\pi$. Thus, the condition for the instability of U(y)=sin(y) is that

$$(y2-y1)>\pi \qquad (4.10)$$

Fjortoft (1950) added another condition to the Rayleigh theorem. His Theorem states that **"a necessary condition for instability is that**

$$\mathbf{U''(U-Ui)\leqslant 0} \qquad \mathbf{(4.11)}$$

some where in the field of the flow". The Rayleigh theorem does not differentiate between inflexion points with absolute maximum vorticity and those with a minimum one. What is clear from Fjortoft's theorem is that flows with absolute maximum vorticity at the inflexion point are the only unstable flows, thus excluding flows such as sinh(y) which has a vorticity minimum at the inflexion point. In other words, not all flows with inflexion points are unstable in the inviscid case. However, close inspection

shows that the number of the flows which can be excluded is very small.

The existence of neutrally stable eigensolutions have been proved by Tollmein(1935) and Mises and Friedriches(1942). They showed that these solutions exist for $c_s=Ui$. The proof of Mises and Friedriches is given next.

It is assumed that $F(y)=-U''(y)/[U(y)-Ui]$ is integrable over the field of the flow. Substituting $c=Ui$ and $\alpha=-\lambda$ in the Rayleigh equation, we have

$$\varphi''+[\lambda+F(y)]\varphi=0 \qquad (4.12)$$

which with the boundary condition (4.4) is the Strum-Liouville problem. By the variational principle, the least stable eigenvalue λ is given by

$$\lambda_s=\min\{{}_{y1}\int^{y2}(f'^2-Ff^2)dy/{}_{y1}\int^{y2}f^2dy\} \qquad (4.13)$$

where the minimum is to be taken for f satisfying the boundary conditions. f should have square-integrable derivatives.

From the inequality

$$(y2-y1)^2\,{}_{y1}\int^{y2}f'^2dy\geqslant\pi^2\,{}_{y1}\int^{y2}f^2dy \qquad (4.14)$$

it is clear that a neutrally stable eigensolution with

real positive α_s exists if and only if $\lambda_s<0$. **Therefore,**

$$F(y)>[\pi^2/(y1-y1)^2] \qquad (4.15)$$

everywhere in the field of the flow. Equation (4.15) should be satisfied by all inviscid unstable flows. Tollmein's counter-example $U(y)=\sin(y)$, has $F(y)=1$ everywhere in the flow. Therefore, according to (4.15), the flow is unstable only if $y2-y1>\pi$ which is exactly (4.10). It is obvious that condition (4.15) is a complementary condition to both Rayleigh and Fjortoft's theorems.

For channel and boundary layer flows, Tollmein (1935) has already shown that the Rayleigh condition, i.e $U''(y)$ must change sign in the field of the flow, is sufficient. The Fjortoft's theorem and (4.15) are then automatically satisfied.

Drazin and Howard(1966) proved that there is instability only for $\alpha<\alpha_s$. In other words, α_s is the asymptotic value of α on the upper branch of the neutral stability curve of the Orr-Sommerfeld equation. However, their argument does not show that if $0<\alpha<\alpha_s$, then $c_i>0$. Therefore, there is a possibility that the φ_s associated with α_s is not that of the least stable mode.

According to the theoretical solutions for some flows, monotone profiles have $c_s=Ui$ when $\alpha=\alpha_s$, where Ui is the velocity at the inflexion point. This is true also for

non-monotone profiles. However, in some cases, $U''_s \neq 0$. In these cases, the method of Foote and Lin (1950) is used to determine α_s and c_s.

There are two more results of practical importance that arise from the inviscid equation:

1) **Howard** Semicircle Theorem

The Theorem is concerned with the range of the eigenvalues of the Rayleigh equation. Rayleigh (1880) limited the range of the eigenvalues to $U_{min} \leqslant c_r \leqslant U_{max}$ when $c_i \geqslant 0$. Howard (1960) has shown that

$$c_r^2 + c_i^2 - (U_{max}+U_{min})c_r + U_{max}U_{min} \leqslant 0$$

In other words, the unstable wave lies in the semicircle

$$\{c_r^2 - 0.5(U_{max}+U_{min})\}^2 + c_i^2 \leqslant \{0.5(U_{max}-U_{min})\}^2 \qquad (4.16)$$

2) The second important result is due to **Hoiland(1953)**, according to which the amplification is given by

$$\alpha c_i < 0.5 \max|U'| \qquad (4.17)$$

4.3: Introduction to the Numerical Work

The numerical calculations which will be presented in this chapter will concentrate on the inflexion instability. Both numerical procedures described in

chapter three were used.

Analytical solutions of the Orr-Sommerfeld equation based on asymptotic expansions are available for a small number of problems. However, general results as those found in the case of the inviscid equation, "the Rayleigh equation", are not available and inflexion instability characteristics so far could not be deduced from the Orr-Sommerfeld equation. In this study it will be shown that this is no longer the case and the numerical solution of this equation can provide very interesting general results.

4.4: Time-Dependent Flow Profiles

The time-dependent flow velocity distribution U(y) was given by (3.2.6) and (3.2.7) [see also (6.11)]. The flow repeats itself every 2π. The beginning of the period of the flow was made to coincide with the zero of the mean velocity for all the frequency parameters β (see details in chapter 6). For $\beta \geq 4$ all profiles have inflexion points. For $\beta < 4$ the inflexion period decreases with β until it is confined to about $\omega_0 t = \pm 5^\circ$ at $\beta = 1$. The inflexion period disappears completely at $\beta = 0$. For small values of β profiles have one inflexion point, while for values of $\beta \geq 5$ they may have more than one inflexion point. The inflexion points can be classified into two types. The first is usually enclosed between the maximum velocity and the wall. The sign of the vorticity (-Ui') is

negative for this type of inflexion point. These are similar to those found in jets and mixing layers. They will be called hereafter **"wall inflexion points"** (figure 4.1, $\omega_0 t = 110^\circ$). The second type are found between the maximum velocity and the centre of the channel. Those will be called **"core inflexion points"** to differentiate between the two types. Both types were found to be unstable according to Fjortoft's theorem (4.11). Equation (4.15) was also found to be satisfied for all profiles. For time-dependent flow profiles (3.2.6) and (3.2.7), only one wall point can be found in one profile, while each profile can have several core inflexion points.

4.5: The Critical Wavenumbers and the Resonance Mechanism

4.5.1: The case of time-dependent flow profiles

Several critical Reynolds numbers and wavenumbers for different velocity profiles at different values of the frequency parameter β and phase angle $\omega_0 t$ have been calculated. Those values have been calculated for more than 80 profiles. It has been observed that there exists a simple relation through which all the critical wavelengths can be obtained if certain proportionality constants and certain lengths in the flow are known. Thus giving evidence to the existence of some resonance mechanism according to which the wavelength of the critical disturbance is selected. Looking to figures 6.2 and 6.3, it can be seen that the profiles to a large extent are

standing waves in the transverse direction. The existence of such a resonance mechanism will be demonstrated here by the following examples both of which are for a core inflexion point. For $\beta=6$

$\omega_0 t=30^\circ$ $\alpha_c=4.3185$ $\lambda_c=1.45500$ $L=0.3614$

$\omega_0 t=60^\circ$ $\alpha_c=5.5265$ $\lambda_c=1.13826$ $L=0.3003$

where α_c the critical wavenumber and λ_c is the critical wavelength. Taking the length L as the distance between the two points at which U'=0, (i.e. between the maximum velocity and the centre of the channel, figure 4.1), the critical wavelength is then given by

$$\lambda_c = 4\ L \qquad (4.18)$$

This relation was found to be satisfied for all values of $\omega_0 t$ at all values of β when there is only one core inflexion point. The first part of table 4.1 gives three more examples of (4.18).

As the number of core inflexion points increases, the relation (4.18) changes to

$$\lambda_c = 4.5\ L \qquad (4.19)$$

where L is the distance between the points U'=0 on both sides of the inflexion point in question.

TABLE 4.1

The critical wavenumbers of time-dependent flow profiles

OSE=Orr-Sommerfeld Equation

I.P.= Inflexion Point

β	$\omega_0 t$ (degs)	Type of I.P.	No of I.Ps	α_c (OSE)	L	α_c (4.18) (4.19)
6	30		1	4.3185	0.36140	4.3464
6	60	One	1	5.2265	0.30032	5.2304
6	90	Core	1	6.6300	0.23950	6.5586
6	110	I.P.	2	8.0900	0.19765	7.9474
4	60		1	8.0340	0.20055	7.8323
10	30	Many	2	5.9865	0.22190	6.2921
14	92	core	3	8.7050	0.15868	8.7981
18	90	I.Ps	4	11.2000	0.12341	11.3137
2	0	Core	1	4.1300	0.38833	4.0450
3	0	I.Ps	1	4.1000	0.39223	4.0048
4	0	with	1	4.0002	0.40065	3.9206
6	340	reverse	1	4.1250	0.39406	3.9867
8	0	flow	2	5.4854	0.27657	5.6790
10	0		2	6.8950	0.22765	7.0500
6	110	One	2	3.3300	0.47458	3.3100
6	120	wall	2	3.5000	0.45400	3.4600
6	145	I.P.	2	3.9400	0.40257	3.9020

When a profile has a reverse flow (e.g. $\omega_0 t=0^\circ$) and if this profile has more than one inflexion point, the critical wavelength relation reverts back to (4.18). In this case also, L is the distance between the two points at which $U'=0$ and which are on either side of the inflexion point considered.

For the wall type inflexion points [fig. 4.1, $\omega_0 t=110^\circ$], the length L is different from the previous cases. In this case, L is the distance between the inflexion point and the centre of the channel and the wavelength is given

again by (4.18).

It is obvious that, for all profiles with core inflexion points, the critical wavelength is given by $\lambda_c = K_c L$, where K_c is either 4 or 4.5, while L is the distance between the zeros of the vorticity of the mean flow. This suggests that the vorticity standing waves play a major role in this mechanism of the instability. This is in agreement with the conclusions of chapter 7 that in the case of inflexion instability the vorticity profile constitutes a profile of a disturbance. This is also true in the case of wall inflexion points except that the wall limits the effective width of the vorticity to the inflexion point only, since in most of the cases the vorticity standing wave has no nodes on the wall. This and other arguments about the origin of inflexion instability will be discussed in chapter 7. It is interesting to note that the critical wavelengths in the direction of the flow are determined solely by the width of the flow. It was well known that the large scale structures have a width equal to that of the flow in the transverse direction, while the wavelength in the direction of the flow is several widths (Bradshaw 1978).

In the third part of table 4.1, the profiles with reverse flow have L as the distance between the points with $U'=0$ and $K_c=4$. The data for the profile at $\beta=6$ and $\omega_o t=0$, is not included in table 4.1 because it is exceptional. The critical wavenumber $\alpha_c=4.2585$ and the

wavelength λ_c=1.4754. K_c=4 is not valid, and the value of λ_c is either given by

λ_c= 3.5 x 0.423, or

λ_c= 4.5 x 0.33

where the first length L=0.423 is the distance between the points with U'=0 and the second L=0.33 is the distance between the inflexion point and the centre of the channel. This does not mean the breakdown of the resonance selection of the critical wavelength since both L are well defined, and at the same time the two values of K_c have an average which is exactly equal 4. Whether this coincidence is the reason for the departure from the value of K_c=4 remains to be investigated in depth. The same behaviour is found at $\omega_0 t$=5°, where α_c=4.27655 and λ_c=1.46922. The two values of L are 0.4125 and 0.32, with an average value of 0.36625. Using this value with the above value of λ_c, we have K_c=4.012. It is clear that while for the majority, the selection of K_c and L follow straightforward rules, for some others like those with reverse flow other factors intervene. Further investigations are required in order to determine these factors.

4.5.2: The case of U=sin(y)

To investigate the existence of the previous mechanism in other flows, the velocity distribution

$$U(y)=\sin(y) \qquad 0 \leqslant y \leqslant n\pi \qquad (4.20)$$

has been considered. n was chosen to be an odd integer in

order to obtain a symmetrical flow. n=1 is excluded according to the condition (4.10). The flow domain increases as n increases. (figure 4.2)

For n=3, there are two inflexion points in each half of the channel. The critical wavenumber obtained from the solution of the Orr-Sommerfeld equation is $\alpha_c=\alpha_0=0.487584$. This value is very close to the value of 0.5 obtained from (4.18) with $L=\pi$, the distance between the zeros of the vorticity ($-U'=0$).

For n=5 there are two inflexion points facing each other in each half of the channel. The two critical wavenumbers are given in table 4.2. It is easy to verify that

$$\alpha_1+\alpha_2=2\alpha_0 \qquad (4.21)$$

and

$$\alpha_1=\alpha_0+\Delta\alpha, \quad \alpha_2=\alpha_0-\Delta\alpha \qquad (4.22)$$

where $\Delta\alpha=0.1$

For n=7, there are three inflexion points in each half of the channel (figure 4.2). Again for the first two points, (4.21) and (4.22) hold with $\Delta\alpha$ being smaller in this case. The third inflexion point has the critical wavenumber $\alpha_{03}=0.33845$. For this point, the constant of proportionality K_c in (4.18) changes from 4 to 6, i.e. $\alpha_{03}=2\pi/6L$, and $\lambda_{03}=6L$
where $L=\pi$ as before.

TABLE 4.2

The critical parameters for $\sin(y)$, $0 \leq y \leq n\pi$, for different values of n

n=3	1 inflexion point	
$Re = 4.1826$	$\alpha_0 = 0.48758$	$c_{r0} = 0.338362$
n=5	2 inflexion points	
$Re_1 = 3.6458$	$\alpha_1 = 0.58823$	$c_{r1} = 0.064111$
$Re_2 = 7.5760$	$\alpha_2 = 0.38597$	$c_{r2} = 0.471270$
n=7	3 inflexion points	
$Re_1 = 2.8785$	$\alpha_1 = 0.53912$	$c_{r1} = 0.021004$
$Re_2 = 6.0692$	$\alpha_2 = 0.44207$	$c_{r2} = 0.488785$
$Re_3 = 8.8808$	$\alpha_{03} = 0.33845$	$c_{r03} = -0.394210$
n=9	4 inflexion points	
$Re_1 = 2.4782$	$\alpha_1 = 0.47807$	$c_{r1} = 0.010722$
$Re_2 = 5.5620$	$\alpha_2 = 0.49720$	$c_{r2} = 0.313168$
$Re_3 = 6.6994$	$\alpha_3 = 0.41870$	$c_{r3} = -0.536034$
$Re_4 = 10.2900$	$\alpha_4 = 0.28731$	$c_{r4} = -0.356892$

For n=9, (4.21) and (4.22) again hold for the first two inflexion points with $\Delta\alpha = 0.01$. In addition we have

$$\alpha_3 + \alpha_4 = 2\alpha_{03}$$

It is easy to verify that for $n \geq 5$, the first pair of inflexion points satisfy the relation

$$\alpha_{1,2} = 0.5\{2\alpha_0 \pm [(3\pi)/(y2-y1)]^2\}^{1/2} \qquad (4.23)$$

where, the sign is + for α_1 and - for α_2.

Similarly, for the second pair of inflexion points, we have

$$\alpha_{3,4}=0.5\{\alpha_{03}\pm[(7\pi)/2(y2-y1)]^2\}^{1/2} \qquad (4.24)$$

Similar relations can be found for higher order pairs. Notice that the second pair of the inflexion points have negative phase velocities.

U=sin(nπx) in a constant domain

In this case, the velocity distribution is given by

$$U(y)=\sin(n\pi x)$$

where $0\leqslant x\leqslant 1$ for odd $n\geqslant 3$. The calculations were carried out for a fixed width of 3π.

The critical values for n=3 are the same as before, but for $n\geqslant 5$, as expected, they are different. From table 4.3, it can easily be verified that critical wavenumbers for odd $n\geqslant 5$ satisfy the relation

$$\alpha_c=2\pi/4.5\ L \qquad (4.25)$$

where the length L in this case is the distance between the first left hand side point where -U'=0 and the centre of the channel. The agreement between (4.25) and the Orr-Sommerfeld solution is very good (table 4.3).

TABLE 4.3

The critical parameters of the first inflexion point of $\sin(n\pi x)$, $0 \leq x \leq 1$, in the constant domain 3π

n	Re_c	c_r	α_c(OSE)	L	α_c(4.19)
3	4.1826	0.33836	0.48758	π	0.5(4.18)
5	3.4148	0.01845	0.36134	1.2 π	0.37037
7	4.1148	-0.00233	0.33433	9/7 π	0.34568
9	5.0668	0.00214	0.33052	12/9 π	0.33333

4.5.3: The case of wake profiles

Wakes, jets and mixing layers flows represent a class of practical importance. These flows have the property of self preservation after a certain distance x from the origin. Although the width of the flow increases as x increases, the velocity profiles are similar in the sense that the profiles at different values of x can be fitted on one profile if the appropriate normalisation is adopted. As a representative of this class of flows, we will consider the stability of the wake behind a circular cylinder. Obviously, as in previous examples, we will concern ourselves only with the two-dimensional instability. The velocity profile of the wake is given by (Schlichting 1968)

$$U(\eta)/U_\infty=(1/4\pi)[U_\infty Cd\ d/\varepsilon_o]^{1/2}[Cd\ d/x]^{1/2}\ \exp(-\eta^2/4) \quad (4.26)$$

where Cd is the drag coefficient, d is the thickness of the cylinder and

$$\eta=y(U_\infty/\varepsilon_o x)^{1/2} \quad (4.27)$$

in which

$$\varepsilon_o=0.0222\ Cd\ d\ U_\infty \quad (4.28)$$

Equation (4.27) using equation (4.28) becomes

$$\eta=1.67789\ y/b_{1/2} \quad (4.29)$$

where the half width of the wake at half depth

$$b_{1/2}=(x1)^{1/2}/4 \quad (4.30a)$$

and

$$x1=\ x\ Cd\ d \quad (4.30b)$$

The half width of the wake is given by

$$b\ =\ 2.267574\ b_{1/2} \quad (4.30c)$$

The velocity distribution (4.26) after using (4.28) becomes

$$U(\eta)/U_\infty=0.946648[Cd\ d/x]^{1/2}\ \exp(-\eta^2/4) \quad (4.31)$$

Equation (4.31) shows that the velocity distribution of a wake behind a circular cylinder has a Gaussian distribution. The distribution (4.31) is valid only when self similarity is established (Schlichting 1968).

In this study the distribution (4.31) is normalised by the velocity at the centre (y=0), in which case

$$U(\eta)/U(0) = \exp(-\eta^2/4) \qquad (4.32)$$

Thus, explicit use of Cd which is Re dependent was avoided. The distance x downstream can be retained using (4.30b) if Re is known. The width of the cylinder d=2. The velocity profiles calculated from (4.32) are shown in figure 4.3 for x1=50, 100, 150, and 200. The width of the flow increases as the distance from the origin x in the form $b \backsim x^{1/2}$.

For stability calculations, since the flow is symmetrical, only half of the domain was considered, and the boundary conditions $\varphi' = \varphi''' = 0$ were applied at the centre (y=0). The finite difference method described in 3.2 was used for solving the Orr-Sommerfeld equation. Calculations were accomplished for several values of $1 \leqslant x1 \leqslant 200$. In the second column of table 4.4, the critical wavenumbers calculated from the Orr-Sommerfeld equation are given. It is not difficult to find that these values satisfy the relation

$$\alpha_c = 2\pi/4.4\ b = 1.42701/b = 3.236/b_{1/2} \approx \pi/b_{1/2} \qquad (4.33)$$

In the second and the third columns of table 4.4, the values calculated from the Orr-Sommerfeld equation and from (4.33) are listed. The two calculations agree to 4 and 5 decimal places. The wavelength is given by

$$\lambda_c = 4.4\ b \backsim 10\ b_{1/2} \qquad (4.34)$$

Thus, **the critical wavelength increases linearly with the**

flow width and is equal to 2.2 times the full width of the wake.

TABLE 4.4

The critical wavenumbers of the wake

from the Orr-Sommerfeld equation (OSE) and (4.33)

x1	α_c(OSE)	α_c(4.33)	λ_c	b
1	2.51728	2.51727	2.4960	0.56690
5	1.12577	1.12568	5.5813	1.26760
10	0.79604	0.79603	7.8931	1.79267
50	0.35600	0.35600	17.6496	4.00850
100	0.25173	0.25173	24.9600	5.66890
150	0.20553	0.20553	39.5701	6.94300
200	0.17799	0.17799	26.4140	8.01710

The critical Reynolds numbers among others are given in table 4.5. The second column shows that the critical phase velocity is constant for all values of x1 and equal to about 1/4 of the velocity at the centre. (It should be remembered that the profiles here are inverted, i.e the free stream velocity is considered zero). From table 4.5 the critical Re looks like adjusting itself in such a way as to keep both the phase and the group velocities constant at all values of x1. The change in the phase velocity with α_c is given by

$$\partial c_{rc}/\partial\alpha_c = (\partial\omega_c/\alpha\partial\alpha_c) - (c_{rc}/\alpha) = 0.4039/\alpha_c = 0.283\ b \quad (4.35)$$

i.e. proportional to b. In table 4.5, the phase velocity c_{rc} is constant for various values of x1, while Re_c decreases with the increase of x1. Therefore, we should expect Re_c to depend on b. This is easily found in the form

$$Re_c = 22.2849/b \quad (4.36)$$

TABLE 4.5

The critical Reynolds numbers and other critical quantities of the wake

x1	Re_c	c_{rc}	ω_c	Re_c/ω_c	$\partial\omega_c/\partial\alpha_c$
1	39.31004	0.257729	0.648777	60.5910	0.6616315
5	17.57998	0.257731	0.290144	60.5906	0.6616318
10	12.43093	0.257730	0.205162	60.5908	0.6616316
50	5.55928	0.257729	0.091751	60.5913	0.6616314
100	3.93100	0.257734	0.064880	60.5893	0.6616317
150	3.20965	0.257728	0.052972	60.5916	0.6616340
200	2.77966	0.257703	0.045868	60.6023	0.6616376

Accordingly, the critical wake Reynolds number

$$Re_c^* = (Uob/v)_c = Re_c b/d = 11.1425 = \text{constant} \quad (4.37)$$

where U_o is the normalisation velocity at the centre y=0. The critical angular frequency is

$$\omega_c = \alpha_c c_{rc} = 0.3677833/b$$

This leads to another critical constant for the wake, namely

$$Re_c/\omega_c = 60.5924 \qquad (4.38)$$

The values of Re_c/ω_c for different values of x1 are given in the fifth column of table 4.5.

The maximum temporal amplification rate at Re=1000 and Re=10000 for different values of x1 are given in table 4.6. In this case also, a relation similar to (4.33) exists. The value of the proportionality factor approaches a constant value at high Re. The relation is given by

$$\alpha_{mt} = 2\pi/3.3757575\ b = 1.8612668/b \qquad (4.39)$$

where the subscripts mt stand for maximum temporal amplification. Thus, the largest amplification rate at high Reynolds numbers occurs when the wavelength is

$$\lambda_{mt} = 3.3757575\ b$$

for all values of x1, i.e. increases linearly with the width of the wake. Comparing the above result with (4.34), we see that the temporal most amplified wavelength is shorter than the critical wavelength in the temporal case.

TABLE 4.6

The temporal maximum amplification of the wake

x1	Re	α_{mt}	c_{rmt}	ω_{imt}	$\partial\omega_{mt}/\partial\alpha_{mt}$	α_{mt}(4.39)
1	1000	3.24675	0.414609	0.578065		
	10000	3.28244	0.422485	0.607437	0.66015	3.28324
5	1000	1.46252	0.419764	0.265586		
	10000	1.46841	0.423286	0.271114	0.66031	1.46824
10	1000	1.03578	0.420964	0.189018		
	10000	1.03836	0.423378	0.191853	0.66023	1.03826
50	1000	0.46406	0.422508	0.085284		
	10000	0.46433	0.423464	0.085892	0.66005	0.46433
100	1000	0.32824	0.422853	0.060437		
	10000	0.32830	0.423465	0.060751	0.65999	0.32833
150	1000	0.26805	0.423001	0.049395		
	10000	0.26804	0.423466	0.049609	0.65997	0.28806

Table 4.6 lists the temporal maximum amplification wavenumbers α_{mt}, the phase and group velocities c_{rmt} and $\partial\omega_{mt}/\partial\alpha_{mt}$ and the amplification rate ω_{imt}. In the last column, the wavenumbers calculated from (4.39) for Re=10000 are given.

It can be noticed that

a) The amplification rate remains almost constant above Re=1000 at large values of x1.

b) The group velocity $\partial\omega_{mt}/\partial\alpha_{mt}$, which is purely real (since ω_{imt}=maximum), is constant for all values of x1 and for all values of Re and equal to 2/3 of the maximum velocity.

c) The phase velocity c_{rmt} of the frequency with the maximum amplification rate has a constant value for all values of x1.

This implies the total dependence of the frequencies with the maximum amplification rates on the wavenumbers α_{mt} and in turn from (4.39) on the half width of the flow b. The frequency with the maximum amplification rate is given by

$$f_{mt}=\alpha_{mt}c_{rmt}U_o/2\pi \qquad (4.40),$$

where U_o is the normalisation velocity at the centre line y=0. The temporal Strouhal number with the maximum amplification rate is then

$$S_t=f_{mt}d/Uo=c_{rmt}d/\pi b \qquad (4.41a)$$

Taking $c_{rmt}=0.423319$ and the theoretical width of the cylinder d=2, we have

$$S_t= 0.2508/b \qquad (4.41b)$$

The spatial amplification is more appropriate for the flows whose velocity distribution depends on the distance x downstream as with the case in hand. The critical quantities given in table 4.4 and table 4.5 are the same for both the temporal and the spatial cases, since the amplification rate is zero. The maximum spatial amplification rates at Re=10000 for several values of x1 are given in table 4.7. The fifth column of table 4.7 gives the values calculated from

$$\alpha_{rms}= 2\pi/3.917177\ b \qquad (4.42)$$

The relation (4.42) like (4.39) is accurate.

TABLE 4.7

The spatial maximum amplification of the wake

x1	ω_{ms}	α_{rms}	α_{ims}	α_{rms} (4.42)	c_{rms} (4.43)
1	1.36186	2.83860	-1.07013	2.82944	0.350456
5	0.50785	1.26767	-0.48052	1.26530	0.350288
10	0.35898	0.89589	-0.34014	0.89476	0.350211
50	0.16039	0.40015	-0.15236	0.40015	0.350070
100	0.11337	0.28280	-0.10777	0.28294	0.350050
150	0.09255	0.23083	-0.08801	0.23103	0.350054
200	0.08014	0.19985	-0.07623	0.20007	0.350067

Following Gaster (1962), the phase velocity in the spatial case is given by

$$c_r = \omega_r \alpha_r / (\alpha_r^2 + \alpha_i^2) \qquad (4.43)$$

The values calculated from (4.43) and given in table 4.7, show that in this case as in the temporal case the phase velocity is close to a constant for all values of x1. The Strouhal number in the maximum amplified spatial case is

$$S_s = \omega_{ms} d / 2\pi \qquad (4.44)$$

Let $P = \omega_{ms} / c_{rms}$, then it is easy to verify that

$$P = \alpha_{mt}$$

The Strouhal number is then

$$S_s=(P\ c_{rms}\ d)/2\pi=0.20743644/b \qquad (4.45)$$

where $c_{rms}=0.3501276$, the average value from table 4.7. The ratio between the Strouhal number with the maximum spatial amplification rate and the Strouhal number with the maximum temporal amplification rate is

$$S_s/S_t=0.8273=\text{ constant} \qquad (4.46)$$

The Strouhal number at the critical Reynolds number is

$$S_c=0.1171/b$$

and the ratio between S_s and S_c is equal to 1.772.

4.6: Experimental Evidence Supporting the Existence of the Resonance Mechanism of Instability for Profiles with Inflexion Points

In this section we will seek the evidence, where possible, in the form

$$\lambda = K\ L \qquad (4.47)$$

where λ is the disturbance wavelength, K is a proportionality constant and L is a characteristic length usually equal to the distance between the points where $U'=0$.

In the last section, it was shown that in the case of the critical Reynolds number, K_c is constant for a group of profiles which have certain similarities. It is also constant for the self similar profile of the wake. It was also shown for the wake that K has a constant value for the most amplified disturbance at all distances downstream, although its value is different from the critical K_c. Since in the critical case as in the most amplified case, λ is the most amplified wavelength, the term resonance is appropriate in describing (4.47) as a resonance equation and the resonance can only occur through the correct value of K, in the two cases K_c and K_m.

In the case of time-dependent flow, comparison is made in chapter 6 between the observed wavenumber and frequency for $\beta=7$ and the corresponding calculated values. Good agreement is found between the two, thus giving support to (4.47).

Large scale structures are the predominant feature of jets, wakes and mixing layers. Despite the fact that such structures are the manifestation of (4.47), real flows are so complex that to make such a direct connection is difficult. It was proved previously that some guidance from outside is useful. Thus, Widnall and Sullivan(1973) found numerically that the instability of a vortex ring occurs when the circumferential wavelength of the unstable disturbance is about 1.5 times the ratio of the ring

radius to the vortex radius. In other words,

λ = 4 core radius

which is exactly in the form of (4.47). This result led Chandrsuda et al (1978) to revise the data of Bradshaw et al (1964) for the circular jet and showed that the wavelengths observed there are in good agreement with Widnall and Sullivan calculations.

Direct evidence is now available from the experimental results in the case of the mixing layer. The layer is defined as the mixing region between two streams of velocities U1 and U2, where U1>U2. The thickness of the layer is very small in the initial stages and it grows as the down stream distance x increases. There is a good agreement between the passage frequency of the initial disturbance and the inviscid calculations of Michalke (1965). (The spatial inviscid linear stability calculations of Michalke show that the most amplified frequency and the amplification rate scale with the momentum thickness).

At relatively large values of the distance downstream x, the least square fit of the wavelengths of large scale structure gives

$$\lambda = 0.561\, q\, x \qquad (4.48)$$

where q =(U1-U2)/(U1+U2) is the velocity ratio [Jimenez (1983)].

The transverse dimension of the structure b is given by

$$b = k\, q\, x$$

where the constant k has been given different values by different authors, ranging between 0.3 and 0.39 (see Herman and Jimenez (1982)). Taking the average value, we have the transverse dimension

$$b = 0.345\, q\, x \qquad (4.49)$$

From (4.48) and (4.49), the wavelength

$$\lambda = 1.653\, b \qquad (4.50)$$

which is exactly (4.47).

Another direct experimental support can be found in the case of the wake. Roshko (1954,1955) formulated a universal Strouhal number for the near wake of a circular cylinder, a 90° wedge and a flat plate. He considered two shear layers of distance s apart, and defined a universal Strouhal number

$$S^* = f\, s/U_b = S\, U\, s/U_b\, d \qquad (4.51)$$

where U_b is the mean velocity at separation (just outside the layers), d is the cylinder diameter, f is the shedding frequency and S is the Strouhal number (4.44). The velocity U_b is related to the free stream velocity by $U_b = kU$, where $k = (1-C_{pb})^{1/2}$ and C_{pb} is the base pressure

coefficient. C_{pb} is obtained by applying the Bernoulli's equation to the flow just outside the boundary layer at separation.

Bearman (1967) showed that if the distance s between the two shear layers is replaced by the lateral spacing between the two individual vortices of opposite signs, the same Strouhal number is universal for various types of bodies and different values of k. He found a constant value of $S^*=0.181$.

Calvert (1967), Simmons (1977) and Griffin (1978) formulated similar Strouhal numbers, but with the distance s being replaced by the width of the wake, i.e. s=2b in our notation. Calvert (1967) found, for various conical shapes with separation angles between zero and 90°, a constant $S^*=0.19$. Simmons (1977) found $S^*=0.163$ for a variety of stationary cylinders with fixed separation points at Re=15000. Griffin (1978) found, for vibrating cylinders with $1.3<k<1.6$ and $700<Re<50000$, a constant value of $S^*=0.178$. The reasons for the variations in the value S^* obtained by different authors were discussed by Griffin (1978).

The spatial Strouhal number was given in subsection 4.5.3 by

$$S^*=0.20743644/b \qquad (4.52)$$

from which the universal Strouhal number is $S^*=0.20743644$. This value is close to the above mentioned experimental

values, remembering that S^* here is for the instability frequencies and not for the shedding frequency. The experiments of Nishioka and Sato (1978) show that both are close and the stability calculations of Nakaya (1976) were used by them for predicting the shedding frequency. It should also be noticed that the Gaussian profile (4.36) is representative of self similar profiles only. There is a shift in the frequency due to the nonlinearity which was shown by Nishioka and Sato to occur at Re>70. It is clear that the difference between the Strouhal number calculated from (4.52) and the experimentally observed Strouhal numbers is small whether it is due to one or all the above mentioned reasons.

4.7: The Phase Velocities at the Critical Reynolds Numbers

We first notice that the phase velocity at any critical Reynolds number does not coincide with the velocity at the inflexion point Ui, although it can be close. In section 4.2, it was mentioned that for the neutrally stable eigensolution α_s, the phase velocity c_{rs}=Ui for monotone and some of the nonmonotone profiles. In addition, at the critical Reynolds number Ui-c_r is different for different profiles. From the fact that, φ''=0 at the critical point, the Rayleigh equation at the apex of the neutral curve (critical Re), can be written as

$$\alpha^2(Ui-c_r)=-m\ U_c'' \qquad (4.53)$$

where m is a constant which is determined from some available calculations of the Orr-Sommerfeld equation at the critical Reynolds numbers. Substituting $\alpha_c=2\pi/K_cL$, (see 4.18), into (4.53) and using the values of the critical c_r calculated from the Orr-Sommerfeld equation for some time-dependent flow profiles it is easy to find that $-mK_c^2=2.6666$, in which case (4.53) is

$$(Ui-c_r)=U_c'' L^2/1.5\pi^2 \qquad (4.54)$$

If the phase velocity c_r is different from the velocity at the inflexion point Ui, equation (4.54) is satisfied only at one point on any time-dependent flow profile.

In the last two columns of table 4.8, the critical phase velocities calculated from both the Orr-Sommerfeld equation and (4.54) are given. The accuracy of (4.54) is very good especially for the wall inflexion points ($\beta=6$, $\omega_0 t=110°, 120°$ and $145°$) where the difference $Ui-c_r$ is very large. Ui and yi, the inflexion point velocity and position in addition to the critical point position y_c are given in table 4.9. In table 4.8, the phase velocities and the derivatives of the velocity at the critical point U_c' and U_c'' are given, in addition to the length L used in (4.54). Except for the the wall inflexion points, as before, L is equal to the distance between the points where U'=0. For the wall inflexion points L now is the distance between the inflexion point and the maximum velocity point U'=0, i.e. in this case L does not include

the vorticity width of the second (core) inflexion point of these profiles.

TABLE 4.8

The phase velocity calculated from the (OSE). and estimated from (4.54)

β	ωσt	U_c'	U_c''	L	c_r(O S E)	c_r(4.48)
6	30	-1.3281	2.94773	0.36140	0.559153	0.558133
6	60	-0.8206	0.96145	0.30030	0.980154	0.972661
6	110	-0.2945	-.19456	0.19765	1.140473	1.140180
4	60	-0.2867	-.33350	0.20055	1.028224	1.029130
10	30	-1.9515	8.94670	0.22190	0.580050	0.577200
14	92	-0.8899	5.44550	0.15868	1.089533	1.088281
18	90	-1.1511	9.77546	0.12341	1.076829	1.075971
2	0	-0.6786	-0.89135	0.38833	0.015177	0.010130
3	0	-1.3298	-1.28194	0.39222	0.030928	0.023904
4	0	-1.7903	-0.31371	0.40065	0.048030	0.046777
6	340	-3.1868	3.69366	0.39406	-0.169443	-0.180608
8	0	-3.3133	13.90344	0.27657	0.107392	0.102160
10	0	-2.7706	8.24440	0.22765	0.118107	0.112940
6	110	7.3616	-22.74073	0.35540	0.387137	0.387169
6	120	6.3026	-14.70227	0.35000	0.397305	0.400120
6	145	4.1379	-5.22920	0.34050	0.307850	0.309632

Equation (4.54)

$$U_c''/(Ui-c_r) = -4\pi^2/mK_c^2L^2$$

turns out to be a special case of Mises and Friedriches (1942) general condition of instability

$$[U''/(Ui-U)] > \pi^2/(y1-y2)^2 \qquad (4.15)$$

where y1 and y2 are the boundaries of the flow.

For the profiles of the wake, there is no need for a relation like (4.54) since the velocity is constant, due to self similarity of the profiles. For U(y)=sin(y), since the left hand of (4.15) is equal to 1 and U_i=0, then c_r=U''(y), i.e. undetermined, and a relation analogous to (4.54) is of no use.

TABLE 4.9

The critical Reynolds numbers of some time-dependent flow profiles

β	ωot	Re_c	U_i	y_i	y_c
6	30	882.1600	0.584133	0.23344	0.251
6	60	1316.3000	0.980154	0.29417	0.303
6	110	5720.2000	1.139966	0.38090	0.378
4	60	5361.5057	1.028224	0.38313	0.378
10	30	2526.8600	0.607000	0.14273	0.156
14	92	10034.6300	1.097817	0.15775	0.167
18	90	13304.0000	1.085971	0.12181	0.130
2	0	602.9400	0.001050	0.27396	0.253
3	0	325.7570	0.010583	0.26396	0.249
4	0	291.3050	0.043376	0.23832	0.236
6	340	856.6000	-0.141865	0.12885	0.137
8	0	860.2000	0.144660	0.13028	0.144
10	0	1119.0000	0.159240	0.10570	0.118
6	110	8742.1400	0.192168	0.02547	0.051
6	120	4752.0000	0.278420	0.04602	0.065
6	145	1399.6000	0.268630	0.09743	0.107

4.8: The amplification (growth) rates in inflexion instability

The wavenumbers with maximum temporal amplification rates $\omega_{imt}=\alpha_{mt}c_{imt}$ for the wake profiles at different values of x1 were given in table 4.6 for Re=10000. In table 4.10, the maximum possible temporal amplification rate ω_{imt} for a selected number of time-dependent flow profiles are given. The inviscid solution (Re->∞) was used for some of those profiles, while for the rest the calculations were carried out at Re=60000. This is a very high Re in comparison to the critical Re, and was considered sufficient to make the error in the values of ω_{mt} very small.

TABLE 4.10:

Time-dependent flow profiles maximum amplification rates

β	ωot	α_{mt}	c_{rmt}	ω_{imt}	$\partial\omega_{mt}/\partial\alpha_{mt}$	A	Re
6	30	4.1140	0.58543	0.12821	0.52155	5.29	∞
	60	4.9723	0.98231	0.08723	0.94396	4.75	60000
	90	6.5003	1.17040	0.05591	1.15119	4.28	60000
	110	7.7456	1.14174	0.03768	1.13120	3.91	∞
	120	9.4665	1.07802	0.02395	1.07877	4.47	60000
6	110	2.4937	0.25864	0.06044	0.37656	63.5	60000
	120	2.4639	0.24363	0.08749	0.38431	36.8	60000
	145	3.3596	0.21210	0.24024	0.36721	8.66	60000
8	30	4.7502	0.59634	0.12981	0.54983	6.45	60000
	95.538	5.1873	1.13904	0.04856	1.10930	5.50	∞
10	30	5.6580	0.60217	0.14910	0.56335	6.75	∞
	60	5.7020	0.96794	0.09046	0.94350	6.60	∞
	90	5.7619	0.11892	0.05507	0.05507	6.40	∞
4	60	8.0202	1.02987	0.03548	1.02010	4.05	60000

The upper limit to the temporal amplification was obtained analytically by **Hoiland (1953)** as

$$\omega_i < 0.5|U'max| \qquad (4.17)$$

For profiles with inflexion points, $|U'|max=|Ui'|$ at the inflexion point. Let

$$A=0.5|Ui'|/\omega_{imt}$$

According to (4.17), A is the minimum value possible. The values of ω_{imt} are given in the fifth column of table 4.10, while A is given in the seventh column. It is clear that A is far higher for a lower bound. In other words, ω_{imt} computed from (4.17) is far higher than the actual value. The smallest value of A in table 4.10 is 3.9, while for the equality in (4.17), A=1. The same is true with the wake profiles. Table 4.11 shows that A is about constant for all values of x1, and the average is

$$A=4.758$$

A constant value for A leads to a useful relation for the determination of the maximum temporal amplification rates. We write

$$\omega_{imt} = |Ui'|/2A = |Ui'|/B\ K_{mt}$$

where K_{mt} is the proportionality factor for the temporal maximum amplified wavelength λ_{mt}. Thus

$$B = 2A/K_{mt} = 1.40777 = \text{constant} \qquad (4.55)$$

and

$$\omega_{imt} = |Ui'|/(1.40777\ K_{mt}) \qquad (4.56)$$

As expected, (4.56) has a good accuracy for the wake. However, upon testing its validity to ω_{im} for time-dependent flow profiles, it soon becomes clear that ω_{imt} from (4.56) has twice the values listed in table 4.10. Therefore, in order to bring the two results in line, the characteristic length L=b, the half width of the wake, is changed to L=2b, the width of the wake. This change, halves the value of K_{mt} and doubles the value of B in (4.55). Then (4.56) becomes

$$\omega_{imt}=|Ui'|/(2.816\ K_{mt}) \qquad (4.57)$$

TABLE 4.11

The maximum temporal amplification rates of the wake profiles

x1	b	yi	Ui'	ω_{imt}	A
1	0.56689	0.2107	2.87840	0.60436	4.763
5	1.26761	0.4712	1.28725	0.27111	4.748
10	1.79267	0.6663	0.91023	0.19185	4.744
50	4.00850	1.4900	0.40707	0.08590	4.740
100	5.66893	2.1072	0.28784	0.06043	4.763
150	6.94300	2.5807	0.23502	0.04939	4.758

yi=The inflexion point position= b/2.69033

The values of ω_{imt} computed using (4.57) for selected time-dependent flow profiles are listed in the sixth column of table 4.12. It is noticeable that (4.57) under estimates the values of ω_{imt} for the profiles with one core inflexion point (-Ui'>0). These are the same profiles which had smaller values of A in table 4.10. However,

(4.57) gives closer estimates for the profiles at high β and generally for those with more than one inflexion point. The error, as can be seen from the seventh column of table 4.12, is closely connected with the ratio (|Ui'|/L), where it is large for small values of this ratio and vice versa. Comparing the critical frequencies ω_c (tables 4.1 and 4.8) and the most amplified frequencies (table 4.10), we notice that generally the error is also large when $\omega_c > \omega_{mt}$ and $\omega_c - \omega_{mt}$ is large. These conditions are characteristic of dissipative systems (systems with damping) as is well known in resonance theory [French (1971)].

In table 4.10, the values of A for the wall inflexion points (-Ui'<0) are very large (These are the profiles at β=6 and $\omega_o t$=110,120° and 145°). The reason again seems to be connected with the fact that the mean flow vorticity -U' has no nodes at the wall for the first two inflexion points. In section 4.5.1, we noticed that for these profiles L does not include that part between the inflexion point and the wall. The value of ω_c is about twice that of ω_{mt} for each of these profiles. Relation (4.57), in its present form, is not applicable to those profiles, and therefore, they were not included in table 4.12.

Adopting the full width of the wake as the characteristic length L is supported by the outcome of (4.57) for the mixing layer whose profile is given by tanh(y). Here we will consider the profile given by

U(y)=0.5(1+tanh(y)). However, it will be called hereafter tanh(y) for simplicity. In section 4.6 the value of K for the most amplified disturbance was estimated as 1.653. This value is supposed to be the value of K_{ms}, the proportionality factor of the maximum possible spatial amplification α_{im}.

TABLE 4.12

Comparison between ω_{imt} from OSE and (4.57)

β	ωot	|Ui'|	K_{mt}	ω_{imt}(OSE)	ω_{imt}(4.57)	|Ui'|/L	Core I.P.
4	60	0.2878	4.1	0.035474	0.02500	1.435	1
6	30	0.1357	4.1	0.128204	0.11756	3.755	1
	60	0.8250	4.1	0.087230	0.07150	2.750	1
	90	0.4780	4.1	0.055909	0.04140	2.000	1
	110	0.2948	4.1	0.037683	0.02550	1.500	1
	120	0.2140	4.1	0.023945	0.01854	1.250	1
8	30	1.6740	4.9	0.129808	0.12134	6.200	2
	95.538	0.5360	4.1	0.048560	0.04640	1.830	1
10	30	2.0162	4.9	0.144687	0.14620	8.800	2
	60	1.2949	4.9	0.090458	0.08660	5.380	2
	90	0.7073	4.9	0.055070	0.05130	3.280	2

However, using the transformation from the temporal to the spatial amplification given by Nayfeh and Padhye (1979), it is easily found that the spatial maximum amplified wavenumber is the same as the temporal one (see the spatial amplification section after (4.59) below). Thus K_{mt}=1.653. Substituting this value in (4.57), we have

$$\omega_{imt}=0.5/(2.816 \times 1.653)=0.1075$$

This value is close to the maximum inviscid amplification

rate calculated by Michalke (1964) of 0.09485. Assuming that (4.57) is accurate, then substituting the value of ω_{imt}=0.09485 into it, we have K_{mt}=1.8723 which is about 12% higher than 1.653 estimated from the experimental data. The characteristic length L is then equal to 7.55.

In conclusion, (4.57) is not only valid for the wake and time-dependent flow profiles, but also for the mixing layer tanh(y) profile. The time-dependent flow profiles concerned are those in the core of the flow. We notice that (4.57) accommodated the tanh(y) profile which is unstable to coupled symmetric and antisymmetric disturbances, despite the fact that it was originally obtained for profiles unstable to antisymmetric disturbances. However, this is not strange since for tanh(y) the values of the frequencies at the critical Re and of the frequencies with the maximum amplification rates are close to the corresponding values in the case of the coupled disturbances. Using (4.56), the temporal amplification rate can now be written as

$$\omega_i \leqslant |U_i'|/(2.816\ K_{mt}) = |U_i'|L/(2.816\ \lambda_{mt}) \qquad (4.58)$$

where $\lambda_{mt}=K_{mt}L$, is the wavelength with the maximum possible temporal amplification. The upper bound in (4.58) is now far more accurate than that given by (4.17). It is interesting to test (4.58) with profiles other than those investigated in this study.

When the subharmonic evolution takes place, the mixing layer doubles its width (Ho and Huang 1982). The subharmonic starts its growth when its phase velocity equals that of the fundamental, i.e it becomes nondispersive. For the first subharmonic with half the frequency of the fundamental, the wavenumber is half of the fundamental wavenumber. The value of K_{mt} in (4.58) is then twice that of the fundamental in order that the subharmonic keeps its linear growth ($0.5\omega_i$). From this it follows that the value of L for all the subsequent subharmonics in (4.58) is the original fundamental L, whatever the number of the mixing layer doubling due subharmonic evolution. The doubling of the width of the layer and consequently merging of vortices increase the entrainment of the fluid, the phenomenon observed first by Brown and Roshko (1974). (For further discussions see section 4.11)

Table 4.10 shows that the phase velocities of the core inflexion points of the time-dependent flow are almost equal to the velocity at the inflexion point of these profiles (table 4.8). In this case, the proof of Tollmein (1935) and Mises and Friedriches (1942) that for the neutral solutions (i.e at the upper branch of the neutral stability curves), $c_s=Ui$ is not valid. The difference is not large but the equality does not exist. For the wake profiles however, $c_s=Ui$ on the upper branch. In the case of the wall inflexion points $c_s \neq Ui$. In this case, the critical group velocities are about twice the most amplified group velocities. At the same time, the critical

group velocities are about 1.5 times the critical phase velocities. This is similar to the situation in the plane Poiseuille flow where at the critical Re c_{rc}=0.264 while $\partial\omega_c/\partial\alpha_c$=0.374. It appears that all wall profiles have such a characteristic. For the core inflexion points, the group velocity is about the mean velocity of the profile. In case of profiles with small |Ui'|, the mean velocity is close to the velocity at the inflexion point.

The spatial amplification has not been investigated in detail as the case of the temporal amplification. However, a relation similar to (4.58) holds for the wake maximum possible spatial amplification and is given by

$$\alpha_{im} > -|Ui'|/(1.366188\ K_{ms}) = |Ui'|L/(1.36618\ \lambda_{ms}) \quad (4.59)$$

where K_{ms} is the maximum spatial amplification proportionality factor. The constant is half that given by (4.42) since now L=2b.

The time-dependent flow profile at $\omega_0 t$=30 and β=6 has α_{im}=-0.2400 from (4.59) which is in a good agreement with the Orr-Sommerfeld solution of -0.2438. However, (4.59) like (4.57) underestimated the value of α_{im} for $\omega_0 t$=110°. Thus, the Orr-Sommerfeld solution gives α_{im}=-0.02857, while (4.59) gives α_{im}=-0.0526. The value of -0.02857 was obtained at Re=35000, and a convergent solution above this value was impossible to obtain. Despite any improvement, the ratio between the Orr-Sommerfeld solution and (4.59) in the spatial case may not be better than the same ratio

for the temporal case of 1.48 (table 4.12). It appears that (4.59) in the case of time-dependent flow profiles gives the same error as (4.57) when |Ui'|/L is small.

There is a parameter which plays an important role in determining the mixing layer stability characteristics, namely the velocity ratio

q=(U1-U2)/(U1+U2)

where U1 and U2 are the velocities of the two streams with U1>U2. The parameter q has not been considered in the above discussions of the temporal stability (equation 4.57) since the only known available calculations are those of Michalke (1964) for q=1. However, in the spatial case Monkewitz and Huerre (1982) made calculations for both tanh and Blasius mixing layers for $0 \leq q \leq 1$. They found that α_{im} is approximately proportional to q. The most amplified frequency was found to decrease as q increases, although not by a great amount. Equation (4.59) when α_{im} is replaced by α_{im}/q gives good estimates for both mixing layers when q=0. Thus for the tanh(y) profile, (4.59) gives $\alpha_{im}/q=-0.1897$ while the inviscid value is -0.19616. The Nayfeh and Padhye (1979) transformation gives -0.1864. In the above calculations, the length L was taken to be that of the temporal case i.e. L=7.55. The maximum amplified wavenumber is 0.4446, giving $K_{ms}=1.866$ which is very close to $K_{mt}=1.8723$. Upon using the value of $\alpha_{ms}=0.42$ given by Monkewitz and Huerre for q=1 and assuming that the value of L remains the same, we have $K_{ms}=1.9814$ which is very close to that of the wake i.e. 1.9586 [incidently Michalke (1965) gives $\alpha_{ms}=0.40313$ for q=1]. Using the above

value of K_{ms} in (4.57), we have $\alpha_{im}/q=-0.18471$ in comparison to the inviscid value 0.2284. In other words, (4.59) underestimates the true value by 19%. For q=0, (4.59) gives for the Blasius mixing layer $\alpha_{im}/q=-0.1891$ for L=7.55. This is in good agreement with $\alpha_{im}=-0.19$ deduced from figure 7 of Monkewitz and Huerre's paper.

4.9: The dependence of the factor K on Re

The importance of the factor K is that it relates the critical and the most amplified wavenumbers to the characteristic length of the flow L for each particular class of profiles. In this respect, it is a unifying or scaling factor for each class. The growth rates of the most amplified disturbances for different flows were found to be unified in a single relation with the help of K as was shown in the last section. Equation (4.47) relating λ to L through K was discovered in the linear stability case. Its validity in real flows was demonstrated by examples from several flows in section 4.6. The validity indicates that the nonlinearity does not alter the form of (4.47), but only changes the value of K_{ms} as seen from the example of the mixing layer in the last section. Consequently, a knowledge of K will be useful in practical situations. For example, from $\lambda_{ms}=K_{ms}L$, if λ_{ms} is known, the thickness of the flow will be determined. Moreover, quantities like spreading rates, mixing, the frequencies and the intermittancy factor are determinable. K will prove to be a very useful tool in the stability theory, even more than that already mentioned. This will be

demonstrated further by more useful relations in this and the next two sections.

Since K so far was found to have two important values, one at the critical Re and the the other for Re->∞, its dependence on Re will be studied in this section. For this purpose, three wake profiles at different values of x1, and two time-dependent flow profiles were considered. The calculations were made in the temporal case. The maximum amplified wavenumbers for selected values Re were found, then from $\lambda=KL$, K was found. For the wake, the minimum Re used was 0.1. In figure 4.4, K vs Re are plotted for the three profiles. Since λ is proportional to K, they behave similarly. K and thus λ have their maximum value at Re=0. For $Re<Re_c$, (Re_c is the critical Re), the disturbance has the maximum damping $[(\partial\omega_i/\partial\alpha)=0]$. Thus the damped disturbance is that whose wavelength is long. Above the Re_c, K changes very slowly to its final value given by (4.39).

It is easy to verify that the three curves in figure 4.4 are self similar. Therefore, they can be replaced by one curve. The curve chosen is that of the profile at x1=50. The values of α, c_r, c_i and K are given in table 4.13. For any other profile at another x1, the listed values of K are correct for the new

$$Re=(Re(x1=50))(4.01094/b) \qquad (4.60)$$

For example, at x1=50, Re=4, K=2.48126. Then at x1=10

(b=1.79267), the same value of K is correct for Re=8.95 which is in a good agreement with the directly calculated value of 2.48028. Relation (4.60) was obtained by using (4.36) in

$$Re=(Re(x1=50))[Re_c(x1)/Re_c(x1=50)]$$

where $Re_c(x1=50)=5.559$ (table 4.6) Thus, using (4.60) the wavelength at any distance upstream or downstream can be found to a good accuracy for the listed values of Re at x1=50. In the table, the changes in α, c_r and c_i with Re above Re=30 are very small.

TABLE 4.13

K vs Re for the wake at x1=50

Re	α	c_r	c_i	K
0.1	.18777	-0.12323	-12.06841	4.1744
0.5	.19255	-0.10995	- 2.33430	4.0708
1.0	.20528	-0.07448	- 1.06580	3.8183
2.0	.24022	-0.02061	- 0.40496	3.2630
3.0	.27903	0.11479	- 0.18531	2.8091
4.0	.31590	0.18973	- 0.08098	2.4813
5.56	.35600	0.35600	0.25773	2.018
10.0	.39942	0.32317	0.08684	1.9624
15.0	.41618	0.34940	0.12205	1.8834
20.0	.42557	0.36433	0.13893	1.8419
25.0	.43207	0.37445	0.14861	1.8141
30.0	.43692	0.38178	0.15483	1.7940
40.0	.44355	0.39164	0.16234	1.7672
50.0	.44780	0.39785	0.16674	1.7504
60.0	.45069	0.40209	0.17330	1.7392
80.0	.45434	0.40747	0.17329	1.7252
100.0	.45657	0.41074	0.17547	1.7168
120.0	.45805	0.41294	0.17693	1.7112
140.0	.45910	0.41457	0.17800	1.7073
160.0	.45988	0.41570	0.17877	1.7044
180.0	.46048	0.41661	0.17940	1.7022
200.0	.46095	0.41735	0.17990	1.7005

K vs Re for the three time-dependent flow profiles of $\beta=6$, and $\omega_0 t=30^\circ, 60^\circ$ and 110° are shown in figure 4.5. The general behaviour is similar to that of the wake profiles. The three profiles have the same value of the critical $K_c=4$ and the maximum possible temporal amplification $K_{mt}=4.1$. They share these values with all other profiles with one core inflexion point (i.e.-Ui'>0) at all values of β. Although these profiles are not similar, the relation already derived for the wake profiles is applicable. The profile at $\omega_0 t=30^\circ$ is chosen as a **reference profile**. For each value of K for $\omega_0 t=30^\circ$, the corresponding Reynolds number for any other profile sharing with it $K_c=4$ and $K_{mt}=4.1$, is given by

$$Re = \{Re(\omega_0 t=30^\circ)/Re_c(\omega_0 t=30^\circ)\}(Re_c) \qquad (4.61)$$

However, unlike the wake profiles, there is a lower limit to the applicability of (4.61) when $Re_c >> Re_c(\omega_0 t=30^\circ)$. This lower Re is about 0.38 Re_c which is well inside the unimportant highly damped region. The reasons for the existence of such a limit are thought to be purely numerical:

a) For the profiles whose critical Re is high, it is difficult for the eigenvalue routine to converge to a point with $\partial\omega_i/\partial\alpha=0$ when $Re << Re_c$, because ω_i is almost constant across the the range of the wavenumbers involved.

b) At Re higher than 0.38 Re_c, the routine converges but to a value of K larger than the largest K for $\omega_0 t=30^\circ$. It is likely that these large values of K are

genuine for these profiles which are not self similar. However, there is a possibility that at least they are affected by some sort of numerical instability and thus they are inaccurate.

Thus, for self similar or nonself similar profiles sharing the same values of K_c and K_m **(i.e. belonging to the same group)**, documentation of the values of K at various Re for a reference profile in the group, will help in

1) finding the value of Re if K is known and vice versa for all other profiles of the group.

2) estimation of the critical Re of any profile, if the estimation is difficult for any reason. This is done by finding K at a suitable Re and then using (4.61) to find the critical Re.

To test the accuracy of (4.61) for the time-dependent flow profiles which are not self similar, two profiles other than that at $\omega_o t=30^\circ$ were considered. These will be compared with $\omega_o t=30^\circ$ at

Re=2000	K=3.8487	ω_i=0.06012
Re=6000	K=3.9790	ω_i=0.11254

The first profile is at $\beta=6$ and $\omega_o t=60^\circ$. From (4.61), the corresponding Reynolds numbers were found. Then, these were used for solving the Orr-Sommerfeld equation and the maximum amplified wavenumbers were found. For $\omega_o t=60^\circ$, the results are

Re=2984.26 K=3.8278 with a relative error of 0.5%

Re=8952.80 K=4.0090 with a relative error of 0.8%

For $\beta=6$, $\omega_o t=110^\circ$

Re=12968.6 K=3.6833 with a relative error of 4%

Re=38905.8 K=3.8300 with a relative error of 4%

While the relative errors for $\omega_o t=60^\circ$ are small, they increased considerably for $\omega_o t=110^\circ$. It is obvious that the error in (4.61) is related to that found in (4.57), i.e related to the value of $|U_i'|/L$. The ratio between the critical Reynolds numbers of $\omega_o t=110^\circ$ and $\omega_o t=30^\circ$ (table 4.9) equal to 6.4843 which is very large. Obviously, using a profile with closer critical Re to that of $\omega_o t=110^\circ$ as a reference will reduce the error considerably. It is expected that the error of the critical Re will be about the same as that of K. Despite the relatively large error,(4.61) is very reasonable for estimations, and is accurate for profiles with high $|U_i'|/L$ and all self similar profiles.

A relation similar to (4.61) was also found for the growth rates. As a reference, the growth rates of $\omega_o t=30^\circ$ will be used. The growth rate associated with any particular profile for which (4.61) is applicable, is given by

$$\omega_i = \omega_i(\omega_o t=30^\circ)\{|U_i'|/|U_i'|(\omega_o t=30^\circ)\} \qquad (4.62)$$

at Re given by (4.61). (These are the maximum growth rates for the particular Re considered). In other words, the ratio between the two growth rates is equal to the ratio of |Ui'| of the two profiles, but at the corresponding Reynolds numbers at the left and the right hand sides of (4.61). This relation is valid for all profiles which share a common K_c and K_m. It is accurate for wake profiles at different values of x1. To test its accuracy to time-dependent flow profiles with $K_c=4$, the values of ω_i for $\omega_o t=30^\circ$ given above for Re=2000 and Re=6000, will be used again for $\omega_o t=60^\circ$ and $\omega_o t=110^\circ$. The values of |Ui'| given in table 4.12 will be used. Thus for $\omega_o t=60^\circ$ and

Re=2984.26 ω_i(O.S.E.)=0.04745, ω_i(4.62)=0.03655

Re=8952.80 ω_i(O.S.E.)=0.07700, ω_i(4.62)=0.06841

The ratio between the two ω_i in the first case is 0.77 in comparison with the ratio between ω_{imt} given in table 4.12 of 0.82. In the second case the ratio is 0.89 which is better than that obtained from table 4.12. For $\omega_o t=110^\circ$

Re=12968.6 ω_i(O.S.E.)=0.02104, ω_i(4.62)=0.01306

Re=38905.8 ω_i(O.S.E.)=0.03293, ω_i(4.62)=0.02445

The ratio of ω_i in the first case is as low as 0.62 compared to that from table 4.12 of 0.676, while in the second case, it is better than (4.57), giving a ratio equal to 0.74.

It is evident that (4.62) suffers from the difficulties of (4.57), and any improvement to the last will improve the first and vice versa. The good accuracy of (4.61) to time-dependent flow profiles with high values of $|Ui'|/L$ is expected also in the case (4.62). Thus (4.62), can be used in place of (4.57) when $\omega_i < \omega_{imt}$ with the above reservations in mind.

The validity of (4.61) and (4.62) at the same time does not mean that the ratio of the critical Re of the two profiles is proportional to the ratio of their $|Ui'|$, except for self similar profiles (the wake). In the case of time-dependent flow profiles, such an assumption can produce a relative error in the determination of the critical Re as large as 40%. Although it was not done here similar relations in the spatial case for $\alpha_i \geq \alpha_{im}$ are evident.

4.10: The neutral stability curves

The neutral stability curve in the α-Re plane is the curve on which the amplification rate equals zero. The curve has two branches: the upper and the lower branches which meet at the critical Re. Inside the curve the disturbances amplify ($\omega_i > 0$), while outside the curve they are damped ($\omega_i < 0$) [figure 4.6]. The disturbance is considered linear if its amplitude is not more than about 2% of the mean velocity [Ross et al (1970)]. For such a range of amplitudes the amplification rate is predicted reasonably well by the linear stability theory as was

shown by Ross et al for the Blasius boundary layer. In reality, the disturbances are in the form of wave packets which have a narrower neutral curve (see section 6.7). Furthermore, the amplitude is larger, giving rise to the nonlinear growth.

Figure 4.6 shows for $\beta=6, \omega_0 t=30^\circ$, the neutral stability curve (the outer) and two constant amplification curves ($\omega_i=0.1$ and $\omega_i=0.2$). On the neutral curve, the spatial amplification $\alpha_i=0$. The constant amplification curves for α_i=constant differ from those for ω_i=constant. Both figure 4.6 and 4.7 show that the neutral curves of time-dependent flow profiles are very wide in terms of wavenumbers involved. This is in marked contrast to those of free shear layers. For example, the tanh(y) profile on the upper branch at infinite Re has $\alpha_s=1$. Again, in comparison with plane Poiseuille flow neutral curve, the time-dependent flow neutral curves are very wide. For $\beta=6$, $\omega_0 t=30^\circ$, the minimum α at infinite Re equal to 0.33, while the maximum (α_s) is 7.23. Another characteristic of the neutral curves of profiles with inflexion points is that the difference between the critical and the most amplified wavenumber at large Re is relatively small in comparison to the case of profiles without inflexion points. The neutral curve of the wall inflexion point of the profile at $\omega_0 t=110^\circ$, as well as lying in the lower range of α, it is several times narrower than the neutral curve of the core inflexion point of the same profile (figure 4.7).

It was easy to discover that the unifying characteristics of K between different profiles with the certain similarities discovered in section 4.5.1 also exists for the neutral curve. Table 4.14 lists the asymptotic values of α_s on the upper branch. The values of $K=2\pi/\alpha_s L$ for time-dependent flow profiles with both one or two inflexion points is about constant. This is in marked contrast to the critical K_c and the maximum amplified K_m, which differ for the two types of profiles. Again in contrast to K_c which was constant for the wall inflexion points, K_s is not which demonstrates that this type of profile is special for the reasons given in section 4.8. The value of K_s for $\beta=6$ and $\omega t=145^\circ$ is close to the range of K_s for the core inflexion points. For this profile, the point with $U'=0$ is very close to the wall.

TABLE 4.14

α_s and K for different time-dependent flow profiles

β	ωt	α_s	L	K_s	No of core I.P.
6	30	7.230	0.36140	2.405	1
6	110	13.956	0.19765	2.416	1
8	95.538	9.388	0.29170	2.300	1
8	30	9.172	0.27657	2.477	2
10	30	11.520	0.22765	2.396	2
12	94	13.183	0.18500	2.396	2
6	110	3.860	0.47460	3.430	wall
6	120	4.283	0.45400	3.230	inflexion
6	145	5.658	0.40260	2.750	points

In the case of the wake, calculations for different values of x1 revealed that α_s is given by simple relations

if the critical or the most amplified α_{mt} are known. Thus

$$\alpha_s = 2.55936\ \alpha_c \backsim \alpha_c/0.4$$

or

$$\alpha_s = 1.9615\ \alpha_{mt}$$

The value of K_s was found to be constant for different values of x1 and equal to 0.8606. Accordingly, α_s is directly related to the half width of the wake by

$$\alpha_s = 7.30094/b$$

It is interesting that for the tanh(y) profile for which α_s=1 (Michalke 1964), upon using L=7.55 (section 4.8), we have K_s=0.8322 which is close to the above given value of K_s for the wake.

The existence of such constants will have important consequences in the analytical work. The neutrally stable solution which is the basic solution in the inviscid stability theory will have to some extent a well defined α_s since it will be directly available for each distinct group of profiles. Having such solutions, further general analytical conclusions about the inflexion instability, at least for each profile group will be easier to obtain. This hopefully will advance at least the linear stability theory from its present qualitative state to a more quantitative one. The same can be said about the critical and the most amplified cases.

4.11: Comments on the subharmonics in the mixing layers

In section 4.8 some observations about the growth of the subharmonic in the mixing layers were made. When the subharmonic reaches its saturation, merging of vortices occurs. Dimotakis and Brown (1976) suggested that, in the mixing layer, the subharmonic evolves because the upstream flow is influenced by perturbations from downstream through a feedback mechanism. The feedback loop was found so far to exist in the free jet as well in in the impinging jet (see Ho and Huang 1982). The feedback loop equation is given by Ho and Nosseir (1981). For water channels it can be approximated by

$$X_m/\lambda_n = N \qquad (4.63)$$

(Ho and Huang 1982).

In (4.63), λ_n is the wavelength after the n th merging and X_m: the distance from the trailing edge to the n th merging is

$$X_m = X1 + X2 + X3 + \ldots$$

where X_n, (n=1,2,3,..), is the distance between the (n-1)th and the nth merging. In (4.63), N is an integer and a constant. Ho and Huang (1982) found that N=4 for the mixing layer, while Gutmark and Ho (1980) found N=2 for the free jet.

For the first merging equation (4.63) can be written as

$$X1/K_{ms}L = 4 \qquad (4.64)$$

where K_{ms} is the proportionality factor for the most amplified subharmonic wave and L is the width if the layer.

Based on averaged values, the width of the mixing layer was in section 4.6 given approximately by

$$L = 0.1553\ x$$

Substituting this value in (4.64), we have

$$K_{ms} = 1.61$$

which is very close to $K_{ms} = 1.653$ obtained in section 4.6. In other words, the wavelength at the position of the merging (i.e when the subharmonic reaches its saturation), is that of the fundamental at that position. The same wavelength would have occurred naturally without the subharmonic evolution. However, the difference the subharmonic makes is that it produces one strong vortex (at least for the first subharmonic) in place of the two counter-rotating vortices of the fundamental and it is this which makes the merging visible (section 7.8). Ho and Huang (1982) observed that the subharmonic growth starts when the fundamental reaches its peak. The growth continues for a distance sufficient for the natural doubling in the width of the layer. The fact that the subharmonic wavenumber at the position of the merging is the fundamental wavenumber was already noticed by Ho and Huang who found that the normalised frequency of the subharmonic is equal to the frequency of the fundamental. What was done here was to prove this using relation (4.47). Using (4.47) in (4.63), this last relation can be written in the form

$$Xn=(2)^2\ N\ K_{ms}\ Lo \qquad (4.65)$$

where Lo is the width of the layer where the fundamental reaches saturation. Herman and Jimenez (1982), following an earlier result by Dimotakis and Brown (1976), gave

$$Xn=(2)^2\ 100\ \theta/q \qquad (4.66)$$

where q is the velocity ratio, and

$$\theta=(1/Uo^2)\int_0^b U(y)[1-U(y)]dy \qquad (4.67)$$

is the momentum thickness of the layer.

Relations (4.65) and (4.66) are similar, although the first was derived from (4.47) and the feedback equation, while the second was derived from direct experimental observations (analysis of cine pictures). Combining (4.64) and (4.65) we have

$$K_{ms}=(100/Nq)(\theta/Lo)=M\ (\theta/Lo) \qquad (4.68)$$

Relation (4.68) gives for the first time an indication about the nature of the factor K_{ms}. For the tanh(y) profile using the values of N=4, q=1, Lo=7.55, and θ=0.5 in (4.68) we have

$$K_{ms}=1.65563$$

in comparison to $K_{ms}=1.653$ obtained previously in section 4.6. Since the tanh(y) profile has been used for calculating the value of $K_{ms}=1.86$ in the linear case, and

the same profile has been used for obtaining the value of θ in the nonlinear value of K_{ms} given by (4.68), it is clear that the value of M differs in the two cases. In practice, the nonlinear effects appear as a thickening of the profiles due to distortion and manifests itself as a shift in the value of the linear frequency. From (4.68), one would have thought that these effects should appear as a difference between the laminar and the turbulent momentum thicknesses of the two profiles, without introducing any change in the value of M, assuming that L_o is a constant in both cases.

Relation (4.68) illustrates the importance of the factor K_{ms} more than any other relation derived previously in this chapter. This is because through (4.68), K_{ms} enters directly into the momentum equation, with all the implications that this equation has in the field of fluid dynamics.

It is easy to verify that substitution of $U(\eta)/U(0)$ from (4.32) into (4.67) gives

$$\theta/b = 0.133167 = \text{constant} \qquad (4.69)$$

for all values of the half width of the wake b. The integral in (4.67) was taken over the half width of the wake b. From (4.47) and (4.69), we have

$$\lambda = 15.02\ \theta\ K_m \qquad (4.70)$$

Or, for the spatially most amplified wavelength ($K_{ms}=1.96$)

$$\lambda_{ms} = 29.43672\ \theta \tag{4.71}$$

Thus generally [(see (4.68)], we have

$$\lambda = \text{constant} \times \theta \tag{4.72}$$

for profiles of free shear layers. Relation (4.72) is valid at the critical Re as well as for both the temporal and the spatial maximum amplified wavelengths. For boundary layer flows, equation (4.72) is not valid in its present form. The calculations of the author for the Falkner-Skan velocity profiles have shown that

$$\lambda_c = \text{constant}/\theta \tag{4.73}$$

for all the profiles with negative pressure parameter b.

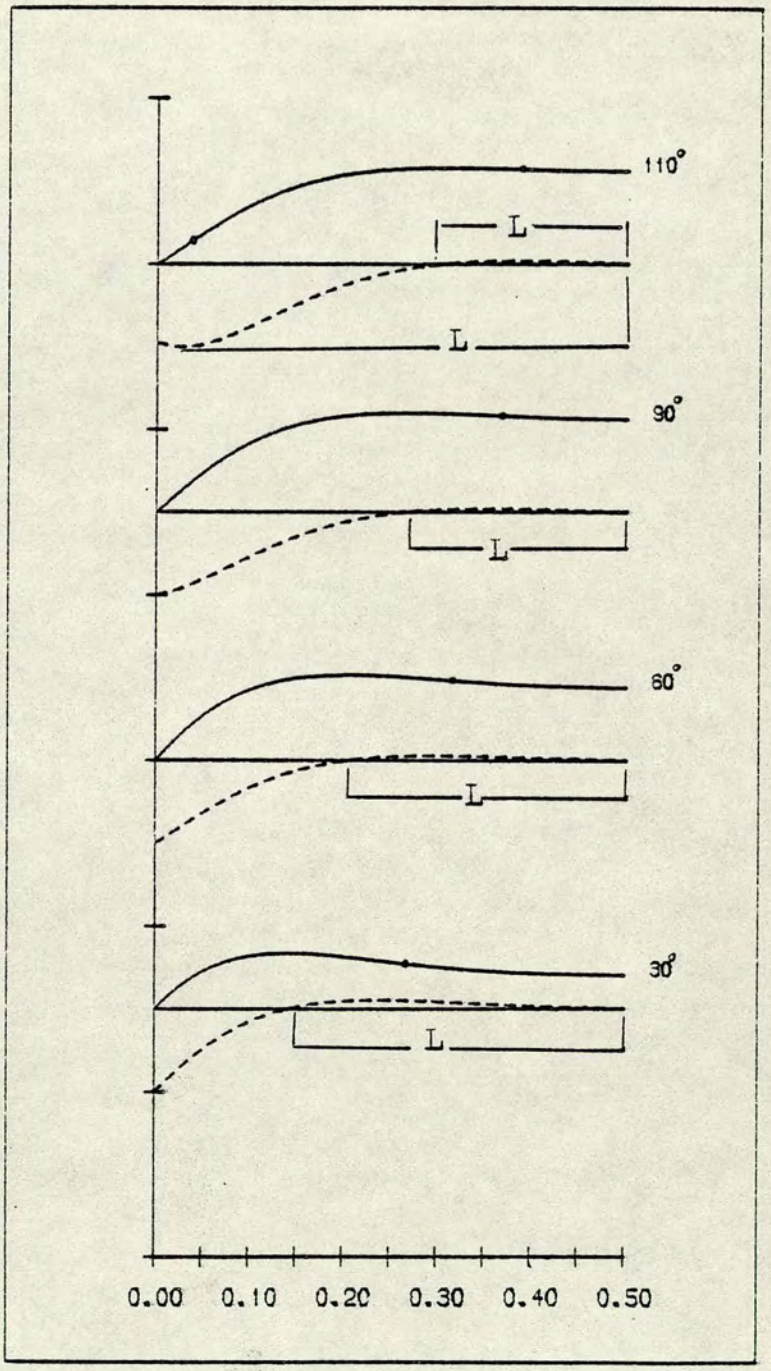

Figure 4.1: Time-dependent flow profiles (β=6)

The length L for different profiles.

•-Inflexion point.

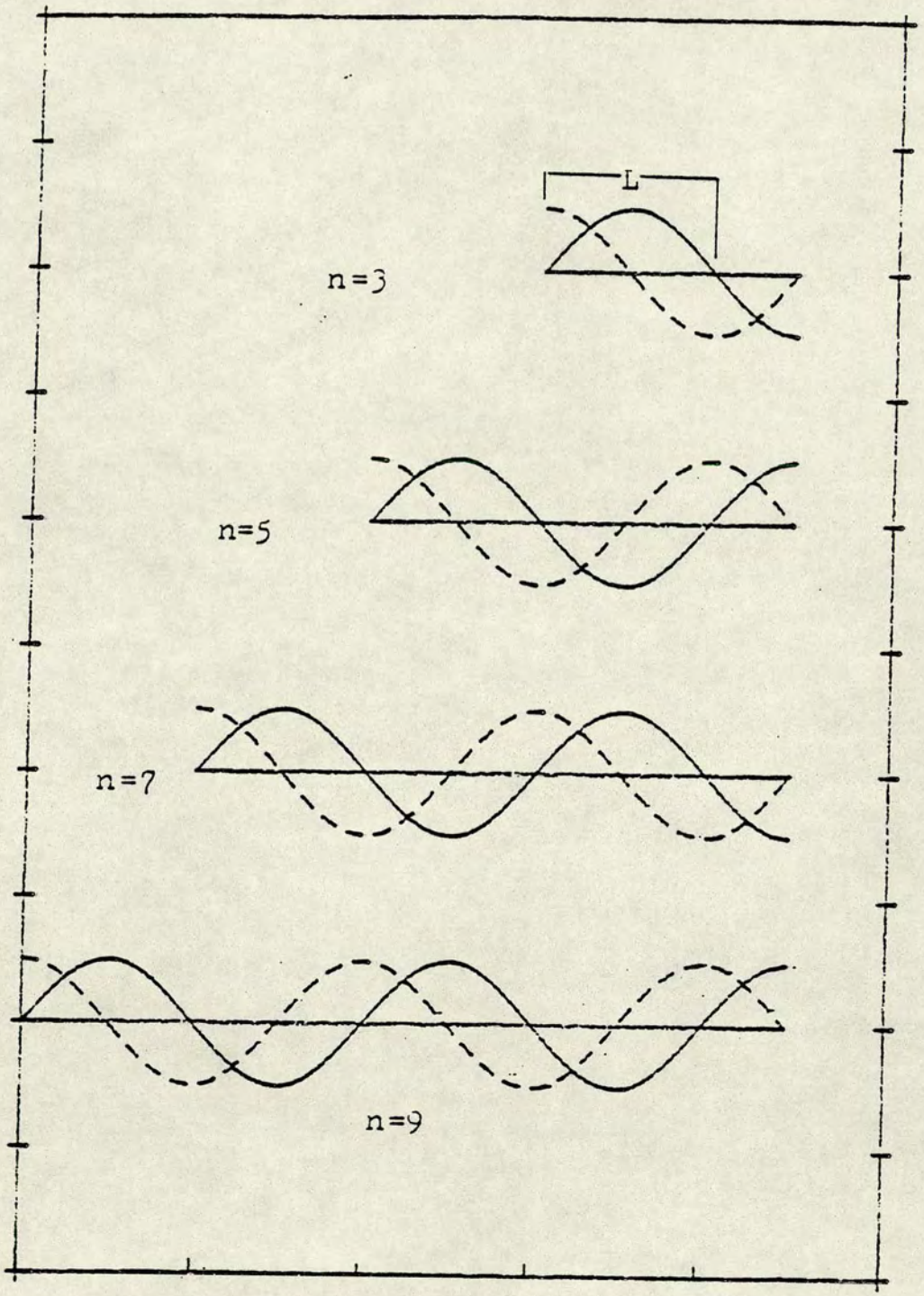

Fig: 4.2:

SIN(Y) VELOCITY PROFILES FOR ODD n IN HALF OF THE CHANNEL

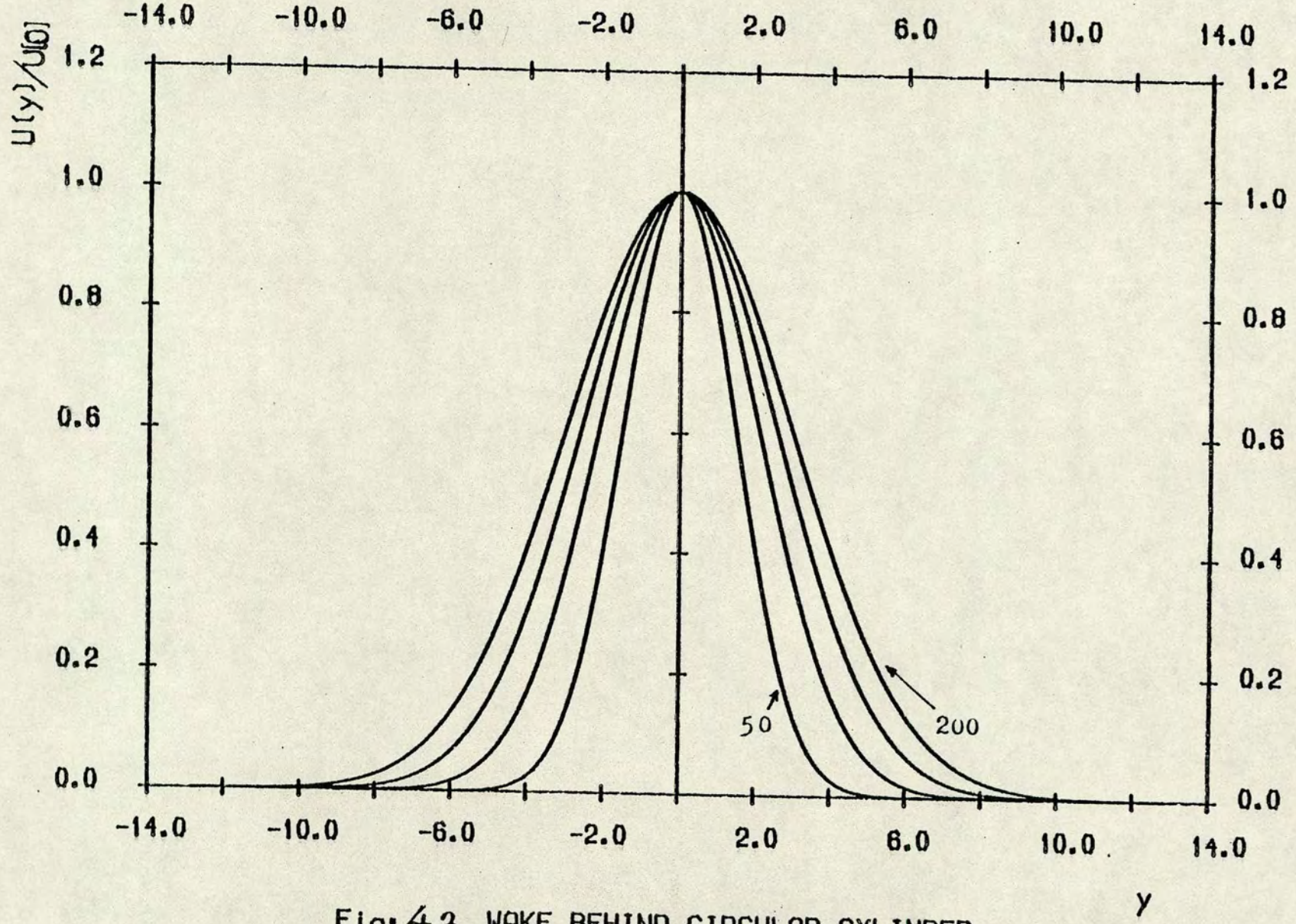

Fig: 4.3 WAKE BEHIND CIRCULAR CYLINDER

PROFILES X/=(X Cd d)= 50 , 100 , 150 , 200

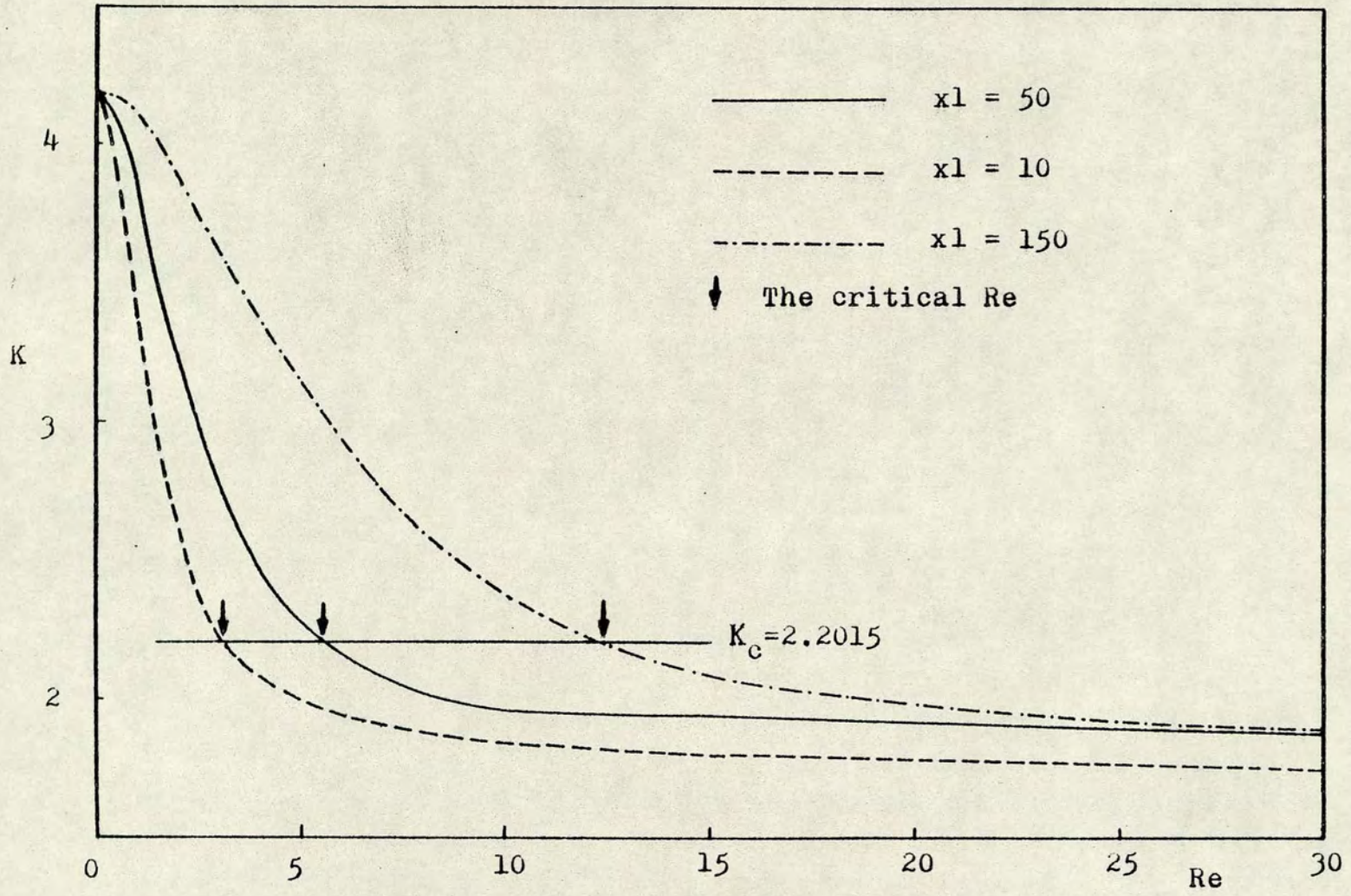

Figure 4.4: K vs Re for the wake at different values of xl= x Cd d.

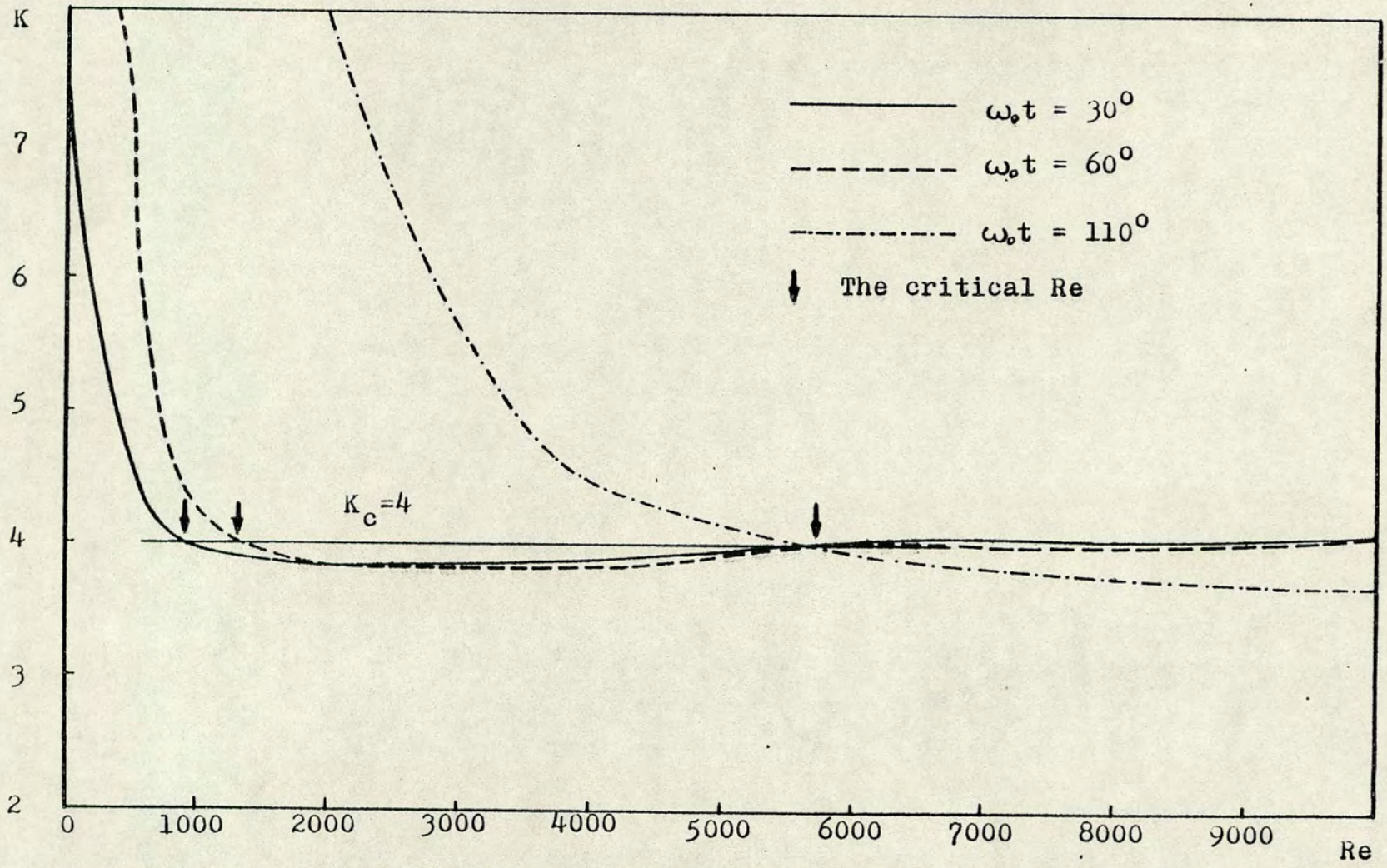

Figure 4.5: K vs Re for time-dependent flow profiles at β =6 and -U'>0.

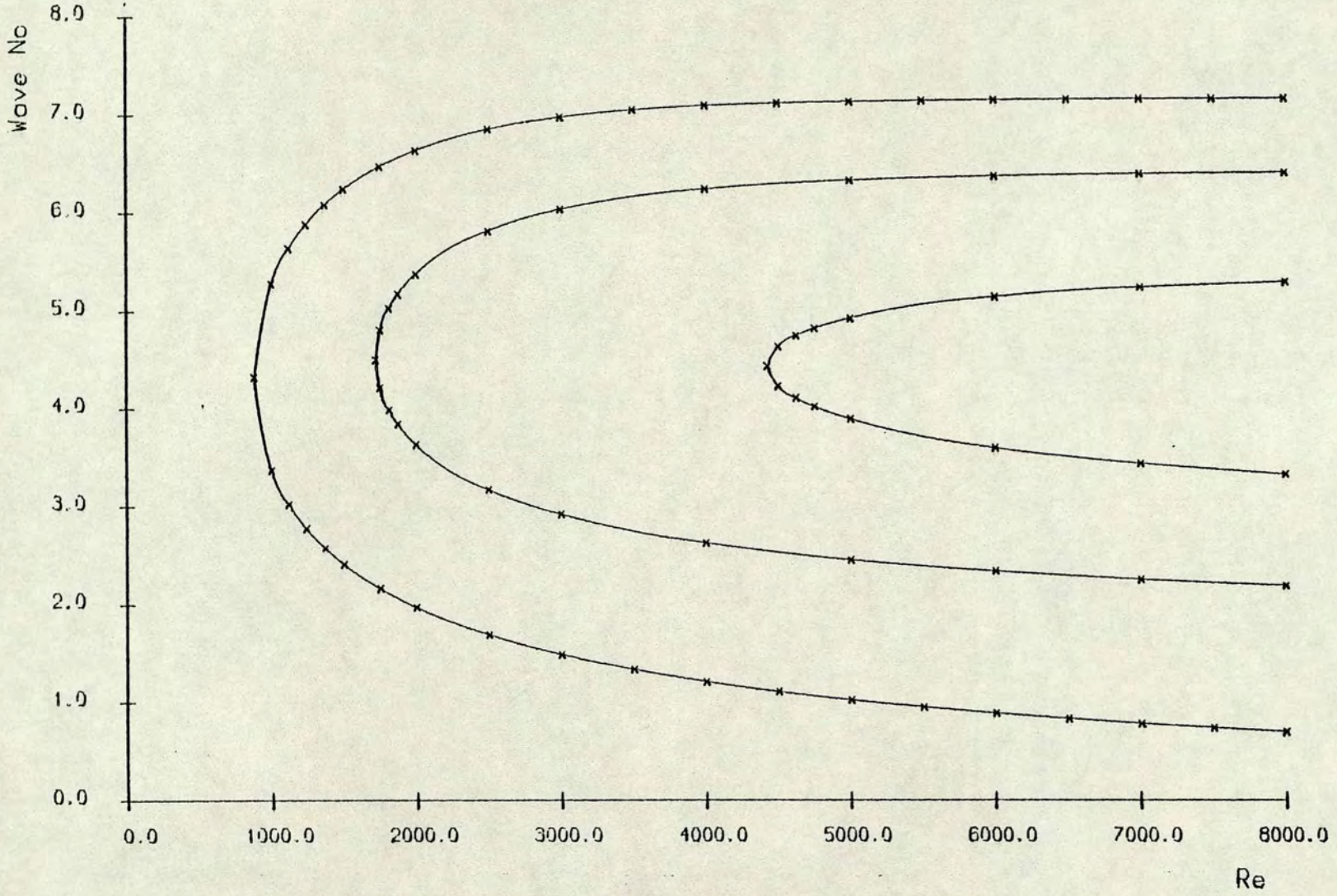

Figure 4.6: Constant amplification curves of time-dependent flow. β=6, w_o t= 30 degrees.

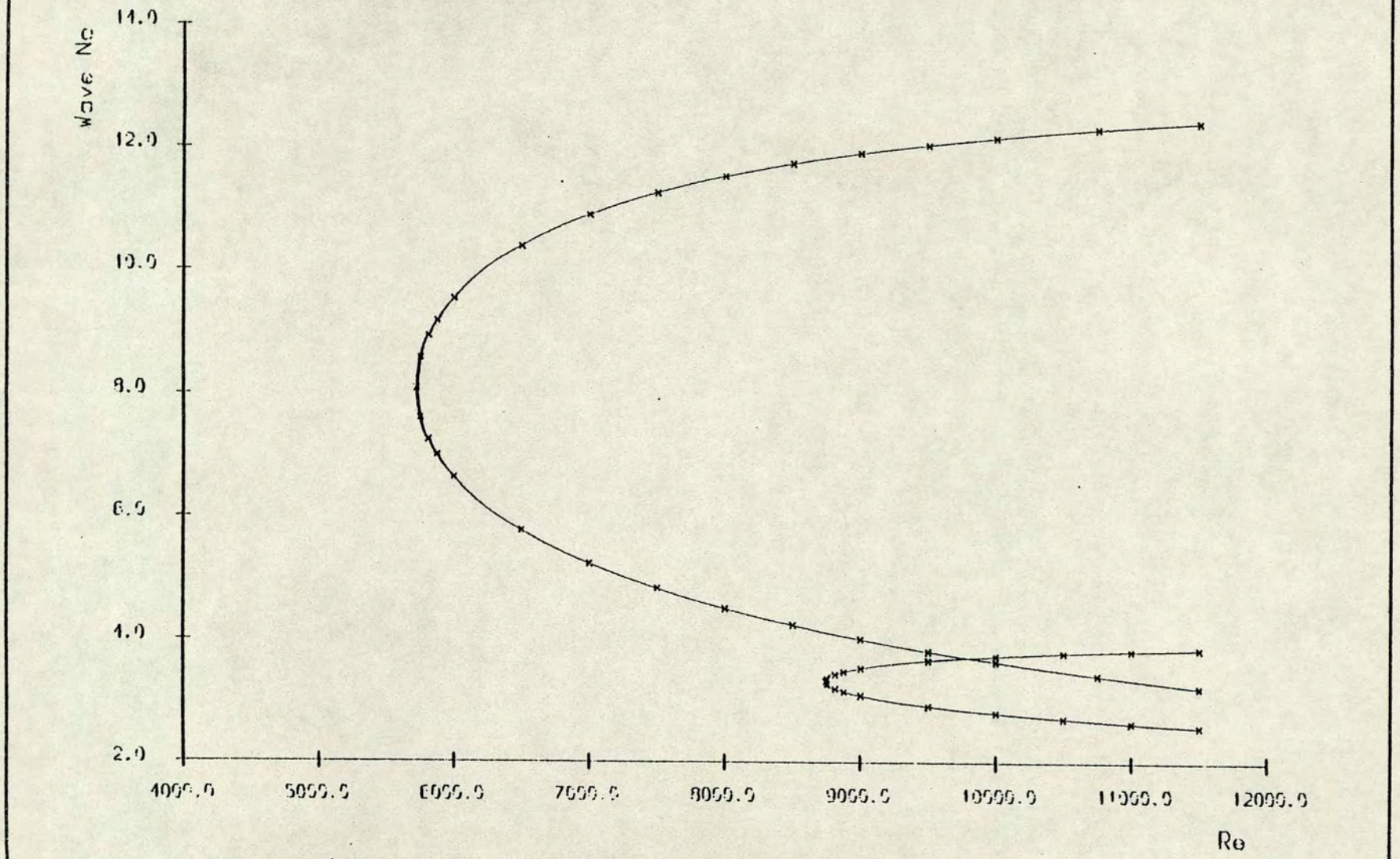

Figure 4.7: Neutral stability curves of time-dependent flow.
β=6, $\omega_o t$ = 110 degrees.

C H A P T E R F I V E

EXPERIMENTAL INVESTIGATION OF TRANSITION IN PURELY OSCILLATORY FLOW AT LOW FREQUENCY PARAMETER

5.1: Introduction

Time-dependent flows are common phenomena in natural and engineering applications. The name is given to all flows whatever the amount of the unsteadiness of the flow. The time dependence of the mean flow makes the turbulence and transition more complicated than in the steady flow case. Despite the importance of many flows which are time-dependent, only recently has attention been directed towards studying in detail turbulence quantities in such flows.

A major part of these studies is concerned with biofluid flows, i.e. blood and respiratory systems. Part of them concentrates on the complications produced by the multiplicity of branching tubes, the distensibility of vessels, the non-Newtonian aspects of the blood and the pulsatility of the flow [Oddou et al (1979)]. Numerical modelling is playing an important part in these studies. Despite the complexity of the blood flow, studies of simpler flows in rigid tubes revealed several points of similarity especially on the theoretical side. Parker (1977) showed that the types of disturbances observed in

arteries can be interpreted in terms of the stability of flows which are suddenly stopped by the action a piston or valve. A parametric study performed by Dantan et al (1976 a) on Poiseuille flow in a circular pipe showed a good agreement with the in vivo experimental results of Nerem (1974). On the experimental side however, as was noted by Nerem et al (1972) and by Oddou et al (1979), the parameters chosen were far away from those observed in in vivo experiments in blood flow. The experiments of Sarpkaya (1966), Gilbrecht and Combs (1963) and the more recent experiments of Lu et al (1973), Acharya and Reynolds (1975) and Ramaprian and Tu (1980) and Tu and Ramaprian (1983) are of this type. The authors have either chosen a small frequency parameter or a small oscillatory component or a combination. Some others chose purely oscillatory flow. Nevertheless, these experiments have been the source of more information about time-dependent flows in rigid tubes. In fact, the results of chapter 6 indicate that exact simulation of the blood flow pulses is more appropriate for comparison. (The pulses usually have a mean of 5-30 percent of the oscillatory part but the duration of the unsteady part is only about 30 percent of the period of the flow). The flow also is associated with steep accelerations and some times with steep decelerations.

In contrast to purely oscillatory flow, there is a large body of literature on fully developed flow which is perturbed by imposing a periodic modulation on it at a

prescribed frequency (some times called oscillatory or pulsatile flow). Also, in contrast to these two types, the unsteady turbulent boundary layers have had more detailed investigations [see e.g. Patel (1977)].

Detailed studies for the determination of the critical Reynolds numbers of the oscillatory flow, with different percentages of the mean part, in a circular pipe were made by Gilbrecht and Combs(1963) and Sarpkaya (1966). In these studies, a fair amount of data relating the critical Re to the unsteadiness parameter η was reported (η is the ratio between the unsteady and steady velocity amplitudes). These experiments showed that the flow pulsation increases the critical Reynolds number if the unsteadiness is small and reduces it if both the unsteady part and the frequency parameter β are large (see fig. 10 of Sarpkaya (1966)). Agreement was found between these results and the theoretical work of Dantan et al (1976 b). The above results are confirmed by Ramaprian and Tu (1980) who reported that the periodic oscillation tends to increase the critical Re of the puff-type transition of the pipe flow when η=0.2-0.3, i.e. small η (puffs are caused by large disturbances at the inlet region of the pipe). Accordingly, if the flow is fully turbulent at a certain frequency it will remain so when it is modulated at a higher frequency. The time mean velocity profiles in the oscillatory flow exhibit a point of inflexion near the wall, resulting in an overshoot of the periodic velocity component in the Stokes layer [Ramaprian and Tu (1980)].

The most comprehensive studies so far have been conducted by Ohmi and Iguchi (1982), Ohmi et al (1982), Hino et al (1983) and Tu and Ramaprian (1983). The first and the second authors have shown that the friction factor in the phase where turbulent bursts appear in oscillatory pipe flow follow the 1/7 power law and Blasius' friction law respectively. Hino et al found that the turbulence in an oscillatory duct flow followed the same phases found in turbulent boundary layers near the wall, i.e. sweep, ejection etc. [see e.g. Nychas et al (1973)]. In the case of turbulent boundary layers, experiments with zero pressure gradient lead to the conclusion that the flow modulation has no effect on the average behaviour of the flow. [Patel (1977)].

5.2: Previous Investigations of Transition in Oscillatory Flows

Gerrard (1971), Merkli and Thomann (1975), Hino et al (1976) and Ohmi and Iguchi (1982) in circular pipe experiments, Hino et al (1983) in a duct and Nerem et al and Nerem and Seed (1972) in in vivo experiments, all observed that turbulence occurs in the form of periodic bursts in the deceleration phase followed by relaminarisation in the acceleration phase (see also section 5.5). This type of instability is termed transient instability [Davis (1976)]. It is different from the monotonic instability which occurs if there exist a disturbance that experiences net growth over each

modulation cycle [Rosenblat (1968)]. A situation similar to this is observed when the oscillatory part is small compared to the steady part. However, the question remains whether this was due to only one disturbance.

Transient instability is more common in time-dependent flows and it affects the transport of heat, mass and momentum as in the case of the fully turbulent cycle [Davis (1976)]. Under certain circumstances (see section 5.5), the flow near the wall can be fully turbulent during the whole cycle, while the centre of the flow is transiently unstable.

Many investigators have used different experimental criteria for defining transition to turbulence. In some in vitro and in vivo experiments, the point of transition is found by considering a large number of turbulent and laminar situations and considering the line dividing the Reynolds numbers of both situations as the line of transition. In the case of in vivo experiments, this is justifiable. Ramaprian and Tu (1980) defined the critical Re as the number at which the puffs disappear, while Sarpkaya defined it as the number at which the puffs cease to amplify. Although it seems that there is no difference, the first authors suggest that this difference in definition cannot be ignored. The definition of transition as the first occurrence of turbulence is used by Merkli and Thomann(1975). Thus, the last three definitions are different and the critical Re according to the first is

lower than that of the last two definitions.

The transition in time-dependent flows is governed by several parameters:

a) The frequency parameter $\beta=(d/2)[\omega_o/\nu]^{1/2}$, where d is the diameter of the pipe, ω_o is the frequency of the oscillation and ν is the kinematic viscosity of the fluid.

b) The Reynolds number

$$Re=U_o d/\nu$$

where U_o is the velocity at the centre of the pipe.

c) The Reynolds number based on the Stokes layer thickness δ:

$$R\delta=U_o\delta/\nu$$

where $\delta=(2\nu/\omega_o)^{1/2}$

(Some authors use U_o for the mean velocity instead of the velocity at the centre of the pipe)

The first reported experimental study of a purely oscillatory flow was due to Li (1954) for the Stokes layer on smooth and rough plates in still water. Using dye dispersion, he found for $\beta>247$ a critical $R\delta=566$. Vincent (1957), for the modified Stokes layer (called also wave boundary layer), also using dye dispersion found $R\delta=110$. Collins (1963), also for the modified Stokes layer and large values of β, found $R\delta=160$ using mass transport velocity measurements. Kamphuis (1975) found the limit of

the laminar range to be $R\delta=141$. Reidel et al (1972) found the transition range $135<R\delta<1100$ for the Stokes layer at very large β using skin friction measurements.

In the case of purely oscillatory pipe flow, Sergeev (1966) for $4<\beta<\infty$ found $R\delta=500$. Merkli and Thomann (1975) in resonance tubes, for $40<\beta<73$, found $R\delta=283$. Hino et al (1976) found, for $1.91<\beta<8.63$, $R\delta=550$. Tromans (1976) found $R\delta=500$ for the onset of turbulence and $R\delta=130$ for the end of the laminar state.

Some important conclusions can be derived from the above results:

1) The Stokes layer is far more stable than the modified Stokes layer.

2) The reported values for the transition in pipe flow, (except for the results of Merkli and Thomann), agree on a lower limit of $R\delta=500$ for large values of β.

3) The critical $R\delta$ for the transition in the Stokes layer, if not equal to, is not less than that of the oscillatory pipe flow.

4) In the case of pure oscillatory flow, increasing the frequency of the oscillation, which requires a larger pressure gradient, will not increase the critical Reynolds number $R\delta$. Laminarisation may only be achieved for steady flows by adding a modulation [see Sarpkaya (1966)].

5.3: The Experimental Apparatus

The Laser Doppler Velocimeter (LDV) was used in this investigation. It is so far the most suitable accurate measuring system for investigating transition since it does not disturb the flow.

The system can be described briefly as follows. The light from a 5 mW Helium-Neon laser is passed through a DISA beam splitter. The frequency of the two emerging beams was shifted using a DISA flow direction adapter. The shifted beams are passed through a lens of a 13 cm focal length. The two beams were made to cross inside the glass tube containing the fluid. The shift in the frequency is necessary in order that the system will sense the direction of the flow. The crossing of the two beams inside the tube form 'the measuring volume' whose size is dependent on the value of the angle θ between the beams. The interference effects cause the light scattered by the small particles carried by the fluid to be modulated at the Doppler frequency f_d. Accordingly the velocity is given by

$$U = f_d \lambda \sin(\theta/2) \qquad (5.1)$$

where $\lambda = 632.8$ nm, the wavelength of the laser light.

A photomultiplier arrangement was used to convert the scattered light into an electrical signal (figure 5.1).

After passing the signal from this arrangement through low and high pass filters, the continuously varying frequency was tracked using the Southampton laser Doppler tracker. The tracker converts the frequency into a DC voltage whose magnitude is proportional to the velocity. The coefficient of proportionality k is determined after the linear relation between the frequency f_d and the voltage V have been established. Using k instead of f_d, equation (5.1) becomes

$$U=k\ V\ \lambda\ \sin(\theta/2) \qquad (5.2)$$

where $k=f_d/V$, the coefficient of proportionality.

In order to reduce the scattering of the laser light from the walls of the glass tube, precision bore tubes of constant internal diameter were used. A tube of 310 cm in length was used. It consists of three shorter tubes joined together using especially shaped perespex joints. Each joint also contain a pressure tap. The overall length of the tube system was considered sufficient since the fluid moves about 50 cm only in either direction from the measuring point at the maximum stroke of the pump (The diameter of the tube=0.8 cm). A view of the measuring section is shown in plate 1.

The pump is shown diagrammatically in figure 5.2 (a) and a general view is shown in plate 2. During one revolution of the wheel A, the half cycles 1 and 2 are

accomplished. The arrows indicate the direction of the motion of the discs B and C and the direction of the motion of the fluid. The fluid in the pump is contained between small and large bellows whose edges are sealed to B and C. During the first half of the cycle, the disc C is forced closer to the disc B in the position C1. The fluid is forced out of the pump. In the half cycle 2 the direction of the flow is reversed. The stroke volume and consequently the Reynolds number can be changed using F. The pulse shape can also be changed using E. The sinusoidal shape is obtainable at position M which is situated at the centre. Three theoretical velocity waveforms at the positions M, R and L are shown in figure 5.3 b. Two actual velocity waveforms at the positions M and L are shown in figure 5.3 (a) and (b) respectively. These are traces of oscilloscope pictures. Although the first is close to the theoretically expected shape (figure 5.2), the second is more distorted. The period is T=1.95 second for β=7.18. This is considered fast since values of T smaller than 1.45 can cause strain on the mechanism of the pump. At slow modulation (large T), the actual velocity shapes deviate from those expected theoretically. As the amplitude increases unexpected velocity waveforms are obtainable. Three such waveforms are shown in figure 5.4. Figure 5.4 (a) is for the position M and the extreme positions L and R are shown in figure 5.4 (b) and (c). Deviations were also found at the extreme positions L and R when the flow is laminar.

5.4: Experimental Results for Transition Reynolds Numbers

The aim of the experiments was to determine as accurately as possible the critical Reynolds numbers for transition from laminar flow for purely oscillatory motion. The experiments have been conducted while keeping the flow as close as possible sinusoidal. The period of the oscillation T varied between 1.45 and 7.65 seconds, the two possible extremes. These values correspond to values of the frequency parameter β between 3.6 and 8.33 . This range has been investigated previously by Hino et al (1976). However, as was mentioned earlier, their results were approximate due to the method they used in deducing the critical Re. In addition to that, the use of the LDV system adds more accuracy to the results obtained here. The velocity at the centre of the pipe was used for determination of the Reynolds numbers.

At low Reynolds numbers, as the amplitude increased, it was noticed that the flow deviated from the laminar shape. These deviations appeared in the form of a low frequency oscillation imposed on both pressure and velocity waveforms. After several trials, it was possible to establish that these low frequency disturbances were not produced by the motion of the pump bellows as the amplitude increased. The values of the Reynolds number Re at which this phenomenon occurred were noted. These are listed in table 5.1, in addition, δ based Reynolds numbers $R\delta$ are also given. It is noticeable that Re is almost

constant through the range investigated. In other words there is total dependence on the Stokes thickness δ, since $R\delta = Re(\delta/d)$. It should be noticed that δ decreases as β increases.

TABLE 5.1

The critical Reynolds numbers of the minor instability of purely oscillatory flow in a pipe

β	T	δ	U_o	Re	$R\delta$
3.63	7.65	0.156	15.21	1210	237
4.50	5.00	0.126	15.21	1216	192
5.10	3.85	0.110	16.38	1310	181
6.20	2.60	0.091	16.38	1310	149
6.76	2.23	0.084	18.72	1498	156
7.20	1.94	0.078	16.38	1310	129
8.00	1.56	0.070	15.73	1246	110

Hino et al (1976) found that a similar form of transition occurs at $R\delta=380$ for $\beta=3.9$, which is almost twice the value deduced from table 5.1 for this value of β. For $\beta=5.5$, they found the same type of transition occurring at $R\delta=180$, ($Re=1420$), which is in good agreement with the table. Tromans (1976), for large values of β using dye streaks in water, found $R\delta=130$ for what he called the onset of instability, in contrast to the onset of turbulence for which he found $R\delta=500$. All these results suggest that this type of transition is genuine and apparently similar instability occurs in the Stokes

boundary layer flow as can be noticed e.g. from the results of Reidel et al (1972). In chapter 6, this instability is referred to as the minor instability in order to differentiate between it and the high frequency transition leading to turbulence occurring at higher Re and which is called the major instability.

TABLE 5.2

The critical Reynolds numbers of the major instability of purely oscillatory flow in a pipe

β	T	δ	U_o	Re	$R\delta$
3.79	7.00	0.150	25.74	2059	385
4.33	5.35	0.130	31.50	2527	410
4.90	4.20	0.116	36.23	2900	421
5.87	2.92	0.096	40.95	3276	393
6.43	2.43	0.088	44.46	3557	391
7.22	1.93	0.078	48.60	3744	365
7.69	1.70	0.074	53.24	4259	393
8.33	1.45	0.068	60.84	4867	413

By increasing the amplitude of the oscillation, high frequency disturbances appear at the peak of the velocity. Slight increase in the amplitude results in turbulence propagating to a certain degree in the deceleration phase. The peak velocities at the centre of the pipe above which the disturbance amplifies have been determined. This

definition of the point of transition to turbulence is similar to that of Sarpkaya (1966). The critical Reynolds numbers Re and Rδ have been determined for $3.6 \leqslant \beta < 8.3$. Their values are given in table 5.2. These values are well below the average values Rδ=550 reported by Hino et al (1976) and Rδ=500 due to Sergeev (1966). It will be shown in chapter 6 that the agreement between the values in table 5.2 and the numerical results for $\beta > 5$ is good. This indicates that in the range of β investigated, the flow is less stable than for high β. In other words, the generalisation of the results at high β to the small values of β, and according to the numerical results of chapter 6 up to β=15, is not correct. The results in table 5.2 also indicate that the critical Rδ is greater than 300 for all values of β taking into consideration the measurements of Hino et al (1976) for $\beta < 3$. Data given tables 5.1 and 5.2 are plotted in figure 5.5.

5.5: High Frequency Disturbances in the Flow

In order to gain more information about the behaviour of the disturbances in the flow, some qualitative study has been made. It is supported by several turbulent velocity records. In figure 5.6, four velocity traces at different values of Re are shown. The velocity waveforms (5.6 (a)) at the centre of the pipe were taken at the critical Re=3700 as a reference. In figure 5.6 (b), both the pressure gradient and the velocity waveforms at the centre of the pipe are shown simultaneously at Re=3738.

The phase lag between the two is approximately 86 degrees, which is in agreement with what is expected theoretically. The disturbances appear at the peak of the velocity and show their effect on the pressure gradient. As the Reynolds number increases, the whole region of the peak velocity becomes turbulent. The beginning of this region, moving from left to right across the oscilloscope time, occurs roughly at the value of the critical velocity [figure 5.6 (c) and (d)]. Figure 5.7, for $\beta=7$, shows turbulent velocity waveforms at four positions across the pipe (normalised by the pipe radius). The flow is more disturbed in the half near to the wall, and completely turbulent (the whole cycle) near the wall. Notice that the maximum velocity occurs at approximately $y=0.65$. It was noticed that in the range of β investigated, the area close to the wall some times became turbulent before the centre. The core flow which stayed stable while turbulence appeared near the wall, covered not less than 70 percent of the pipe diameter. This demonstrates the importance of the acceleration in inhibiting the disturbance growth in the core area where the acceleration is large.

Three turbulent nonsinusoidal velocity waveforms are shown in figure 5.4. They show clearly that severe deceleration inhibits turbulence. Turbulence appears in the deceleration phase when the deceleration is relatively small. It appears also when the acceleration is small. These observations are supported by the in vivo velocity waveforms of Nerem and Seed (1972). No disturbances exist

in large acceleration or large deceleration phases [Nerem and Seed figure 5 (b)]. In the case of small deceleration [Nerem and Seed fig.5 (c)], turbulence persists all along to almost zero velocity exactly as that shown in our figures 5 (b) and (c). This suggests the possibility of reducing the effect of turbulence in the case of purely oscillatory flows by making the pulses sharper, but only if the shape could be maintained when Re is high.

Figure 5.8 shows three highly turbulent velocity waveforms at $\beta=7$. It is noticeable that turbulence reappears when the flow stays steady even for a very short time. A duration of one period of the disturbance is necessary for it to grow to a large magnitude.

Wavenumbers and frequencies of the disturbance have been found for two cases when Re>Re critical. For $\beta=7$, the wavenumber α is about 4.5 and the frequency f=40 Hz, while for $\beta=5$, f=25 and $\alpha=4.3$. These values are in good agreement with those obtained theoretically in chapter 6. Large wavenumbers are always associated with inflexion instability in a narrow domain (chapters 4 and 6). One characteristic of this instability is the wide vortices resulting from it (large scale structures). These will be discussed further in both chapter 6 and chapter 7.

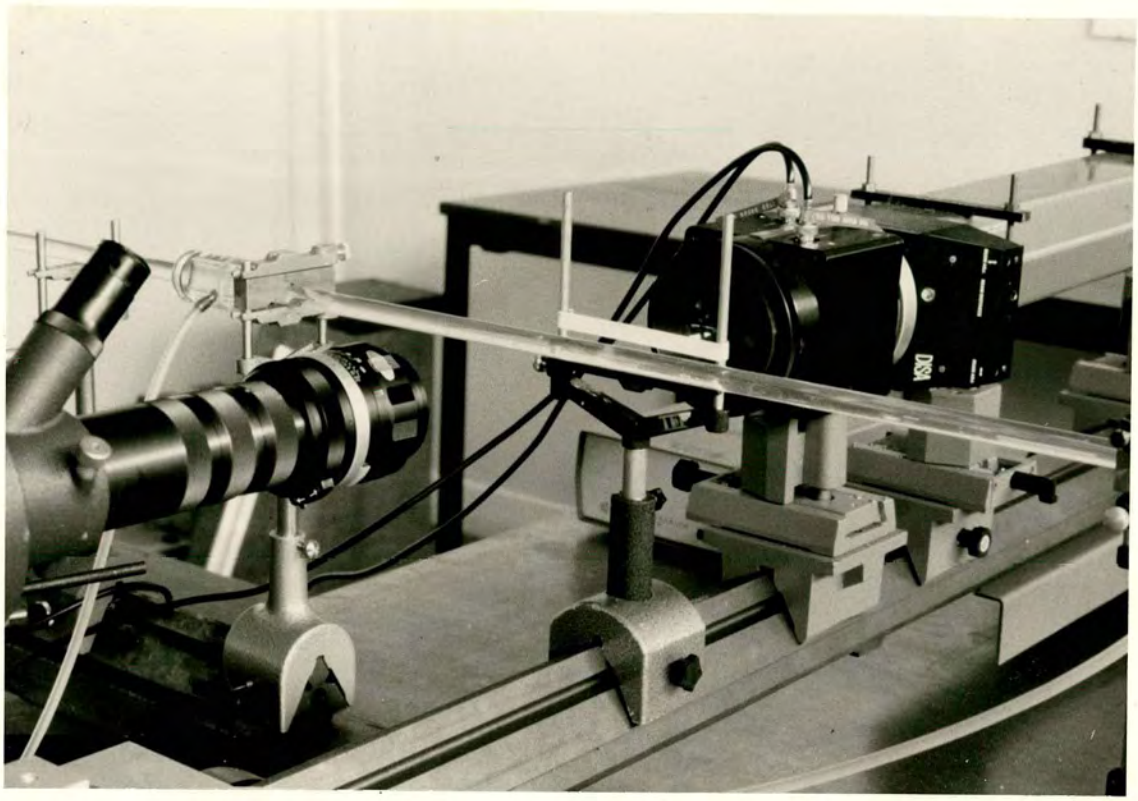

PLATE 1: A view of the measuring section

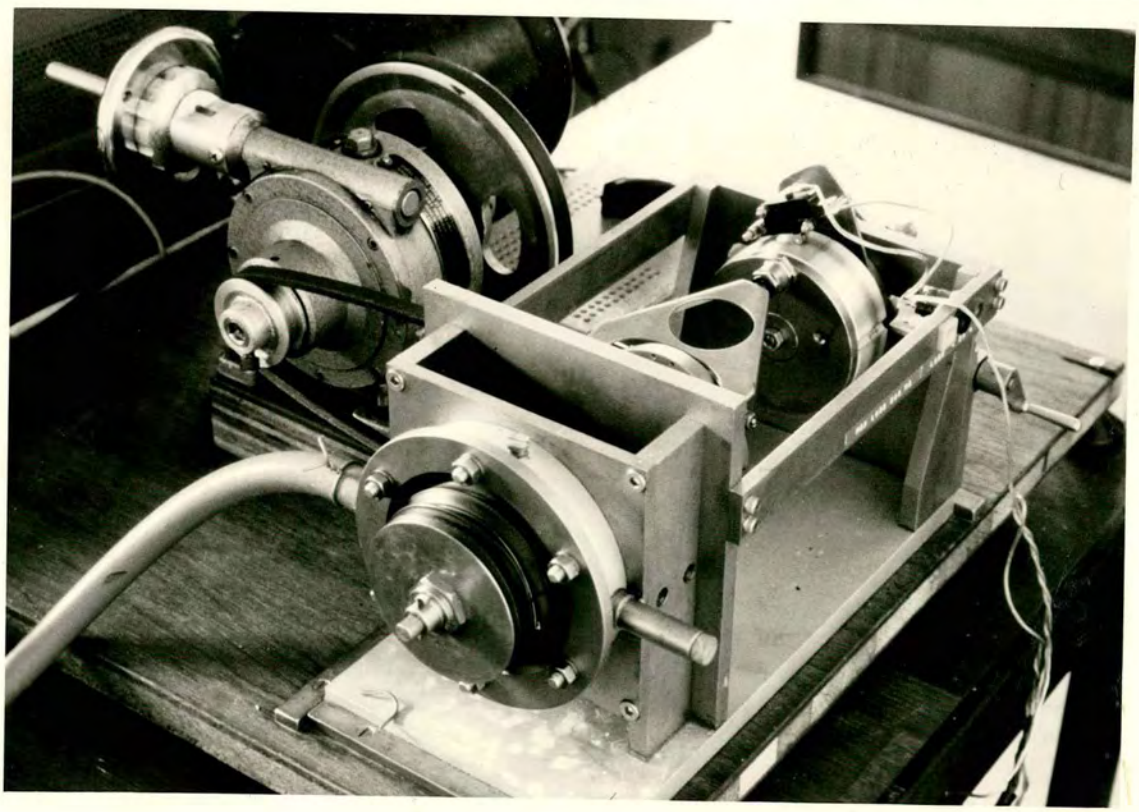

PLATE 2: General view of the pump

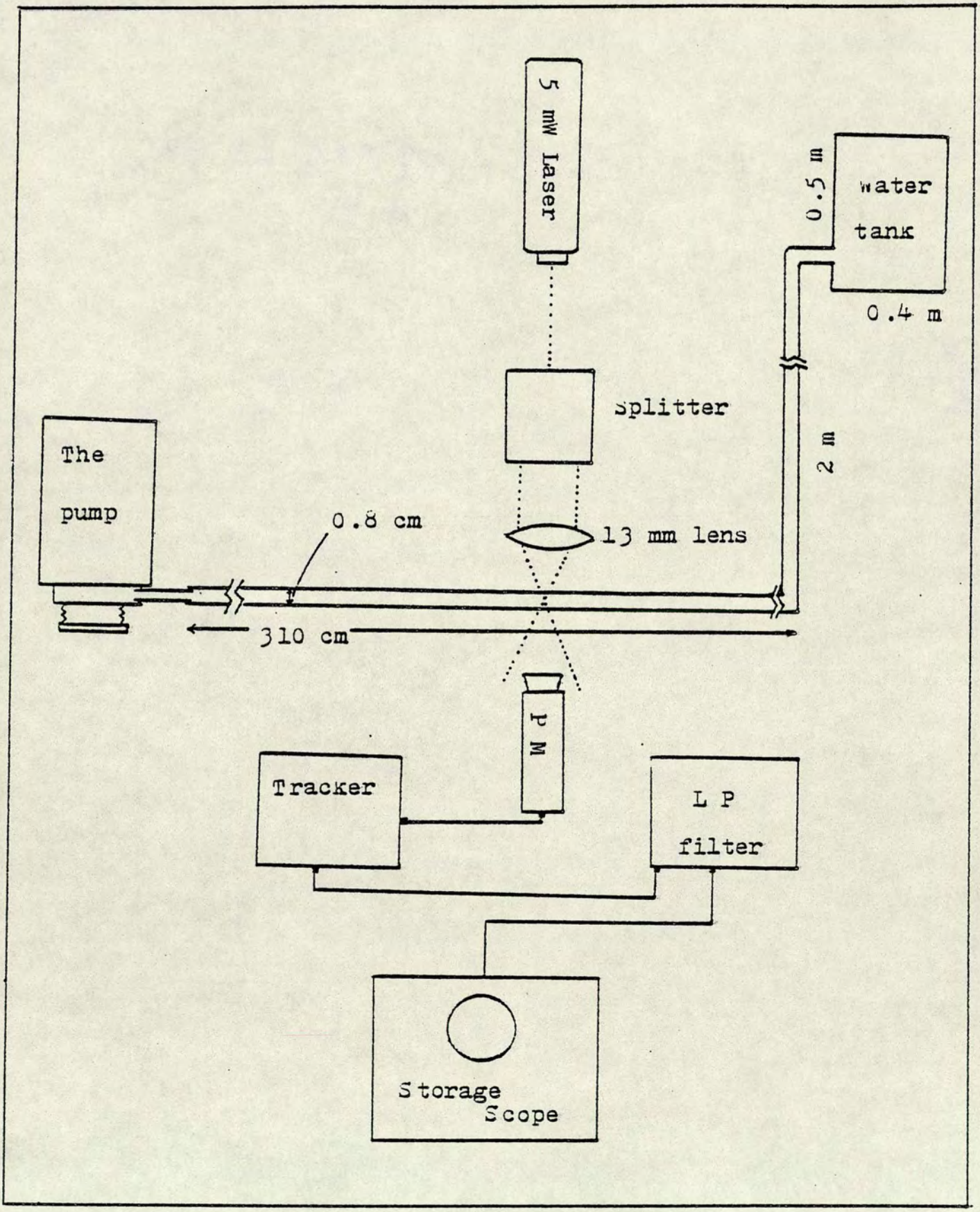

Figure 5.1: The experimental apparatus.

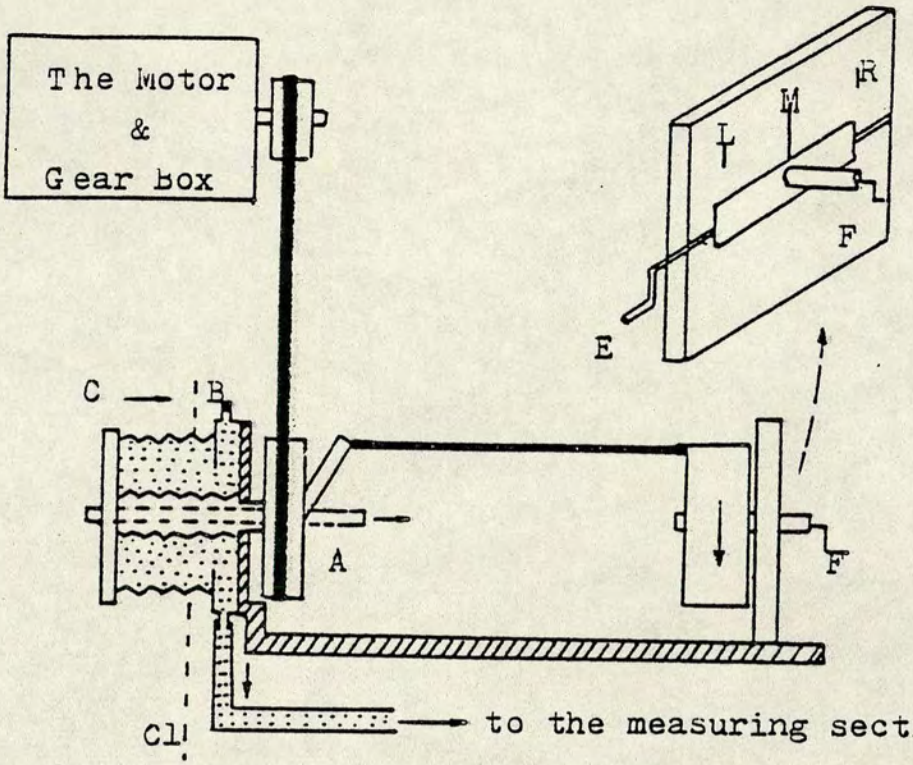

(a)

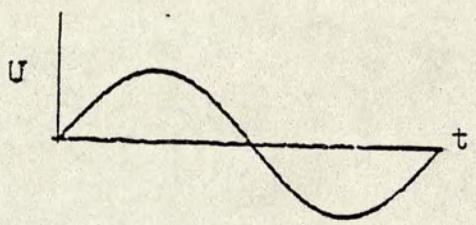

Position M

(b)

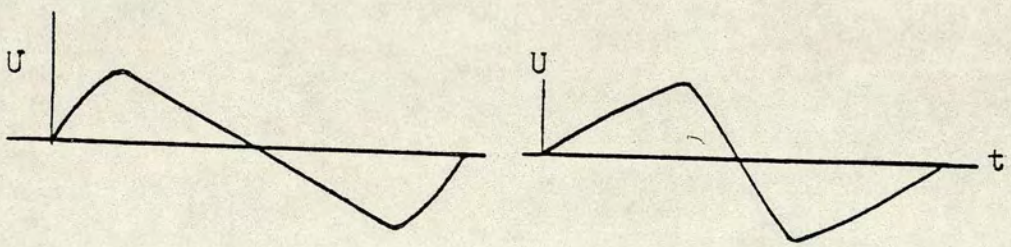

Position L

Position *R*

Figure 5.2: The Pump

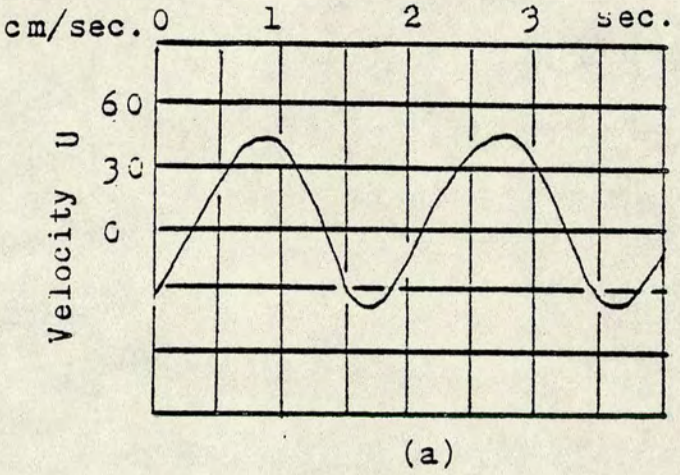

(a)

Position M

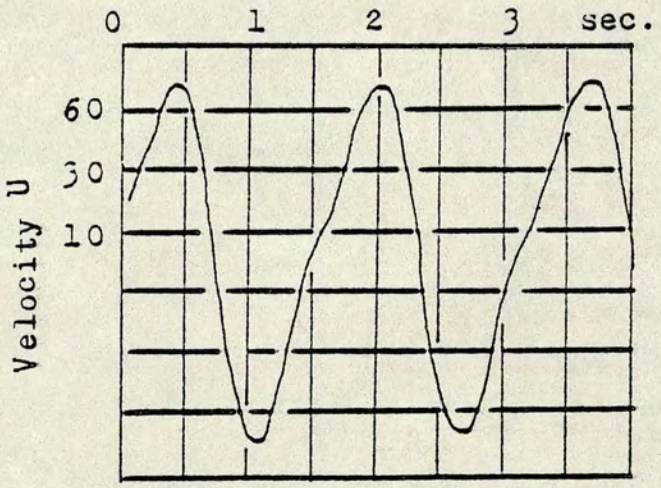

(b)

Position R

Figure 5.3: Sinusoidal(a) and non-sinusoidal velocity waveforms generated by the pump.

.TURBULENT OSCILLATORY PIPE FLOW.

.LDV INSTANTANEOUS VELOCITY TRACES AT THE PIPE CENTRE.

T=3.44 sec.

β =5.226

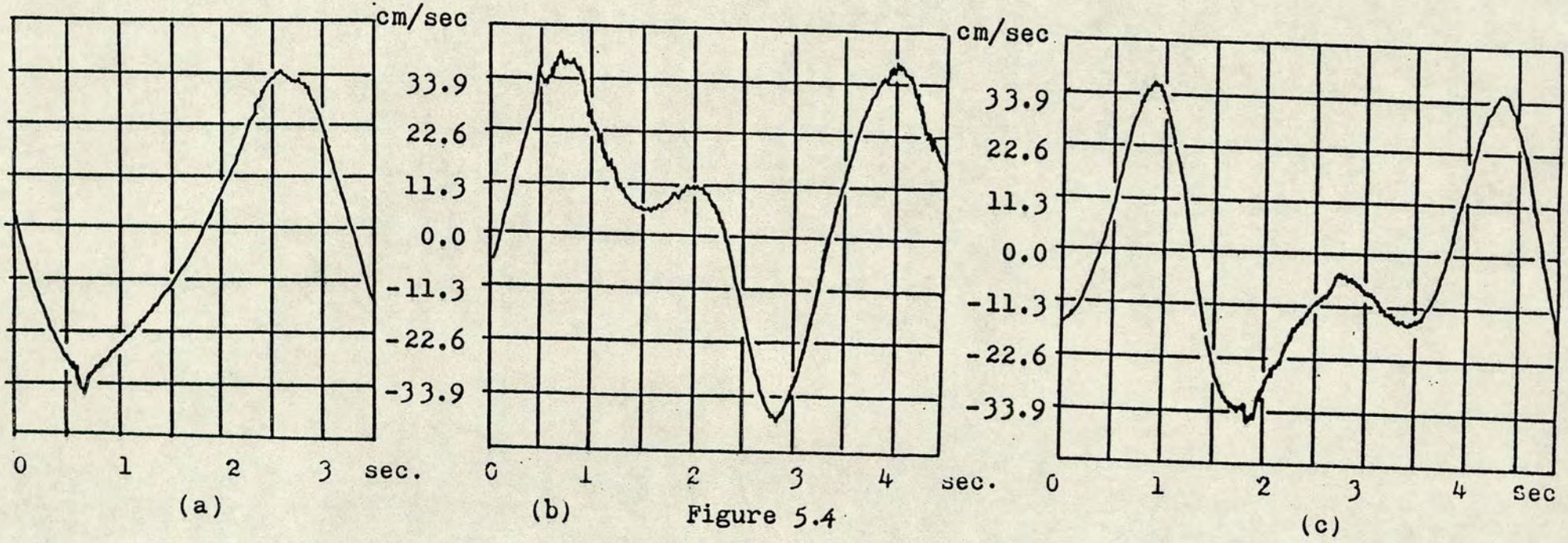

Figure 5.4

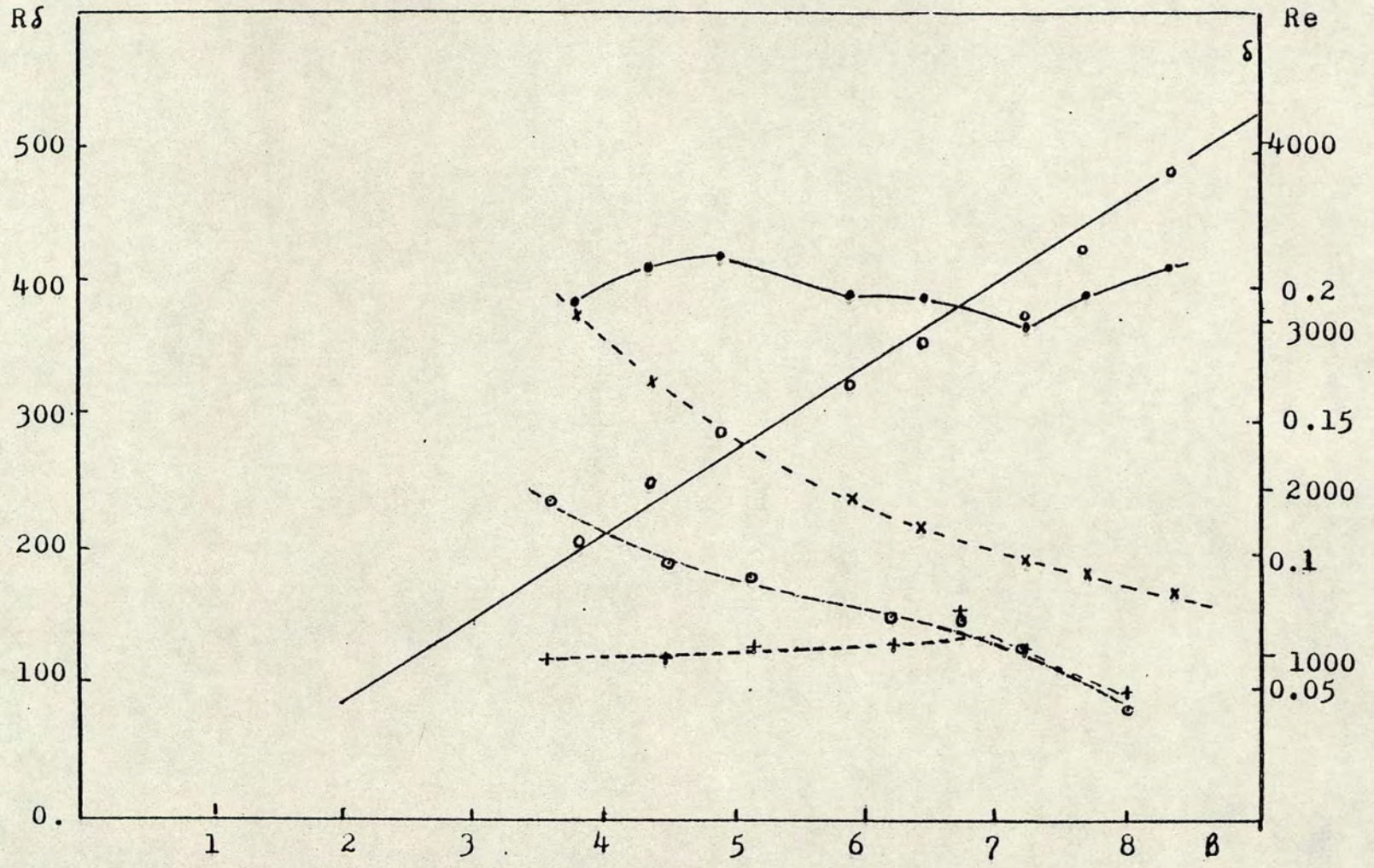

Figure 5.5: The major and the minor instability of pure oscillatory flow in a pipe.
Solid lines: The major instability. •-β vs Rδ o-β vs Re

Dashed curves: The minor instability. x - β vs δ , ⊙ - β vs Rδ , + - β vs Re.

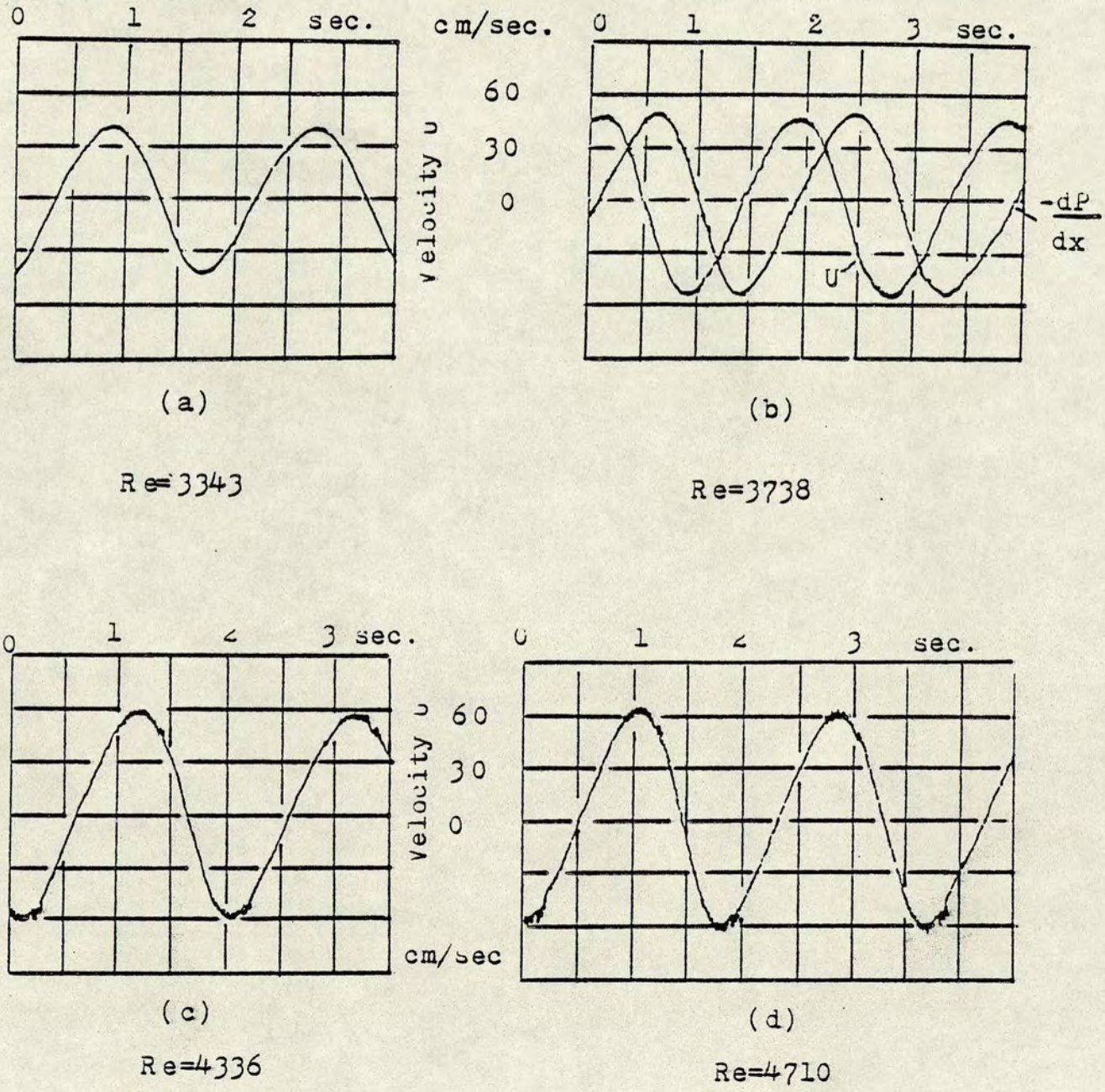

Figure 5.6: Velocity waveforms at different Re. (β=7.0)
Re critical =3700

Figure 5.7: Turbulent velocity waveforms at different positions across the pipe.

T=1.96 β=7.0 Re=3960 Re critical =3700

y=r/a r=the distance from the centre, a= the radius of the pipe

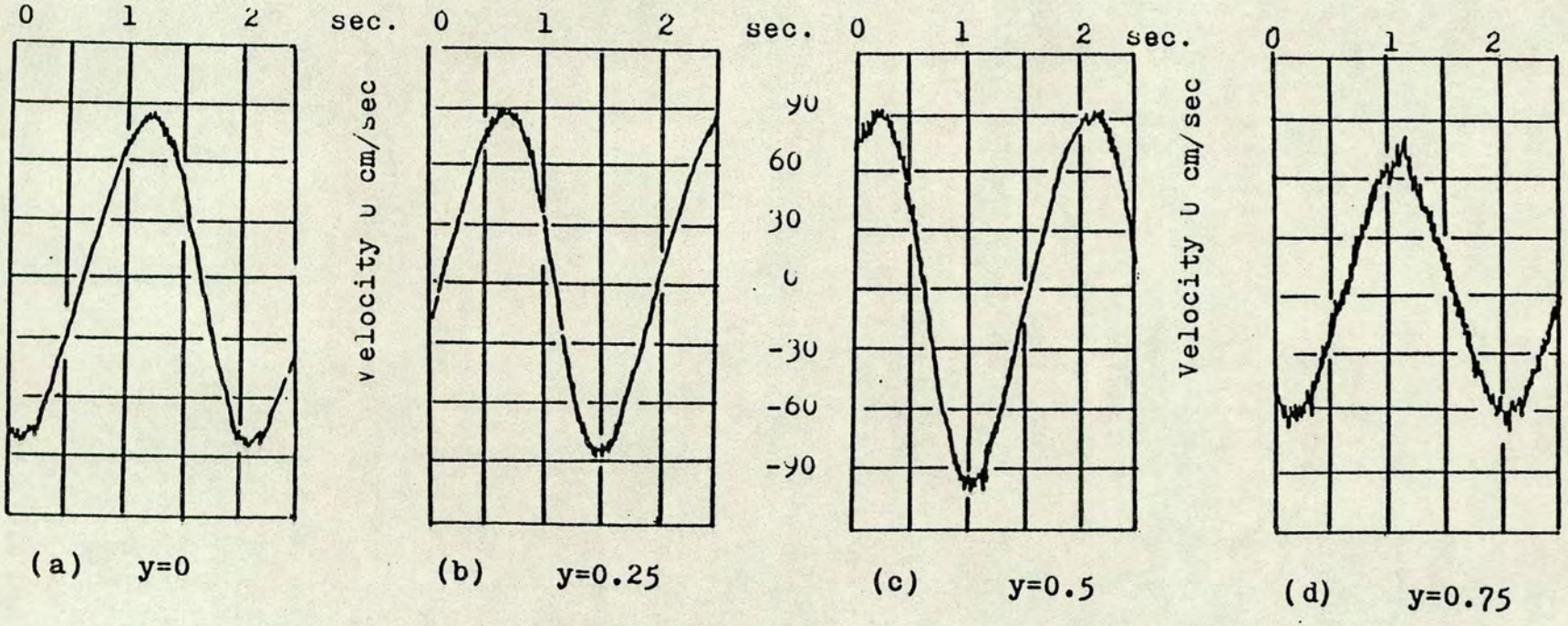

(a) y=0 (b) y=0.25 (c) y=0.5 (d) y=0.75

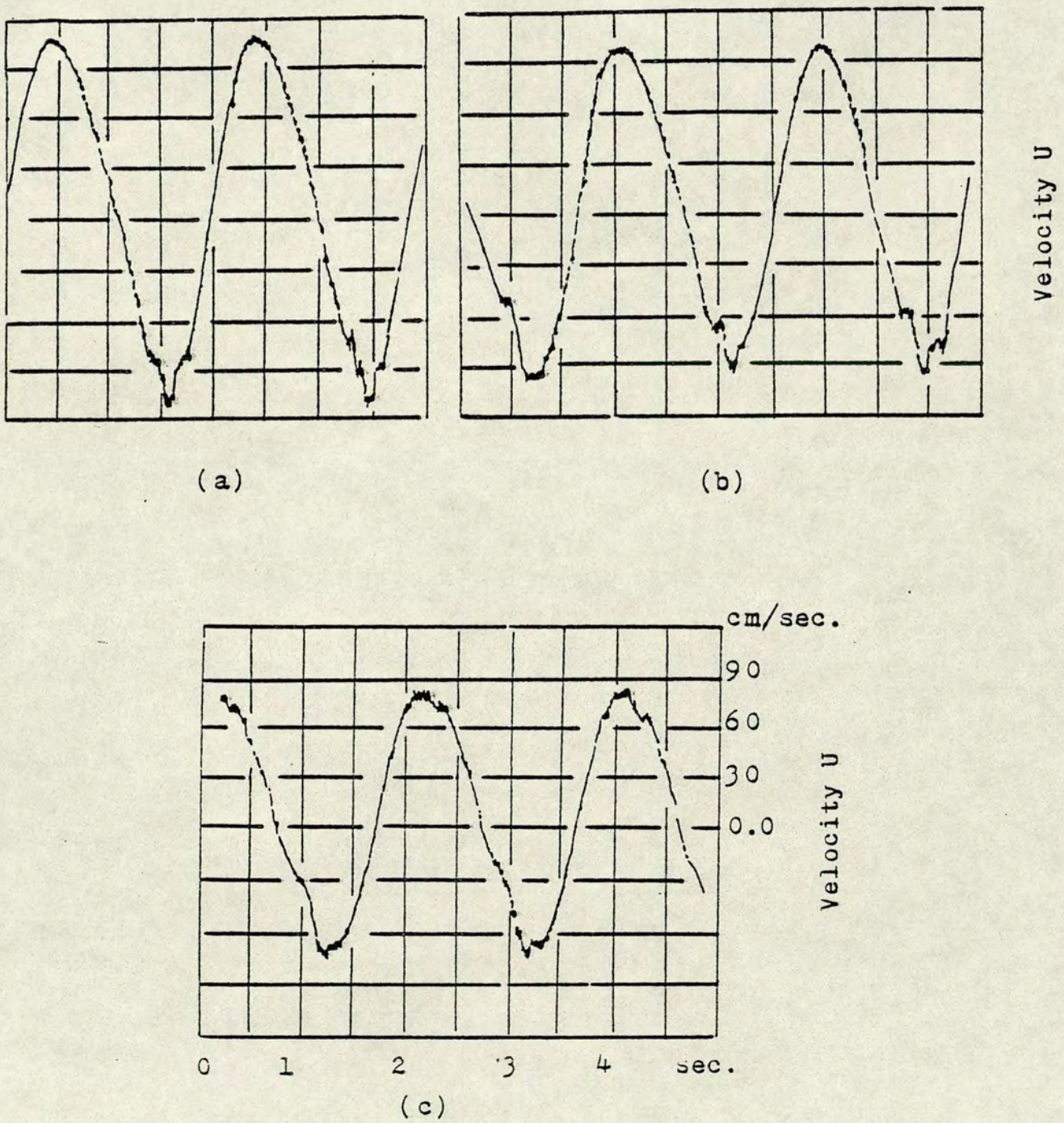

Figure 5.8: Highly turbulent waveforms at the centre of the pipe. (β =7.0)

C H A P T E R S I X

NUMERICAL STUDY OF THE STABILITY OF TIME-DEPENDENT FLOW

6.1 : Introduction

In contrast to the experimental investigations of transition in oscillatory flows, the number of successful theoretical investigations is limited. The first known investigation was due to Shen (1961) who proved that the acceleration phase is more stable than the deceleration phase. Collins (1963) investigated the stability of the wave boundary layer (also called modified boundary layer), and using Lin's formula (1955) for the critical Reynolds numbers in boundary layers, he obtained a critical $R\delta=U_o\delta/\nu=21.4$. The first comprehensive numerical investigations were made by Grosch and Salwen (1968) for modulated plane Poiseuille flow with a large mean. Modulations with amplitudes of less than 5% were shown to stabilise the flow, while larger amplitude modulations destabilised the flow. The most successful investigation so far for pipe flow is due to Ohmi and Iguchi (1982). It is based on the Blasius' friction law and the 1/7 power law, an approach totally different from the above mentioned investigations. The results of this investigation will be discussed in section 6.6.

Most of the theoretical work on the stability of Stokes layers have been carried out by Kerczek and Davis who investigated their stability using both the energy and linearised theory. The energy theory for all flows gave very low critical Reynolds numbers in comparison to the linearised theory (the exception is the case of stratified flow where both more or less agree). Kerczek and Davis (1972) found for the frequency parameter $\beta \rightarrow \infty$, that $R\delta_c = 19$ for 3 dimensional disturbances (3D) and $R\delta_c = 38.9$ for 2D, for the case of monotonic stability (the state in which every disturbance decays at every moment). For transient stability, i.e. when disturbances grow for part of the cycle, Davis and Kerczek (1973) found for $\beta \rightarrow \infty$ that $R\delta_c = 24.8$ for 3D and $R\delta_c = 46.6$ for 2D. Notice that $R\delta_c$ for 3D is almost exactly half of that for 2D. This is also confirmed by their results for small β.

The linear analysis of Kerczek and Davis (1974) showed that the Stokes layer is stable for $R\delta \leqslant 800$, when $\beta = 8$. Similarly, Yang and Yih (1977) showed complete stability of purely sinusoidal flow in a circular pipe. Both investigations used the integration procedure.

The integration procedure, using the criterion that small disturbances should show a net increase over one full cycle has been criticised by Merkli and Thomann (1975) as being too restrictive, since according to their observations a disturbance may grow, lead to turbulent bursts and decay by relaminarisation in the same period.

Indeed, all experimental studies of purely sinusoidal flow agree with these observations and as has been shown in chapter 5, the peak of the velocity region is the main area where the disturbances grow and after which they may continue during a large part of the deceleration phase.

However, the integration procedure as a means of studying instability cannot be completely disregarded when one disturbance is expected to survive the effect of the modulation, as is the case when the oscillatory part is very small compared to the steady part. However, von Kerczek (1982) has shown numerically that for such small modulations the disturbance grows, but its growth after several cycles is still relatively very small, in contrast to the physical disturbance which may have gone through larger amplification leading to turbulence. In our view, application of the Floquet exponent theory to oscillatory fluids with large oscillation amplitude is unrealistic due to the finite value of the viscosity. Therefore, in order to establish the theoretical criterion for the instability of purely sinusoidal flow, close examination is required to determine the situation where the disturbance growth is likely to be inhibited and the durations when this situation exists are to be excluded. Doing this, as can be seen, will lead to the quasi-steady approach, i.e. the instability is determined by the instability of the first profile where the growth will not be inhibited.

It is well known [chapter 4, and for a pipe Uchida (1956)], that the time-dependent flow profiles contain inflexion points and according to the Rayleigh criterion such profiles are unstable. Nerem et al (1972) showed that the wavenumbers of the disturbances of a highly disturbed aortic flow follow closely the neutral curve of the Falkner-Skan velocity profile with b=-0.1 (b is the pressure parameter). They suggested that the aortic blood flow instability is determined by the velocity profile inflexion points. Sarpkaya (1966) stated that the presence of inflexion points during part of the cycle is a necessary but not sufficient condition for the amplification of finite disturbances. However, he also showed that the critical Reynolds number of the pulsating flow started to decrease when the duration of the profiles with inflexion points in the flow became more than 53% of the period of the pulsation (this increase happens when the ratio of the oscillatory part to the steady part increases). In other words, the last two observations suggest that the time-dependent flow instability has the characteristics of inflexional instability which support our conclusion that the investigation of the stability of the frozen profiles (quasi-steady approach) is more appropriate than the integration method.

6.2: The Time-Dependent Plane Poiseuille Flow Solution

The flow is considered in a channel of an infinite length in the x direction an infinite depth in the z direction, and a width of 2h=1 in the y direction. It is assumed that the flow is parallel to the x axis. The velocity in the y direction is assumed zero. Let the velocity in the x direction be

$$U = U(y,t)/U_o$$

where U_o is the mean velocity. Since from the equation of continuity $\partial U/\partial x=0$, the Navier-Stokes equation reduces to

$$\partial U/\partial t - \nu\, \partial^2 U/\partial y^2 = -\partial P/U_o\partial x \qquad (6.1)$$

The pressure gradient is given by

$$\partial P/\partial x = A\, e^{i\omega_o t} + \text{the complex conjugate}$$

where ω_o is the frequency of the pulsation of the flow and ν is the kinematic viscosity of the fluid (water with $\nu=0.01004$ at 20 C°).

Let $U=W(y)e^{i\omega_o t}$ + the complex conjugate (6.2)

Substituting (6.2) in (6.1) and after normalisation, we have

$$\gamma\, W(y) - \partial^2 W(y)/\partial y^2 = hA/\nu U_o \qquad (6.3)$$

where, $\gamma = (h/2)[i\omega_o/\nu]^{1/2} = \beta(1+i)/1.414214$, and $\beta=(h/2)[\omega_o/\nu]^{1/2}$ is the non-dimensional frequency parameter of the oscillation

The solution of (6.3) is given by

$$W(y) = B1\ e^{\gamma y} + B2\ e^{-\gamma y} - hA/\nu U_o \qquad (6.4)$$

The coefficients B1 and B2 are determined from the boundary conditions $W(0)=W(1)=0$ and from the symmetry of the flow $\partial W(0.5)/\partial y=0$.

Finally

$$U = [W(y)\ e^{i\omega_o t} + W^*(y)\ e^{-i\omega_o t}]/2$$

$$= W_r(y)\cos(\omega_o t) - W_i(y)\sin(\omega_o t) \qquad (6.5)$$

where,

$$W(y) = A1\frac{[e^{2\gamma y} - e^{-2\gamma y} + e^{2\gamma(1-y)} - e^{-2\gamma(1-y)}]}{[e^{2\gamma} + e^{-2\gamma}]} - 1$$

and $A1=hA/\nu U_o$

The zero of the pressure gradient does not coincide with the zero of the mean velocity. For sinusoidal pressure whose zero is at $\omega_o t=0^\circ$, the zero of the velocity occurs at the phase angle $\theta(y)$ the value of which determines the phase lag of the velocity behind the pressure gradient. From (6.5), $U=0$ occurs at $\omega_o t=\theta(y)$ given by

$$\theta(y)=\arctan(W_r(y)/W_i(y)) \qquad (6.6)$$

From (6.5) and (6.6), it can be verified that for large values of the frequency parameter β at the centre of the channel , $W_r(0.5)=-1$ and $W_i(0.5)=0$ in which case $\theta(y)=90^\circ$ the maximum possible phase lag behind the pressure

gradient. The phase lags calculated from (6.6) are larger than their equivalents in the case of time-dependent flow in a circular pipe [see Uchida (1956)].

It can be verified that the phase lag of the velocity near the wall is much smaller than that of the velocity at the centre. The direct consequence of this is the generation of inflexion points which would not have occurred if the phase lag across the channel did not vary. From (6.5) the complex mean velocity amplitude is given by

$$\tilde{W}_o = A1(2/\gamma)\left\{\frac{e^{2\gamma} + e^{-2\gamma} - 2}{e^{2\gamma} - e^{-2\gamma}}\right\} - 1 \qquad (6.7)$$

The phase lag of the mean velocity is

$$\theta_o = \arctan(\tilde{W}_{o_r}/\tilde{W}_{o_i}) \qquad (6.8)$$

where $\tilde{W}_{o_r}$ and $\tilde{W}_{o_i}$ are the real and the imaginary parts of $\tilde{W}_o$ respectively. θ_o is less than but close to the lag $\theta(0.5)$ at the centre. The mean velocity phase lag θ_o tends to 90° at β about 100.

In order to remove the dependence of the velocity distribution (6.4) and (6.5) on the pressure amplitude, normalisation was carried out by the complex mean velocity (6.7). This normalisation, besides facilitating easier comparison between profiles of different values of β, also equates the phase lag θ_o to exactly 90°.

On assuming a cosine pressure gradient

$$-\partial P/\partial x = A\cos(\omega_o t) \qquad (6.9)$$

for all values of β, profiles with $\omega_o t = 0^\circ$ will have zero mean velocity.

Substituting (6.7) into (6.5), the velocity distribution is then given by

$$U/W_o = \text{Real}(W(y)e^{i\omega_o t}/\tilde{W}_o) \qquad (6.10)$$

The only disadvantage of this normalisation is that the phase and group velocities and the disturbance frequency are normalised by W_o.

6.3: The Velocity Profiles At Different Values Of β

Velocity profiles at certain phase angles $\omega_o t$ for $\beta=1$, $\beta=6$ and $\beta=12$ are shown in figures 6.1, 6.2 and 6.3 respectively. These are representative of profiles which occur in time-dependent flow

For $\beta=1$ the profiles with inflexion points are confined to $-5^\circ \leqslant \omega_o t \leqslant 5^\circ$. Whilst profiles with inflexion points are known to be unstable (chapter 4), the profiles which do not possess inflexion points are highly stable. An extensive search for instability in these profiles using the Orr-Sommerfeld equation has failed for all $0 \leqslant Re \leqslant 35000$ and wavenumber $0 \leqslant \alpha \leqslant 15$. This examination has been carried out for a wide range of $\omega_o t$ for $\beta=1$, 2 and 3 when there is no inflexion point. Thus the only unstable time-dependent flow profiles are those having inflexion points.

Figure 6.2 for $\beta=6$ and figure 6.3 for $\beta=12$ show that all profiles contain inflexion points and some of those of $\beta=12$ have more than one inflexion point. In chapter 4 we classified the inflexion points into two types. Those near the wall where the shear is the strongest, we called wall inflexion points. Those confined between the maximum velocity and the centre of the channel we called core inflexion points. The wall inflexion points are usually inside the Stokes length $\delta=(2\nu/\omega_o)^{1/2}$ except after the point of flow reversal near the wall about $\omega_o t=150^\circ$. Core inflexion point are always outside the Stokes length. The core inflexion points dominate the acceleration phase, while the wall inflexion points come into being in the deceleration phase until they finally convert to core inflexion points when the flow starts to reverse near the wall. From the results of chapter 4, the most unstable are the core inflexion points at $\omega_o t=0^\circ$. In the acceleration phase, the core inflexion points become more stable as $\omega_o t$ increases and continue so during the deceleration phase, whilst in the deceleration phase the wall inflexion points start very stable and become more unstable as the the phase progresses (figure 6.11). In other words the acceleration phase becomes more stable when it ends, while the deceleration phase ends more unstable than when it begun. This apparent contradiction to the experimental observations will be clarified later.

Near the wall the velocity changes very slowly inside the Stokes layer for most of the acceleration phase, the situation in which the damping effect of the acceleration will be minimal (figures 6.2 and 6.3). This conclusion is supported by the observation mentioned in chapter 5, that the area near the wall, when unstable, continues so during the whole cycle (i.e. no transient instability).

6.4: The Instability Criterion

It is well established that for steady flow in the range of decreasing pressure (accelerated flow), the boundary layer remains laminar, whereas a very small pressure increase (decelerated flow) almost always brings transition with it [Schlichting (1968)]. These facts generally agree with the observations in time-dependent flow. The experiments of chapter 5 supported the fact found by other authors that in most of the acceleration phase the flow is stable, while the early part of the deceleration phase is always unstable at high Re and possibly the last part of it depending on the amount of deceleration. In steady flow the adverse pressure gradient is responsible in producing profiles with inflexion points (wall inflexion points). In contrast, the acceleration phase of the time-dependent flow (favourable pressure gradient) also contains inflexion points (which we called core inflexion points), which do not exist in the case of slender bodies.

However, as already mentioned, the profiles in the acceleration phase according to the linearised theory are highly unstable for small values of $\omega_0 t$ and the critical Reynolds numbers increase as the acceleration phase progresses (figure 6.11). Nevertheless, since the the whole phase can be considered stable according to experimental observations, the inhibition of the growth of the disturbance is an established fact especially when the acceleration of the flow is large. The large increase in the kinetic energy of the mean flow will be far greater than the loss of the energy of the mean flow to disturbances, since the last will be very small in comparison. In other words, whether the disturbances grow or decay, their effect will be minimal when the mean flow acceleration is large except maybe near the wall where the flow is almost steady. It appears that the large loss of the kinetic energy of the flow also reduces the efficiency of the extraction of energy by the disturbance from the flow. This point is supported by the experimental observations in the last chapter where fast growth of the disturbance occurred whenever there was a small duration of steadiness whether in the acceleration or in the deceleration phases.

Accordingly, the instability of the velocity profiles at the maximum velocity is the one which will be crucial. To be precise, the profile concerned is that whose inflexion point velocity is the maximum. From the equation

$$\partial U/\partial t = -\partial P/\partial x + \nu\, \partial^2 U/\partial y^2 \qquad (6.1)$$

it follows that the inflexion point ($U''=0$) has a maximum velocity ($\partial U/\partial t=0$) only if the pressure gradient $-\partial P/\partial x=0$.

This criterion is similar to the criterion of instability on slender bodies where the point of instability coincides with the point of minimum pressure [Schlichting (1968)].

The zero of the pressure gradient in (6.1) also coincides with the beginning of the appearance of wall inflexion points in the deceleration phase. However, the critical Reynolds numbers of these points in their early stages (close to the wall) are usually considerably higher than the critical Reynolds numbers of core inflexion points. They become more unstable as ωt increases.

From the velocity profiles at different values of β, it is found that for $\beta \geq 4$, the profiles with maximum velocity contain inflexion points. For $\beta<4$, these profiles do not possess inflexion points in which case the instability of the flow when $\beta<4$ is not deteremined completely by the instability of these profiles since these are highly stable. The question will be raised again later in section 6.10.

6.5: The Numerical Procedure

The same numerical procedure described in section 3.2 was used for solving the Orr-Sommerfeld equation. The number of terms in the expansion N=30 was considered to be

sufficient. The results were made more accurate using the finite difference method described in section 3.3. With a step size of 0.01, accuracy to 7 significant figures was achieved.

Special routines have been written in order to calculate the critical Re in one run. For a chosen Reynolds number, the wavenumber α at which the maximum amplification (or damping) rate occurs (i.e. $\partial\omega_i/\partial\alpha=0$), was determined first. The Newton-Raphson method was then used to iterate along the maximum amplification rate line, every time determining α and Re, until the critical point at which $\omega_i=\partial\omega_i/\partial\alpha=0$ is found. The method is successful for $\beta\leq 12$, because the least stable eigenvalue is well spaced from the damped eigenvalues. The time required to find the critical Re,(Re_c), starting from some $Re>Re_c$, is on average about 30 seconds. For $\beta>12$ however, the procedure sometimes fails due to the convergence of the eigenvalue routine to one of the damped eigenvalues, thus making the process tedious. For $\beta>17$, the procedure fails completely, in which case a similar procedure is used where the LR algorithm provides the eigenvalues. In this case, it is always possible to select the least stable eigenvalue from amongst the eigenvalues provided by the LR algorithm every time it is required until the critical values are found. The computational time in this case is considerable. Since for the same matrix order, the accuracy of the eigenvalues decreases as Re increases, the results for $\beta>17$ are slightly inaccurate.

6.6: The Major Instability Of Sinusoidal Flow with $\beta \geq 6$

The points of the instability satisfying the criterion $-\partial P/\partial x=0$ and whose phase angle $\omega_0 t=\theta_i$ were determined. Table 6.1 lists, among others, both the critical Re and $R\delta$ in addition to the critical wavenumber α. The error in α is one part in 10^5 and in Re is in the third decimal place. The error is larger by one order of magnitude for $\beta>12$. The values given for $\beta=18,19,20$ are less accurate than the others since they have been determined using the LR algorithm with a matrix of order 35 only.

The values of the critical Re are very large for large β in comparison with those for small β. However, the change in the critical $R\delta$ is becoming small as β increases above 10 due to the fact that $R\delta=(Re\ \delta)/d$, and δ decrease as β increases.

In figure 6.4, the critical $R\delta$ are plotted against the frequency parameter β. On the same figure the experimental data obtained by various authors is also shown. Those values given by Hino et al (1976) and by Sergeev (1966) are averaged values of $R\delta$ for a wide range of β, some of which are inside the range of the theoretical calculations. The results of Merkli and Thomann (1975) were obtained for $40 \leqslant \beta \leqslant 73$. On the same figure, the experimental data obtained by the author for small values of β are also plotted. These show a very good agreement with the theoretical values, which indicates that averaging of the critical $R\delta$ is inappropriate for small values of β.

TABLE 6.1

The major instability critical parameters

($6 \leq \beta \leq 20$)

β	θ_i	α_c	Re_c	$R\delta_c$	δ	θ_o
6	97.609	7.1182	3419.603	403.004	0.11785	82.391
7	96.412	5.9593	3003.060	303.355	0.10102	83.588
8	95.538	5.5413	4443.390	392.744	0.08830	84.462
9	94.874	6.2596	5838.160	458.690	0.07857	85.126
10	94.351	6.2596	6872.211	485.940	0.07071	85.650
11	93.930	6.7948	7845.508	504.328	0.06430	86.070
12	93.583	7.3974	8788.616	517.874	0.05890	86.417
13	93.292	8.0421	9683.945	526.737	0.05050	86.708
14	93.045	8.6997	10540.602	532.381	0.05050	86.966
15	92.832	9.3561	11373.062	536.131	0.04710	87.168
16	92.641	10.0072	12121.072	538.845	0.04420	87.350
17	92.485	10.6164	12984.599	540.160	0.04160	87.515
18	92.342	11.2860	13762.593	540.650	0.03926	87.658
19	92.214	11.9229	14546.135	541.407	0.03722	87.786
20	92.099	12.5636	15367.200	542.000	0.03536	87.901

θ_i = The phase $\omega_o t$ (in degrees) at which $-\partial P/\partial x=0$

α_c = The critical wavenumber

Re_c = The critical Reynolds number

$R\delta_c$ = The critical Reynolds number based on the Stokes length δ

θ_o = The phase lag of the mean velocity behind the pressure gradient.

Figure 6.5 shows the relation between Re and β and between Re and $R\delta$. It can be seen that the relation between Re and β can be represented by several straight lines A,B,C, and D (more for $\beta>20$). They differ in the value of their slope with D having the largest. The existence of these different slopes was found to be strongly connected with the number of core inflexion points in the velocity profile at the particular β and θ_i for which the critical Re has been calculated. For each of the values $\beta=10$, $\beta=14$ and $\beta=18$, the number of core inflexion points of the profile with $\omega_o t=\theta_i$ increases by one over the previous values of β. It can be noticed that the difference between the slopes becomes smaller as β increases. Over the range D, the critical Re was found to be given to a good accuracy by

$$Re = \alpha W_o 1274.2 \qquad (6.11)$$

where W_o is the mean velocity at $\omega_o t=90^\circ$. For the ranges A,B, and C, similar relations give only approximate values.

The critical wavenumbers for the profiles with $\omega_o t=\theta_i$ fall into two groups according to the value of the factor K_c (section 4.5). For $\beta \leq 10$, where the profiles have only one core inflexion point, the critical wavenumber is given by

$$\alpha_c = 2\pi / 4L \qquad (6.12\ a)$$

For $\beta>10$, where the number of core inflexion points is more than one,

$$\alpha_c = 2\pi / 4.5\, L \qquad (6.12\ b)$$

where L is the distance between the two points where $U'=0$ on both sides of the inflexion point. The values of α_c calculated from the Orr-Sommerfeld equation and those from (6.12) are listed in table 6.2. The maximum relative error in estimating the critical wavenumbers using (6.12) is about two percent. This accuracy is better than that obtained by some numerical procedures used in solving the Orr-Sommerfeld equation.

In figure 6.6, α_c is plotted against β, and there is a fairly accurate linear relation between the two for $\beta \geqslant 11$, i.e. in the range where (6.12 b) holds. Application of (6.12 b) to different values of $\beta \leqslant 60$ led to an exact expression for α_c which is

$$\alpha_c = 0.628539776 \times \beta \qquad (6.12\ c)$$

$$\text{for } 11 \leqslant \beta < \infty$$

The advantage of this formula is that it is completely independent of any parameter directly related to the velocity profile. This indicates that for all values of $\beta \geqslant 11$, all profiles with equal phase difference from θ_i will have relations similar to (6.12 c).

TABLE 6.2

Comparison between the critical wavenumbers α_c calculated from the Orr-Sommerfeld equation and those calculated from equation (6.12 a) for $\beta \leq 10$ and from (6.12 b) for $\beta \geq 11$

β	α_c	L	α_c (6.12)
6	7.11817	0.2238855	7.01607
7	5.95927	0.2624868	5.98429
8	5.54126	0.2917035	5.38500
9	5.78413	0.2761700	5.68779
10	6.25950	0.2221285	6.28584
11	6.79480	0.2012985	6.93628
12	7.39737	0.1850759	7.54428
13	8.04205	0.1709102	8.16957
14	8.69970	0.1586787	8.79931
15	9.35610	0.1480949	9.42817
16	10.00715	0.1388396	10.05667
17	10.61640	0.1306729	10.59292
18	11.28500	0.1234130	11.31375
19	11.92290	0.1169170	11.94235
20	12.56360	0.1110720	12.57098

Figure 6.6 also shows the relation between β and the frequency $\omega_c=\alpha_c c_r$. Again, a linear relation exists between the two for $\beta \geq 11$. The relation of β vs f is also shown in figure 6.6 [$f=c_r U_o/\lambda_c$, where λ_c is the critical wavelength]. As was the case with β vs Re, this relation can also be represented by several straight lines. The lines in figure 6.6 begin and end at the same values of β as in figure 6.5. The most important consequence of this relation is the continuous increase in the frequency as the frequency parameter β increases. In other words, the point at which the mean flow frequency ω_o will be equal to the disturbance angular frequency ωU_o will never exist however large β may be. This conclusion is also supported by (6.12 c) from which it follows that $\alpha_c \rightarrow \infty$ as $\beta \rightarrow \infty$, i.e. the wavelength $\lambda_c \rightarrow 0$ and as a result $f=(c_r U_o/\lambda_c) \rightarrow \infty$ as $\beta \rightarrow \infty$. The flow therefore, is highly susceptible to high-pitch audio frequencies at high β. The normalised frequency ω, however, will be equal to the mean oscillation frequency $\omega_o=4\beta\nu$ at $\beta=17$ ($\omega_o=11.6$). For $6 \leq \beta \leq 20$, i.e. in the range calculated, the ratio ω/ω_o ranges between 100 and 129. For $\beta \geq 17$ this ratio is almost constant at 129. From this ratio, a good estimate to the critical Re can be obtained. Since U is normalised by W_o, so also will c_r, f and ω be normalised by W_o. Writing $c_r=c_r/W_o$, the critical Re is given by

$$Re=129\ \omega_o/[(c_r/W_o)\nu\alpha_c] \qquad (6.13\ a)$$

For large values of β, $c_r/W_o \rightarrow 1.0346$ while $W_o \rightarrow 1$, in

which case

$$Re = (129\ \omega_o)/(1.0346\ \nu\ c_r) = 793.4955\ \beta \qquad (6.13\ b)$$

for $\beta > 100$

It was estimated that at $\beta=100$, W_o is very close to 1. The formula still gives good estimates at low β, if it is multiplied by the corresponding value of W_o. In this case

$$Re = 796.4955\ W_o\ \beta \qquad (6.13\ c)$$

From (6.13 c) a fairly accurate estimate could also be obtained for $R\delta$, remembering that $\delta = 0.7071068/\beta$. Thus

$$R\delta = Re\ \delta = 563.207\ W_o \qquad (6.13\ d)$$

This formula is independent of β and shows that the asymptote to the critical $R\delta$ is 563.207.

The fact that the critical $R\delta$ will not be greater than 563 is interesting. There is some experimental evidence that the critical $R\delta$ for this major instability will not be smaller than about 300 (chapter 5). It is interesting to notice that the value of $R\delta=563$ coincides almost exactly with $R\delta=565$ for the Stokes layer on a smooth bed measured by Li (1954). It also coincides exactly with the critical $R\delta=563$ for the Stokes layer profile chosen by Collins (1963) and recalculated by Kerczek and Davis (1972). It was noticed in chapter 5 that the critical Reynolds number for transition in the Stokes layer, if not equal is not smaller than that of the pipe oscillatory

flow. Evidently, they are close to each other. The modified Stokes layer (the wave boundary layer) is less stable.

Nerem et al (1972), from in vivo experimental measurements, found the critical Re for small values of β to be

$$Re = \text{constant } \beta$$

where the constant ranges between 250 and 1000. For the descending thoracic aorta, the same formula was given as

$$Re = 250\ \beta$$

From our results for the same range of β, $Re = 800\ \beta$. In other words, the in vivo blood flow is more unstable than the pipe flow. Ohmi and Iguchi (1982) gave a similar theoretical relation for $\beta \geq 7$, i.e.

$$Re = 882\ \beta$$

This relation is based on assumptions and a method completely different from the one used here. These are:

(a) Due to the fact that the instantaneous friction factor where the turbulence appears follows the 1/7 power law and the Blasius' friction law, they used both of them to derive a formula for the critical Re for time-dependent flow in a pipe.

(b) Thus, they assumed that the mechanism of generating turbulence in oscillatory flow is similar to that in steady flow, and hence they assumed that the generation region of turbulence is the same as that in the steady flow.

Assumption (b) cannot be rejected, since (a) suggests that this is the case. Moreover, Hino et al (1983) reached conclusions similar to (a) in a duct. In this study, the instability of the flow was considered entirely due to the instability of the profile at the phase with $-\partial P/\partial x=0$, and that will bring the instability to the whole flow. Since the wall region is more susceptible to disturbances, the two definitions of the region of instability do not differ except that ours may be slightly earlier.

Table 6.3 lists the critical c_r, the velocity at the inflexion point Ui(y), the frequency f and $\partial\omega/\partial\alpha$ at the points of instability. As can be seen, the difference between c_r and Ui is very small compared to the large difference associated with other profiles for which Re critical is small. The difference increases until $\beta=14$, and then falls to an almost constant value of 0.00885 for $\beta \geq 15$. It was mentioned in chapter 4 that the group velocity $\partial\omega/\partial\alpha$ is very close to the mean velocity. The profiles of $\beta>10$ have a mean velocity very close to the velocity Ui at the inflexion point. Since the last is also very close to the phase velocity, the group velocity can be considered equal to the phase velocity at the critical point and at the most amplified frequency. This leads to a useful simplification in the calculation of the spatial amplification

$$\alpha_i = -\omega_i/(\partial\omega_r/\partial\alpha) = -\omega_i/c_r \qquad (6.14)$$

TABLE 6.3

The critical phase velocities and frequencies

β	c_r	U_i	f	$\partial\omega/\partial\alpha$	W_o
6	1.172980	1.725610	40.6	1.1525	0.88992
7	1.121239	1.151435	32.8	1.1213	0.90464
8	1.132277	1.138816	44.5	1.1093	0.91590
9	1.128157	1.128157	60.6	1.1019	0.92478
10	1.111693	1.119376	76.4	1.0952	0.93198
11	1.104115	1.112256	94.1	1.0897	0.93800
12	1.109791	1.106368	114.1	1.0821	0.94300
13	1.092729	1.101401	135.4	1.0810	0.94720
14	1.088368	1.097149	159.5	1.0774	0.95084
15	1.084629	1.093484	184.4	1.0741	0.95400
16	1.081396	1.090285	210.8	1.0712	0.95680
17	1.078586	1.087467	236.6	1.0695	0.95930
18	1.076059	1.084964	267.1	1.0673	0.96152
19	1.073844	1.082730	297.6	1.0660	0.96350
20	1.071869	1.080000	340.0	1.0620	0.96530

W_o= The mean velocity at $\omega_o t=90^\circ$

c_r= The phase velocity of the disturbance

U_i= The velocity at the inflexion point

f= The frequency of the disturbance

$\partial\omega/\partial\alpha$ = The group velocity ($\partial\omega_i/\partial\alpha=0$)

U_i, c_r, f and $\partial\omega/\partial\alpha$ are all normalised by W_o.

This is usually called the Gaster relation (1962) and can be used only for small ω_i. The full relation is given by Nayfeh and Padhye (1979).

At the end of chapter five, the experimentally observed wavenumbers and frequencies for $\beta=5$ and $\beta=7$ were given. For $\beta=7$, $\alpha=4.5$ and $f=40$ Hz. From tables 6.2 and 6.3, the corresponding theoretical values are $\alpha=5.96$ and $f=33$ Hz. In order to bring these values in line with the experimental values above, normalisation by the pipe diameter is necessary. This amounts to multiplication of both the wavenumber and the frequency by 0.8. Thus $\alpha=4.77$, which is very close to the experimental value of 4.5 given above. Taking the experimental Re=3960 into consideration, it is easy to show that $f=43$ Hz which is also in good agreement with the experimental value given above. It is clear that the transition parameters of the circular pipe time-dependent flow are very close to the theoretical parameters of the channel time-dependent flow.

6.7: The Neutral Stability Curve

To get a more comprehensive view about the stability of the profiles considered, the neutral stability curve for the profile with $\theta_i=92.538^\circ$ and $\beta=8$ has been calculated. Experimental verification is not as straight forward as in the case of steady flows, since the profile concerned exists only for a short period of time. The curve is shown in figure 6.7, while the data of the curve is given in

tables 6.4 and 6.5. The wavenumbers covered by the unstable region is very large for large Re. On the lower branch, the phase velocity is approaching the maximum velocity in the channel of 1.1651355, while on the upper branch it is slightly smaller than the inflexion point velocity Ui=1.138816.

The values of $\partial\omega/\partial\alpha$ have a small relative change and on both branches its value approaches Ui as Re -> ∞. From table 6.5 we notice that the phase velocity c_r -> Ui as Re -> ∞. At the same time, $\partial\omega_r/\partial\alpha$ does not change much as Re increases $[(\partial\omega_i/\partial\alpha)=0]$. However, the value of

$$\partial c_r/\partial\alpha=[(\partial\omega_r/(\alpha\partial\alpha))-c_r/\alpha] \rightarrow 0$$

as Re -> ∞ which means that $(\partial\omega_r/\partial\alpha) \rightarrow Ui$ as Re -> ∞.

The neutral stability curve shown is much wider than the one inside which wavepackets amplify. In this respect, it appears that this is the general trend, since the calculations of Itoh (1979) for plane Poiseuille and Blasius flows showed that the wavepackets neutral curve is far narrower than that for sinusoidal disturbances. {The author's calculations, which are not presented in this thesis, have shown the same behaviour for several profiles with inflexion points}. The frequency with the maximum amplification for wavepackets is the same as that of the sinusoidal disturbance.

TABLE 6.4

The neutral stability curve parameters

(β=8, ω_{ot}=95.538°)

Re	α	c_r	$\partial\omega/\partial\alpha$	
12000.0	9.90782	1.1304166	1.130800	-0.017189
11000.0	8.99830	1.1293804	1.128816	-0.016009
10000.0	8.88510	1.1290632	1.127728	-0.015496
9000.0	8.73110	1.1287137	1.126327	-0.014861
8000.0	8.51830	1.1283447	1.124501	-0.014025
7000.0	8.21510	1.1279983	1.122080	-0.012829
6000.0	7.25660	1.1278125	1.118774	-0.010907
5500.0	7.42250	1.1279144	1.116627	-0.009399
5000.0	6.94640	1.1283995	1.113975	-0.007120
4500.0	5.99670	1.1306006	1.110246	-0.002308
4443.4	5.54130	1.1322767	1.109073	0.000000
4500.0	5.08950	1.1343640	1.109073	0.002199
5000.0	4.20630	1.1397203	1.111048	0.005841
5500.0	3.77760	1.1429302	1.113502	0.007117
6000.0	3.47640	1.1454095	1.115951	0.007747
7000.0	3.05240	1.1491728	1.120547	0.008192
8000.0	2.75390	1.1519749	1.124653	0.008168
9000.0	2.52550	1.1541739	1.128291	0.007960
10000.0	2.25670	1.1584748	1.133270	0.007989
11000.0	2.11020	1.1599884	1.136258	0.007754
12000.0	1.98540	1.1612668	1.138919	0.007325

TABLE 6.5

The temporal maximum amplification parameters

(β=8, ω_{ot}=95.538°)

Re	α	c_r	c_i	ω_i	$\partial\omega/\partial\alpha$
4443.4	5.5413	1.1322767	0.000000	0.000000	1.109319
4500.0	5.5344	1.1329075	0.003644	0.002017	1.109567
5000.0	5.6096	1.1329807	0.001123	0.006301	1.110661
5500.0	5.6612	1.1329807	0.001762	0.010000	1.111519
6000.0	5.6979	1.1330983	0.002310	0.013160	1.112310
7000.0	5.7376	1.1333913	0.003201	0.018370	1.113616
8000.0	5.7538	1.1337080	0.003900	0.022440	1.114629
9000.0	5.7562	1.1340199	0.004465	0.025700	1.115445
10000.0	5.7503	1.1343167	0.004931	0.028356	1.116111
11000.0	5.7396	1.1345950	0.005324	0.030548	1.116663
12000.0	5.7259	1.1348541	0.005660	0.032410	1.117127

6.8: The Minor Instability Of Time-Dependent Flow

At Reynolds number of about 1200, it has been found that the flow starts to distort from its laminar shape. This phenomenon has been observed by Hino et al (1976) and Tromans (1976). It will be referred to as the minor instability. The critical Reynolds number appeared to be constant over the range investigated by the author {$3.3 \leqslant \beta \leqslant 8$, table 5.1 and fig. 5.5}, in contrast to high Reynolds numbers transition to turbulence. At low Reynolds numbers the damping effect of the acceleration on the disturbances is expected to be smaller due to less stress and the low value of the increase in the kinetic energy of the main flow. In the case of slow modulations, this makes the flow closer to the steady flow state. There are two reasons to expect the instability at low Re to arise from low velocity phases:

1) The low frequency of the disturbances generated by the instability of the profiles at the early stages of the acceleration phase.
2) The low critical Reynolds numbers of the profiles with small value of $\omega_0 t$.

Putting these together, we have convincing reasons to expect that this minor instability is the result of the instability of the profiles in the region of zero mean velocity, i.e. with $\omega_0 t \backsim 0$. However, there is one

important condition for the disturbances from such phases to show their effect on the flow, namely the frequency of these disturbances, $\omega=\alpha c_r U_o$, has to be several times larger than the frequency of the mean flow ω_o, i.e. $(\omega/\omega_o)>1$. ($U_o=Re/100$).

To test the validity of these assumptions, the critical Re has been calculated for profiles at $\omega_o t=0^\circ$ for several values of β. From previous calculations we know that the profiles at $\omega_o t=0^\circ$ can be considered the most unstable ones. (For some values of β, $0\leqslant\omega_o t\leqslant 10^\circ$ have slightly less critical $R\delta$). Therefore, the critical Re calculated represents approximately the minimum possible value for any unstable profile in the whole flow. Comparing the values presented in table 6.6 with those given in table 5.1 for $2\leqslant\beta\leqslant 6$, the theoretical $R\delta$ are about three times smaller. The experimental value for $\beta=5.1$ is $R\delta=180$, while Hino et al (1976) found $R\delta=180$ for $\beta=5.52$. Tromans (1976) put a lower limit of $R\delta=130$ for large β, while the author measured $R\delta=110$ for $\beta=8$. From table 6.6, the calculated $R\delta$ approaches an asymptotic value of 90 as $\beta \rightarrow \infty$. This value is not far from the experimental values for $\beta=8$. It can be seen that the values of ω/ω_o are small enough for disturbance to have a noticeable effect on the flow. From the results of chapter 4 for $\beta=6$ and $\omega_o t=60^\circ$, the critical $R\delta=145$ which is in good agreement with the experimental value of 151 for $\beta=6.2$. The corresponding theoretical $(\omega/\omega_o)=40$, i.e. ten waveforms per quarter of the flow wave. This frequency is in good agreement with the

frequency of disturbances shown in figure 4 of Hino et al (1976). It is evident that in order for the condition $(\omega/\omega_o) >> 1$ to be satisfied, the Reynolds number should be high enough to cause the instability of some profiles with $\omega_o t > 0°$. In other words, the Reynolds numbers presented in table 6.6 are about the least possible.

TABLE 6.6

The minor instability critical parameters

β	α	Re	Rδ	c_r	ω/ω_o	$\partial\omega/\partial\alpha$
1	4.1378	2299.525	1626.020	0.0038941	0.400	-0.013536
2	4.1289	602.937	96.830	0.0151950	2.550	-0.051930
3	4.0911	325.753	76.780	0.0312094	0.413	-0.098561
4	4.0002	291.306	51.500	0.0480209	0.871	-0.116832
5	3.9460	399.950	56.560	0.0692287	1.089	-0.082158
6	4.2617	577.678	68.080	0.0888323	1.519	-0.030039
7	4.8839	726.639	73.405	0.1000550	1.802	0.004084
8	5.4854	860.201	75.956	0.1073992	1.970	0.026364
9	6.1740	991.500	77.902	0.1131907	2.128	0.042905
10	6.8950	1119.439	79.156	0.1181066	2.268	0.055143

An interesting phenomenon can be noticed from the values of c_r and $\partial\omega/\partial\alpha$ in table 6.6. Whilst the phase velocity is always positive for these profiles with $\omega_0 t=0^\circ$, the group velocity $\partial\omega_r/\partial\alpha$ has negative values for $\beta<6$ and positive values (apparently) for all $\beta\geq 7$. Whilst sinusoidal disturbances travel in the direction of increasing velocity, wavepackets travel in the opposite direction of the main flow. This is apparently due to the fact that the core of the flow has a negative velocity. At which $R\delta$, $\partial\omega/\partial\alpha$ becomes positive has not fully been investigated. It is not obvious also that $\partial\omega/\partial\alpha$ will be equal or close to c_r for $\beta>10$, the situation which as already mentioned is always satisfied for profiles at $\omega_0 t=\theta_i$ for all values of β.

There is one more point to notice, namely that the critical $R\delta$ for $\beta=1$ and $\beta=2$ are far higher than those of $\beta\geq 3$ for the same $\omega_0 t=0^\circ$. This may also be the case for the major instability since Hino et al (1976) did not detect any major instability at $\beta<2$ and $R\delta<1000$.

6.9: The Eigenfunctions Of The Disturbances

The disturbances at the critical point for $\beta=6$, $\beta=8$ and $\beta=14$ are shown in figures 6.8, 6.9 and 6.10 respectively. There are several interesting features associated with both the x and y-direction disturbance amplitudes u(y) and v(y). Detailed discussions will be presented in chapter 7. Another interesting feature is that the pressure amplitude p(y) starting from the wall remains constant even where

u(y) and v(y) are very small, until about the position of the inflexion point where it starts to follow closely the behaviour of u(y).

Due to the fact that v(y) is small compared to u(y), the vorticity amplitude r(y) is determined by -du(y)/dy. This produces a pair of strong vortices filling most of the flow. They are similar to the large scale structures of jets, mixing layers and wakes which are known to be strong and persistent. However, what will happen to these as they propagate in time remains to be studied carefully.

Large vortex systems have been observed by several investigators. Merkli and Thomann (1976) observed large vortices just before transition and these fade away at the onset of turbulence. The plates in their paper show clearly that these appear as vortex rings. They were tempted to suggest the possibility that these vortices may have been produced by waviness in the tube wall. It is known that the disturbances in the pipe unlike those in the channel are symmetrical and in a circular pipe these show as vortex rings. Despite this difference the position at which these vortices occur suggest that they originate from the instability (see figures 6.8,9 and 10). For large β, i.e. the situation considered in the experiments just mentioned, δ is very small and the vortices move towards the wall as can be found by comparing figure 6.8 with figure 6.10. Other investigators have also observed vortex systems. Tromans (1976) observed such vortices in a

circular pipe. Pelissier and Clarion (1975) observed similar vortices in free surface flow. More detailed observations were made by Hino et al (1983) for the flow in a duct. The large eddies were observed at different stages of the flow whose $\beta=18.1$. During the acceleration phase, the eddies appear and disappear several times. In the final stages of the turbulent deceleration phase ($\omega_0 t \backsim 145^\circ$), they observed that the whole region is covered by large eddies which are not accompanied by high frequency turbulence.

6.10: The Major Instability For $\beta<6$

Nothing has been said so far about the instability of time-dependent flows when $\beta<6$. This is because they represent a special problem. From the experimental data of chapter 5 the flow is also unstable except possibly for $\beta<2$ at very high $R\delta$ [Hino et al (1976)]. It was soon discovered that applying the criterion already applied in the case of $\beta \geqslant 6$ will not fit with the experimental data. The calculations performed for $\beta=5$ and $\theta_i=99.331^\circ$ produced a critical $R\delta \backsim 2300$ which is about six times higher than the experimental value of $R\delta=420$. For $\beta=4$ and $\theta_i=102.076^\circ$, the critical $R\delta$ is far higher than that for $\beta=5$. The situation is even worse for $\beta=3$, since as mentioned in section 6.3, the profile at $-\partial P/\partial x=0$ has no inflexion point and thus it is highly stable.

In conclusion the disagreement is complete between the criterion for $\beta \geq 6$ and the experimental values for $\beta < 6$. The Ohmi and Iguchi (1982) method discussed earlier was more successful in this range of β. However, faced with choosing a characteristic length for their calculations, they used the diameter of the pipe for $\beta \leq 5.026$ due to the fact that there is no other velocity maximum than in the centre for this range. This gave a constant Re=1800. In other words, the difficulty they faced is the same as in the linear stability case, i.e. there is no profile with a core inflexion point. The value 1800 may be considered as a lower limit as can be seen from table 5.2 and figure 6.4. There is a gap in their results between this value and that for $\beta \geq 7$.

Obviously some mechanism is responsible for transition in this case. The possibility that the instability occurs as a result of secondary instability remains the likely one. Velocity traces presented in chapter 5 and those in the paper by Hino et al (1976) show the occurrence of transition when the low frequency disturbances arising from the minor instability persist to the peak of the velocity. The magnitude of the amplitude of the primary oscillation which causes secondary instability remains to be investigated. It is obvious that for slow modulation, i.e. $\beta < 6$, disturbances can survive the increase in the kinetic energy of the mean flow.

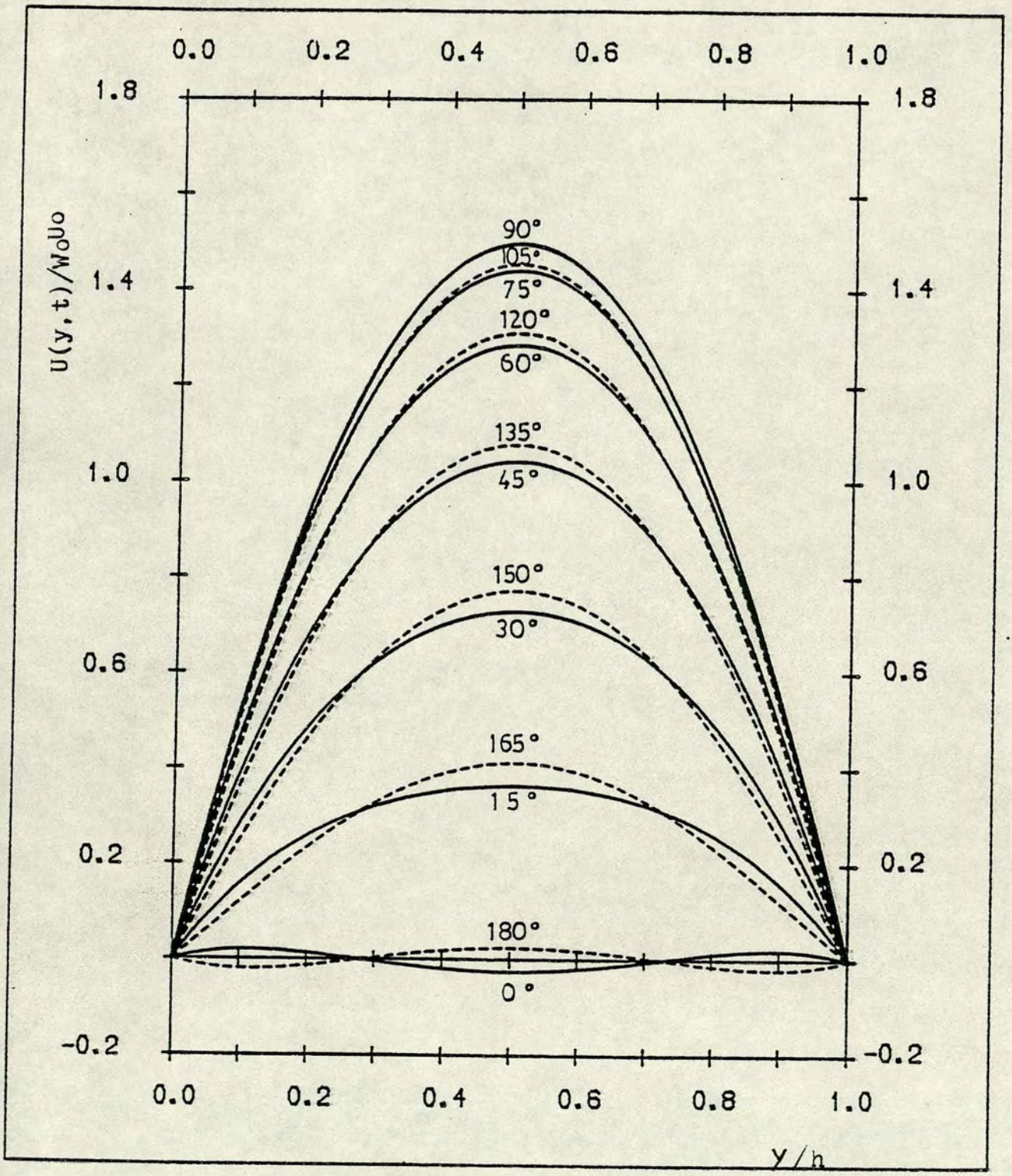

Fifure 6.1: Velocity profiles of time-dependent plane Poiseuille flow with zero mean at different phase angles. $\beta=1$.

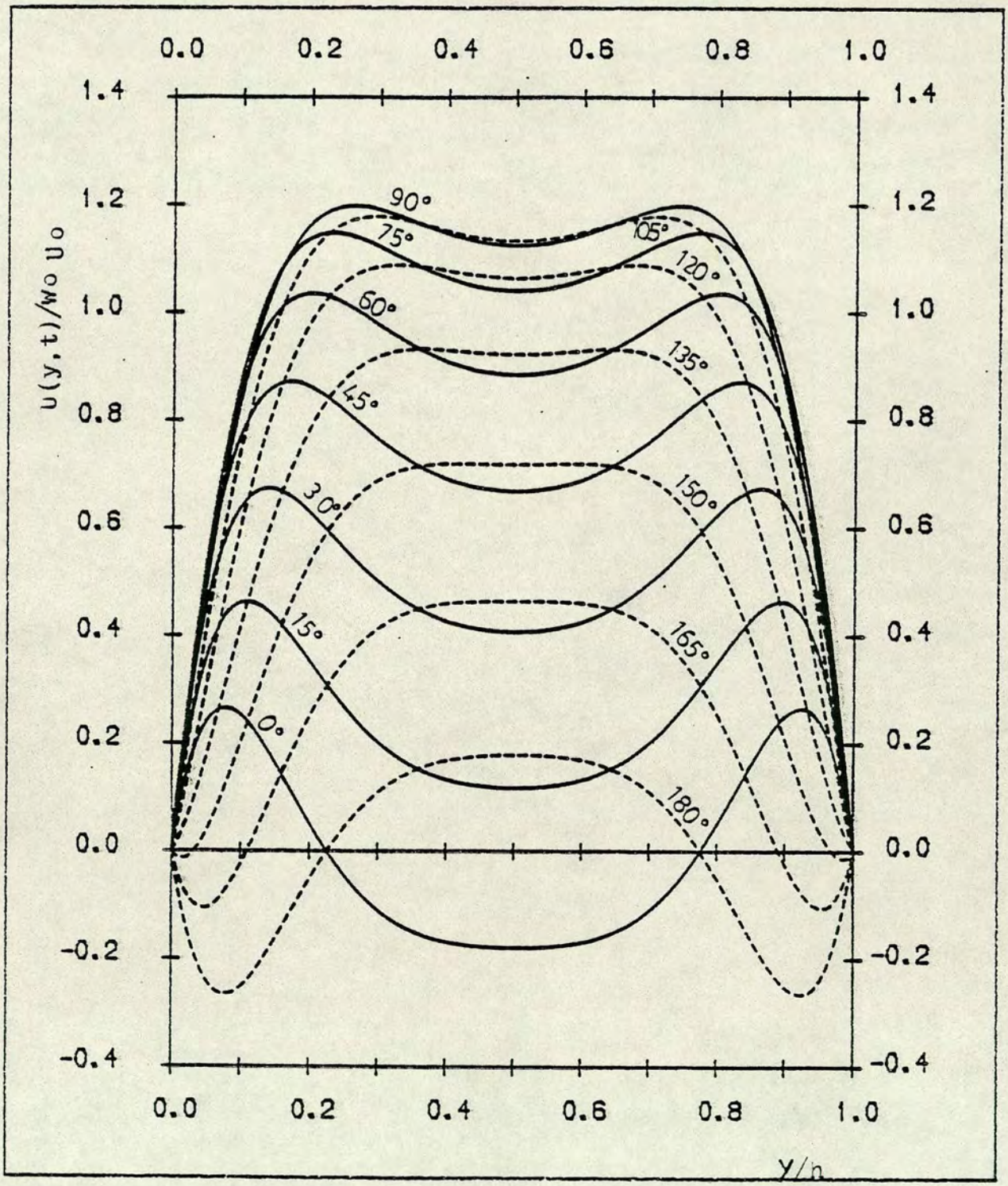

Figure 6.2: Velocity profiles of time-dependent plane Poiseuille flow with zero mean at different phase angles . β=6.

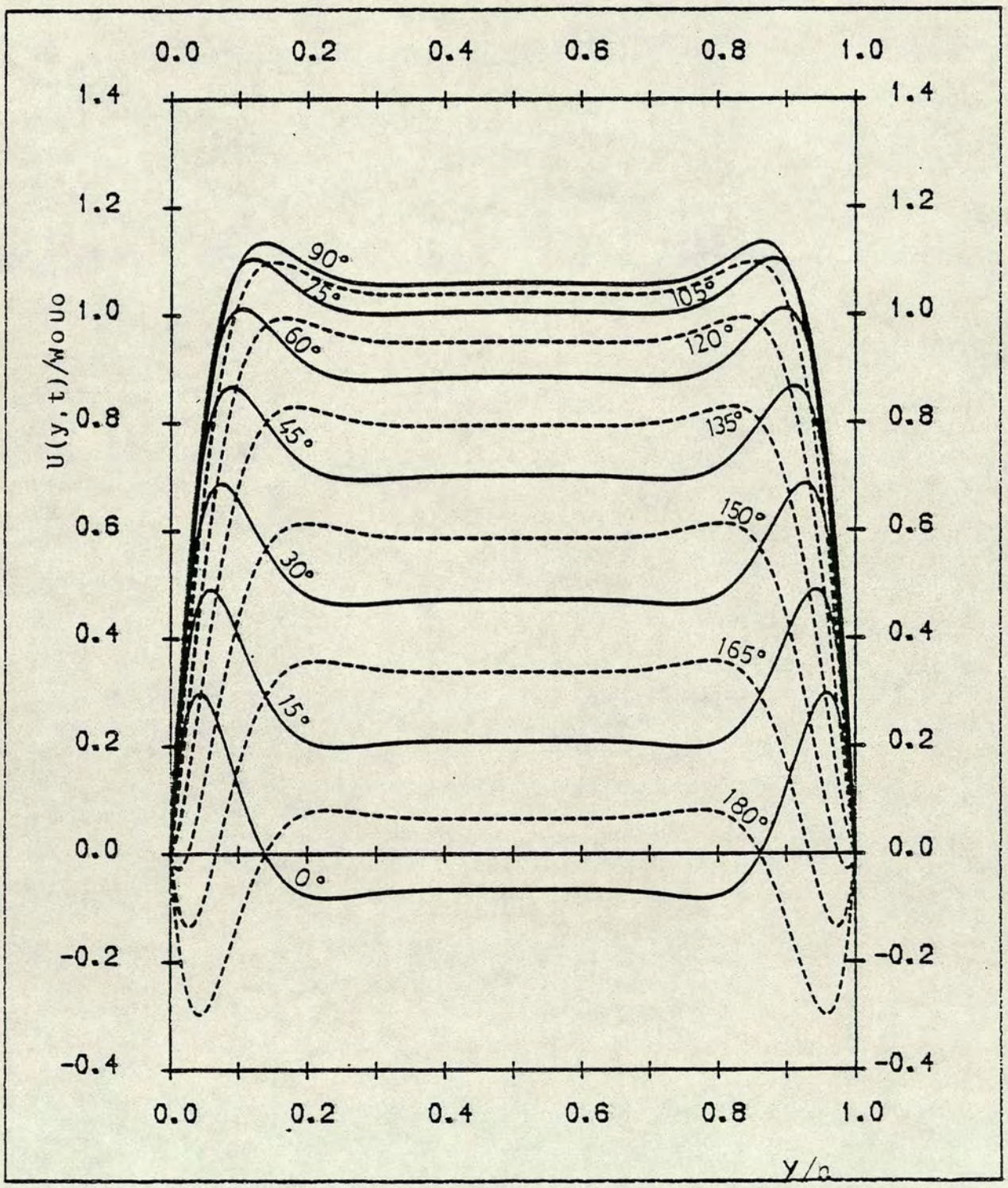

Figure 6.3: Velocity profiles of time-dependent plane Poiseuille flow with zero mean at different phase angle. β=12.

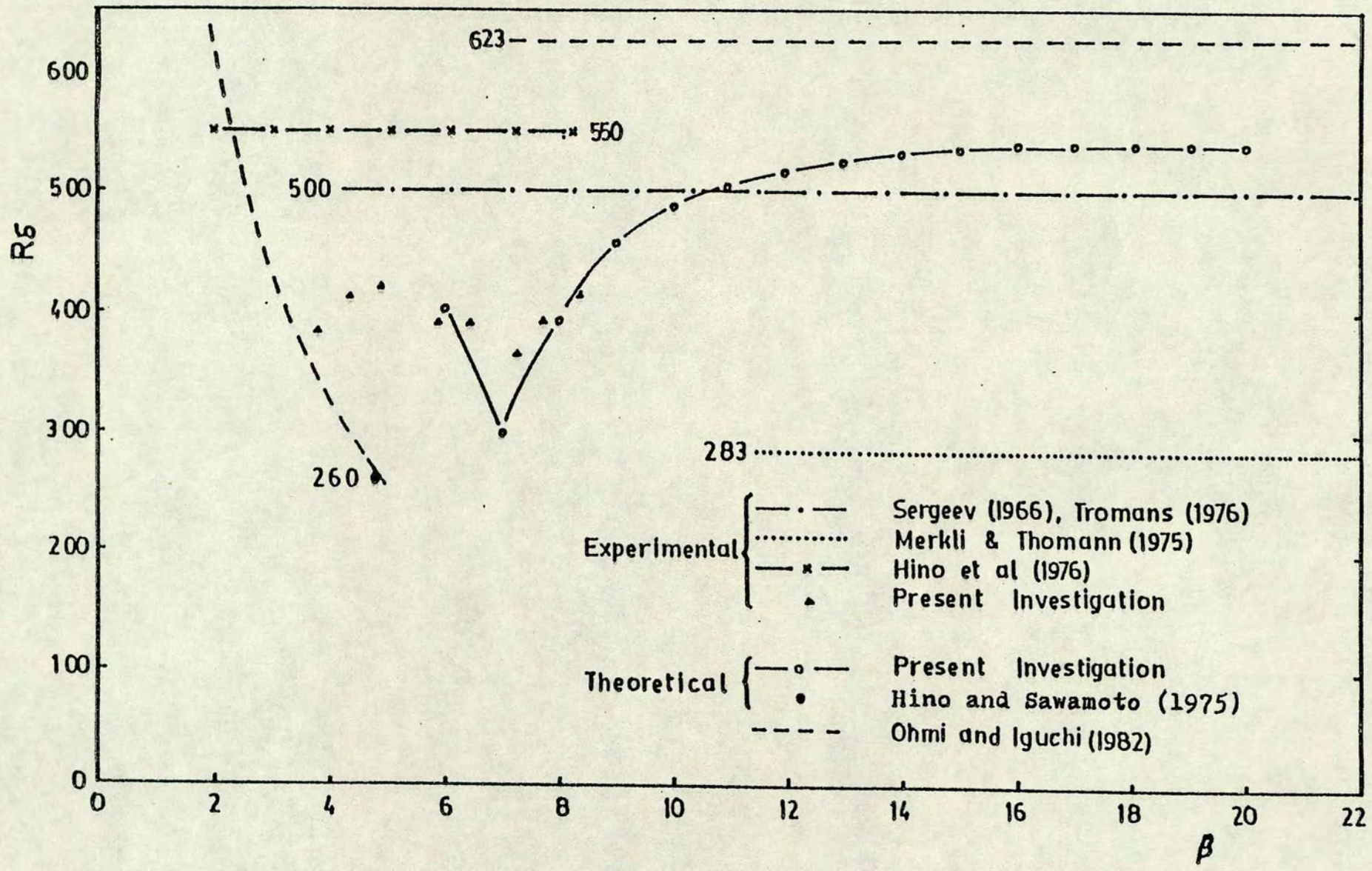

Figure 6.4: Experimental and theoretical $R\delta$ vs β.

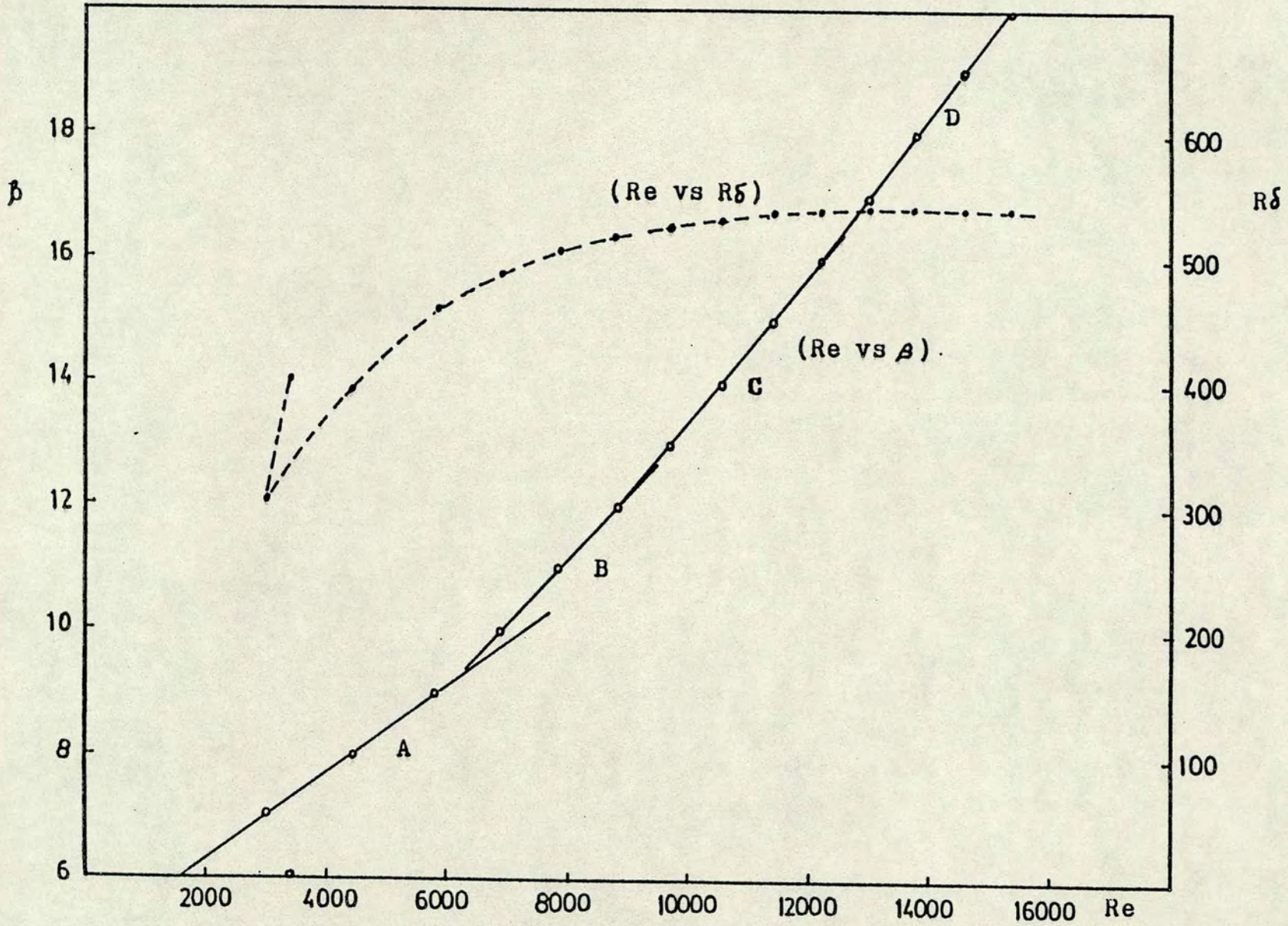

Figure 6.5: The critical Re vs β and vs Rδ.

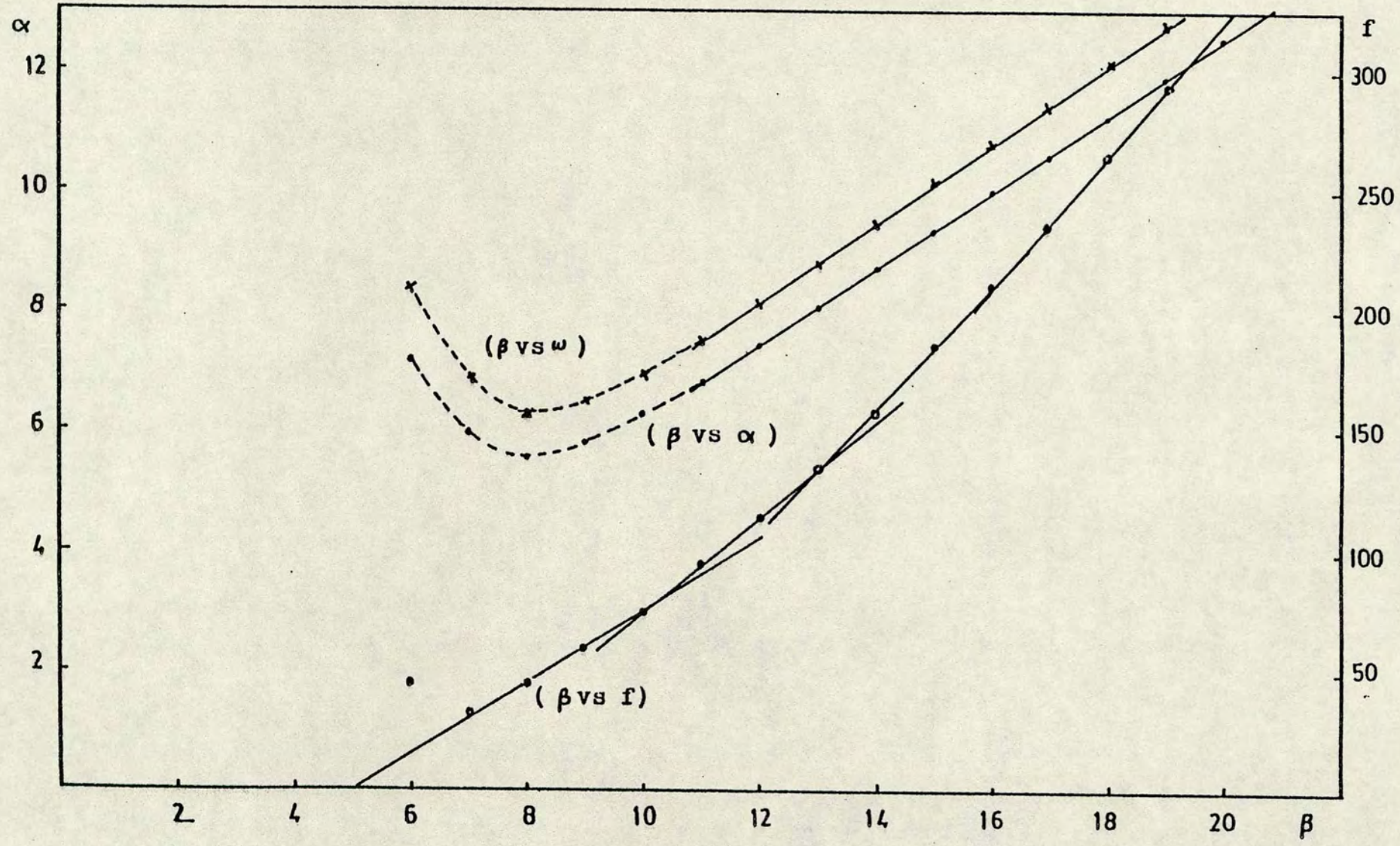

Figure 6.6: β vs the critical wavenumber α and the critical frequency f.

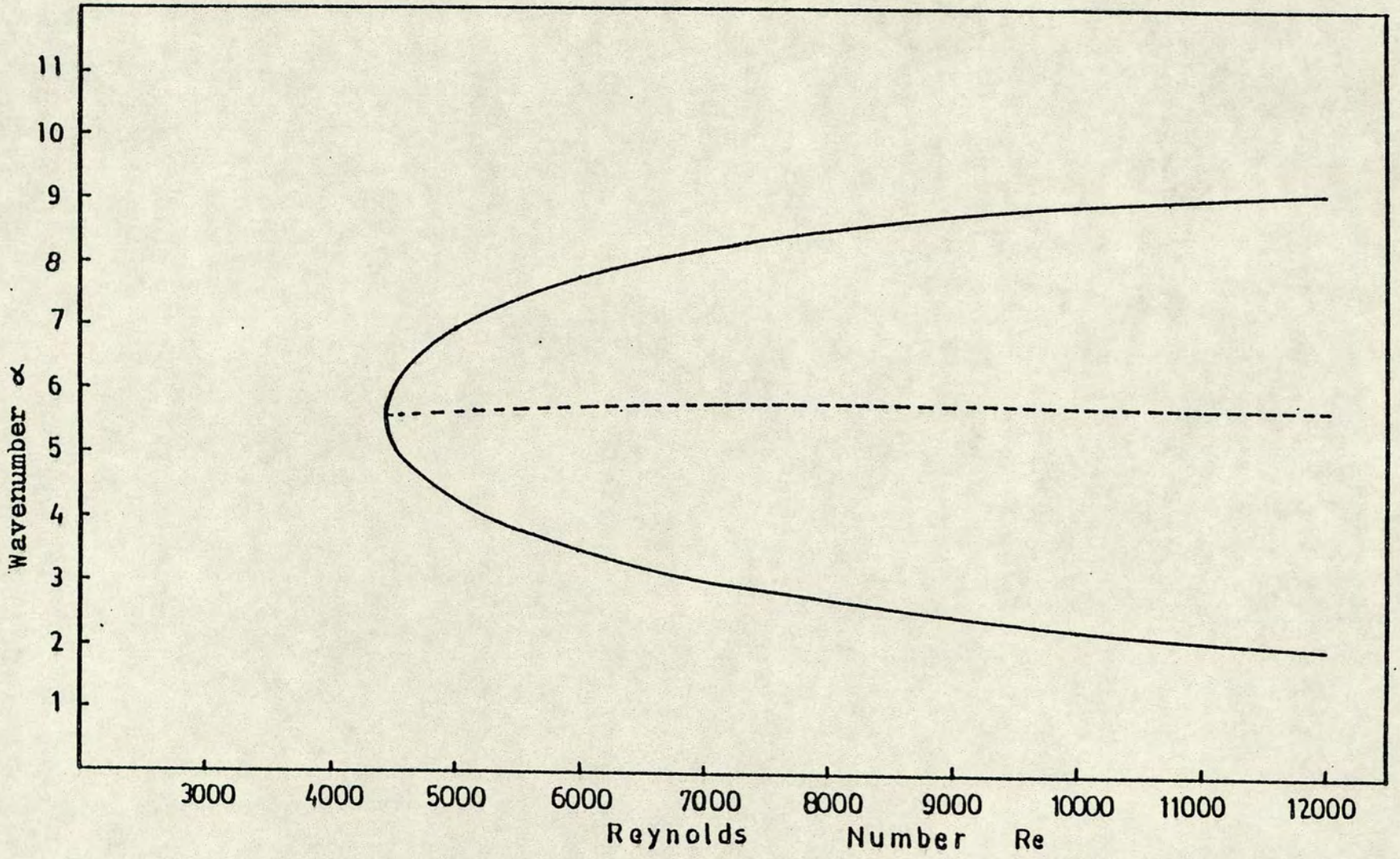

Figure 6.7: The neutral stability curve (solid) and the maximum amplification line (broken) for $\beta = 8$, wot=95.536°.

Figure 6.8: The disturbance quantities distribution.
(β =6, $\omega_s t$=97.609°)

u - The disturbance velocity in the x direction, v - in the y direction, p - the pressure, r - the vorticity.

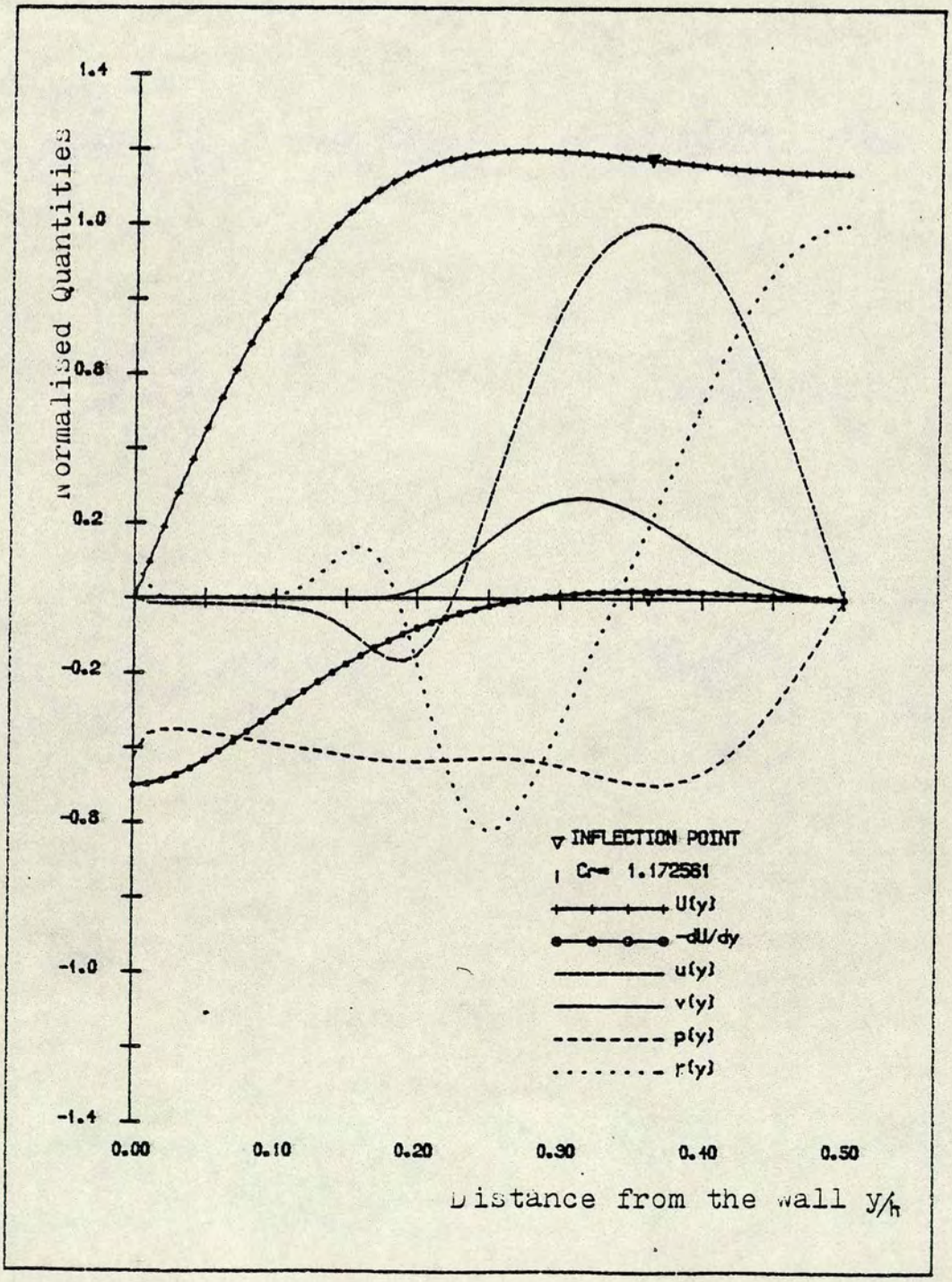

Figure 6.9: The disturbance quantities distribution.

(β =8, $\omega_o t$=95.538°)

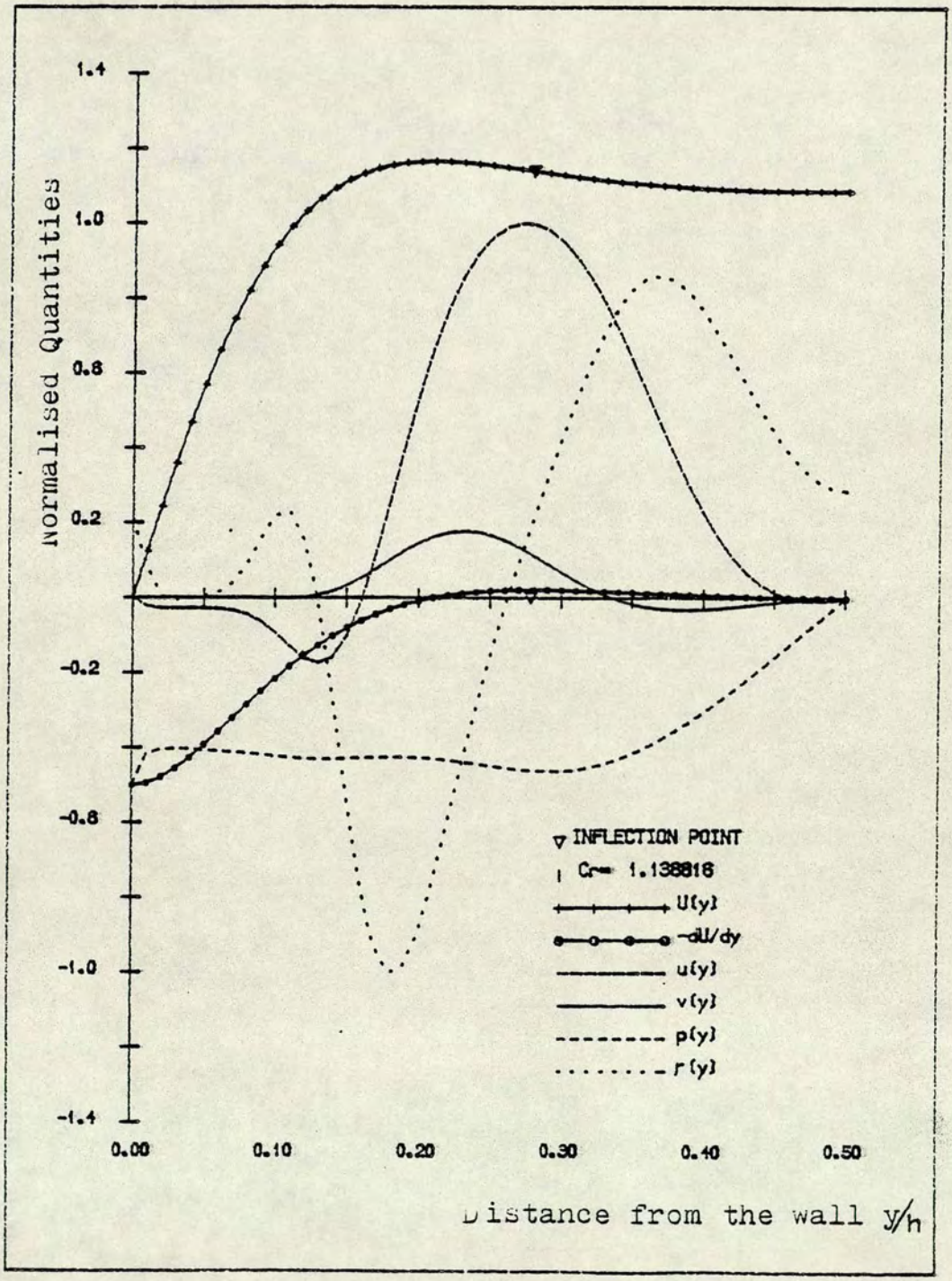

Figure 6.10: The disturbance quantities distribution.

(β =10, $\omega_s t$=94.351°)

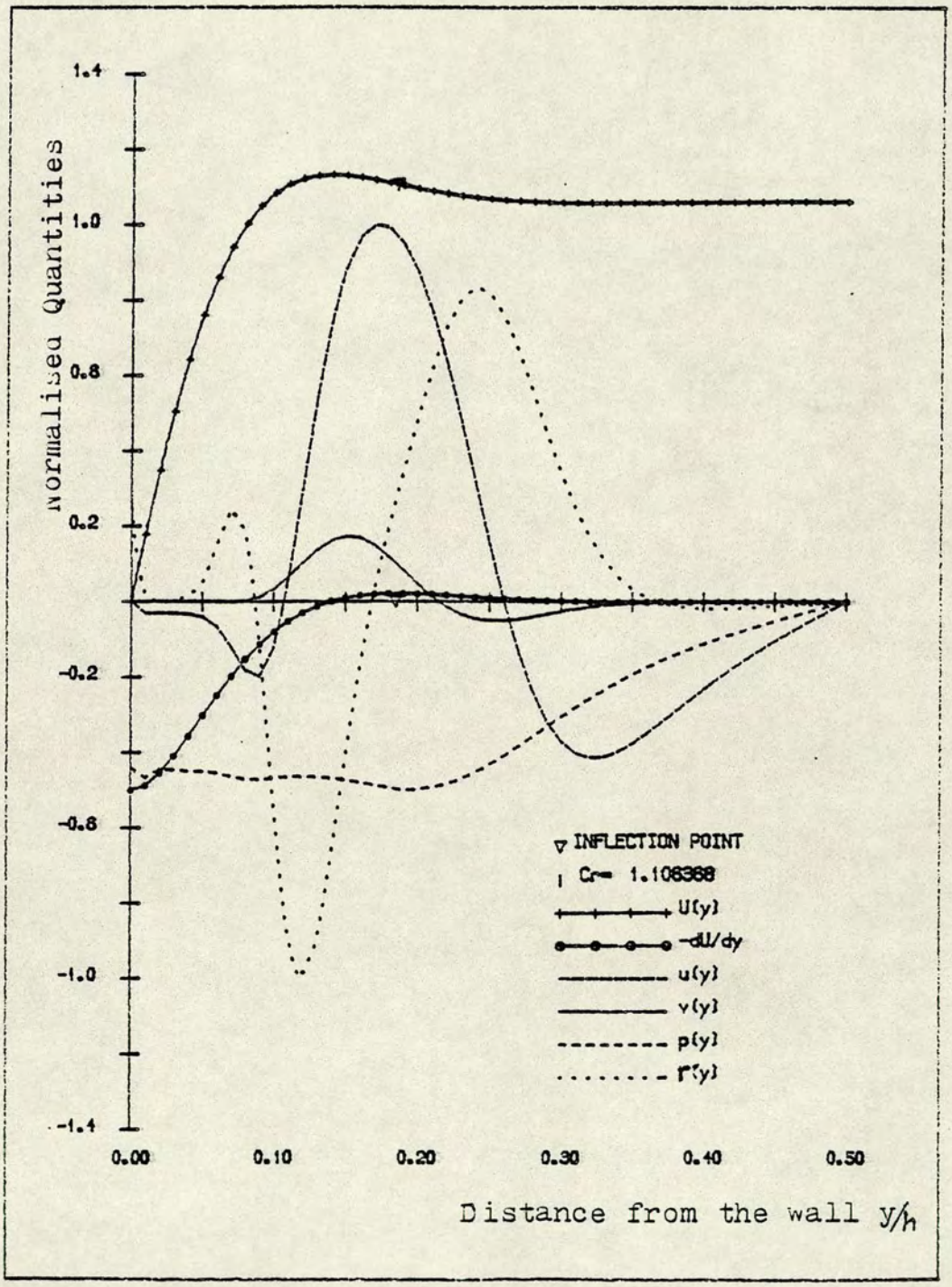

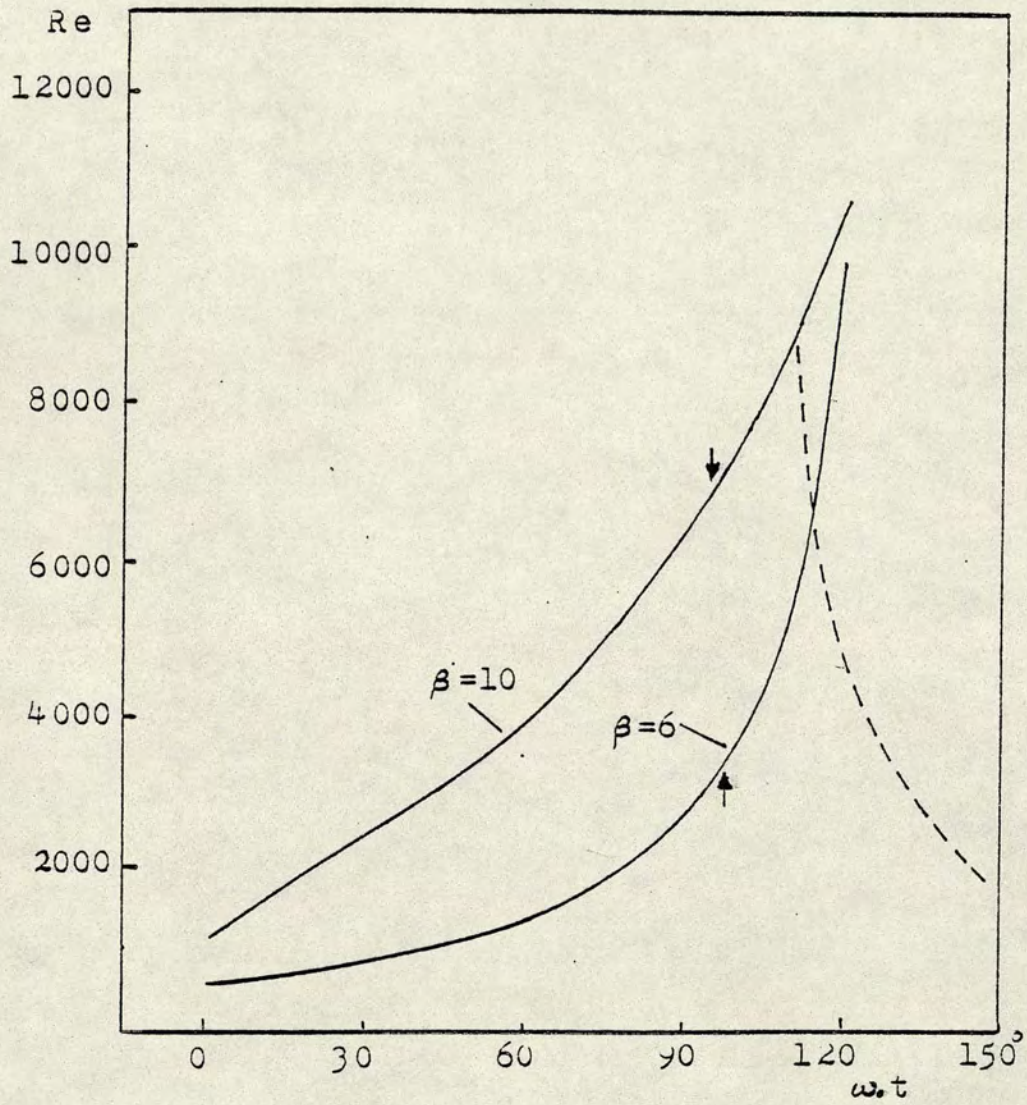

Figure 6.11: Time-dependent flow critical Re vs $\omega.t$.

——— Core inflexion points ($\beta=6$, $\beta=10$)

- - - - - Wall inflexion points ($\beta=6$)

↑ The peak inflexion point velocity $\omega.t=97.61^{\circ}$ for $\beta=6$, and 94.351° for $\beta=10$.

CHAPTER SEVEN

THE ENERGY BALANCE IN LINEAR INFLEXION INSTABILITY

7.1: The Origin Of The Inflexion Instability

Speculations about the origin of inflexion instability go back to Taylor (1915). We will concentrate our attention here on the three most recent attempts to explain this phenomenon. These explanations concentrate on physical insight into the problem without implicating much mathematics.

(a) Lin's Explanation (1945,1955)

Let L1 and L2 be two adjacent fluid layers, where L2 has a higher vorticity than L1 in the undisturbed state. Let an element E1 of the fluid of the layer L1 be interchanged with an element E2 of a neighbouring layer L2. Since E1 preserves its vorticity, it will appear to have a defect of vorticity. Lin (1945) has shown that a fluid element with an excess of vorticity is accelerated in the direction of the opposite y axis with an acceleration

$$a=\Gamma^{-1}\iint\{v(x,y)\}^2\zeta dxdy$$

where Γ is the total strength of the vortex filaments, $\zeta(y)$ is the gradient of vorticity of the main flow and

v(x,y) is the component of the disturbance velocity in the y direction. By examining the various signs in the acceleration formula it can easily be seen that E2 is accelerated towards a region of higher vorticity if the gradient of vorticity does not change sign anywhere in the fluid. The same is true for E1. Therefore, 'the fluid element is returned to the layer where it belongs'. Thus the motion is stable when the gradient of vorticity does not vanish.

When there is an extremum of vorticity, the gradient of vorticity vanishes there and has opposite signs on opposite sides. Therefore the restoring tendency expressed above is largely impaired in this case. In other words the exchanged fluid elements are not strongly forced back. **An exchange of fluid elements constitutes a disturbance** and that disturbance may tend to persist and perhaps augment so that the motion is not necessarily stable.

(b) Lighthill Explanation (1963)

Figure 7.1 shows a velocity profile with an inflexion point. The main flow vorticity has a maximum at that point. Weak vortices are produced at both sides of the inflexion point as a result of convection by the main flow. These vortices in return convect the main flow vorticity. Lighthill's argument is based on the following [Lighthill (1963,1970)]. Near each vortex, the motion induced by each of the two nearest vortices is in such a

direction that the convection of the main flow vorticity which it produces amplifies the strength of the vortex. Thus to the right of the inflexion point, motion to the right amplifies positive vortices and motion to the left amplifies negative vortices, whereas to the left of the inflexion point the opposite is the case. It can be noticed that a positive vortex in the right row generates motion to the left directly ahead of it convecting fluid with reduced vorticity and hence slowing itself. A correspond increase for the left row will keep both in step and the whole pattern remains in phase.

(c) Gill's Explanation (1965)

Both Lin's and Lighthill's explanations do not differentiate between a maximum and a minimum of vorticity, since they take into account only the effect of moving material elements in the y direction. For self excited disturbances the disturbed motion will transfer vorticity to the disturbance in such way that the motion induced by the acquired vorticity will be a strengthening of the original disturbance motion. In figure 7.1, the element displaced to the right will have positive vorticity relative to its surroundings, whilst that displaced to the left will have negative vorticity. If the undisturbed vorticity has a minimum instead of a maximum, the signs of the acquired disturbance vorticity would everywhere be reversed so the the disturbance would be

inhibited. For monotone variation of the vorticity distribution the field could not be self excited according to the above arguments.

(d) The Viscous Force Explanation

In stream function amplitude notation (equation (7.6)) the vorticity is given by

$$r=\varphi''-\alpha^2\varphi \qquad (7.1)$$

Substituting this into the Rayleigh equation (4.2), we have

$$r=(U''\varphi)/(U-c) \qquad (7.2)$$

In order to avoid the singularity in (7.2) , it is assumed that the growth rate $\alpha c_i \neq 0$, i.e. $c_i \neq 0$. Multiplying the numerator and the denominator in (7.2) by $(U-c^*)$, where c^* is the complex conjugate of the phase velocity c, then the real part of r is

$$\text{Real}(r)= -\{U''[\varphi_r(U-c_r)+\varphi_i c_i]\}/[(U-c_r)^2+c_i^2] \qquad (7.3)$$

Hence,

$$\text{Real}(r)=-(U''\varphi_i)/c_i \qquad (7.4)$$

It follows that for the maximum amplification case, r changes sign at the inflexion point (U''=0). This is exactly the picture described by Lighthill and Gill.

On the other hand $\mu U''$ is equal to the viscous force per unit volume [Tritton (1977)]. This force tends to oppose the flow. Since U'' changes sign at the inflexion point,

it follows that there is no viscous force holding the fluid at the inflexion point, while such a force increases on both sides of that point with opposite signs. In this respect, **the main flow vorticity U' represents a profile of a disturbance**. Therefore, the most amplified self excited disturbance will be that whose velocity u in the direction of the flow has a profile which can lock to the main flow vorticity U'. In other words, the main flow vorticity shape and width control the shape of the u velocity of the disturbance. Depending on the shape of the v fluctuation the u shape will be shifted accordingly. Comparison between the u and U' profiles will be made in section 7.5. In chapter 4, it has been shown that the critical and the most amplified wavelengths are determined by

$$\lambda = K L$$

where K is a proportionality factor, and L is generally the distance between the two points where U'=0 on both sides of the inflexion point. It is evident that not only the width of the main flow vorticity is proportional to the wavelength of the critical and of the maximum amplified disturbance, but also the shape of the disturbance is controlled by the main flow vorticity shape.

The viscous force explanation given above was for profiles known to be unstable, i.e. satisfying Fjortaft's (1950) condition $U''(U-Ui) < 0$, where Ui is the velocity at the inflexion point. All the profiles studied in this

thesis are of this type. For one such profile, namely $U(y)=\sin(y)$, the viscous force $\mu U''$ is equal to $-\mu\sin(y)$. It can be shown for all other unstable profiles also that the viscous force opposes the flow as seen from its sign. In other words, the viscous force works to reduce itself. Consequently, it helps the growth of the disturbance. An example of profiles possessing an inflexion point but stable since $U''(U-Ui) \geq 0$ is $U(y)=\sinh(y)$. The viscous force $\mu U''$ is equal to $\mu\sinh(y)$ and the viscous force works to increase itself. Together with the fact that there is a sharp increase in the viscous force ($->\infty$) on both sides of the inflexion point, we see that the behaviour of the viscous force is opposite to that of the unstable profiles.

7.2: The Disturbance Equation

In this chapter for simplicity, the differentiation by x will be denoted by $(,)$,e.g. $u_{,}=\partial u/\partial x$; while $\partial u/\partial y$ will be replaced by u'.

The Navier-Stokes equations for two-dimensional incompressible flow are

$$\tilde{u}_{,}+\tilde{v}=0 \qquad \text{(a)}$$

$$(\partial\tilde{u}/\partial t)+\tilde{u}\tilde{u}_{,}+\tilde{v}\tilde{u}'+\tilde{p}_{,}=\nu(\tilde{u}_{,,}+\tilde{u}'') \qquad (7.5)\ \text{(b)}$$

$$(\partial\tilde{v}/\partial t)+\tilde{u}\tilde{v}_{,}+\tilde{v}\tilde{v}'+\tilde{p}'=\nu(\tilde{v}_{,,}+\tilde{u}'') \qquad \text{(c)}$$

where $\tilde{u}=\tilde{u}(x,y,t)$ is the velocity in the flow direction x; $\tilde{v}=\tilde{v}(x,y,t)$ is the velocity parallel to the y axis (the transverse direction). $\tilde{u}$ and $\tilde{v}$ are called the Eulerian

components of the velocity. $\tilde{p}=\tilde{p}(x,y,t)$ is the pressure divided by density (the kinematic pressure).

The velocity and the pressure of two-dimensional laminar flow are given as

$$\tilde{u}=U(y)$$

$$\tilde{v}=0$$

$$\tilde{p}=P(x)$$

Upon imposing two-dimensional disturbances on a laminar two-dimensional flow, the above quantities can be expanded in the following form

$$\tilde{u}=U(y)+ \varepsilon\, u(x,y,t)+ \varepsilon^2\, \hat{u}(x,y,t)+ \ldots\ldots \qquad (a)$$

$$\tilde{v}= \varepsilon\, v(x,y,t) + \varepsilon^2\, \hat{v}(x,y,t) + \ldots\ldots \qquad (7.6)\ (b)$$

$$\tilde{p}= P(x) + \varepsilon\, p(x,y,t) + \varepsilon^2\, \hat{p}(x,y,t) + \ldots\ldots \qquad (c)$$

In this form, the fundamental disturbance whose velocities are u and v and pressure p enters with order ε, where ε is a scaling factor whose value is chosen in such a way that εu is equal to a specified fraction of the mean velocity U_o. The disturbance with $\hat{u}$, $\hat{v}$, and $\hat{p}$ which enters with ε^2 is usually the second harmonic. However, depending on the choice it can be a subharmonic. Higher orders of ε can be added in which case the problem is more complicated.

In order to account for the distortion resulting from the interaction of the disturbances, the main flow velocity is written as [Stuart (1960)]

$$U(y,t) = U(y)+ \varepsilon^2\, W$$

where W is the distortion of the main flow velocity distribution which is produced by the fundamental disturbance. Therefore, it appears as a second order quantity. Higher order distortions are added as the contributions of higher harmonics are included.

Inserting $\tilde{u},\tilde{v}$ and $\tilde{p}$ given by (7.6) into the two-dimensional Navier-Stokes equation (7.5) and equating equal powers of ε to zero, we have for order ε^1

$$(\partial u/\partial t)+ U\, u_{,} + U'\, v + P_{,} = \nu(u_{,,} + u'') \qquad (a)$$

$$(\partial v/\partial t)+ U\, v_{,} + p' = \nu(v_{,,} + v'') \qquad (7.7)\ (b)$$

$$u_{,} + v' = 0 \qquad (c)$$

Differentiating (7.7a) by y and (7.7b) by x, subtracting the second from the first and using the continuity equation (7.2c), we have

$$\partial(u' - v_{,})/\partial t + U\,(u'_{,} - v_{,,}) - U''\, v =$$

$$\nu(u'_{,,} + u''' - v_{,,,} - v''_{,}) \qquad (7.8)$$

The stream function of the fundamental disturbance is assumed to be in the form

$$\psi_1(x,y,t)=\varphi_1(y)e^{i\alpha(x-ct)} \qquad (7.9)$$

where as before, α is the wavenumber of the disturbance and c its complex phase velocity. The disturbance velocities are then given by

$$u=u(x,y,t)=\partial\psi_1/\partial y \text{ and } v=v(x,y,t)=-\partial\psi_1/\partial x \qquad (7.10)$$

Equation (7.8) after substitution of (7.10) is the Orr-Sommerfeld equation given previously by (2.5) and (4.1).

For order ε^2, following the same procedure used to obtain (7.8), the equation for the second (or the sub) harmonic is given by

$$\begin{aligned}&\partial(\hat{u}' - \hat{u}_{,})/\partial t + U(\hat{u}_{,}' - \hat{v}_{,,}) + U''\hat{v}\\ &= v(\hat{u}'_{,,}+\hat{u}''' - \hat{v}_{,,,} - \hat{v}''_{,})\\ &-\{u_{,}(u'-v_{,})+u(u'_{,}-v_{,,})+v'(u'-v_{,})+v(u''-v'_{,})\}\end{aligned} \qquad (7.11)$$

The stream function of this harmonic is defined in the same form of (7.9) with ψ_1 and φ_1 replaced ψ_2 and φ_2 and α is replaced by $a\alpha$, where a=2 for the second harmonic and a=0.5 for the subharmonic. The computational form of (7.11) is

$$\begin{aligned}&(U-c)(\varphi_2'' - a^2\alpha^2\varphi_2) - U''\varphi_2 +\\ &(i/a\alpha Re)(\varphi_2'''' - 2a^2\alpha^2\varphi_2'' + a^4\alpha^4\varphi_2) =\\ &(1/a)(\varphi_1'\varphi_1''' - \varphi_1\varphi_1''')\end{aligned} \qquad (7.12)$$

7.3: The Energy Equation

Multiplying the first equation of (7.7) by u and the second by v and after adding and averaging, we have the energy equation for the fundamental disturbance

$$\overline{(u(\partial u/\partial t)} + \overline{v(\partial v/\partial t)} + U(y)\overline{(uu,+vv,)} + \overline{uv}U'(y) + \overline{(up,+vp')} =$$
$$v[\overline{u(u,,+u'')} + \overline{v(v,,+v'')}] \qquad (7.13)$$

where the bars denote the averaging in the direction of the flow.

In a compact form

$$\overline{(\partial q^2/\partial t)} + U(y)\,\overline{\partial q^2/\partial x} + \overline{uv}\,U(y) + PT = TED$$

where $q^2=(u^2+v^2)/2$, and (u^2+v^2) is the disturbance intensity per unit volume. $PT=\overline{(up,+vp')}$ is the pressure transport term and TED is the right hand side of (7.13) and stands for the total dissipation of energy. All terms in (7.13) will be explained in details below.

7.3.1: The averaging procedure

Since equation (7.8) is a linear equation, any combination of its solutions is a solution. Thus, the real quantities u,v and p in (7.6) are retained if the complex solutions of (7.8) u_1 and v_1 and their complex conjugates u_1^* and v_1^* are used in the form

$$u=(u_1+u_1^*)/2$$
$$v=(v_1+v_1^*)/2$$
$$p=(p_1+p_1^*)/2$$

where u_1 and v_1 are given by (7.10). This form also helps in averaging the quantities in equation (7.13). In the temporal case (c is complex), the average is taken over one disturbance wavelength λ, while in the spatial case (α

is complex) the average is taken over one period of the disturbance. It is easily shown that the average of the product of any complex quantity and a complex conjugate is nonzero, while all other product combinations are zero. Thus $\overline{u_1 v_1} = \overline{u_1 u_1} = \overline{v_1 v_1} = 0$, while $\overline{u_1 v_1^*} \neq 0$ and

$$\overline{u^2} = 0.5(\overline{u_1^2} + 2\,\overline{u_1 u_1^*} + \overline{u_1^{*2}}) = \overline{u_1 u_1^*}$$

7.3.2: The increase in energy and advection terms

The first quantity in the energy equation (7.13) is

$$\overline{\partial q^2/\partial t} = \overline{(u\partial u/\partial t + v\partial v/\partial t)} \qquad (7.14)$$

which represent the amount in change in the kinetic energy of the disturbance. In the temporal case, this quantity is equal to

$$0.5\omega_i(|\varphi'|^2 + \alpha^2|\varphi|^2)\exp(\omega_i t)$$

where $\omega_i = \alpha c_i$. In the spatial case it is equal to

$$0.5\alpha_i(|\varphi'|^2 + \alpha^2|\varphi|^2)\exp(-\alpha_i x)$$

It is obvious that in both the spatial and the temporal cases this quantity is small especially when the amplification rates ω_i and α_i are small.

The second quantity in the energy equation is

$$\overline{U(y)\partial q^2/\partial x} = U(y)\overline{(uu_r + vv_r)} \qquad (7.15)$$

This quantity contributes to the energy of the disturbance due to advection of the energy of the disturbance by the main flow. It is easily shown that in the temporal case this quantity is equal to zero, while in the spatial case it is equal to

$$-0.5\ \alpha_i U(y)[|\varphi''|^2+(\alpha^2+\alpha_i^2)|\varphi|^2]\ \exp(-\alpha_i x)$$

Again this quantity is small.

7.3.3: The energy production

The third term in the energy equation taken with a negative sign is

$$-\overline{uv}\,U'(y) \qquad (7.16)$$

The quantity $-\varrho\overline{uv}$ has the dimension of stress ,i.e. force per unit area. Therefore, it is called the Reynolds stress and it acts in the y direction. It transports the x momentum through a surface normal to the y direction. By analogy to the known work of the viscous stress against the velocity gradient to remove energy from the main flow which appears as heat, the Reynolds stress works against the velocity gradient to remove energy from the main flow. This energy gained by the disturbance is $-\overline{uv}U'(y)$ = the energy production.

7.3.4: The pressure transport

The fourth term in the energy equation is

$$PT=\overline{(up,+vp')}$$

This quantity is equal to

$$\overline{p(u,+v')}-\overline{\partial(up)/\partial x}+\overline{\partial(vp)/\partial y}$$

By the continuity equation the last term is equal to zero. The remaining term is a spatial gradient term, therefore, it represents transport from one place to another. Its integral over the volume of the flow is zero. Therefore, it is called the pressure transport term. It corresponds to a loss in the disturbance kinetic energy when a transfer to a region of high pressure occurs and vice versa. In more practical terms: if this quantity is negative it is then a gain to the disturbance energy, and if it is positive it is a loss. Therefore, in order to show the correct sign for the loss or the gain, we define

$$PT= -\overline{(up,+vp')} \qquad (7.17)$$

p, and p' in (7.17) are obtained directly from (7.7 a and b).

7.3.5: The energy dissipation and the viscous transport

The last term in the energy equation is

$$TED= v\ \overline{[u(u,,+u'')+v(v,,+v'')]}$$

It can be divided into two quantities, i.e.

$$TED=0.5\ v\ [\overline{u,,}+\overline{v,,}+\overline{u''}\ +\overline{v''}\ )$$

$$- \nu \left(\overline{u_i \frac{\partial u'}{\partial x_i}} + \overline{u' \frac{\partial v_i}{\partial x_i}} + \overline{v_i \frac{\partial v'}{\partial x_i}} + \overline{v' \frac{\partial v'}{\partial x_i}} \right) \qquad (7.18)$$

= Viscous Transport + Energy Dissipation

Due to the fact that the first term in (7.18) is a product of second drivatives, it is a transport quantity whose integral over the volume of the flow is zero. Therefore, it is a diffusion term transferring energy from one part of the flow to another. In this respect, it has the same effect as the pressure transport term. Its magnitude amounts to the acceleration of the fluid in that region.

The dissipation term with the negative sign in (7.18) included represents the energy loss due to viscous friction which finally appears as heat.

7.4: Notes On The Large Scale Coherent Structures

The large structures have been observed under a wide range of flow conditions and there is much argument about the effect of the three-dimensionality on it. Miksad (1972), Chandrsuda et al (1978), Brownd and Troutt (1980) and Jimenez (1983) observed the effect of the three-dimensionality on mixing layers. Jimenez found in a plane shear layer that the fluid is dominated by lateral undulations that persist downstream to form longitudinal structures. The amplitude and the spacing of such structures suggest that they are due to secondary instability of the flow field. Chandrasuda et al (1978) argued that, where such structures are observed, the

three-dimensionality is small. They also observed that the large scale structure does not form at all if the nozzle-exit boundary layer is fully turbulent. Brownd and Troutt (1980) found that the three-dimensionality does not destroy the large scale structure, while Wygnanski et al (1972) noticed that the structure has a strong resistance to interfering influences.

The fact that the structure at the nozzle-exit boundary layer is turbulent is understandable since such organised structures arise from an instability close to the place of the formation of the shear layer and they need time to grow without any interference.

It is evident that for such structures, once established, the effect of three-dimensionality is small and the two-dimensional structure remains strong for a relatively long distances downstream. Having this in mind, the energy balance of two-dimensional disturbances which will be presented next will be close to the actual one except for the expected deviations due to nonlinearity. It is expected that these deviations will not alter the general picture. To avoid the deviations occurring due to the use of the temporal equation rather than the spatial one, all calculations will be presented at the critical Re where both coincide.

7.5: The Fundamental Disturbance Velocities, Pressure And Vorticity Distributions

Three flows have been considered in this study. The first is the plane Poiseuille time-dependent flow which has an infinite number of profiles. These profiles, however, can classified into a distinct number of types (chapters 4 and 6). The second is a profile of the wake behind a circular cylinder which is a Gaussian distribution (section 4.3, eqn 4.36). The third is the tanh(y) profile representing a mixing layer. The form used in this study is $U(y)=0.5(1+\tanh(y))$, where $0 \leq U(y) \leq 1$ for $|y| \leq 4$. The inflexion point is at $y=0$, while the velocity at the inflexion point $U_i=0.5$.

The fundamental disturbance velocity in the x direction is given by

$$u(x,y,t)=\varphi' e^{i\Xi}=\varphi_r' \cos(\Xi)-\varphi_i' \sin(\Xi)$$

where $\Xi=i\alpha(x-ct)$. Similar expressions are found for the other nonaveraged quantities using (7.7) and (7.10). Only the dependence on the transverse direction y will be calculated here, on the understanding that the fluctuating quantities will have a sinusoidal distribution in the x direction. Thus, at $x=0$ and $t=0$

$$u(0,y,0)= u(y) = \varphi_r' \qquad (a)$$

$$v(y) = \alpha\varphi_i \qquad (b)$$

$$p(y) = p_r/\alpha \qquad (c) \qquad (7.19)$$

where p_r is found directly from (7.7).

The vorticity distribution is given by

$$r(y) = \varphi_r'' - \alpha^2\varphi_r \qquad (d)$$

All calculations have been carried out using the finite difference scheme described in section 3.3. To achieve reasonable accuracy in the case of the sensitive higher derivatives φ''' and φ'''', 201 points were used with some improvement over 101 points.

For symmetrical (time-dependent flow and wake) profiles, only symmetrical disturbances were considered since those are the unstable ones. For the only nonsymmetrical profile considered here, i.e. tanh(y), both symmetrical and antisymmetrical disturbances are coupled. The boundary conditions (2.5) are to be applied at both ends. Figures 7.2 to 7.8 show the main velocity U(y), the main flow vorticity U', the fundamental disturbance velocities u and v, the pressure p and the vorticity r.

First, several introductory situations will be explained using time-dependent profiles, and later, a general summary of the fundamental disturbance distributions in all flows examined will be given. The distributions of u,v,p and r of some of the profiles

responsible for the instability of the time-dependent flow were already presented in chapter 6. Here for the purpose of general demonstration, two velocity profiles will be used. Both are at the frequency parameter $\beta=0.5(\omega_o/\nu)^{1/2}=6$, where ω_o is the frequency of the main flow and ν is the kinematic viscosity. The phases chosen are $\omega_o t=30$ and 110 degrees. Figure 7.2 show the distributions for $\omega_o t=30$, at the critical Re=882.16, $\alpha_c=4.3185$ and the critical phase velocity $c_r=0.559157$.

The close similarity between the main flow vorticity -U' and the disturbance velocity u is evident, thus supporting the conclusions already drawn in the beginning of this chapter. However, u tends to be wider than expected. This last point needs explanation. The explanation is based on the well known rules determining the sign of the u velocity using that of the v velocity and vice versa [Schlichting (1968)]. First we notice that the peak of v velocity, which incidentaly also has a similar distribution to -U', is shifted to the left. Thus, particles are moved from the left where the velocity of the main flow U is high to a region of a low velocity U. Since such particles preserve their velocity, they will add more positive contribution to u. The regions of the negative u are due to the motion of particles from regions of low velocity to regions of high velocity. In other words, the u shape is exactly that of U' and the deviations from this shape are due only to the v velocity.

The pressure distribution of the fundamental disturbance is interesting. It is constant over most part of the flow and deviates from this constant value at two regions. First, near the wall where the viscosity is dominating and p reaches its maximum value at the wall (since from (7.7 a) only $\varphi''' \neq 0$ there). The second region is near the centre of the channel where it steadily decreases to zero (only half of the channel is shown here). The area where this decrease starts coincides with the band of the phase velocities on the upper branch of the neutral stability curve. This band is narrow and the difference between c_r at the critical Re and that at very large Re does not exceed 5 % in the case of time-dependent flow profiles. The fact that the disturbance pressure is constant where the disturbance is dominant is also the case in Blasius flow as the results of Hama et al (1979) show.

Two cases at two extreme wavenumbers have been considered for the same profile ($\omega_o t=30°$). The two wavenumbers chosen on the neutral curve at Re=5000. The two cases are unrealistic since they do not occur in real flows. However, they are useful in demonstrating the changes in the eigenfunctions of the Orr-Sommerfeld equation with the change in the wavenumber. Figure 7.3 shows the distribution for $\alpha=7.07$ (i.e on the upper branch) and phase velocity $c_r=0.56000$, while figure 7.4 is for $\alpha=1.02$ and phase velocity $c_r=0.67487$. It is

interesting that the peak of the u velocity at one wavenumber occurs at the position of the phase velocity of the other wavenumber.

The profile of $\beta=6$ and $\omega_0 t=110^\circ$ represents a special case since it has two inflexion points. One is near the wall and the other is a core inflexion point. Both points were considered at the critical Re. The complete stability data is given in tables 4.1,4.8 and 4.9. Figure 7.5 shows the disturbance velocity, pressure and vorticity distributions for the core inflexion point. Their behaviour is very close to that shown in figure 7.2 for $\omega_0 t=30^\circ$ except near the wall, since the maximum velocity of $\omega_0 t=110^\circ$ is further from the wall.

In figure 7.6, the distribution of the disturbance originating from the instability of the wall inflexion point is shown. The u velocity to the right of the inflexion point is similar to U' but with opposite sign. In contrast to u in figure 7.5, it does not vanish in the area of the second inflexion point. The v velocity is negligibly small and negative in this case. The pressure is again negative in the area of the inflexion point. The main concentration of vorticity occurs in the area of the inflexion point with the zero of the vorticity at about the inflexion point position.

7.6: Summary And Comments On The Fundamental Disturbance Distribution

(a) The disturbance velocities, pressure, and vorticity distributions

For the wake, the curves presented in figures 7.7 are for the wake width b=4.008 (i.e for x1=x Cd d =50, where x is the distance downstream, Cd is the drag coefficient, d is the cylinder diameter). These are at the critical Re=5.559, α_c=0.42557 and the phase velocity c_r=0.2573.

For the mixing layer U(y)=0.5[1+tanh(y)], {referred to as tanh(y)}, the critical wavenumber is α_c=0.38 and the phase velocity c_r=0.5, while the critical Re=12. The results for this profile are shown in figure 7.8.

TABLE 7.1

The fundamental disturbance p and r maximum values

The Profile		p	r	U'i
	$\omega_0 t=0^\circ$	2.9307	11.7663	2.2600
	$\omega_0 t=30^\circ$	0.8028	11.7080	1.3580
β=6	$\omega_0 t=110^\circ$ (1)	0.0168	21.5692	0.2970
	$\omega_0 t=110^\circ$ (2)	0.6708	56.3860	-7.3600
	$\omega_0 t=145^\circ$ (2)	1.6422	26.8716	-4.0000
WAKE	x1=50	0.4634	3.2153	-0.4071
TANH(Y)		0.2892	1.3524	-0.5000

(1): Core inflexion point.
(2): Wall inflexion point.

In all figures, each quantity shown is normalised by its maximum or twice the maximum value except for the v velocity [see (2) below]. Therefore, tables were found necessary in order to show their relative magnitudes to each other. However, both the fundamental and the subharmonic disturbances maximum values presented in table 7.1 and table 7.3 are normalised by the maximum value of the fundamental disturbance velocity u_{max}. The energy quantities table 7.2 and 7.4 are normalised by $(u_{max})^2$ and $(\hat{u}_{max})^2$ respectively.

The general distribution of the velocities, the pressure, and the vorticity can be summarised as follows:

(1) In symmetrical flows, the u velocity is positive, [according to the definition (7.10)], for all velocity profiles whether their main flow vorticity is positive or negative. It has strong resemblance to -U'. In the case of the mixing layer (figure 7.8), the peak of the u velocity almost coincides with that of U'. However, it differs from the symmetrical profiles case in that it has strong positive as well as negative parts. Both the u and v velocities are similar to the inviscid calculations of Monkewitz and Huerre (1982).

(2) The v velocity in most of the cases has a shape similar to that of -U'. For symmetrical profiles, its amplitude peak generally occurs at U'(y)<U'max and it always has the same sign as -U'. Its maximum value is

smaller than that of the u velocity. The ratio between the two varies and can be inferred directly from the figures provided, where the v(y) curves shown are for $v(y)/u_{max}$. For time-dependent flow profiles, it was found that $v_{max}/u_{max}<0.4$. This is about the value estimated from Hino et al (1983) results. In the case of tanh(y), the ratio of the two velocities is about 1.0 possibly the largest in all flows. In this case the sign of u is opposite to that of -U'.

(3) Since, for symmetrical profiles, u is always positive while the sign of v is opposite to that of $-U_i'$ (U' at the inflexion point), the Reynolds stress is always negative for profiles whose inflexion point has $-U_i'>0$ and vice versa. As a result, the energy production in the disturbed part of the flow is always positive. More details about the energy production will be given below.

(4) The vorticity distribution usually consists of several counter-rotating vortices. For symmetrical profiles, there is always a strong vortex in the centre of the flow counter-rotating with another two on both of its sides. Each of the outer vortices can also have counter-rotating neighbours. When the disturbance near the wall is strong, there is a vortex attached to the wall.

It is interesting to note that, the vortex structure of the linearly unstable wake does not resemble that of the two counter-rotating vortices shed behind the cylinder

despite the fact that their frequencies are very close (section 4.6). The tanh(y) profile has two counter-rotating vortices occupying the greater part of the flow. The one in the faster part of the flow is weaker. Due to the fact that $r(y)=\varphi_r''-\alpha^2\varphi_r$ and $\alpha^2\varphi_r<<\varphi_r''$, r(y) changes sign where φ_r'' is maximum. Therefore, velocity distributions with wide peaks have comparatively weaker vortices, while those with narrow peaks, as those of the wall inflexion points, have stronger vortices (table 7.1).

(5) The disturbance pressure has always an opposite sign to that of the main flow vorticity -U'i. The pressure is about constant over most of the disturbed part. For bounded flows its maximum value is always at the wall. The same conclusions apply to the tanh(y) profile at the critical Re. In contrast, the pressure of the temporally most amplified frequency (high Re) of tanh(y) profile has the same sign as -U'. It is clear, from table 7.1, that the disturbance pressure becomes weaker when -U'i is positive and small. This is true for time-dependent flow profiles with -U'i>0. For the wall inflexion points ($\omega_o t$=110 and 145 degrees), and for the wake and the tanh(y) profiles where -U'<0, the opposite is the case and the pressure is stronger where U'i is large.

b) The energy distribution of the fundamental disturbance

The energy balance for several time-dependent profiles at b=6, $\omega_0 t=30^\circ$ is shown in figures 7.9, while for $\omega_0 t=110^\circ$ (the core inflexion point) is shown in figure 7.10. The energy balance of the wall inflexion point of the same profile is shown in figure 7.11. All figures are at the same Re,α and c_r as before. The wake energy balance is shown in figure 7.12 and that of the tanh(y) profile in figure 7.13. Table 7.2 lists the maximum values of the energies shown in the figures.

From these figures the following conclusions can be drawn:

(1) The energy production is always concentrated in the area where the u velocity is concentrated. Their peaks roughly coincide with each other. However, the energy production width is about half the width of the u velocity, while the production is concentrated in the strong shear area as expected from (7.15). Therefore, it is narrow for the tanh(y) profile covering only one third of the whole flow width since U' is weak at the edges of the flow.

(2) As a rule (for the fundamental disturbance), there is always a concentration of loss of energy by viscous transport in the area between any two vortices, with more concentration on one of the vortices some times. At the

same time the dissipation has a valley in this region, while it is more concentrated in the areas where the vortices are strong. In the area between the strongest vortices (at least one is strong) there is a loss in energy due to the pressure transport. The energy production is high there in order to balance the loss in the area between the strongest vortex system. Thus, while both the viscous and the pressure transport weaken the region between the vortices, they add more to the core of the vortices where the energy production is smaller and the dissipation is large. In fact, the energy of the vorticies outside the production area is completely due to both transports. The fact that the transport contributes to the energy at the edge of the flow is now well established [Townsend (1976),p 206]

TABLE 7.2

The fundamental disturbance's energies maximum values

The Profile	Energy Prod.	Energy Diss.	Viscous Tt	Press. Tt
$\omega_0 t = 0°$	0.35561	0.69640	0.69640	0.23151
$\omega_0 t = 30°$	0.18863	0.11242	0.11242	0.10097
$\omega_0 t = 110°$ (1)	0.06269	0.02404	0.03134	0.03349
$\omega_0 t = 110°$ (2)	0.08282	0.35930	0.35930	0.09547
$\omega_0 t = 145°$ (2)	0.18454	0.58870	0.58870	0.16298
THE WAKE	0.18088	0.14334	0.08451	0.05848
TANH(Y)	671150.0	269800.0	214510.0	408160.0

(1) Core inflexion point
(2) Wall inflexion point

7.7: Summary And Comments On The Subharmonic Distribution

The subharmonic frequency is half the fundamental frequency. Considering the same phase velocity c_r for both of them, the wavenumber of the subharmonic is half that of the fundamental. Two time-dependent flow profiles, one wake profile and one tanh(y) profile were selected for demonstration. In all these cases, Re and c_r are the same as those of the fundamental while α is half that the fundamental. Table 7.3 lists the subharmonic maximum values of u,p and r. For each profile, the first line gives the maximum values normalised by the maximum u of the fundamental disturbance. The values listed in the second line are normalised by the maximum value of u of the subharmonic disturbance. This will facilitate easier comparison with the fundamental quantities given in table 7.1. In table 7.4, the maximum values of the energies are listed. These are already normalised by the square of the maximum of the subharmonic velocity u.

(a) The subharmonic velocities, pressure and vorticity distributions

Figures 7.14-7.17 show these distributions for the four cases considered. The essential features are:

(1) The v velocity at the centre of symmetrical profiles is not zero as in the case of the fundamental disturbance. The wake profile v has its maximum value at the centre. The maximum value of v of the tanh(y) profile, now, is

only about one third of the $\hat{u}$ maximum value and it is completely negative. Its maximum occur in the low velocity side.

(2) In the case of the wake, the central vortex becomes weaker with a valley at the centre of the flow. In the case of the tanh(y) profile, the two counter-rotating vortices in the central part of the flow are replaced by one vortex counter rotating with another two smaller vortices at the boundaries.

TABLE 7.3

The subharmonic maximum values

The Profile	$\hat{u}$	$\hat{p}$	$\hat{r}$
$\omega_0 t = 0°$	72.1980	117.58400	284.1650
	1.0	1.62860	9.1744
$\omega_0 t = 30°$	17.8280	7.92930	284.1650
	1.0	0.44480	15.9390
$\omega_0 t = 110°$ (1)	306.5142	177.87000	6465.0000
	1.0	0.58030	21.0920
$\omega_0 t = 110°$ (2)	464.3700	13.17300	4315.2860
	1.0	0.02837	9.2927
$\omega_0 t = 145°$ (2)	96.3970	122.63630	1048.8776
	1.0	1.27220	10.8808
THE WAKE	28.5070	15.23507	23.0112
	1.0	0.53443	0.8072
TANH(Y)	215200.0	155053.00	269215.00
	1.0	0.72051	1.2510

(1): Core inflexion point.
(2): Wall inflexion point.

(3) The pressure, of the subharmonic disturbance of the

tanh(y) profile, (figure 7.17), in the high velocity side, remains about the same as that of the fundamental disturbance pressure, while at the low velocity side it become stronger. For the wake profile (figure 7.16), the pressure as well as $\hat{u}$ have the same sign as -U'. The pressure again is about constant in the outer part of the flow. The time-dependent flow wall inflexion point [$\omega_o t = 110°^{(2)}$] pressure also has the same sign as -U', in contrast to that of the core inflexion point [$\omega_o t = 110°^{(1)}$] where it has the same sign as the pressure of fundamental disturbance (figures 7.14 and 7.15).

(b) The energy balance of the subharmonic

The same energy equation (7.13) is used for the subharmonic except that the equation now has a right hand side in the form of triple products. This quantity is practically zero, therefore, it will not be shown here. The essential features of the subharmonic energy balance can be summarised as follows: (1) The subharmonic normalised energy quantities (table 7.4) are several times larger than the fundamental normalised quantities in the case of time-dependent flow profiles (table 7.2). For the two free shear layers, (the wake and tanh(y)), these are about half of those of the fundamental energies.

(2) The energy production is similar to that of the fundamental disturbance in all cases, except that of the wall inflexion point. In this case, it is completely negative, and because of negative dissipation, the production is completely due transport in general and to

the pressure transport in particular.

(3) The viscous transport is almost exactly that of the fundamental disturbance.

TABLE 7.4

The subharmonic energies maximum values

The Profile	Energy Prod.	Energy Diss.	Viscous Tt	Press. Tt
$\omega_0 t = 0°$	2.1669	1.7382	2.5472	4.4867
$\omega_0 t = 30°$	7.9926	6.0831	5.7383	15.0509
$\omega_0 t = 110°$ (1)	2.5366	1.4496	1.2466	1.2816
$\omega_0 t = 110°$ (2)	2.9778	7.1995	7.1995	5.3316
$\omega_0 t = 145°$ (2)	8.5233	5.5680	8.3554	13.3464
THE WAKE	0.0863	0.0877	0.0766	0.0218
TANH(Y)	215942.0	152717.0	126849.0	122599.0

(1): Core inflexion point.
(2): Wall inflexion point.

(4) The pressure transport distribution also is similar to that of the fundamental, except that it is stronger in the areas where it was weaker in the first case.

Therefore, in the cases of both the wake and the tanh(y) profiles, the transports will transfer energy from the areas where the subharmonic vortices are strong and where the production is large, to the areas where the vortex is weak. Consequently, in the case of the tanh(y) profile, the energy of the vortices outside the core of the flow is completely due to the pressure transport,

while at the extreme edges of the flow it is largely due to viscous transport.

7.8: Comments on Tanh(y) and Time-Dependent Flows

7.8.1: The subharmonic of tanh(y) profile

It is interesting that in the central area of the flow, the subharmonic has one strong vortex replacing the counter-rotating vortex system of the fundamental disturbance. This is exactly what has been observed experimentally where vortices merge into a single vortex when the subharmonic reaches its saturation [Winant and Brownd (1974)]. Corcos and Sherman (1976) using a different approach showed the coalescence of the double-vortex structure into a single vortex at the subharmonic frequency. They also showed that large strain rates occur during pairing. Kelley (1967) suggested that the subharmonic grows through resonance interaction with the fundamental and has shown that for this to occur the fundamental disturbance amplitude should reach a threshold level of 12 % of the mean flow velocity. His analysis was based on the weak nonlinear theory. Recent experiments of Ho and Huang (1982) have shown, in the case of forcing, that the level required is as low as 0.02 %. Equation (7.8) and (7.12) also give different levels for different profiles as is evident from a comparison of table 7.1 with table 7.3. In equation 7.6, it is generally assumed that

$$\varepsilon u \geq \varepsilon^2 \hat{u} \qquad (7.20)$$

For equality in (7.20) to be satisfied, the profile at

$\omega_o t=145^\circ$ requires $\varepsilon u=1.03\%$, while for $\omega_o t=110^\circ$[2], $\varepsilon u=0.2\%$ only. However, it is as high as 5.61 % for $\omega_o t=30^\circ$. For the wake profile at $x1=50$, $\varepsilon u=3.5$ %. The tanh(y) profile however, has a very large value of $\hat{u}$ which corresponds to the unrealistically small value of $\varepsilon u=0.00046\%$. In fact, comparison between the energies in table 7.2 (and table 7.4) shows that the tanh(y) profile has levels of energies about a million times those of the wake for the same levels of u (and $\hat{u}$). The same is true for time-dependent flow profiles in the case of u, and about one order of magnitude less in the case of $\hat{u}$. This, despite the fact that both its pressure and the vorticity maximum values are less than those of the other profiles (tables 7.1 and 7.3).

7.8.2: Disturbances in time-dependent flow

In section 7.5, the fundamental disturbance velocities pressure and vorticity distributions were discussed in some details for the profiles at $\omega_o t=30^\circ$ and $\omega_o t=110^\circ$. Here, another two profiles will be added. These are also for $\beta=6$, and at $\omega_o t=0^\circ$ and $\omega_o t=145^\circ$. In this way, a clear picture of the disturbance behaviour in half a cycle of the flow oscillation can be built up.

The profile at $\omega_o t=0^\circ$ has a negative velocity for $y>0.23$, (figure 7.22). The disturbance v velocity changes sign exactly where the profile does. The change in the sign of the velocity did not affect the pressure distribution in any form. Following the disturbance

changes from $\omega_{ot}=0^{\circ}$ through $\omega_{ot}=30^{\circ}$ to $\omega_{ot}=110^{\circ}$ (figures 7.22,7.2 and 7.5), it is clear that the disturbance starts strong near the wall ($\omega_{ot}=0^{\circ}$) and its effect remains strong there at $\omega_{ot}=30^{\circ}$, while it moves completely away from the wall ($\omega_{ot}=110^{\circ}$,core inflexion point). Remembering that the mean flow velocity near the wall increases slowly at low ω_{ot} and remains almost constant at $\omega_{ot}>30^{\circ}$ (chapter 6, figures 6.2 and 6.3), it clear that the effect of the disturbances (if they grow) on the wall area in the acceleration phase will be strong at Re less than the transition Re of the flow, since the critical Re of the profiles at low ω_{ot} is far less than the transition one. Plates produced by Hino et al (1983) show such effects on the wall area and at the same time they show the vortices at the core area. It is evident that the growth of such disturbances in the wall area in the acceleration phase of the flow will not bring the whole flow into transition to turbulence which was shown in chapter 6 to occur at high Re (for $\beta=6$ Re critical=3420). However, it produces a more disturbed flow in the wall area and may bring transition at relatively lower Re than that of the core flow as was observed experimentally in chapter 5. The critical Re of the wall inflexion point ($\omega_{ot}=110^{\circ}$) is very high (5720), while that of $\omega_{ot}=145^{\circ}$ is lower than that of the flow as a whole. The growth rate of the last profile is larger than those of the core inflexion points (chapter 4), while the vorticity is stronger (figure 7.23). The vortices of profiles at about $\omega_{ot}=145^{\circ}$ were observed to be persistent and strong (Hino et al (1983).

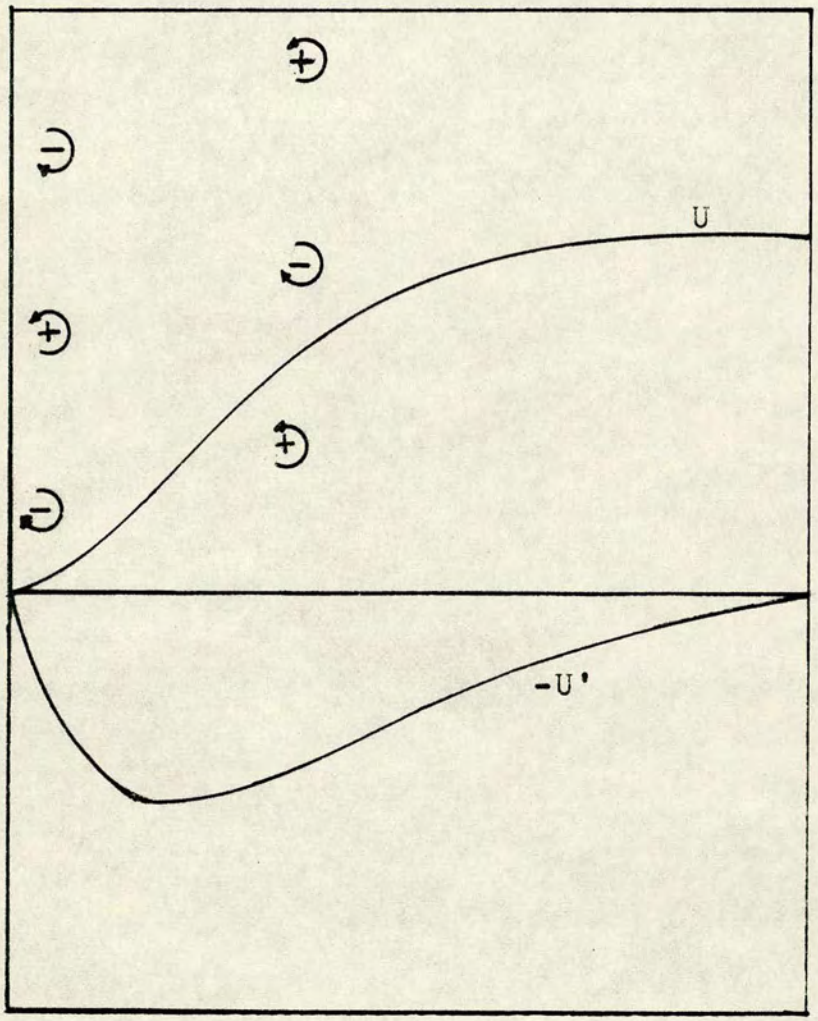

Figure 7.1: Schematic representation of disturbances to which an inflexional parallel shear flow is unstable.

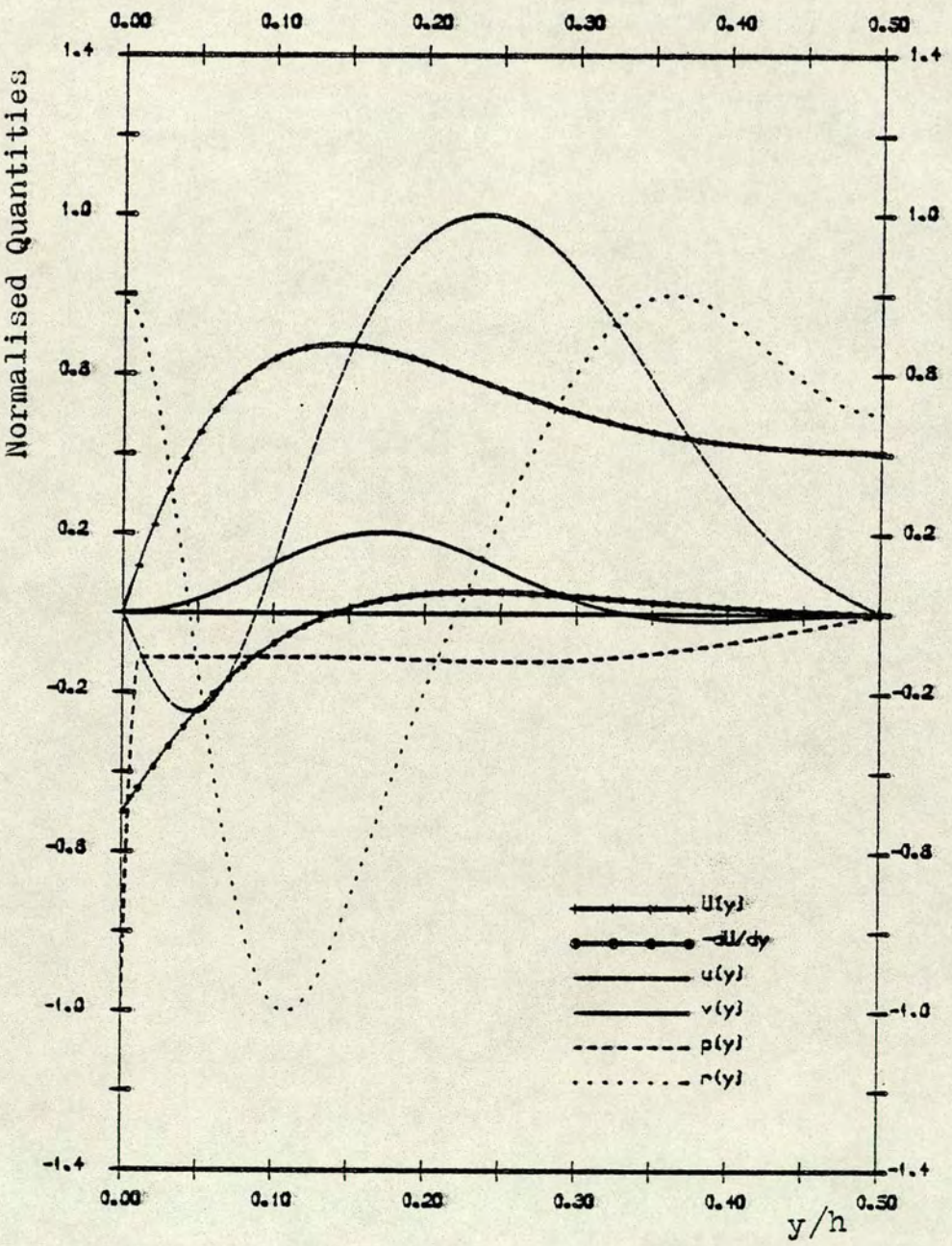

Figure 7.2: The fundamental disturbance velocities u(y), v(y), pressure p(y) and vorticity r(y). Time-dependent flow: $\beta = 6$, $\omega_0 t = 30^\circ$. Re = 882.16, $\alpha = 4.3185$ and $c = 0.559157$

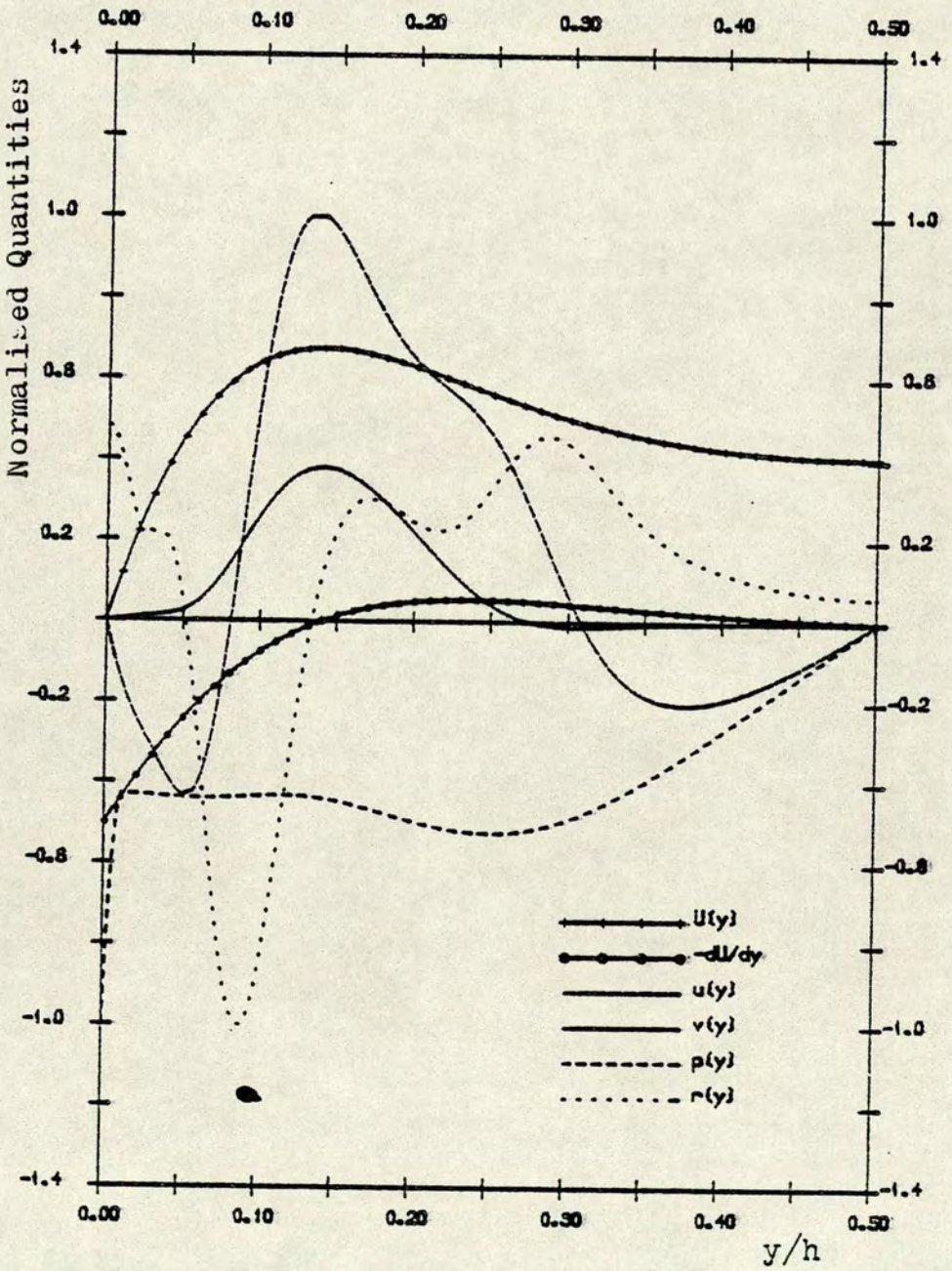

Figure 7.3: The disturbance velocities u(y),v(y), pressure p(y) and vorticity r(y). Time-dependent flow: β=6, 30°. On the upper branch of the neutral stability curve. Re=5000, α=7.133, c =0.55887.

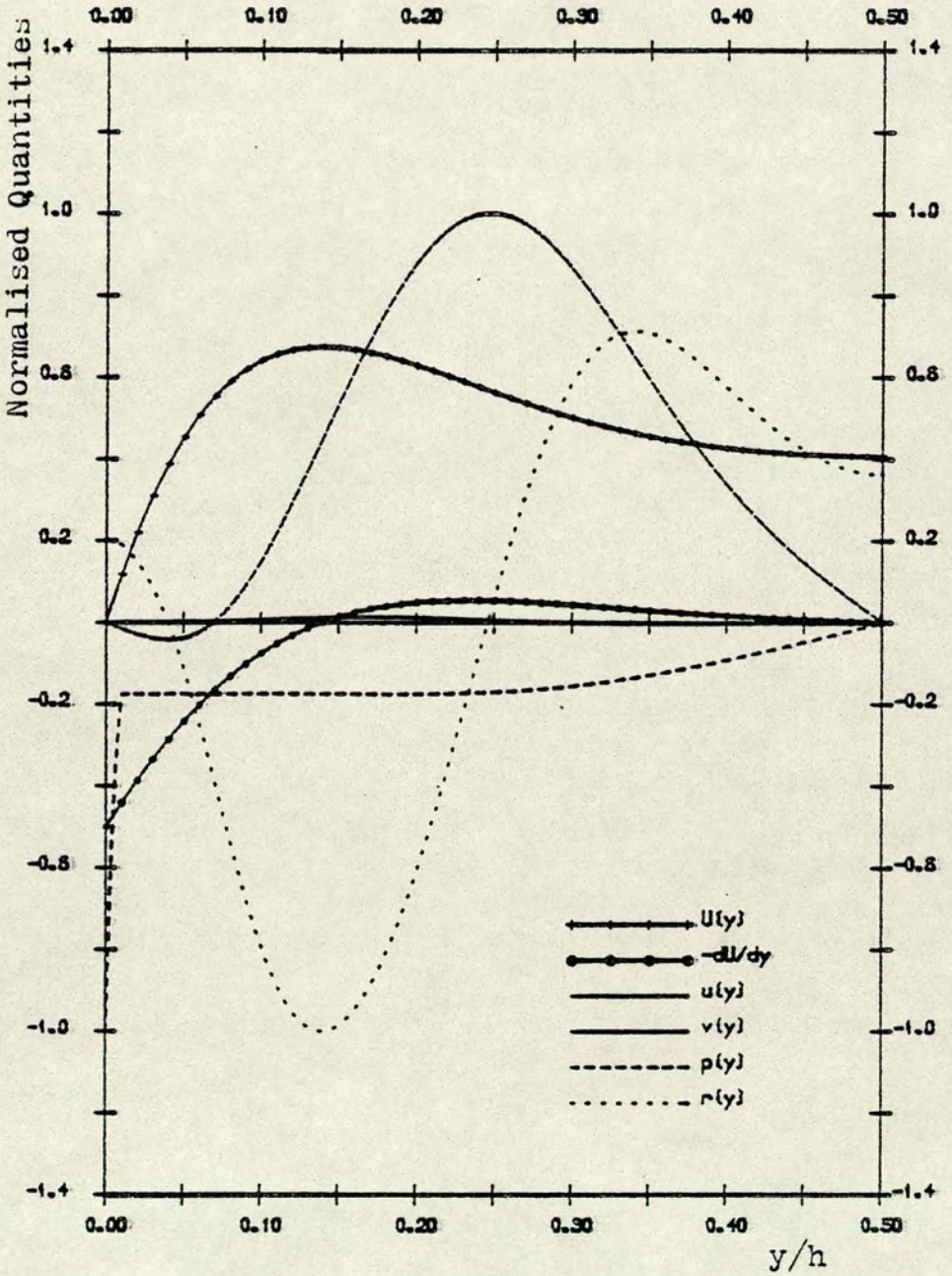

Figure 7.4: The disturbance velocities u(y),v(y), pressure p(y) and vorticity r(y). Time-dependent flow: β=6, 30°. On the lower branch of the neutral stability curve Re=5000 , α =1.02 , c =0.67487.

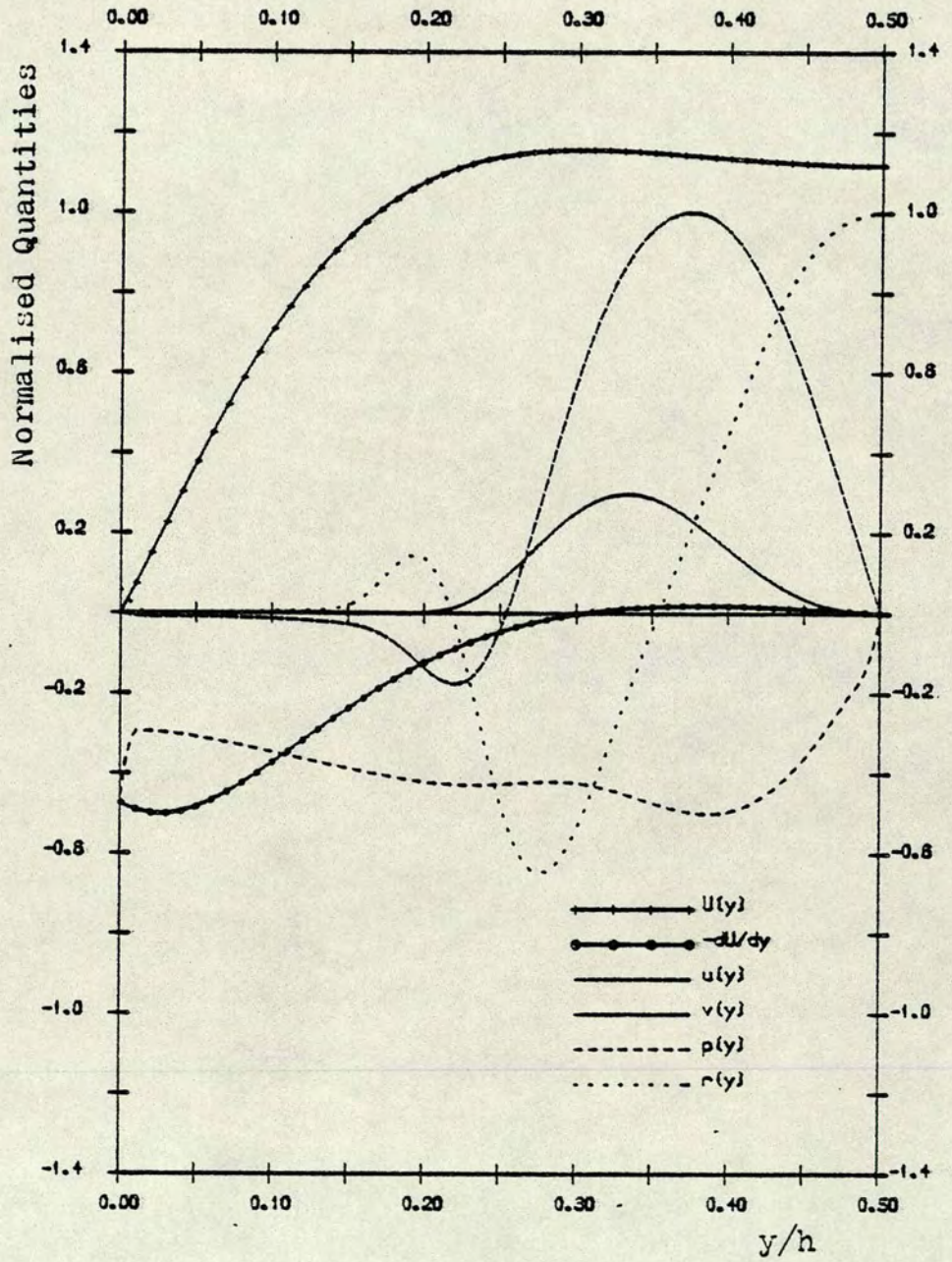

Figure 7.5: The disturbance velocities u(y),v(y), preasure p(y) and vorticity r(y). Time-dependent flow: β=6, 110°. The core inflexion point , Re(criticalk=5720.17, α=8.09 , c = 1.14047.

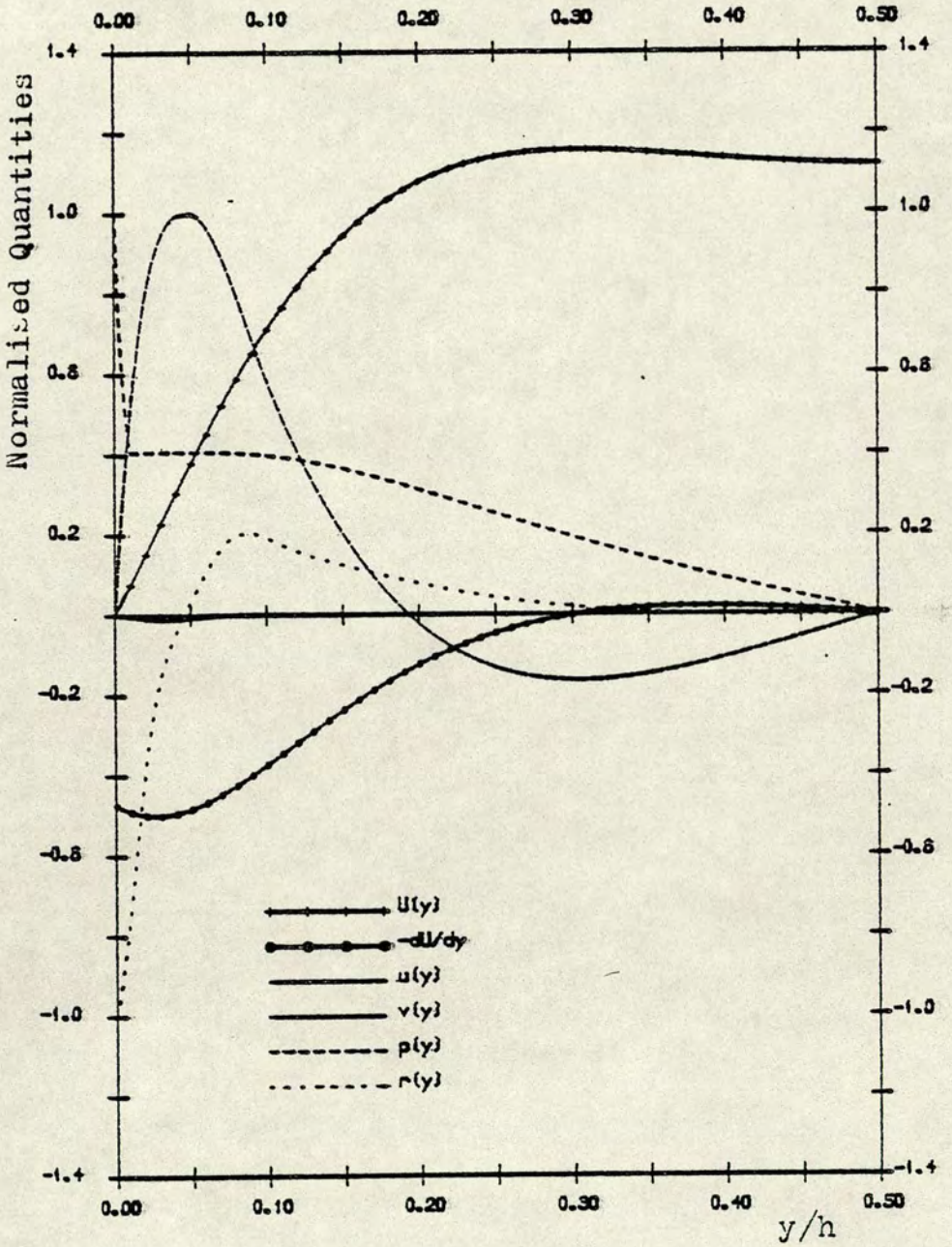

Figure 7.6: The disturbance velocities u(y),v(y), pressure p(y) and vorticity r(y). Time-dependent flow: β=6, 110°. Near the wall inflexion point , Re(critical)=8742.2, α =3.33, c =0.387137.

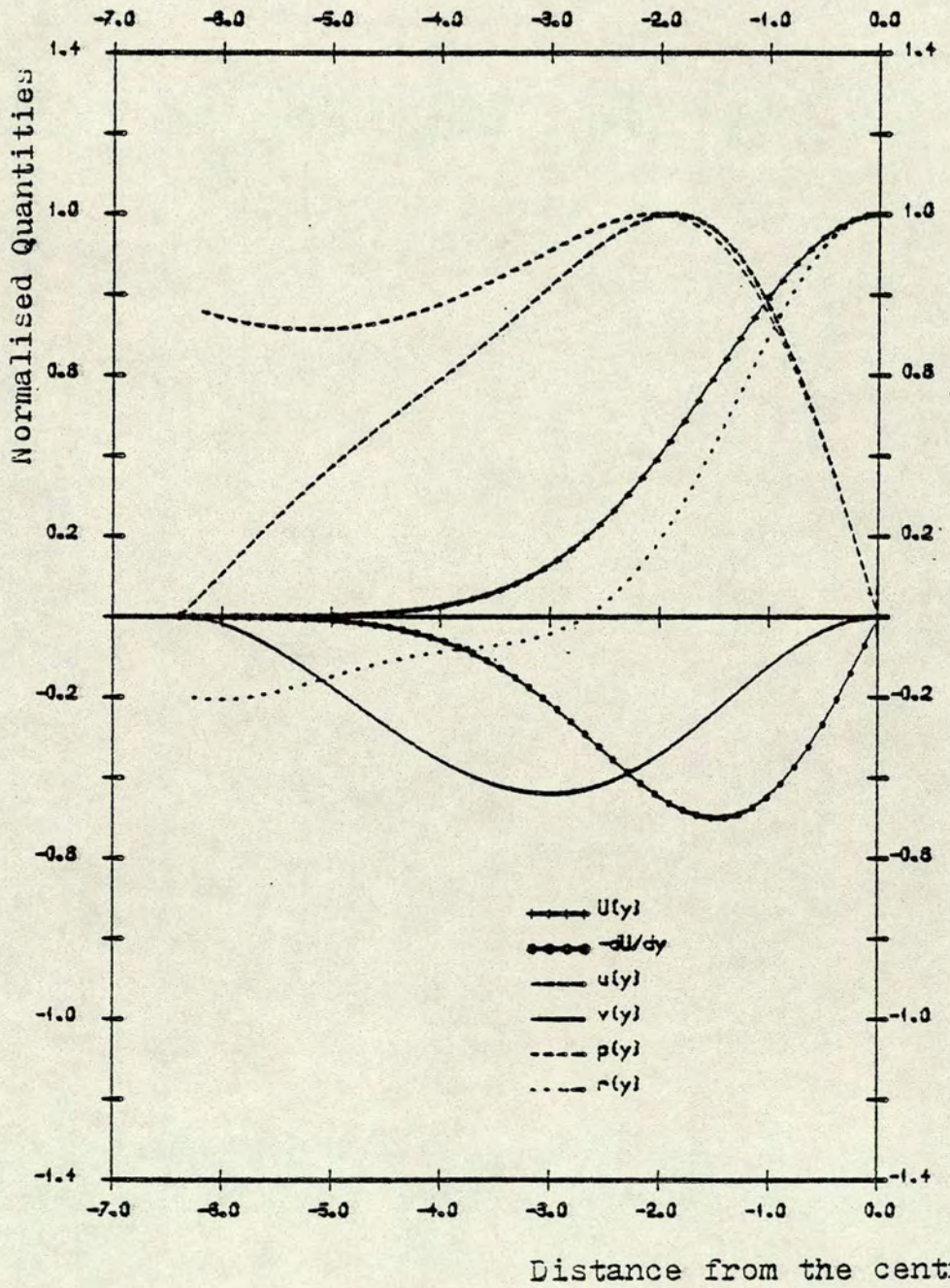

Figure 7.7: The fundamental disturbance velocities u(y) and v(y), pressure p(y) and vorticity r(y). The wake: xl=50; Re =5.559, α =0.42557, c =0.2573.

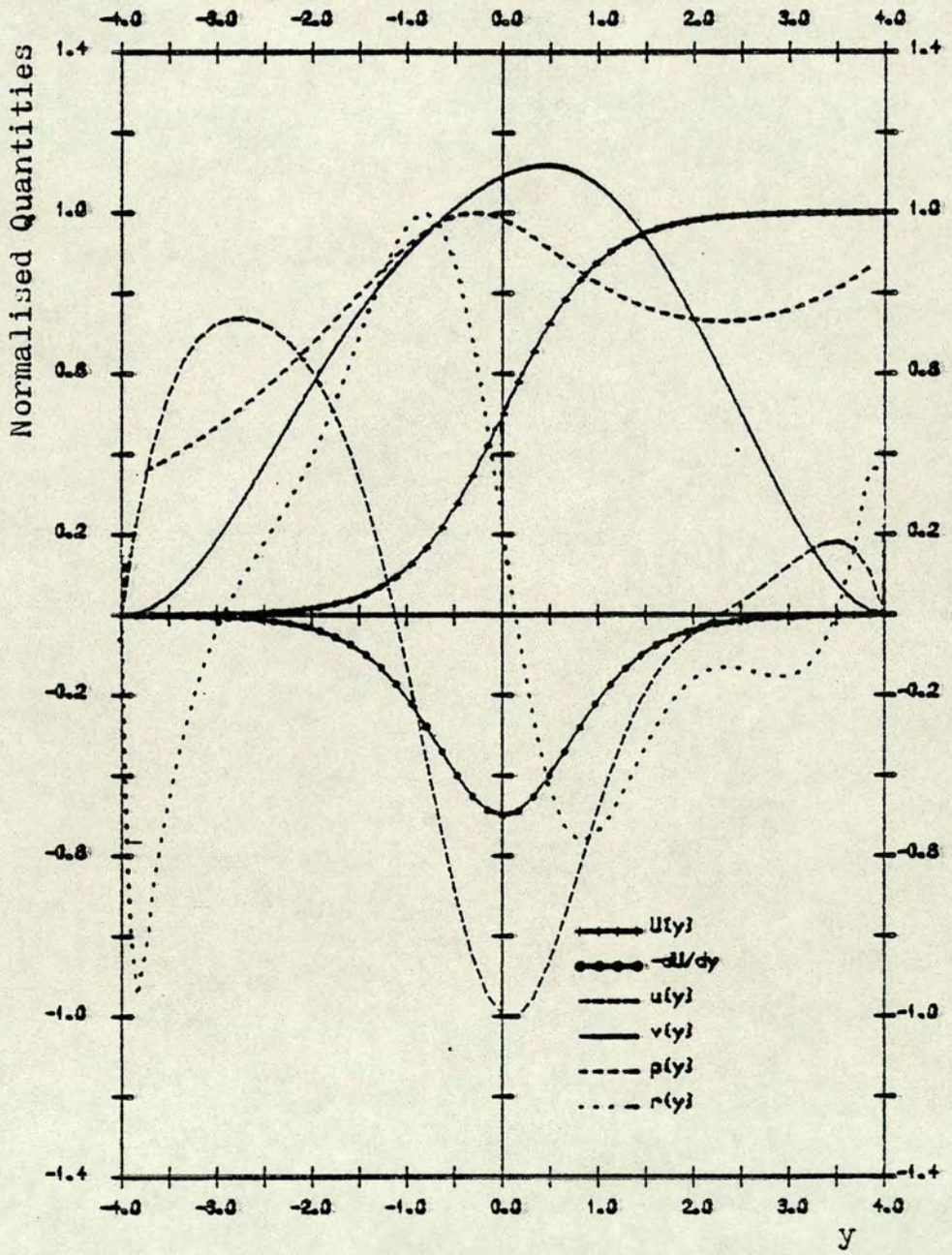

Figure 7.8: The fundamental disturbance velocities u(y) and v(y), pressure p(y) and vorticity r(y). Tanh(y) profile: Re =12, α =0.38, c =0.5.

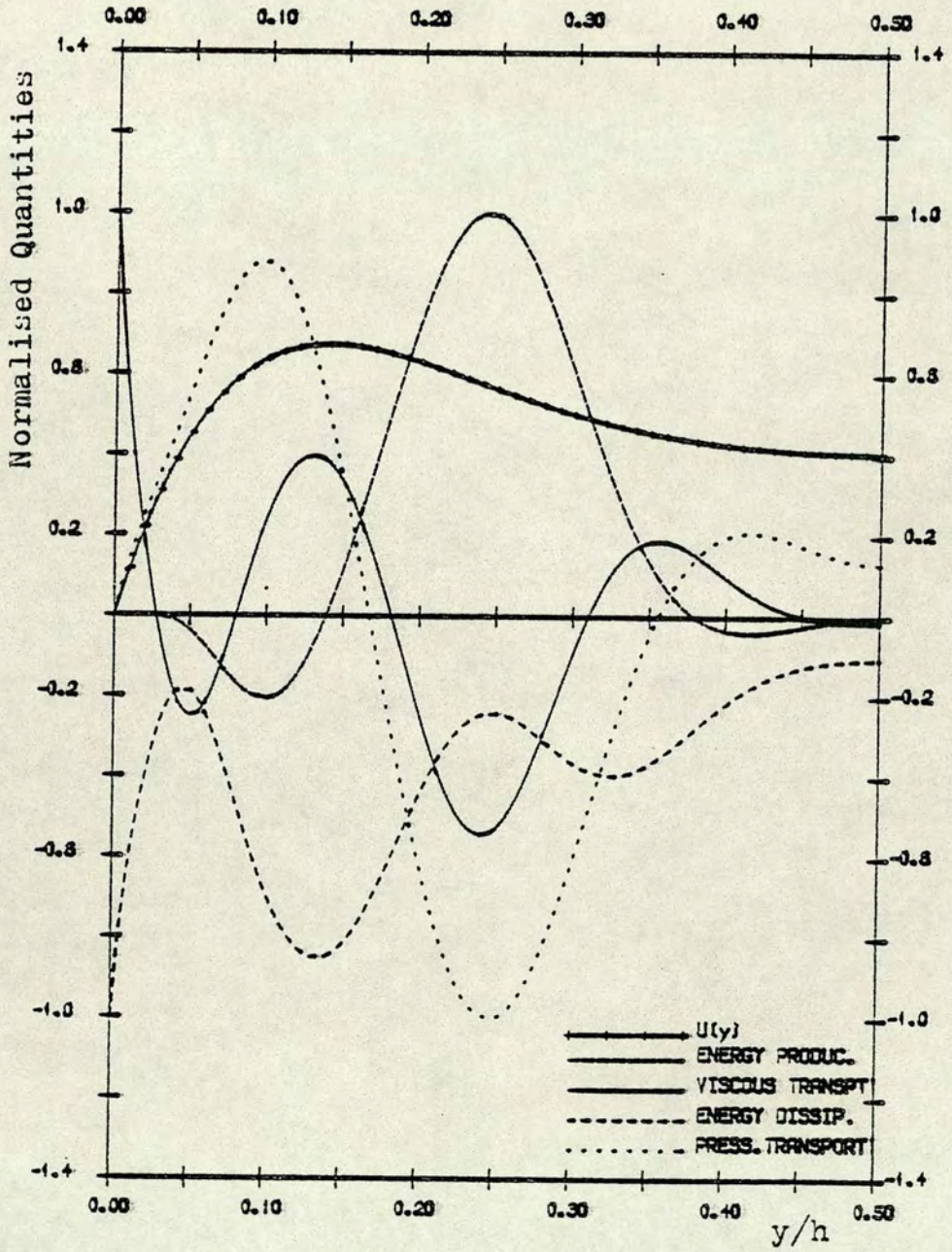

Figure 7.9: The disturbance energy balance. Time-dependent flow: β=6, 30°. Re, α, c as in figure 7.1 .

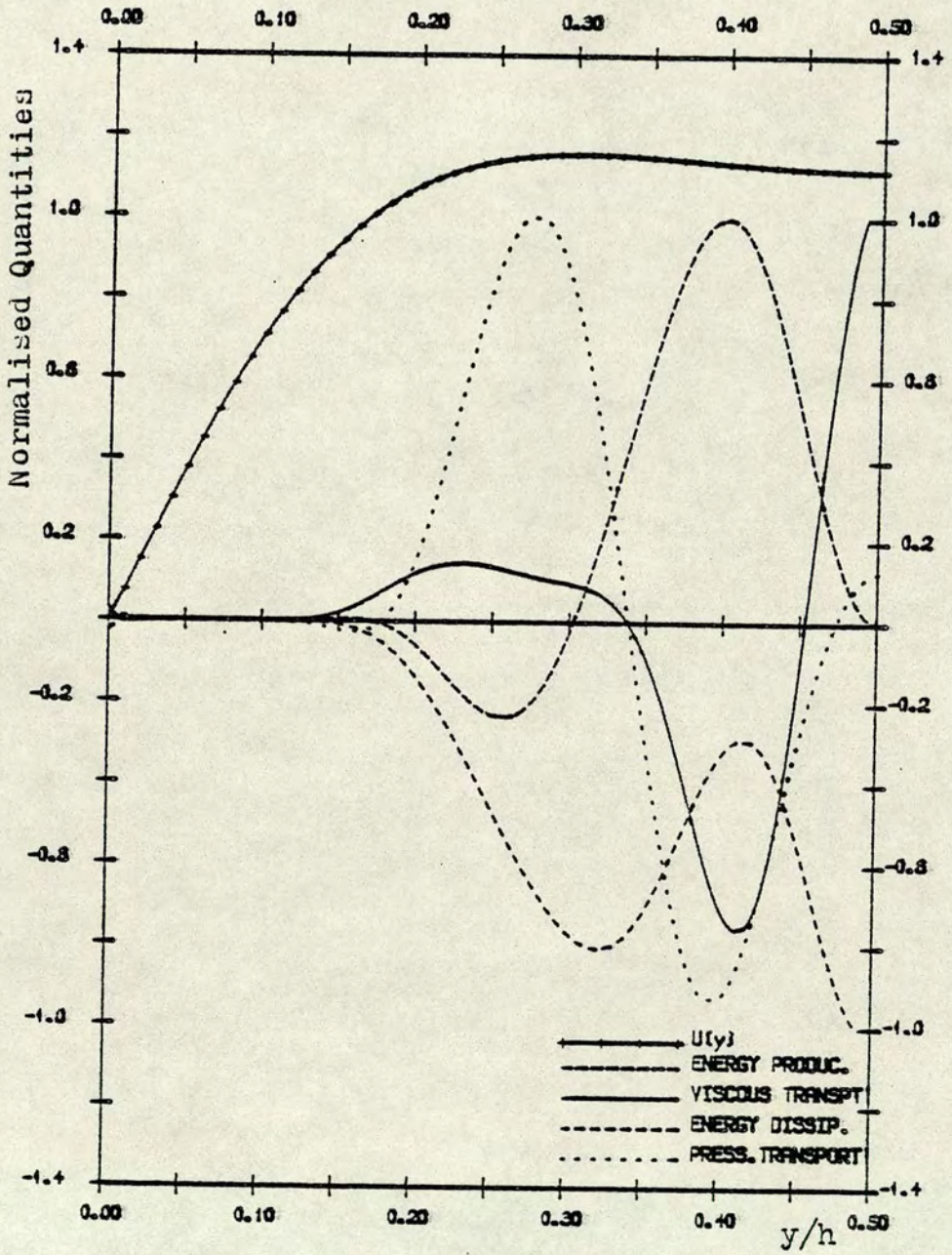

Figure 7.10: The disturbance energy balance. Time-dependent flow: β=6, 110°. The core inflexion point.

Re, α, c as in figure 7.4 .

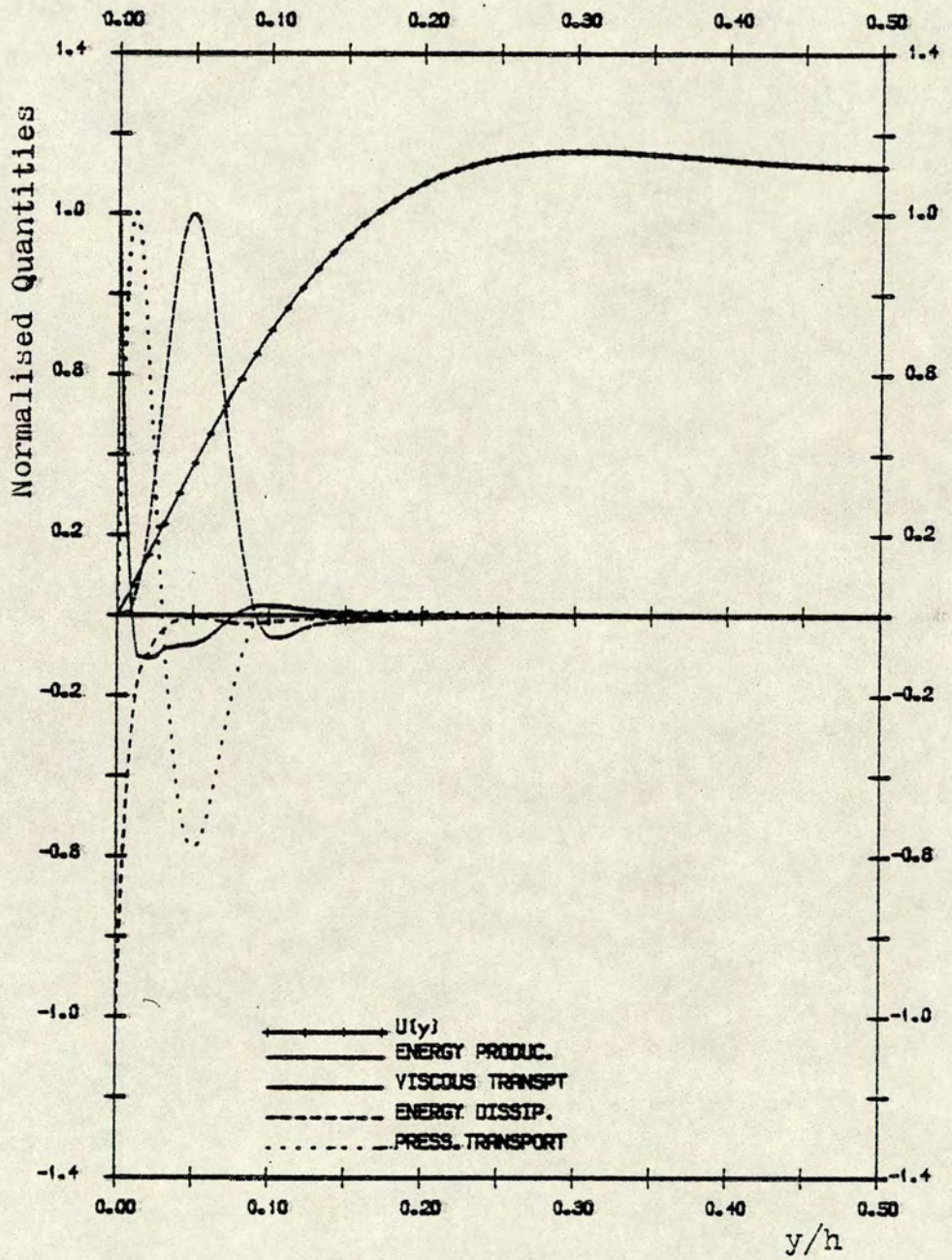

Figure 7.11: The disturbance energy balance. Time-dependent flow: β=6, 110°, near the wall inflexion point .
Re, α, c_r as in figure 7.5 .

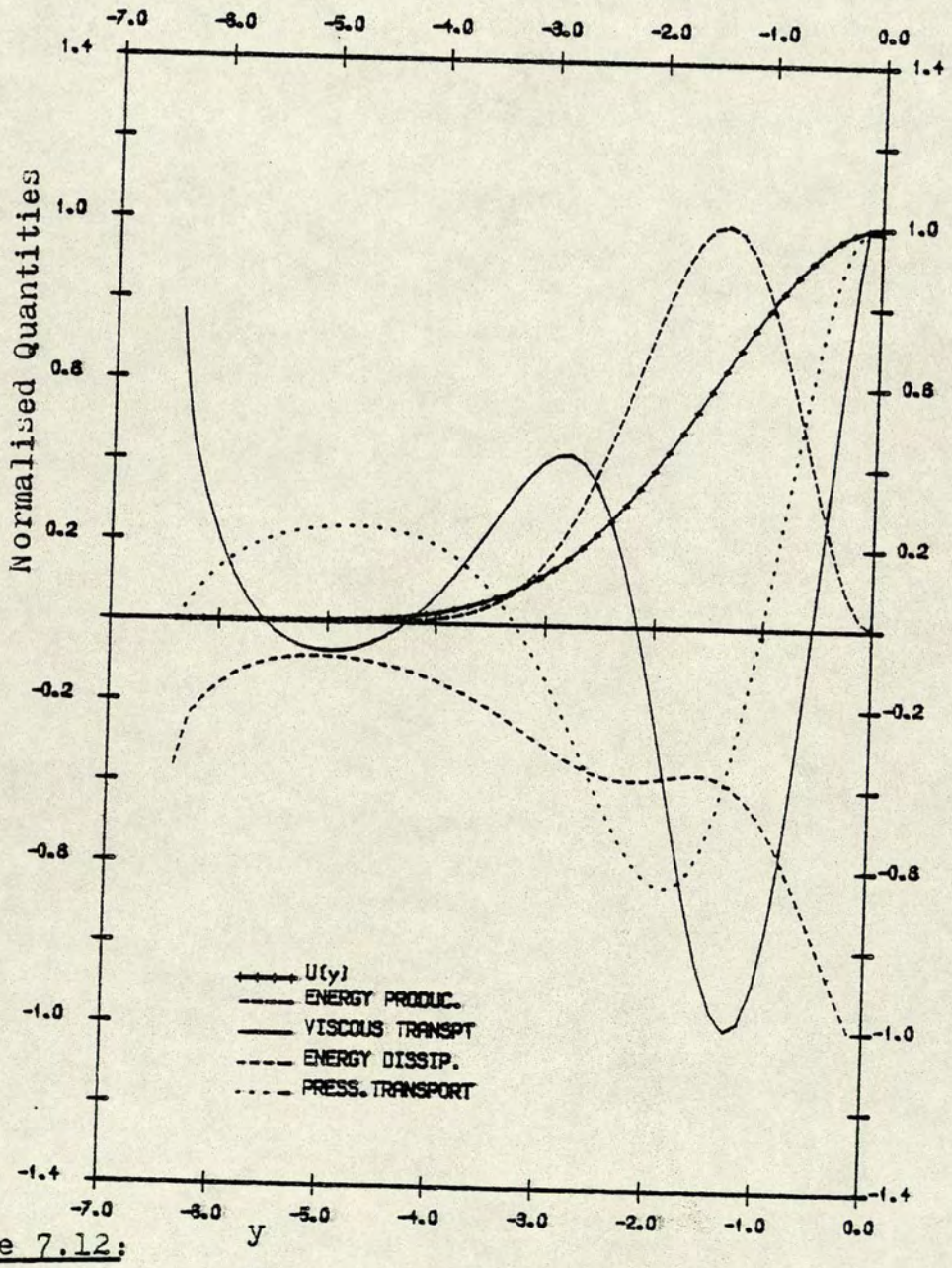

Figure 7.12:

The fundamental disturbance energy balance.
The wake: x1=50. Re, α and c as in figure 7.7.

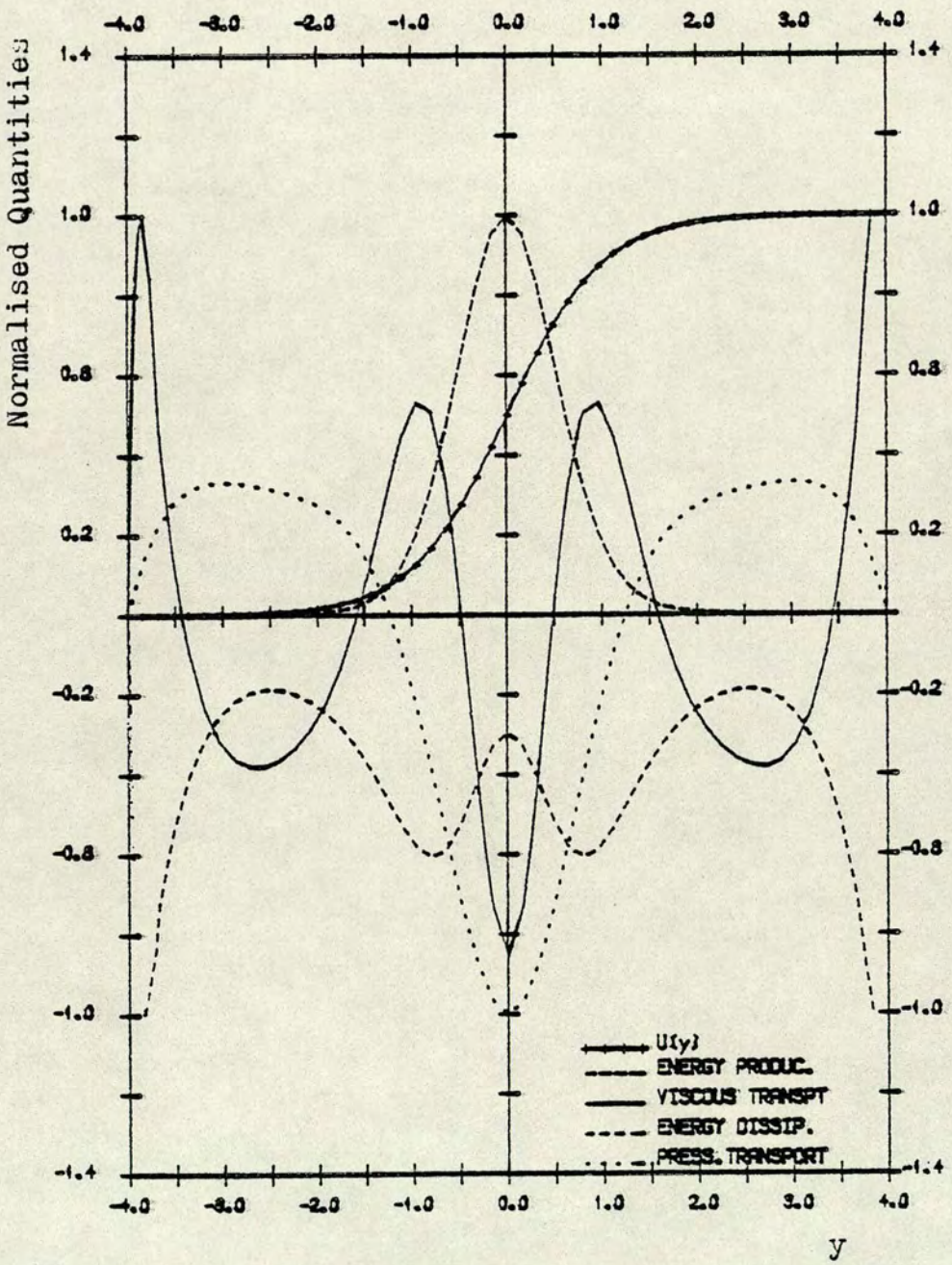

Figure 7.13: The fundamental disturbance energy balance. Tanh(y) profile: Re, α and c as in figure 7.8.

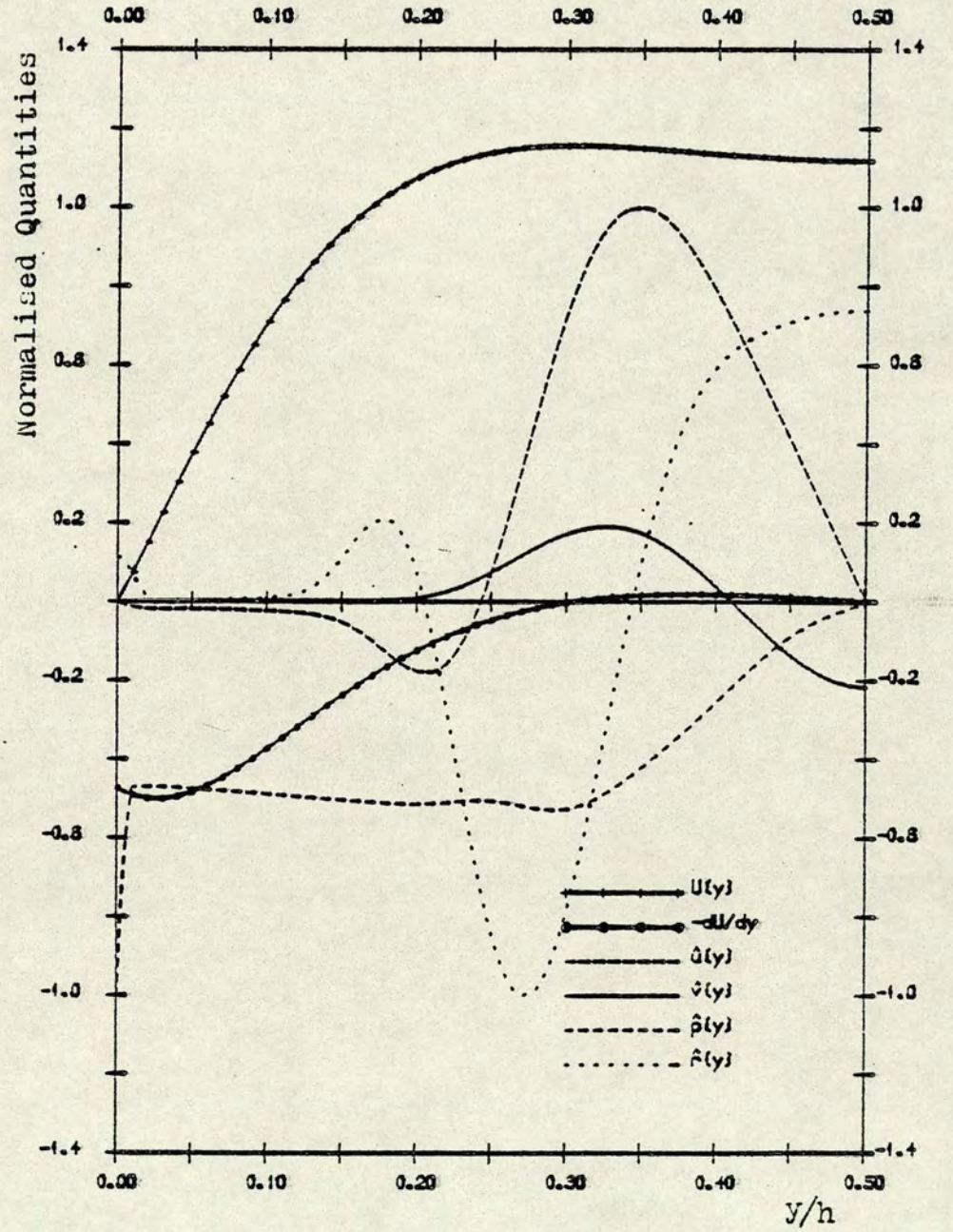

Figure 7.14: The subharmonic velocities $\hat{u}(y)$,$\hat{v}(y)$, pressure $\hat{p}(y)$ and vorticity $\hat{r}(y)$. Time-dependent flow: β=6, 110°, the core inflexion point . Re,c as in figure 7.4 α =4.045.

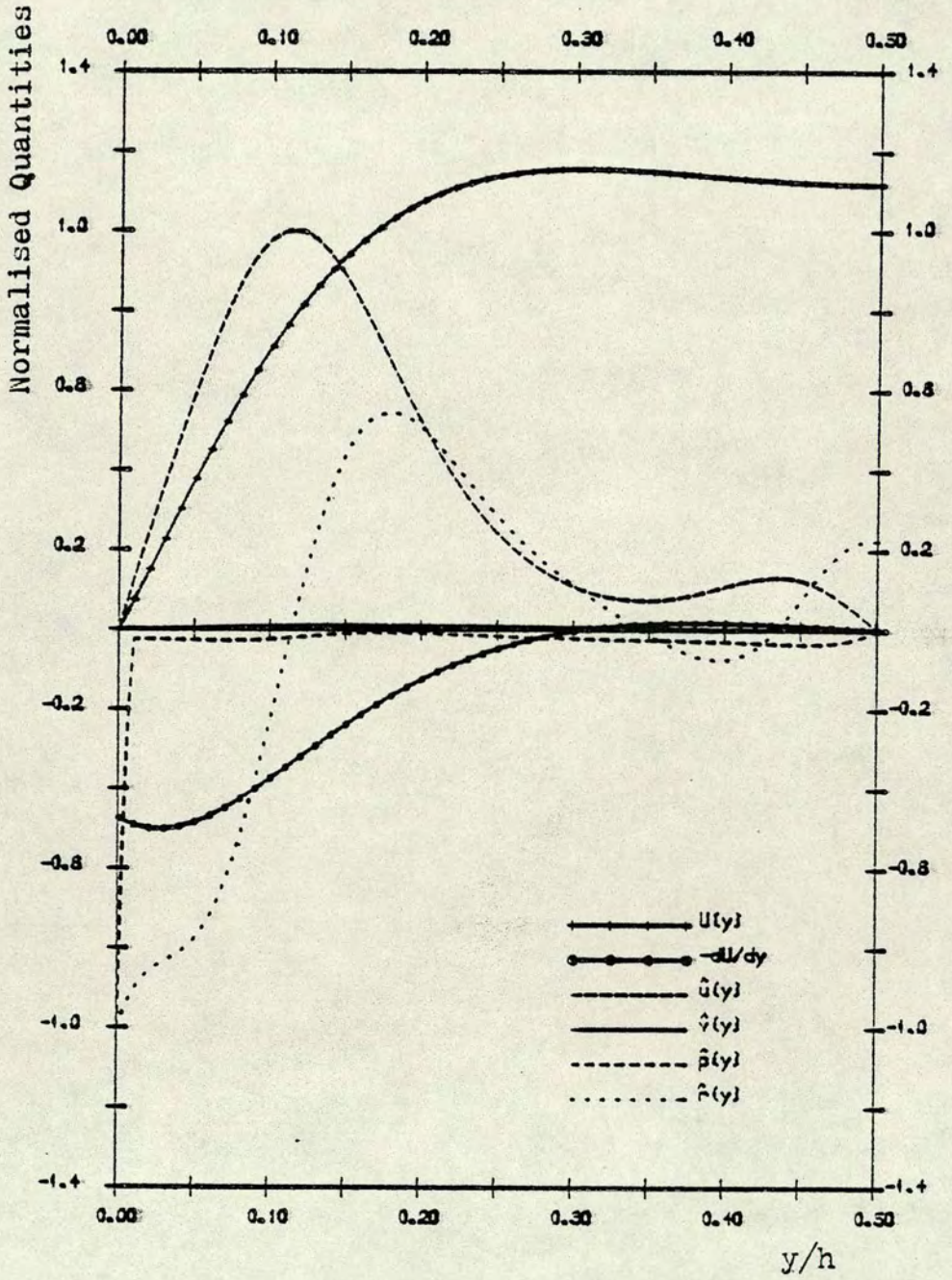

Figure 7.15: The subharmonic velocities $\hat{u}(y)$,$\hat{v}(y)$, pressure $\hat{p}(y)$, and vorticity $\hat{r}(y)$. Time-dependent flow: β=6, 110°, near the wall inflexion point . Re,c as in figure 7.5 α =1.665.

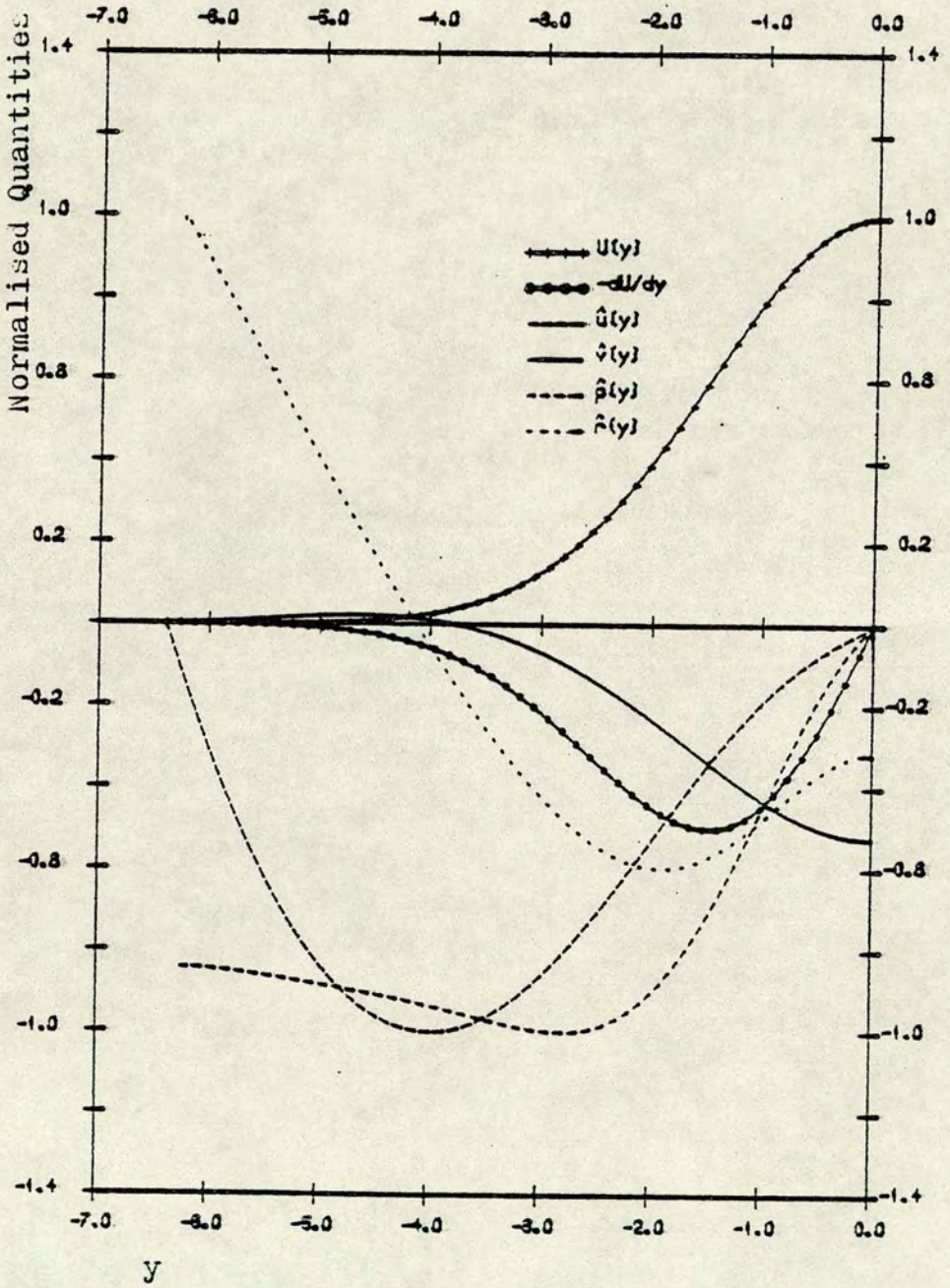

Figure 7.16: The subharmonic velocities $\hat{u}(y)$ and $\hat{v}(y)$, pressure $\hat{p}(y)$ and vorticity $\hat{r}(y)$. The wake profile: x1=50. Re and c as in figure 7.7. α=0.212785.

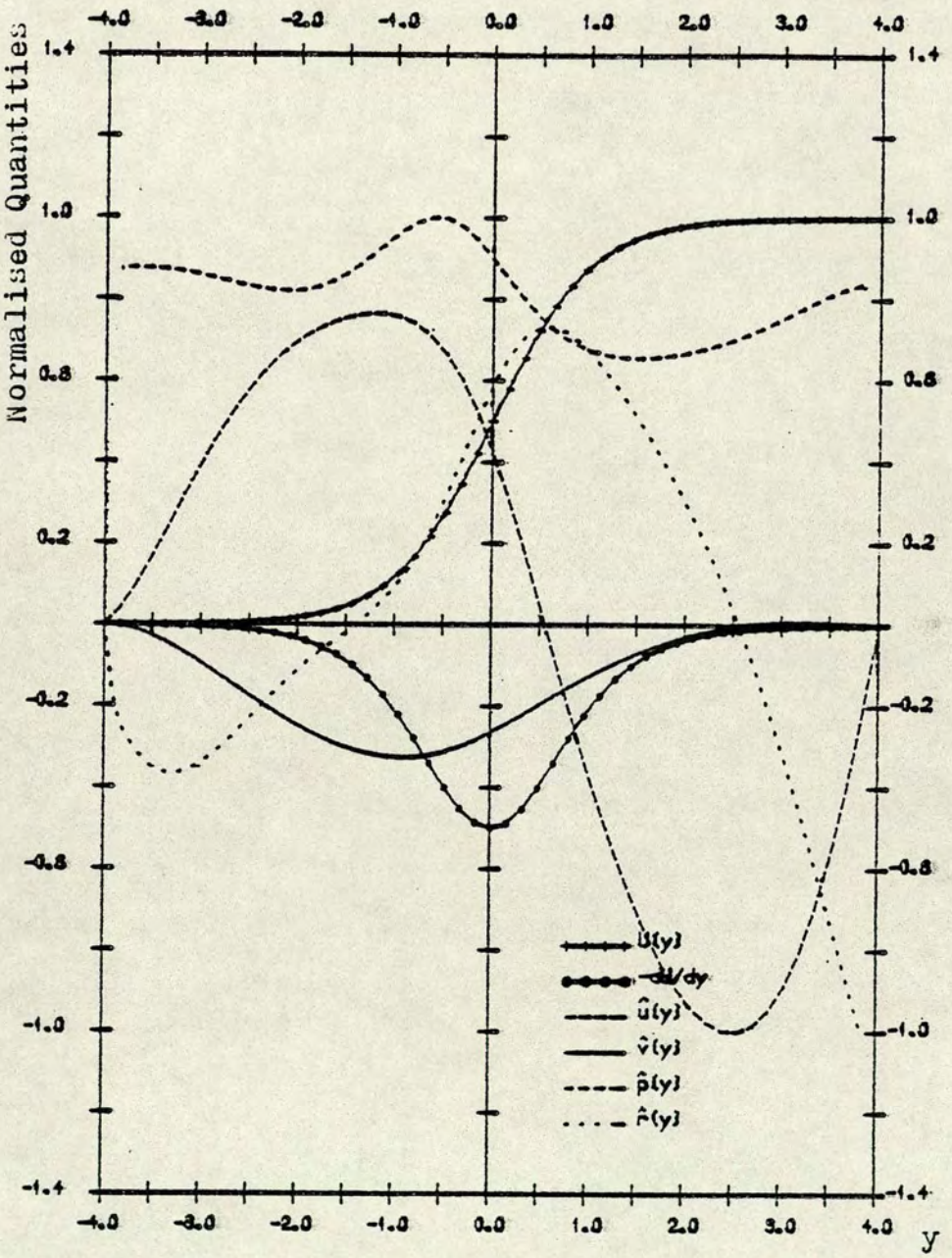

Figure 7.17: The subharmonic velocities $\hat{u}(y)$ and $\hat{v}(y)$, pressure $\hat{p}(y)$ and vorticity $\hat{r}(y)$. Tanh(y) profile: Re=12, α =0.19, c=0.5.

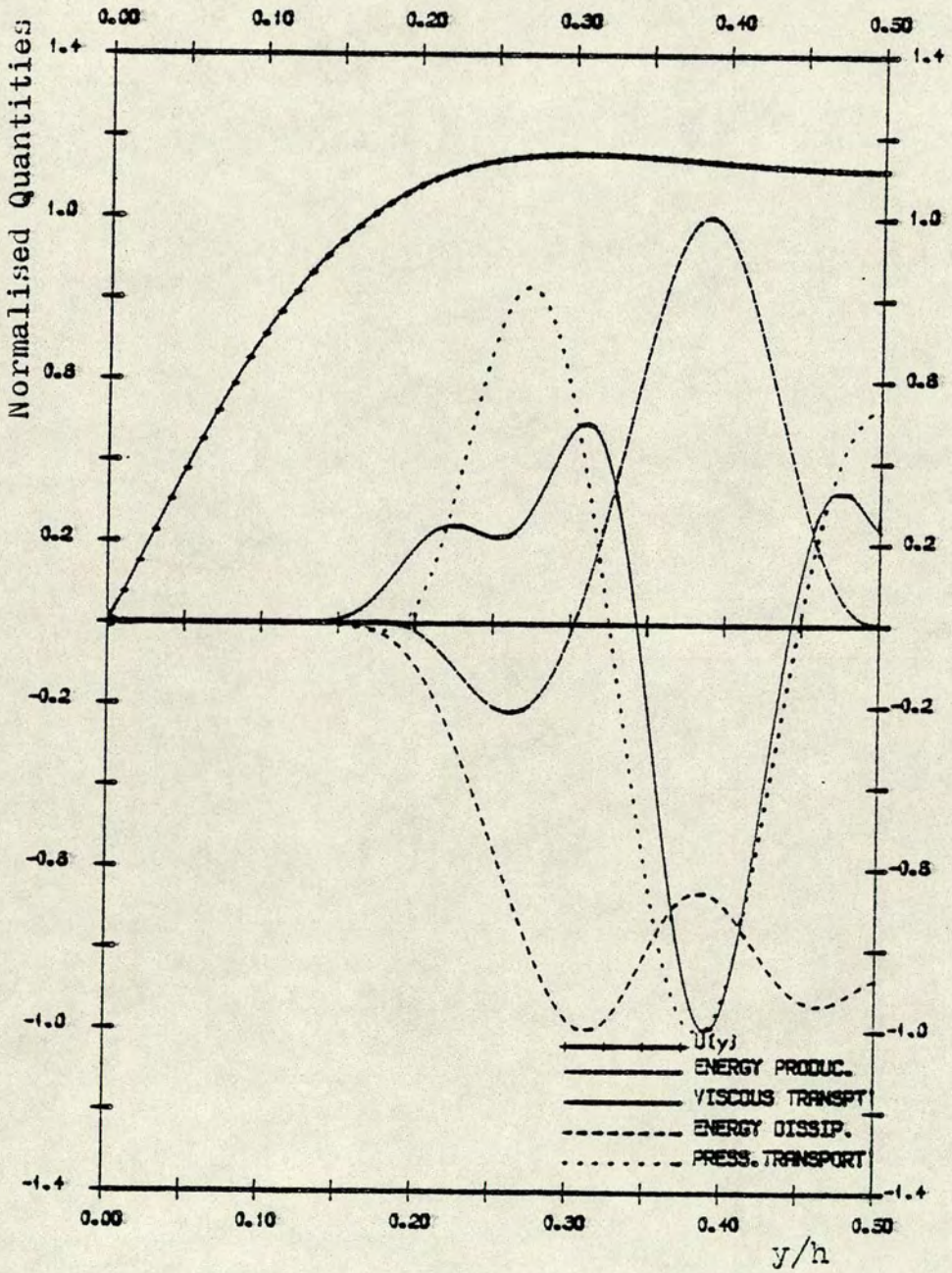

Figure 7.18: The subharmonic energy balance. Time-dependent flow: β=6, 110°, the core inflexion point. Re, c, as in figure 7.13.

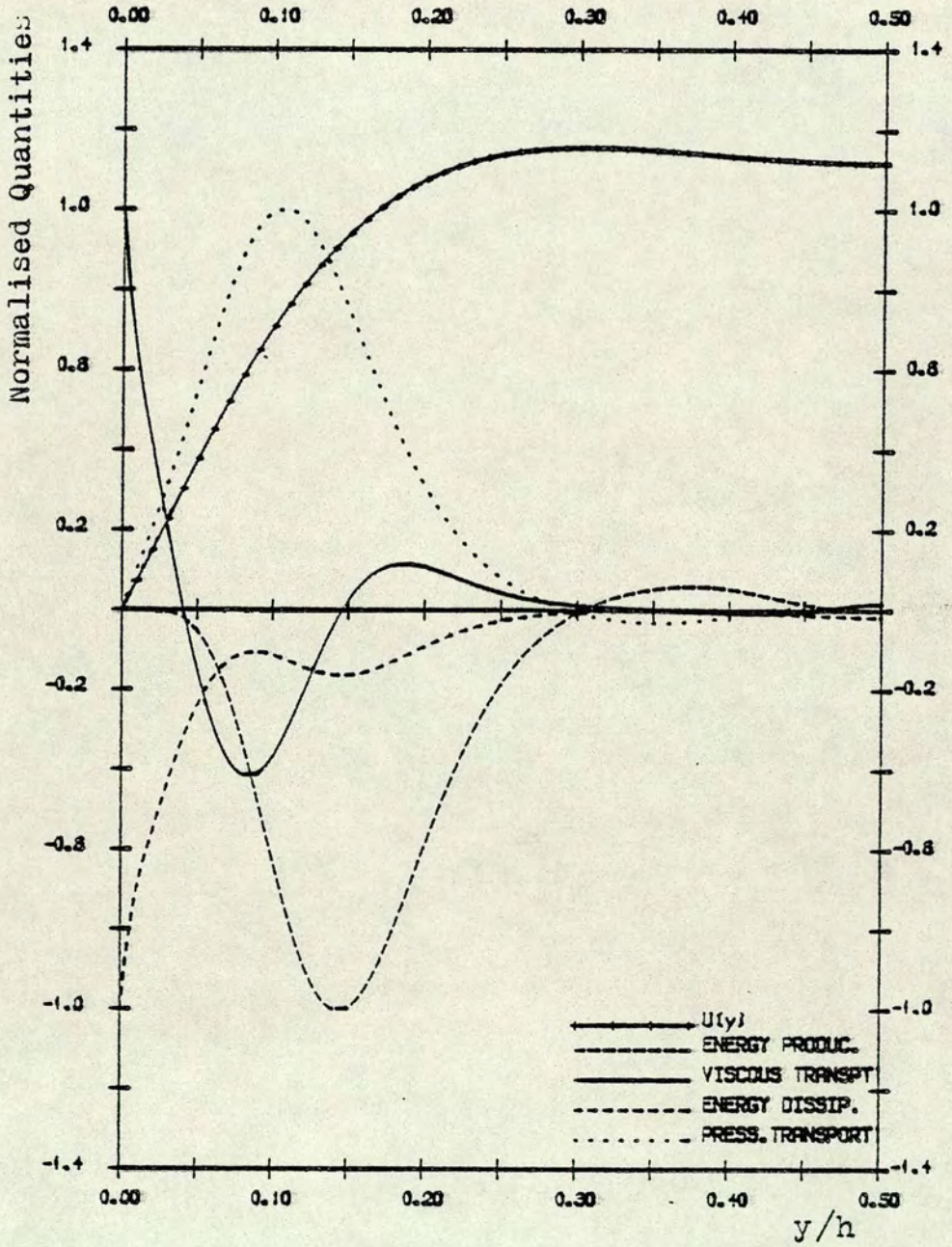

Figure 7.19: The subharmonic energy balance. Time-dependent flow: β=6, 110°, near the wall inflexion point.
Re, α, c as in figure 7.14.

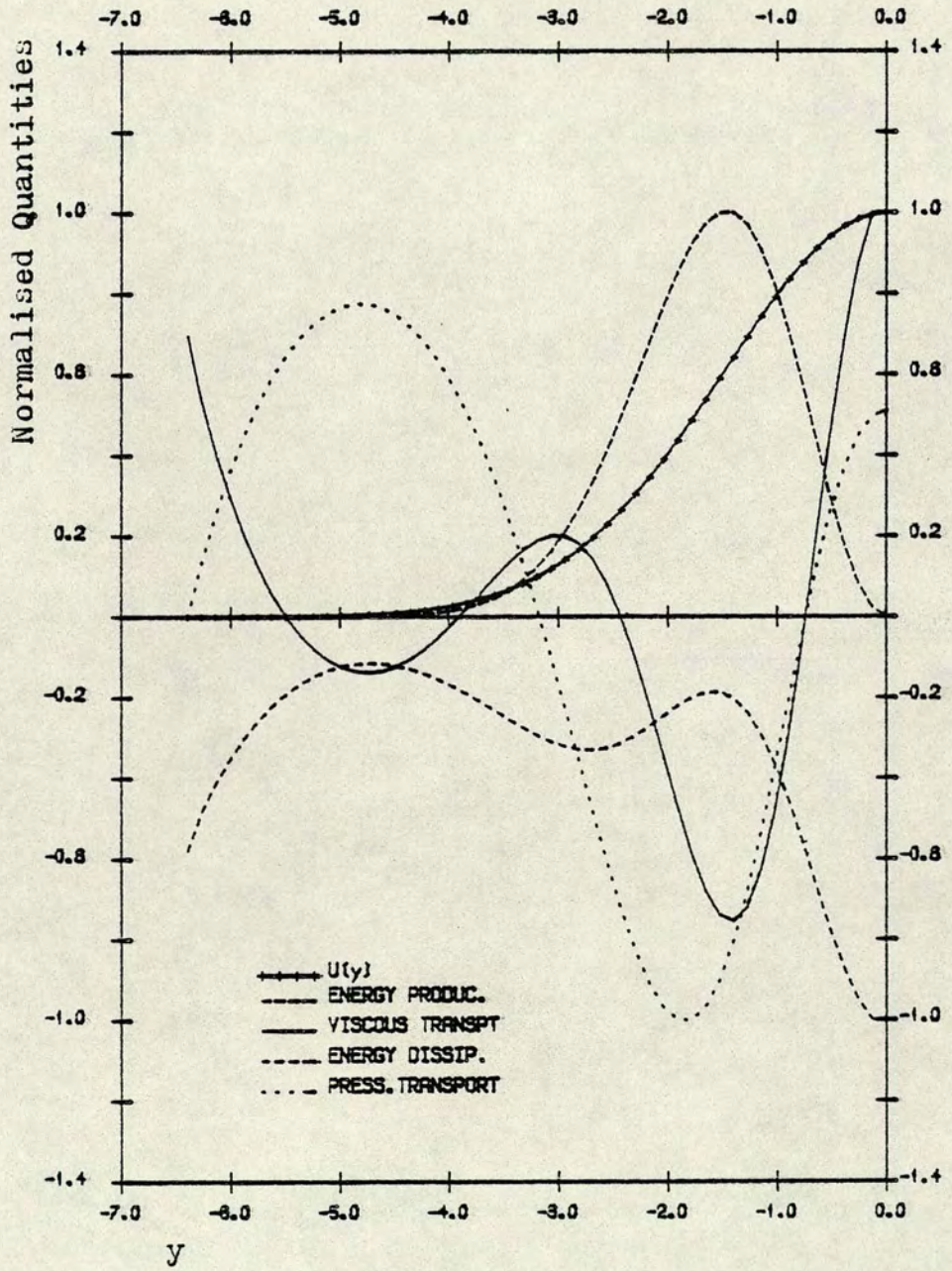

Figure 7.20: The subharmonic energy balance. The wake profile: xl=50, Re, α and c as in figure 7.16.

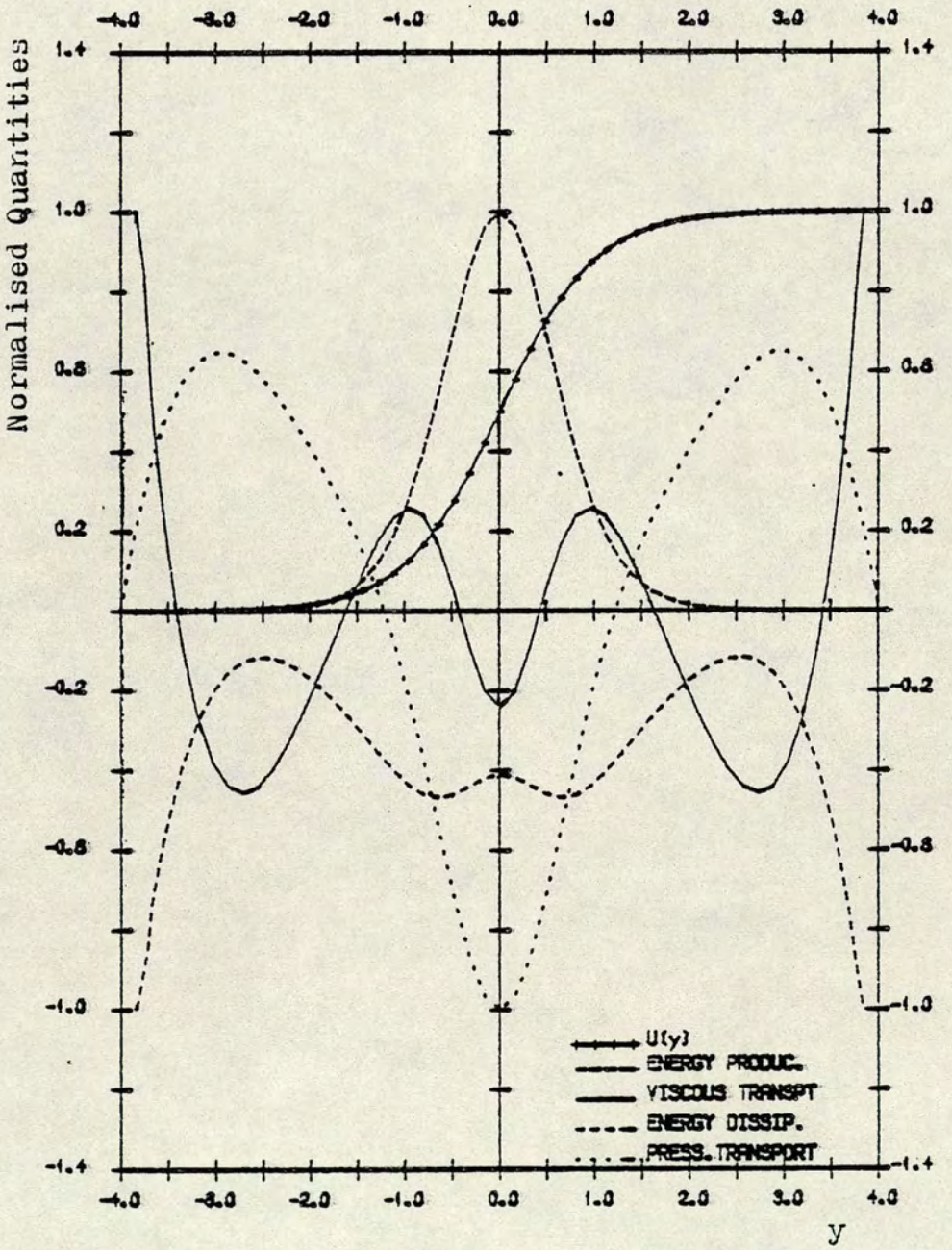

Figure 7.21: The subharmonic energy balance.

Tanh(y) profile: Re, α and c as in figure 7.17.

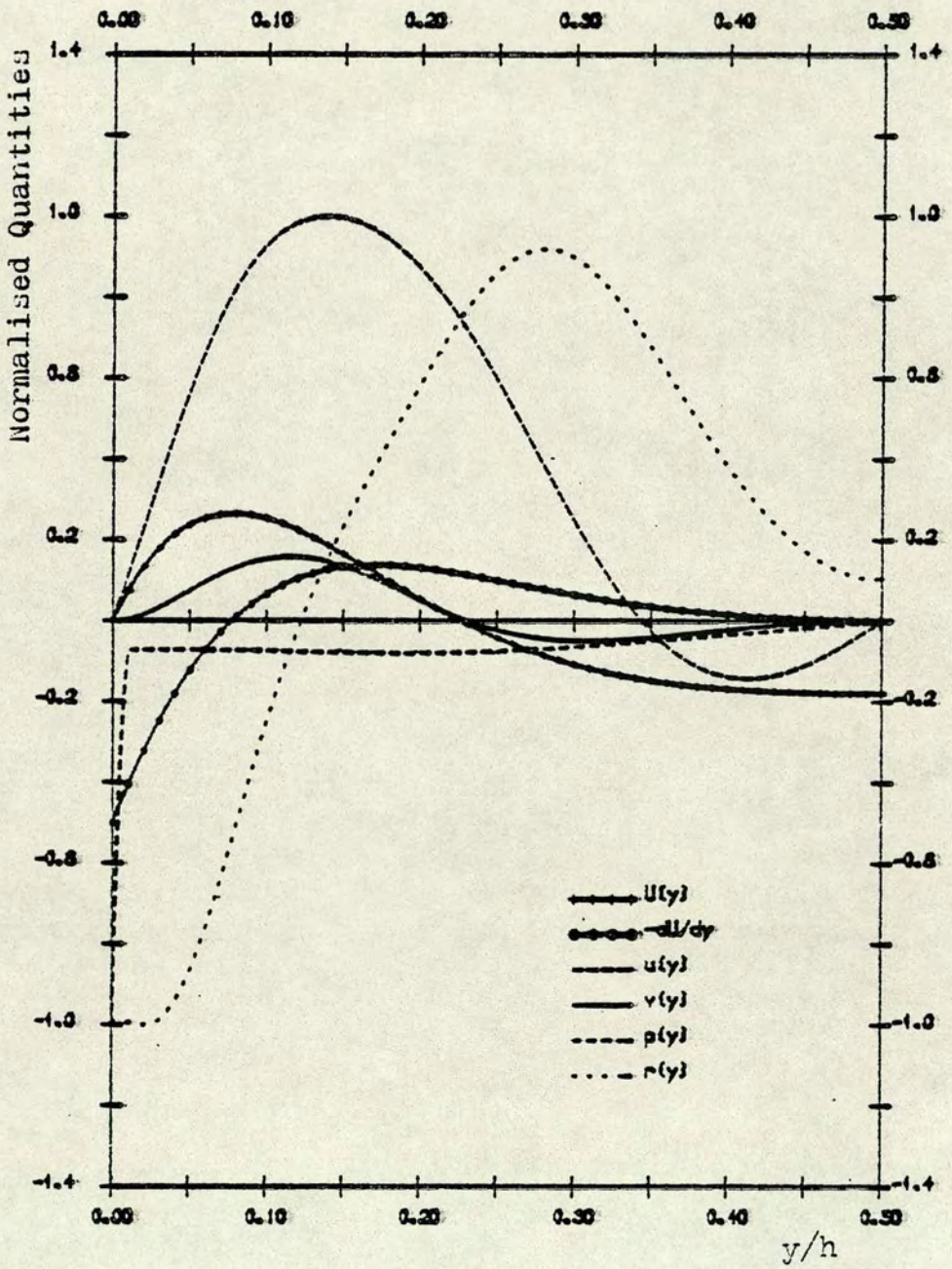

Figure 7.22: The fundamental disturbance velocities u(y), and v(y), pressure p(y) and vorticity r(y). Time-dependent flow: $\beta = 6$, $\omega_s t = 0^{\circ}$, $Re = 577.69$, $\alpha = 4.2585$ and $c = 0.0869$.

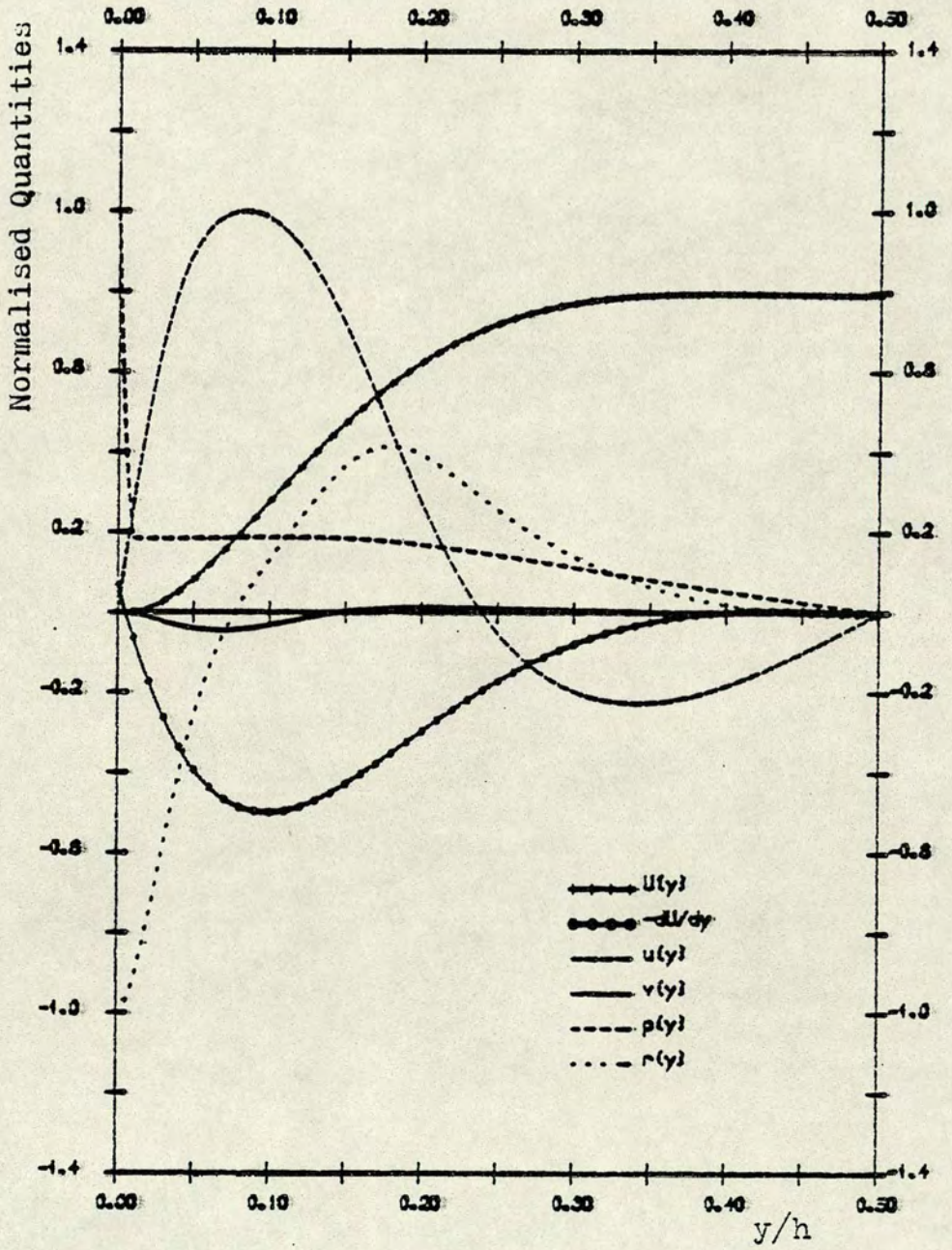

Figure 7.23: The fundamental disturbance velocities u(y) and v(y), pressure p(y) and vorticity r(y). Time-dependent flow: $\beta = 6$, $\omega_0 t = 145^\circ$. Re=1399.60, $\alpha = 3.94$ and c=0.30785.

CHAPTER EIGHT

CONCLUSIONS AND FUTURE WORK

1) Two numerical procedures have been investigated and used in this study: one spectral expansion technique and a finite difference method. The second was found to be superior in finding single eigenvalues and consequently for the determination of the critical Reynolds numbers, maximum amplification and neutral stability curves. It is superior in terms of computational efficiency and adaptation to different profiles. **For further stability investigations, two developments are required:**

a) Its extension to accommodate three dimensional stability. This is a straightforward task since the existing procedure can be extended easily to serve this purpose.

b) Extension to cylindrical coordinates especially to study the stability of time-dependent flow in circular pipes and the stability of other flows such as circular jets and wakes, whose stability have been studied in detail only in the inviscid form.

2) The simplest expansion, namely expansion in cos(y), was used during this study. An accelerated form which reduces the amount of computation time of the original expansion by 3 times has been developed. The method can be used directly for all types of flow in cylindrical coordinates. The expansion can be used with the LR algorithm as well as for finding individual eigenvalues. Accordingly, it can be used for the temporal as well as the spatial calculations, although in this case it will be more expensive than the finite difference method.

3) The linear stability theory has been used to investigate the stability characteristics of several flows: a) time-dependent flow b) U=sin(y) profiles c) wake behind a circular cylinder at different values of the distance x downstream d) the eigenfunctions and the energy balance of the mixing layer between two streams represented by a tanh(y) profile. A resonance mechanism which selects the critical and the most amplified wave numbers of profiles with inflexion points has been discovered. It is given in the form

$$\lambda = K\ L \qquad (A)$$

where λ is the wavelength of the disturbance in the two cases and L is the characteristic length of the flow which is generally equal to the distance between the points where U'=0 on both sides of the unstable inflexion point (for a free shear layers L is the width of the flow). The proportionality factor K plays a very important role in the instability characteristics of profiles with inflexion

points. The existence of (A) has very important consequences, and the results discovered in this study can be summarised as follows:

(i) The profiles are divided into groups according to the value of K :

(a) The value of K in the case of the temporally most amplified disturbance differs from that of the spatially most amplified one.

(b) These two values differ from the value of K at the critical Re.

(c) The common group to which the profile belongs is the one in which all its members share the same three values of K. These were designated K_c for the critical and K_{mt} and K_{ms} for the most amplified wavelengths in the temporal and the spatial cases respectively.

(d) Each self similar profile is a group by itself. Its members are the profiles at different distance downstream x. Each of these has a different width L.

(e) The time-dependent flow contains several groups of profiles. So far two groups have been studied in some detail. To the first group belong the profiles which have one core inflexion point (-U'>0) and to the second group belong the

profiles with more than one core inflexion point. The inflexion points near the wall ($-U'<0$), by their values of K belong to the first group despite the difference in the definition of L in the two groups.

(f) The sin(y) flow for $0 \leqslant y \leqslant n\pi$, where n is odd, has been investigated. The first pair of inflexion points was found to belong to the first time-dependent flow group. The second pair was found to belong to a different group. At the same time the first inflexion point of the profile sin(y) in the constant domain 3π was found to belong to the second group of the time-dependent flow profiles.

(ii) The values of K_s at the upper branch of the neutral curve for $Re \to \infty$ was also found to satisfy relation (A). However, this time, K_s was found to be constant for both groups of the time-dependent flow profiles with core inflexion points. For the wake profiles, K_s is also constant but different from that of the time-dependent flow profiles. K_s for the wall inflexion points is not a constant, apparently due to the truncation of U' by the wall.

(iii) Experimental evidence supported the validity of relation (A) in real flows. This means that the nonlinearity does not alter the mechanism of the

selection of the most amplified wavelengths, although it changes the value of K_m found in the linear case. In the case of the mixing layer the shift in the value of K_{ms} appears to be less than 20 percent of its linear value. The shift reduces the value of K_{ms} and thus reduces the wavelength for the same phase velocity. In other words it increases the frequency. In the case of other flows, the shift remains to be determined. This in turn will reveal more about the nonlinear behaviour of disturbances originating from inflexion instability in general. The value of K_{ms} was found to be proportional to the momentum thickness. The importance of this discovery is that the most amplified wavelength can be derived from the momentum equation.

(iv) The linear maximum growth rates were found equal to (constant x $|Ui'|/K_m$) for all groups of profiles and all flows in both the temporal and the spatial cases with the exception of the time-dependent wall inflexion points (see vii b below). This way, by knowing the maximum growth rate, K_m can be determined and vice versa.

(v) K is a function of Re. Away from the critical and the most amplified Reynolds numbers, the values of K differ from one profile to another inside the same group. However, for each group it was found that they are related to each other. Thus, by knowing the relation of K to Re for any profile inside the group,

the K of any other profile which a member of the group can be determined if Re is known and vice versa. This also will prove to be useful in estimating the critical Re for any specific member of the group.

(vi) It was shown, in the case of the mixing layers (and Jets), that the wavelength of the subharmonic, when its amplitude reaches saturation, is that of the fundamental disturbance.

(vii) In order to extend the scope of the work presented here, **the following investigations are suggested:**

(a) Experimental work is required, especially in free shear layers, in order to gain more information about the nonlinear growth and saturation amplitudes of the disturbances in the hope that they will scale directly to the factor K_m as was already done in the case of the linear growth rates or at least replace the higher order terms in the nonlinear (Landau) equations by factors which scale with K_m. If this proves possible, a considerable simplification of the nonlinear stability theory will be in sight. This task, of course, will be simpler for monochromatic disturbances. However, the experimental evidence given in chapter 4 indicates that even in the case of wave packets, the picture will be simplified when only the most amplified disturbance is

considered. (See also (iii) above).

(b) Further numerical work is required to reveal the other profile groups in the time-dependent flow system. There are several important flows which require further investigation in the light of the new approach. Examples are: the Falkner-Skan velocity profiles (boundary layer at separation) and Jets.

(c) Improvement in the accuracy of equations (4.57) and (4.59) for profiles which are not self similar is essential. This in turn may lead to the improvement in the accuracy of (4.61) and (4.62) which as was already mentioned are useful in experimental situations.

(d) The fact that the instability wavelength is proportional to the momentum thickness opens the door for analytical work to play an important role in stability theory.

4) The critical Reynolds number (Re_c) for profiles with inflexion points is generally lower than that of profiles whose instability is due to viscosity like plane Poiseuille flow. However, its value has some obscure relation to $|U'|_{max}$ and possibly to the wavenumber α. One of the tasks is to find such a relation since Re_c now remains the only parameter which can only be found by solving the full Orr-Sommerfeld equation. The lowest

critical Re_c was found in the case of U=sin(y), where Re_c=2. The next higher are those of the wake at large values of the distance downstream x. The U=tanh(y) profile has Re_c=7.6 for antisymmetric disturbances and Re_c=12 for coupled disturbances. For time-dependent flow profiles Re_c varies depending on the value of the frequency parameter β and the phase angle $\omega_0 t$. It was found to be high for high β. For the wall inflexion points, Re_c was found to decrease as the inflexion point moves away from the wall.

5) The critical phase velocity does not coincide with the velocity at the inflexion point. A general relation for the determination of the position of the critical point which is valid for all time-dependent flow profiles has been derived. The relation was found to have a good accuracy when used for the determination of the critical phase velocity.

6) The group velocities of the time-dependent flow wall inflexion points are about 1.5 times higher than their phase velocities. This is exactly the situation in the steady plane Poiseuille flow. The core inflexion points group velocity is about equal to the phase velocity. Profiles with small |Ui'| have mean velocities very close to the above two.

7) A short experimental investigation has been carried out to determine as accurately as possible the critical

Reynolds numbers of transition in pure oscillatory flow in circular pipe for $3.6 \leqslant \beta \leqslant 8.3$. The transition values have been determined at the centre of the pipe. These values were found to be lower than the average value given in the literature. Steep acceleration and deceleration were found to inhibit disturbance growth. It was found, in several cases, that near the wall the flow become turbulent for the whole cycle. The existence of the minor instability which marks the beginning of the instability at low Re was confirmed. The critical Re for this instability were also determined. These were found to occur at about a constant Re=1400 for all values of β.

Further work is required as follows:

a) The determination the critical Re for $0<\beta<3$ and $8<\beta<20$, since these are the ranges not investigated fully.

b) the stability of pulsatile flow, i.e. oscillatory flow with nonzero mean, in the range of the in vivo flows should be investigated since such an investigation has not been accomplished yet. In this case the mean part should be between 5 and 30 percent of the oscillatory part, while $5<\beta<20$ [Nerem and Seed (1972)].

c) Detailed measurements of turbulent quantities especially u, v fluctuations and the Reynolds stress are necessary. Some measurements have already been made by Ramaprian and Tu(1980) and Tu and Ramaprian (1983) for oscillatory flow with a mean component

and by Hino et al (1983) for pure oscillatory flow in a duct. Those concentrated more on the variation of these quantities with time. The last authors concentrated their work on the viscous sublayer. The author could not find any measurements which can be compared directly to the numerical calculations, some of which are given in chapter 7. More flow visualisation experiments are necessary in order to understand:

(i) the role of the instability of the central region in the onset of the instability of the flow near the wall and the flow in general. The numerical approach used in chapter 6 was based on this idea. The inflexion period of the central area is about twice that of the wall area and this area represents about 70 % of the flow field.

(ii) the role of the instability of the profiles with small phase angle $\omega_0 t$ in onsetting the minor and especially the major instability through secondary instability when β is small.

(iii) the role of the large scale structure in the turbulent time-dependent flow especially that of the wall region.

8) A numerical investigation of the stability of time-dependent flow in a channel has been accomplished. The profiles which determine the instability of the flow are those with $\partial P/\partial x=0$. Since the instability is due to

inflexion points, the above criteria is not applicable on the profiles with $\partial P/\partial x=0$ for $\beta<4$, since these do not possess inflexion points. The agreement between the experimentally measured critical Re and those calculated theoretically is good for $6\leqslant\beta\leqslant 20$. A formula for the critical Re at large β was derived. Another formula for the critical wavenumber was given for $\beta\geqslant 11$. The frequency of the disturbances are then automatically found. The calculations show that the instability frequency increases as β increases. The origin of the minor instability has also been investigated. The calculations suggest that it originates from the instability in the early part of the acceleration phase.

Further work is required as follows:

a) Investigation of the stability of the flow with $\beta<6$. Some ideas were given in section 7.8 about the approach recommended.

b) The instability of the flow with nonzero mean is also important.

c) Numerical study of the instability of the circular pipe flow is also important. It is expected that the critical Re would be close to those already calculated for the duct flow. This is because the experimental data used for comparison with the numerical results in chapter 6 were for circular pipes. However, the effects of torsional and the meridianal modes are important [Pekeris (1948)]. It is also important to understand the contributions of

these modes to the inflexion instability in general.

9) The energy balance of both the fundamental and the subharmonic disturbances in several profiles with inflexion points has been investigated. The energy quantities have been explained. The disturbance velocities, pressure and vortices were also obtained. The interesting feature is that certain rules governing the disturbance velocities, pressure, vorticity and the energies were found to be general for all symmetrical profiles. The method in general may prove useful in the now widely used modelling of the energy quantities through the main flow quantities since the comparison will be easier in the studies similar to the one here. This can be considered a project for further research.

R E F E R E N C E S

ACHARYA, M. and REYNOLDS, W.C. (1975):
Measurements and predictions of a fully developed turbulent channel flow with imposed controlled oscillations. Stanford Univ. Thermoscience Div, Tech. Rep. no. TF-8.

ARFKEN, G. (1970):
Mathematical methods for physicists. Academic Press.

AYRES, F.J. (1962):
Matrices. Schaum's Outline Series. MacGraw-Hill.

BARRY, M.D.J. and ROSS, M.A.S. (1970):
The flat plate boundary-layer. Part 2: The effect of increasing thickness on stability. J. Fluid Mech. 43, p 812.

BEARMAN, P.W. (1967):
On vortex sheet wakes. J. Fluid Mech. 28, p 625.

BRADSHAW, P., FERRISS, D.H. and JOHNSON, R.F. (1964):
Turbulence in the noise-producing region of a circular jet. J. Fluid Mech. 19, p 591.

BRADSHAW, P. (1976):
Turbulence. Topics in applied physics. Vol 12. Springer-Verlag.

BROWN, G.L. and ROSHKO, A. (1974):
On density effects and large structure in turbulent mixing layers. J. Fluid Mech. 64, p 775.

BROWND, F.K. and TROUTT, T.R. (1980):
A note on spanwise structure in the two-dimensional mixing layers. J. Fluid Mech. 97, p 771.

CALVERT, J.R. (1967):
Experiments on the low-speed flow past cones. J. Fluid Mech. 27, p 273.

CEBECI, T. and KELLER, H.B.
Stability calculation for a rotating disk. AGARD PC 224, Paper 7.

CHANDRASEKHAR, S. (1954):
On the characteristic value problems in high order differential equations which arise in studies of hydrodynamic stability. Amer. Math. Monthly 61, p 32.

CHANDRASEKHAR, S. (1961):
Hydrodynamics and hydrodynamic stability. Clarendon Press, Oxford.

CHANDRSUDA, C., MEHTA, R.D., WEIR, A.D. and BRADSHAW, P. (1978):
Effect of free stream turbulence on large scale structure in turbulent mixing layers. J. Fluid Mech. 85, p 693.

COLLINS, J.I. (1963):
Inception of turbulence at the bed under periodic gravity waves. J. Geophys. Res. 18, p 6007.

CORCOS, G.M. and SHERMAN, F.S. (1976):
Vorticity concentration and the dynamics of unstable free sheer layers. J. Fluid Mech. 73, p 241.

CORNER, D., HOUSTON, D.J.R. and ROSS, M.A.S. (1976):
Higher eigenstates in boundary layer stability theory. J. Fluid Mech 77, p 81.

COURANT, R. and HILBERT, D. (1953):
Methods of mathematical physics. J Wiley & Sons.

DANTAN, P., de JOUVENEL F., and ODDOU C. (1976 a):
A transition laminaire-turbulent en ecoulement pulsatile. Application a la circulation souguine. J. Phys. 37, p 157.

DANTAN, P., de JOUVENEL F., and ODDOU C. (1976 b):
Stabilite´ d´un ecoulement pulse´ incompressible en tube cylindrique rigide. J. Phys. 37, p 233.

DAVEY, A. (1977):
On the numerical solution of difficult eigenvalue problems. J. Comput. Phys. 30, p 137.

DAVIS, S.H. (1976):
The stability of time-periodic flow. Annual Review of Fluid Mechanics, Vol. VIII, p 57, Annual Review, Inc. Palo Alto.

DAVIS, S.H. and KERCZEK, von C. (1973):
A reformation of energy stability theory. Arch Rat. Mech. Anal. 52, p 112.

DIMOTAKIS, P.E. and BROWN, G.L. (1976):
The mixing layer at high Reynolds number: Large-Structure dynamics and entrainment. J. Fluid Mech. 78, p 535.

DIPRIMA, R.C. and SANI, R. (1965):
The Convergence of Tyler-Dean stability problem. Quart. Appl. Math. 23, p 183.

DOLPH, C.L. and LEWIS, D.C. (1958):
The application of infinite system of ordinary differential equations to perturbations of plane Poiseuille flow. Quart. Appl. Math. 16, p 97.

DRAZIN, P.G. and HOWARD, L.N. (1966):
Hydrodynamic stability of parallel flow of inviscid fluid. Adv. Appl. Mech. 9, p 1.

DRAZIN, P.G. and REID, W.H. (1981):
Hydrodynamic stability. Cambridge University Press.

FJORTAFT, R. (1950):
Application of integral theorems in deriving criteria of instability for laminar flows and for baroclinic circulations. Geofys. Pupl., Oslo 17, No 6, pp 1-52 and p 132.

FOOTE, J.R. and LIN, C.C. (1980):
Some recent investigation in the theory of hydrodynamic stability. Quart. Appl. Math. 8, p 265.

FOX, L. and PARKER, I.B. (1968):
Chebychev polynomials in numerical analysis. Oxford University Press.

FRANCIS, J.G.F. (1961,1962):
The QR transformation. Parts I and II. Computer J. 4, p 265 and p 332.

FRENCH, A.P. (1971):
Vibrations and waves. The M.I.T. Introductory Physics Series, Nelson.

FROBERG, C-E (1969):
Introduction to numerical analysis. (Second ed.), Addison-Wesley.

GARY, J. and HELGASON R. (1970):
A matrix method for ordinary differential eigenvalue problems. J. Comput. Phys. 5, p 169 .

GASTER, M. (1962):
A note on the relation between temporally increasing and spatially increasing disturbances in hydrodynamic stability. J. Fluid Mechanics 14, p 222.

GATASKI, T.B. (1978):
Sound Production due to large-scale coherent structures. AIAA Journal 17, p 614.

GERRARD, J.H. (1971):
An experimental investigation of the pulsating turbulent flow in a water tube. J. Fluid Mech. 46, p 43.

GILBRECHT, D.A. and COMBS, G.D. (1963):
Critical Reynolds numbers for incompressible pulsating flow in tubes. Developments in theoretical and applied mechanics. Vol. 1, p 292. Plenum Press, New York.

GILL, A.E. (1965):
A mechanism for instability of plane Couette flow and of Poiseuille flow in a pipe. J. Fluid Mech. 21, p 503.

GRIFFIN, O.M. (1978):
A universal Strouhal number for the 'locking on' of vortex shedding to the vibrations of bluff cylinders. J. Fluid Mech. 85, p 591.

GROSCH, C.E. and SALWEN, H. (1968):
The stability of steady and time-dependent plane Poiseuille flow. J. Fluid Mech. 34, p 177.

GROSCH, C.E. and SALWEN, H. (1978):
The continuous spectrum of the Orr-Sommerfeld equation. Part 1: The spectrum of the eigenfunctions. J. Fluid Mech. 87, p 33.

GUPTA, S.C. and GARG V.K. (1981):
Effect of velocity distribution on the stability of developing flow in a channel. J. Phys. Soc. of Japan 50(2), p 673.

GUTMARK, E. and HO, C-M. (1980):
Feedback mechanism in a free jet. Bull. Am. Phys. Soc. Sec.II. 25, p 1102.

HAMA, F.B., WILLIAM, S.D. and FASEL, H. (1979):
Flow field and energy balance according to the spatial linear stability theory of the Blasius boundary layer. In Proc. IUTAM SYMPOSIUM STUTTGART/GERMANY, Sep. 16-22, 1979: Laminar-turbulent transition. Edited by EPPLEN, R. and FASEL, H., Springer-Verlag (1980).

HEISENBERG, W. (1924):
Ann. Phys. Lpz 74, p 577. Translated as: On the stability and turbulence of fluid flows. Tech. Memor. Nat. Adv. Comm. Aero. Wash. No 1291 (1951).

HERMAN, M. and JIMENEZ, J. (1982):
Computor analysis of a high-speed film of the turbulent plane mixing layer. J. Fluid Mech. 119, p 323.

HINO, M. and SAWAMOTO, M. (1975):
Linear stability analysis of an oscillatory flow between parallel plates. Proc. 7th symp. on Turbulence, (ed. Sato, H. and Ohji, M.), pp 1-7. Institute of Space and Aeronautics, University of Tokyo.

HINO, M., SAWAMOTO, M. and TAKASU, S. (1976):
Experiments on transition to turbulence in oscillatory pipe flow. J. Fluid Mech. 75, p 193.

HINO, M., KASHIWAYANGI, M., NAKAYAMA, A., and HARAT, T. (1983):
Experiments on the turbulence statistics and structure of a reciprocating oscillatory flow. J. Fluid Mech. 131, p 363.

HO, C-M. and HUANG L. (1982):
Subharmonics and vortex merging in mixing layers. J. Fluid Mech. 119, p 443.

HO, C-M. and NOSSEIR, N.S. (1981):
Dynamics of an impinging jet. Part 1: The feedback phenomenon. J. Fluid Mech. 105, p 119.

HOILAND, E. (1953):
On two dimensional perturbation of linear flow. Geofys. Pupl. 18, No 9, p 1.

HOUSTON, D.J.R. (1976):
Numerical studies in hydrodynamic stability theory. PhD thesis.

HOWARD, L.N. (1960):
Note on a paper of John W. Miles. J. Fluid Mech. 10, p 509.

ITOH, N. (1979):
Theory for wave-packet disturbances in parallel and nearly parallel flows. In Proc. IUTAM SYMPOSIUM STUTTGART/GERMANY, September 16-22, 1979: Laminar-turbulent transition. Edited by EPPLEN, R. and FASEL, H., Springer-Verlag, (1980).

JIMENEZ, J. (1983):
A spanwise structure in the plane shear layer. J. Fluid Mech. 132, p 319.

JOHNSON, L.W. and RIESS, R.D. (1977):
Numerical analysis. Addison-Wesley.

JORDINSON, R. (1968):
The transition from laminar to turbulence flow over a flat plate. Space amplification. Numerical solution of Orr-Sommerfeld equation. PhD thesis.

JORDINSON, R. (1971):
Spectrum of eigenvalues of the Orr-Sommerfeld equation for Blasius flow. Phys. Fluids 14, p 2535

KAMPHUIS, J.W. (1975):
Friction factor under oscillatory waves. Proc. Am. Soc Civ. Engrs. J. Waterways harbors and coastal Engng. Div. Vol. 101, no. WW2, p 135.

KAPLAN, R.E. (1964):
The stability of laminar incompressible boundary layers of compliant boundaries. Aeroelastic and structures research laboratory. Report No ASRL-TR 166-1, Massachusetts institute of technology.

KELLY, R.E. (1967):
On the stability of an inviscid shear layer which is periodic in space and time. J. Fluid Mech. 27, p 657.

KERCZEK, von C. (1982):
The instability of oscillatory plane Poiseuille flow. J. Fluid Mech. 116, p 91.

KERCZEK, von C. and DAVIS, S.H. (1972):
The stability of oscillating Stokes layer. Studies in Applied Math. 51, p 239.

KERCZEK, von C. and DAVIS, S.H. (1974):
Linear stability theory of oscillatory Stokes layers. J. Fluid Mech. 62, p 753.

KIM, H.T., KLINE S.J. and REYNOLDS, W.C. (1971):
The production of turbulence near a smooth wall in a turbulent boundary layer. J. Fluid Mech. 50, p 133.

LANCZOS, C. (1957):
Applied analysis. Prentice-Hall Math. Ser.

LANCZOS, C. (1966):
Discourse in Fourier analysis. Oliver & Boyed, Edinburgh.

LI, H. (1954):
Stability of oscillating laminar flow along a wall. U.S Army, Beach Erosim Board, Tech. memo No 47.

LIGHTHILL, M.J. (1963):
Chapters 1 and 2 of 'Laminar Boundary Layers'. Edited by L. Rosenhead, Clarendon Press, Oxford.

LIGHTHILL, M.J. (1970):
Osborne Reynolds and Engineering Science Today. Edited by McDowell, D.M. and Jackson, J.D., Manchester University Press.

LIN, C.C. (1945):
On the stability of two-dimensional parallel flows. Quart. Appl. Math. 3. Parts 1-3, pp 117-42,218-34 and 277-301.

LIN, C.C. (1955):
The theory of hydrodynamic stability. Cambridge University Press.

LU, S.Z., NUNGE, R.J., ERIAN, F.F. and MOHAJERY, M. (1973):
Measurements of pulsating turbulent water flow in a tube. Prog. 3rd Symp. On turbulence in liquids. University of Missouri Rolla, p 375.

MACK, L.M. (1976):
A numerical study of the temporal eigenvalue spectrum of the Blasius boundary layer. J. Fluid Mech. 73, p 497.

MERKLI, P. and THOMANN, H. (1975):
Transition to turbulence in oscillatory pipe flow. J. Fluid Mech. 68, p 567.

MICHALKE A. (1964):
On the inviscid instability of hyperbolic tangent velocity Profile. J. Fluid Mech. 21, p 543.

MICHALKE, A. (1965):
On spatially growing disturbances in an inviscid shear layer. J. Fluid Mech. 23, p 521.

MICHALKE, A. (1969):
A note on spatially growing three-dimensional disturbances in a free shear layer. J. Fluid Mech. 38, p 765.

MIKSAD, R.W. (1972):
Experiments on the nonlinear stages of free shear layer transition. J. Fluid Mech. 56, p 695.

MISES, R., and FRIEDRICHES, K.O. (1942):
Fluid dynamics. Applied mathematical sciences Vol. 5 (1971), pp 285-97. New York. Springer-Verlag.

MOLER, C.B. and STEWART, G.W. (1973):
An algorithm for generalised matrix eigenproblems. SIAM J. Numer. Anal., Vol 10, p 241.

MONKEWITZ, M.A. (1978):
Analytic pseudoorthogonalization methods for linear two point boundary value problems, illustrated by the Orr-Sommerfeld equation. ZAMP 29, p 861.

MONKEWITZ, P.A. and HURRE, P. (1982):
Influence of the velocity ratio on spatial instability of mixing layers. Phys. Fluids 25, p 1137.

MULLER, D.E. (1956):
A method for solving algebraic equations using automatic computer. Math. Tables Aids Comp. 10, p 208.

NAKAYA, C. (1976):
Instability of the near wake behind a circular cylinder. J. Phys. Soc. Japan 41, p 1087.

NAYFEH, H.A. and PADHYE, A. (1979):
Relation between temporal and spatial stability in three-dimensional flows. AIAA J. 78, p 1084.

NEREM, R.M. (1974):
Paper presented as an invited lecturer to the Laenne society of the American Heart Association 47th scientific sessions meeting. Dallas, November 18-21.

NEREM, R.M. and SEED, W.A. (1972):
An in-vivo study of aortic flow disturbances. Cardiovascular Research 6, p 14.

NEREM, R.M., SEED, W.A. and WOOD, N.B. (1972):
An experimental study of the velocity distribution and transition to turbulence in the aorta. J. Fluid Mech. 52, p 137.

NG, B.S. and REID, W.H. (1979):
An initial value method for eigenvalue problems using compound matrices. J. Comput. Physics 30, p 125.

NISHIOKA, M. and SATO, (1978):
Mechanism of determination of the shedding frequency of vortices behind a cylinder at low Reynolds numbers. J. Fluid Mech. 89, p 49.

NYCHAS, S.G., HERSHEY, H.C. and BRODKEY, R.S. (1973):
A visual study of turbulent shear flow. J. Fluid Mech. 61, p 513.

ODDOU, C., DANTAN, P., FLAUD, P. and GEIGER, D. (1979):
Aspects of hydrodynamics in cardiovascular research. Chapter 10 of Quantitative Cardiovascular studies Clinical and Research Applications of Engineering Principles, Edited by Hwang N.H.C, Gross D. R. and Patel D. J. University Park, Baltimore.

OHMI, M. and IGUCHI M. (1982):
Critical Reynolds number in an oscillating pipe flow. Bulletin of the JSME. Vol. 25, p 165.

OHMI, M., IGUCHI M. and URAHATI, I. (1982):
Transition to turbulence in a pulsatile pipe flow. Part 1: Wave forms and distributions of pulsatile velocity near the transition region. Bulletin of the JSME, Vol. 25, p 173.

ORR, W.M.F. (1907):
The stability or instability of the steady motions of a perfect fluid and viscous liquid. Proc. Roy. Irish Acad. A. 27, p 9 and p 69.

ORSZAG, S.A. (1971):
Accurate solution of the Orr-Sommerfeld stability equation. J. Fluid Mech. 50, p 689.

OSBORNE, M.R. and MICHAELSON S. (1964):
On the numerical solution of eigenvalue problems in which the eigenvalue parameter appears nonlinearly with an application to different equations. Computer J. 7, p 66.

OSBORNE, M.R. (1967):
Numerical methods for hydrodynamic stability problems. SIAM J. Appl. Math. 15, p 539.

PARKER, K.H. (1977):
Instability in arterial blood flow. In Hwang N.H.C. and Normann N.A. (eds.) Cardiovascular flow dynamics and measurements, p 439-47. University Park Press, Baltimore.

PATEL, M.H. (1977):
On turbulent boundary layers in oscillatory flow. Proc. Roy Soc. A 353, p 121.

PEKERIS, C.L. (1948):
Stability of the laminar flow through a straight pipe of circular cross-section to infinitesimal disturbances which are symmetrical about the axis of the pipe. N.A.S. 34, p 285

PELISSIER, R. and CLARION, C. (1975):
A theoretical and experimental study of the velocity distribution and transition to turbulent in free oscillatory flow. J. Fluid Mech. 70, p 59.

RAMAPRIAN, B.R. and TU, S.W. (1980):
Experiments on transitional oscillatory pipe flow. J. Fluid Mech. 100, p 544.

RAYLEIGH, W.S. (1880):
On the stability or instability of certain fluid motions. Proc. London Math. Soc. 9, p 57.

RECHISHAUSER, H. (1958):
Solution of eigenvalue problems with LR-transformation. Appl. Math. Ser., nat. Bur. Stand. 49, pp 47-81.

REIDEL, H.P., KAMPHUIS, J.W and BREBNER, A. (1972):
Measurements of bed shear stress under waves. Proc. of 13th coastal Engineering conference, Vancouver, pp 587-603.

ROSENBLAT, S. (1968):
Centrifugal instability of time-dependent flows. Part 1: Inviscid periodic flows. J. Fluid Mech. 33, p 321.

ROSHKO, A. (1954):
On the drag and shedding frequency of two-dimensional bluff bodies. NACA Tech. Note No 3169, pp 1-28

ROSHKO, A. (1955):
On the wake and drag of bluff bodies. J. Aeron. Sci. 22, p 124.

ROSS, J.A., BARNES, F.H., BURNS, J.G. and ROSS, M.A.S. (1970):
A flat plate boundary layer. Part 3: Comparison of the theory and the experiment. J. Fluid Mech. 43, p 819.

SALWEN, H. and GROSCH, C.E. (1972):
The stability of Poiseuille flow in a pipe of circular cross section. J. Fluid Mech. 54, p 93.

SARPKAYA, T. (1966):
Experimental determination of the critical Reynolds number for pulsating Poiseuille flow. Trans. ASME 88, p 589

SCHLICHTING, H. (1933):
Zur Entstchung der turblenz bei der plattenstromung. Nachr. Ges. Wiss. Gottingen Math-Phys. k1., p 181.

SCHLICHTING, H. (1968):
Boundary layer theory. (6th ed.) MacGraw-Hill.

SERGEEV, S.I. (1966):
Fluid oscillations in pipes at moderate Reynolds numbers. Fluid Dynamics (Mekh. Zhid.), No.1, p 21-22.

SHEN, S.F. (1961):
Some considerations of laminar stability of incompressible time-dependent basic flow. J. Aerospace Sci. 28, p 397.

SIMMONS, J.E.L. (1977):
J. Aero. Quart. 28, p 15.

SOMMERFELD, A. (1908):
Ein Beitrag zur hydrodynamischen Erklaerung der turbulenten Fluessingkeitsbewegungen Proc. 4 th International Congress Mathematics Rome, Vol III, p 116.

STUART, J.T. (1960):
On the nonlinear mechanics of wave disturbances in stable and unstable parallel flows. I: The basic behaviour in plane Poiseuille flow. J. Fluid Mech. 9, p 353.

TAYLOR, G.I. (1915):
Phil. Trans. A. 215, p 23.

TAYLOR G.I. (1923):
Stability of viscous liquid contained between two rotating cylinders. Phil. Trans. Roy. Soc. A 223, p 289.

THOMAS, L.H. (1953):
The stability of plane Poiseuille flow. Phys. Rev. (2) 91, p 780.

TOLLMEIN, W. (1929):
Ncht. Ges. Wiss. Gottingen, Math-Phys. kl., p 21. Translated as: The production of turbulence. Tech. Memo. Nat. Adv. Comm. Aero. Wash. No 609 (1931).

TOLLMEIN, W. (1935):
English translation: "General instability criterion of laminar velocity distributions". Tech. Memor. Nat. Adv. Comm. Aero. Wash. No 792 (1936). p 124.

TOWNSEND, A.A. (1976):
The structure of turbulent shear flow. (Second ed.) Cambridge University Press.

TRITTON, D.J. (1977):
Physical fluid dynamics. Van Nostrand Reinhold Company.

TROMANS, P. (1976):
The stability of oscillating pipe flows. Lectures given at the Colloquim Euromech 73 on oscillatory flows in ducts. Marseille, France. April 1976.

TU, S.W. and RAMAPRIAN B. R. (1983):
Fully developed periodic turbulent pipe flow. Parts 1 and 2. J. Fluid Mech. 137, p 31 and p 59.

UCHIDA, S. (1956):
The pulsating viscous fluid superposed on the steady motion of incompressible fluid in circular pipe. ZAMP 7, p 403.

VANSTIJN, TH.L. and VAN de VOOZEN A.I. (1980):
An accurate method for solving the Orr-Sommerfeld equation. J. Engng. Math. 14, p 17.

VINCENT, G. E. (1957):
Contribution to the study of sediment transport on a horizontal bed due to wave action. Proc. conf. Coastal Engng, Florida 1957, p 326. Council on Wave Res., The Engng. Foundation.

WAZAN, A.R., OKAMURA T.T and SMITH A.M.O. (1967):
Stability of laminar boundary layers at separation. Phys. Fluids 10, p 2540.

WIDNALL, S. and SULLIVAN J.P. (1973):
On the stability of vortex rings. Proc. Royal. Soc. A 332, p 335.

WILKINSON, J.H. (1965):
The algebraic eigenvalue problem. Clarendon Press, Oxford.

WINANT, C. D. and BROWND F.K. (1974):
Vortex pairing, the mechanism of turbulent mixing-layers growth at moderate Reynolds number. J. Fluid Mech. 63, p 237.

WYGNANSKI, I., OSTER D., FIEDLER H. and DZIOMBA B. (1970):
On the pressure of a quasi two-dimensional eddy-structure in a turbulent mixing layer. J. Fluid Mech. 93, p 325.

YANG, W.H. and YIH C.S. (1977):
Stability of time-periodic flows in a circular pipe. J. Fluid Mech 82, p 497.